Correlative approach towards integrated casting-heat treatment route and machining for sustainable ADI manufacturing

Anil Meena

École doctorale n° 432 : Sciences des Métiers de l'Ingénieur

Doctorat ParisTech

T H È S E

pour obtenir le grade de docteur délivré par

l'École Nationale Supérieure d'Arts et Métiers

Spécialité " Procédés de fabrication "

présentée et soutenue publiquement par

Anil MEENA

le 13 Juillet 2012

Correlative approach towards integrated casting-heat treatment route and machining for sustainable ADI manufacturing

Directeur de thèse : **Mohamed EL MANSORI**
Co-encadrement de la thèse : **Patrick GHIDOSSI**

Jury
M. Jean-Marie DREZET, Professeur, Ecole Polytechnique Fédérale de Lausanne, Suisse   Président
M. Thomas R. KURFESS, Professeur, BMW Chair of Manufacturing, Clemson University, USA   Rapporteur
M. François BAY, Professeur, CEMEF, Mines ParisTech, France   Rapporteur
M. Mohamed EL MANSORI, Professeur, LMPF-EA 4106, Arts et Métiers ParisTech, France   Examinateur
M. Patrick GHIDOSSI, Maître de Conférences, LMPF-EA 4106, Arts et Métiers ParisTech, France   Examinateur
M. Mohamed BOUDIFA, Ingénieur R&D, CRITT-MDTS, France   Invité
M. Frank KOPPKA, Chef de Service, Renault, France   Invité

T
H
È
S
E

Arts et Métiers ParisTech - Centre de Châlons en Champagne
Laboratoire de Mécanique et Procédés de Fabrication - (LMPF, EA 4106)

2012-ENAM-0026

Dedicated to my parents

Acknowledgements

I would like to express my deep and sincere gratitude to my thesis director, Prof. Mohamed EL MANSORI for his guidance and encouragement throughout this research. I would also like to acknowledge the support and guidance provided by my co-director, Dr. Patrick GHIDOSSI. I really appreciate his co-operation, continuous support and kind assistance during my stay in France.

I would like to sincerely thank Prof. Jean-Marie DREZET for accepting of being the president of the PhD committee as well as for his insightful comments on the thesis. I am extremely grateful to Prof. Thomas KURFESS and Prof. François BAY for accepting to be the referees and for their valuable time and effort in reviewing the thesis. I would also like to thank Dr. Mohamed BOUDIFA and Dr. Frank KOPPKA for their participation in my PhD committee.

I would also like to thank CRITT-MDTS (technical developments and research centre) and Dr. Mohamed BOUDIFA (R&D engineer) for providing technical assistance in material characterization throughout this research.

I am very grateful to the Region Champagne-Ardenne and program CPER-UCOFAM for providing financial support for this project, which enabled me to undertake the PhD program at Arts et Métiers ParisTech, France.

I would also like to thank all colleagues and technicians who have worked with me on some aspects of this project and provided their support and encouragement.

Last but not least, I would like to thank my family for all their support, love and encouragement.

Abstract

The use of iron and steel, in particular, in automotive and construction industries, is considerable and widespread. However, the environmental impacts of material production and processing, particularly those related to energy, are rapidly increasing. These impacts can be reduced, to some extent, by development of either a suitable material or by implementing a novel process route to improve the material efficiency of the existing materials. The introduction of new or modified materials and processes for a given application is dependent on satisfying a lot of different parameters (production costs, recyclability and machinability, etc.). In such circumstances, the recent emergence of near-net shape austempered ductile iron (ADI) castings can be considered as a significant economic advantage to the increasing industrial demand for cost and weight efficient materials.

The present study is thus dedicated to the development of an innovative methodology for austempered ductile iron (ADI) manufacturing considering all production aspects such as melt treatment, casting, heat treatment and machining. The innovative process design introduces the integrated approach towards casting and heat treatment practices for the production of near-net shape light weight ADI casting in a permanent mould. It is based on the fundamental correlation between the production conditions and its combined influences on the microstructure and mechanical properties of ADI. The both casting and heat treatment practices are implemented efficiently in a control manner using thermal analysis adaptive system (melt quality) and fluidized bed heat treatment facility (controlled and uniform heat treatment) respectively to enhance the foundry practice for ADI production. In addition, the present study introduces a correlative thermal methodology approach to understand the castability of ductile iron in a permanent mould for the novel ADI production. The approach utilizes the thermal characteristics of the melt to correlate the combined influence of the heat transfer at melt/mould interface, and melt flow through the critical sections of the casting to produce a sound ductile iron casting and to predict the casting defects. Finally, the green manufacturing of the novel ADI was introduced by implementing the dry and near dry machining process. The key aspect of the machining characteristics of novel ADI was investigated with respect to the tool wear mechanisms, chip formation characteristics and the machined surface quality.

The combined correlative approaches utilize in the present study comes out with the foundation of the green manufacturing of ADI. In addition, it provides the key findings aim to (i) understand the influence of microstructural characteristics of novel ADI on its mechanical properties, (ii) demonstrate the influence of thermal characteristics of melt on the castability of ductile iron in a permanent mould, and (iii) correlating the machining characteristics of ADI with its microstructure and production conditions.

Contents

List of Figures

List of Tables

Résumé en français

Ce travail de thèse s'attachera à l'étude de l'influence des paramètres de process de fabrication sur l'usinabilité d'un nouveau type de fonte ADI élaborée dans la chaude de coulée.

Une première partie d'introduction expose l'objectif de cette thèse.

Le deuxième chapitre consistera en une analyse bibliographique concernant l'état de l'art associé à la fonte ADI, en particulier les process d'obtention de lit de fusion, les influences des différents éléments d'alliages et des cycles de traitements thermiques sur les caractéristiques métallurgiques et mécaniques de la fonte ADI. L'usinabilité de la fonte ADI est également analysée (paramètres intrinsèques de la fonte, outils utilisés, process d'usinages écologiques).

Le troisième chapitre présente les différentes techniques et équipements expérimentaux utilisés pour ce travail de recherche.

Le quatrième chapitre s'attachera à analyser expérimentalement les influences des paramètres des traitements thermiques de ce processus innovant sur les caractéristiques mécaniques et métallurgiques de cette nouvelle fonte ADI obtenue dans la chaude de coulée.

Le cinquième chapitre prolonge le précédent et présente une méthode de simulation du refroidissement d'une éprouvette réalisée en fonte ADI obtenue dans la chaude de coulée.

Le sixième chapitre étudie expérimentalement un process d'usinage très courant dans ce type de fonte ADI (le perçage) dans un double objectif d'optimisation de l'usinabilité et d'usinage écologique (perçage à sec et avec micro-lubrification).

Enfin, une conclusion générale avec les perspectives de développement termine ce manuscrit de thèse.

Chapitre 1 : Introduction

Les fontes montrent de grandes variations dans les propriétés mécaniques en fonction des teneurs en carbone et en silicium, des éléments d'alliage métalliques ou non métalliques, mais aussi du process de fusion, de moulage, des traitements thermiques. L'objectif fondamental est de manipuler le type, la qualité, et la morphologie de la structure métallurgique dans le but d'atteindre les propriétés mécaniques souhaitées.

La forme sphéroïdale du graphite dans la fonte (fonte à graphite sphéroïdal ou FGS) est favorisée par l'ajout de petites quantités de magnésium au métal fondu dans la poche de coulée. Les propriétés des fontes à graphite sphéroïdal peuvent être commodément modifiées en utilisant une gamme de traitements thermiques, qui conduisent à l'obtention de matrices perlitiques, ferritiques, martensitiques et/ou bainitiques.

Dans ce travail, un mode de production innovant de la fonte ADI (Austempered Ductile Iron) utilisant le processus de transformation bainitique d'une fonte à graphite sphéroïdal directement dans la chaude de coulée (c'est-à-dire en intégrant le traitement thermique pendant le refroidissement de la pièce immédiatement après son moulage) a été développé. Grâce à sa remarquable combinaison de propriétés mécaniques et de résistance à l'usure, cette fonte ADI est prédestinée se substituer à l'acier forgé ou à des pièces en fonte dans de nombreux secteurs industriels comme par exemple dans l'automobile. Dans ce scénario, cette fonte ADI est apparue comme une occasion de répondre à la demande industrielle croissante de minimiser les coûts de pièces soumises à de hautes sollicitations mécaniques, tout en préservant l'énergie consommée dans un contexte de développement durable.

Chapitre 2 : Analyse bibliographique

La production de pièces en fonte ADI est contrôlée par les trois étapes importantes : la fonderie, le traitement thermique et l'usinage. Avant de mettre en œuvre une technologie de fabrication verte pour la fonte ADI, il est nécessaire de considérer chacune de ces étapes de production.

Dans la deuxième étape, le processus classique de traitement thermique pour l'obtention de la structure métallurgique de la fonte ADI se compose de deux phases:

- La pièce en fonte GS est chauffée puis maintenue jusqu'à une plage de température de 850 à 950 ℃ pour convertir la matrice métallique ferrite/perlite en matrice austénitique. L'austénitisation est le premier stade du traitement thermique. La température d'austénitisation et le temps de maintien conditionne la teneur en carbone de l'austénite qui à son tour influe sur la structure et les propriétés de la fonte ADI. L'austénitisation se produit par nucléation et croissance. Augmenter la température d'austénitisation accélère la cinétique d'austénitisation et la teneur en carbone de l'austénite. La forte teneur en carbone de l'austénite augmente sa trempabilité et sa stabilité. Erdogan et al. ont montré que la teneur en carbone augmente avec celle de l'austénite pendant le processus d'austénitisation.

- La pièce est ensuite refroidie rapidement jusqu'à une plage de température (250-450 ℃) pour éviter le nez de transformation perlitique. Elle est maintenue ensuite pendant une période de temps appropriée pour générer complètement la transformation bainitique,

mais sans atteindre la formation de ferrites et de carbures. La fenêtre de ce palier isotherme dépend de la composition chimique et des paramètres du traitement thermique. Ces paramètres modifient la microstructure ausferritique et les propriétés mécaniques de la fonte ADI.

La pièce est ensuite refroidie à l'air jusqu'à température ambiante.

La troisième étape analyse l'état de l'art en usinage des fontes ADI. La médiocre usinabilité des fontes ADI est due principalement à la microstructure austénitique, à la faible conductivité thermique, et à une forte limite d'élasticité, un module d'Young et une dureté élevé. Les matériaux d'outils utilisés pour ce type de fonte sont, par ordre de décroissance, la famille des carbures métalliques revêtus, les outils en CBN et ceux en céramique.

Chapitre 3 : Techniques expérimentales

Le but de ce chapitre est d'introduire les techniques expérimentales retenues et les équipements utilisés tout au long de ce projet pour la fabrication de la fonte ADI dans une démarche de développement durable en intégrant le traitement thermique dans la chaude de coulée.

Le lit de fusion est réalisé dans un four à induction avec une contenance de 100 kg. Un outil basé sur Excel a été développé pour calculer les masses des différents composants de base (acier, fonte, éléments d'alliage) constituant la charge du lit de fusion.

Le traitement de sphéroïdisation est effectué par ajout de ferrosilicate de magnésium dans la plage de température de 1450-1470 ℃ afin que la phase graphite précipite sous forme de nodules. La masse de ferrosilicate de magnésium est calculée en fonction de la masse de fonte liquide à traiter pour donner une teneur en magnésium résiduel de 0.030 à 0.040%. La température de la fusion a été mesurée en utilisant un thermocouple platine-platine rhodium.

Une analyse du lit de fusion est effectuée en utilisant l'outil commercial d'analyse thermique ATAS (système d'analyse thermique adaptative). Ce système mesure et surveille la composition chimique en analysant la courbe de solidification de la fonte.

Les pièces d'essais sont coulées dans un moule métallique réalisé dans le cadre du laboratoire, maintenu à température stable durant les essais. Elles sont de forme rectangulaire de dimensions 182×29×16mm.

Le traitement thermique a été réalisé immédiatement à la suite du processus de coulée (dans la chaude de coulée) afin de développer l'approche novatrice d'une production intégrée dans une optique de développement durable. Dans ce processus, les échantillons en fonte GS solidifiée sont éjectés du moule métallique et immédiatement introduites dans un four à atmosphère contrôlée à 930 ℃ pendant 90 min pour la phase d'austénisation. Les pièces sont ensuite refroidies à une vitesse moyenne de 7℃/s jusqu'à une plage de 400/500 ℃ dans un lit fluidisé de sable de

zirconium maintenu à température ambiante. Elles sont ensuite plongées dans un second lit fluidisé isotherme pour le temps de la transformation bainitique. Dans ce travail de thèse, les paramètres de cette transformation bainitique sont réalisés à 3 températures différentes (320, 350 et 380 ℃) et 4 temps de maintiens (60, 90, 120 et 150 min).

La caractérisation microstructurale des échantillons a été réalisée après polissage et attaque au Nital 4% pendant 2 à 5 secondes à température ambiante. Les microstructures ont été observées au microscope optique et au microscope électronique à balayage.

Les caractéristiques mécaniques ont été mesurées sur machine de traction INSTRON et une machine de dureté Buehler MacroVickers 5112 avec une charge appliquée de 20 kgf. La valeur de dureté est la moyenne des cinq valeurs différentes prises dans les différentes zones pour chaque échantillon. Les valeurs des propriétés mécaniques qui sont présentés sont des moyennes d'au moins quatre échantillons.

Les essais d'usinabilité ont été réalisés en perçage sur des éprouvettes de dimensions 182x29x16mm avec un centre d'usinage Deckel Maho DMU 60. Les essais d'usinage ont été menés en utilisant différents outils en carbure monobloc revêtus de diamètre 8 mm détaillés dans le Tableau 3.4.

Les essais de perçage ont été réalisés avec trois vitesses de coupe (30, 60 et 90 m/min) et trois vitesses d'avance (0.05, 0.10 et 0.15 mm/tr). La profondeur de perçage pour chaque trou débouchant est de 16 mm. L'acquisition des composantes de l'effort de coupe a été menée pour chaque essai (composante de poussée et couple) avec un dynamomètre à deux composantes Kistler de type de 9271A. Il en est de même pour l'acquisition et la mesure de puissance avec un wattmètre DIGITAL WAY. Les copeaux et surfaces usinées on été caractérisées en micro-dureté et par microscope électronique à balayage équipé de système EDS.

Chapitre 4 : Processus innovant de fabrication de la fonte ADI

Une technologie innovante a été développée dans ce travail de recherche pour la production d'éprouvettes en fonte ADI en intégrant le traitement thermique immédiatement après la solidification. Les modifications microstructurales et les influences sur les propriétés mécaniques des échantillons obtenus ont été étudiées dans la présente étude. Basé sur les résultats obtenus, les conclusions suivantes peuvent être tirées:

- Le procédé innovant de traitement thermique intégré dans la chaude de coulée conduit bien à la production de fonte ADI avec une microstructure ausferrite (en forme d'aiguilles de ferrite et d'austénite haute teneur en carbone) et un nombre élevé de nodules de graphite. Les quantités de nodules élevées sont associées à des vitesses de refroidissement accrues. Cette technologie de traitement innovante conduit donc à économiser énergie et temps lors de la production de fonte ADI optimisée.

- Les paramètres du traitement thermique bainitique de 380 ℃ pendant 120 min conduit
  à la production de la fonte ADI ayant résistance à la traction de 866 MPa et une duc-
  tilité de 10.3%. Ces paramètres permettent d'obtenir une fonte ADI de caractéristiques
  mécaniques plus élevées que celles de la norme ASTM grade 1.

- Les propriétés mécaniques des fontes ADI qui en résultent sont significativement influ-
  encées par la variation de la morphologie de ferrite, de la fraction volumique d'austénite et
  de sa teneur en carbone en raison de variations des paramètres du traitement bainitique.

- Les faibles duretés sont obtenues pour un maintien du palier de traitement bainitique de
  90-120 minutes.

Chapitre 5 : Simulation de la coulabilit de la nouvelle fonte ADI par corrélation thermique

La simulation de remplissage du moule métallique utilisé et de la solidification ont été simulées
utilisant les logiciel commerciaux CVM et CV de NOVAFLOW. Dans la présente étude, le
modèle de simulation adopte la théorie de quasi-équilibre de la zone à deux phases pour la
solidification. Contrairement aux métaux purs, les alliages cristallisent dans l'intervalle de
température entre le liquidus et le solidus.

L'analyse thermique a montré quatre paliers de température lors de la solidification. Elle
a révélé la variation de la nature de l'alliage au cours de la solidification en raison des varia-
tions de l'eutectique et du carbone équivalent de la phase liquide. Les résultats des simulations
numériques montrent un temps de remplissage du moule de 4.948 s à une vitesse de remplis-
sage de 0.666 kg/s. La simulation a montré des vitesses moyennes fusion bien en dessous de la
vitesse critique de 0.45 m/s pour éviter une turbulence au cours du processus de remplissage
du moule. La solidification est progressive et commence à partir des côtés extérieurs. L'analyse
de simulation a révélé l'absence de porosité et des défauts de retrait à la fin de la solidifica-
tion. Cependant, des résultats expérimentaux montrent quelques petits défauts de porosité à
la section supérieure de la pièce qui sont considérés comme étant des défauts courants dans
le processus de coulée par gravité, qui se produisant par l'entrainement de bulles pendant le
processus de remplissage du moule. En conclusion, le système d'analyse thermique ainsi que
l'outil de simulation aident à améliorer le processus de coulée pendant la production de pièces
en fonte ADI, en fournissant l'évolution thermique et la solidification de la masse fondue, et la
prévision des défauts de retrait se produisant pendant le processus de coulée.

Chapitre 6 : Usinabilité

Toujours avec un objectif de développement durable, les essais d'usinabilités ont été décomposés en plusieurs phases : essais de perçage à sec suivis d'une analyse des copeaux, puis essais de perçage avec micro-lubrification, et enfin comparaison de différents revêtements d'outils de coupe.

Perçage à sec

L'influence des paramètres de coupe sur l'usinabilité de la fonte ADI a été étudiée dans la présente section. Les expériences de perçage à sec ont été effectuées à des conditions de coupe en utilisant plusieurs outils carbure revêtus PVD-TiN/TiAlN. L'usinabilité a été évaluée à l'aide des forces de coupe spécifiques (ratio effort/surface coupée), de la rugosité de la surface usinée et de l'usure de l'outil. Il a été constaté que la combinaison d'une vitesse d'avance faible associée à une grande vitesse de coupe conduit à des charges mécaniques et thermiques plus élevées sur les arêtes de coupe de l'outil, ce qui entraîne une hausse des forces spécifiques de coupe. La vitesse de coupe est plus influente sur la qualité de la surface usinée que la vitesse d'avance au cours de processus de perçage à sec. L'usure en cratère à la pointe extérieure de l'arête de coupe est le mode d'usure principale, due de fortes abrasion et adhésion au cours du perçage à sec. Il a également été constaté que la vitesse de coupe influence de manière significative la durée de vie de l'outil par rapport à la vitesse d'avance. L'influence de la microstructure bainitique sur l'usinabilité de la fonte ADI a également été étudiée au cours du processus de perçage à sec. Les caractéristiques mécaniques et métallurgiques du matériau influencent de manière significative le process d'usinage de la fonte ADI. Une grande dureté engendre une importante force de poussée sur le foret lors de l'usinage. La température de maintien du traitement thermique pendant la transformation bainitique a un effet prépondérant sur l'usinabilité par rapport au temps de maintien. La forte teneur en ferrite de la fonte ADI obtenue à faible température de maintien (320 ℃) conduit à une adhésion des copeaux sur la face de coupe, pour déboucher sur un écaillage rapide de l'arête de coupe.

Analyse des copeaux

L'analyse expérimentale des caractéristiques morphologiques des copeaux, de son taux de compression et de sa micro-dureté ont été réalisés. Sur la base des résultats expérimentaux, les conclusions peuvent être résumées ainsi :

- A basse vitesse de coupe (30 m/min), les copeaux se présentent sous forme de cônes brisés et d'un diamètre de cône croissant avec la vitesse d'avance. L'augmentation de la

vitesse de coupe à faible vitesse d'avance (0.05 mm/tr) conduit à la formation de copeaux continus.

- A hautes vitesses de coupe (60, 90 m/min) et pour toutes les vitesses d'avance, les copeaux présentent coté surface libre une structure composée de fines lamelles. A vitesse de coupe inférieure (30 m/min) une structure lamellaire plus grossière a été observée à toutes les vitesses d'avance.

- Aux faibles vitesses d'avance (0.05 et 0.10 mm/tr), une augmentation significative du taux de compression CCR (ratio épaisseur section coupée/épaisseur copeau) a été observée avec la vitesse de coupe dans la gamme de 30 m/min et 60 m/min. Aux vitesses de coupe supérieures, le ramollissement thermique dans la zone de coupe conduit à une diminution du taux de compression. D'autre part, à une grande vitesse d'avance (0.15 mm/tr), le taux de compression est linéairement croissant avec la vitesse de coupe.

- A grande vitesse d'avance (0.15 mm/tr), la micro-dureté des copeaux est croissante avec la vitesse de coupe. Aux vitesses d'avances inférieures (0.05 et 0.10 mm/tr), le phénomène est inversé.

Lubrification par micro-lubrification

L'usinabilité en perçage avec micro-lubrification par brouillard d'huile (MQL), avec des outils en carbure de tungstène revêtus PVD-TiN/TiAlN, a été analysée expérimentalement dans un objectif d'usinage écologique de fonte ADI.

Sur la base des résultats expérimentaux obtenus, et par comparaison avec le perçage à sec, les conclusions suivantes peuvent être tirées:

- La micro-lubrification réduit l'effort de coupe appliqué à l'outil (en moyenne le couple de 6% et la force de pénétration de 10%) par rapport à l'usinage à sec. Il faut noter que la force de poussée est d'un niveau comparable à celui mesuré en perçage sous lubrification conventionnelle.

- Le même effet est observé avec la micro-lubrification en ce qui concerne la rugosité de surface : niveau de rugosité amélioré par rapport au perçage à sec, comparable au perçage sous lubrification conventionnelle.

- la micro-lubrification augmente la durée de vie de l'outil de 25% et diminue l'usure des arêtes de coupe de 40% par rapport à l'usinage à sec.

- Sous micro-lubrification, le mode dominant d'usure des arêtes de coupe est l'usure en cratère. Elle est la conséquence de frottements élevés et d'adhésion à l'interface copeau/face de coupe. Elle débouche sur un écaillage des arêtes de coupe sur les bords externes de l'outil.

Comparaison des revêtements d'outils

Les comportements de deux revêtements d'outil différents, multicouches (Ti,Al,Cr)N (Outil 1) et monocouche TiAlN (Outil 2) sont comparés. La comparaison a porté sur une analyse de l'usure de l'outil, de l'énergie spécifique de coupe (ration puissance consommée/débit copeaux), la rugosité de surface et de la morphologie des copeaux. Sur la base des résultats obtenus, les conclusions suivantes peuvent être tirées :

- L'énergie spécifique de coupe reste constante avec l'outil 1(2,80 J/mm^3), tandis qu'elle est croissante jusqu'à 3.73 J/mm^3 avec le nombre de trous percés pour l'outil 2.

- L'outil 1 présente une forte résistance à l'usure par adhésion par rapport à l'outil 2. Sur l'outil 2, l'adhésion de matière usinée a été observée principalement sur l'arête de coupe à la périphérie du foret alors que, le revêtement de l'outil 1 a été détérioré par abrasion.

- L'analyse EDS des arêtes de coupe a révélé la formation d'oxydes d'aluminium et de chrome pour outil de 1, ce qui améliore les caractéristiques tribologiques à l'interface outil/copeau et limite l'usure par adhérence.

- La présence de matière usinée adhérant sur la face de coupe de l'outil 2 au niveau du sur le substrat provoque une augmentation de la rugosité de surface usinée et de l'énergie spécifique de coupe.

- La structure lamellaire de la surface libre du copeau a été observée pour les deux outils. Pour l'outil 1, la surface écrouie des copeaux présente des motifs lisses de type pliage. Pour l'outil 2, la présence de micro-pores de graphite croissants et coalescents lors de la déformation de cisaillement est la conséquence des dommages au niveau de l'arête de coupe de l'outil 2.

Chapitre 7 : Conclusions générales

Dans cette étude, un processus innovant a été développé pour la production de fonte ADI en corrélation avec la microstructure et l'usinabilité. Il est basé sur lintégration du traitement thermique aussitôt la solidification, associée à une méthodologie de corrélation thermique. Les principales conclusions, sur la base de la recherche menée dans cette thèse, sont:

- Ce processus innovant conduit à une microstructure ausferrite avec un nombre élevé de nodules de graphite. Dans la phase de transformation bainitique, une faible température conduit à une densité de fines aiguilles de ferrite, mais à une structure ferritique plus grossière à haute température.

- Une simulation de coulabilité de la fonte ADI dans un moule métallique par corrélation thermique a été mis en œuvre. Elle est basée en analysant les paliers de solidification au cours du refroidissement. L'évolution thermique et la propagation de la solidfication dans le moule est simulée. Les défauts usuels dans la pièce sont ainsi prévisibles.

- L'usinage à sec de la nouvelle fonte ADI a été étudié pour différentes conditions de coupe en corrélation avec sa microstructure et des paramètres de traitement thermique. La force et l'énergie spécifiques de coupe ainsi que la température de coupe sont élévées pour une grande vitesse de coupe associée à une faible vitesse d'avance. Le mode prépondérant d'usure de l'outil est la cratérisation de la face de coupe.

- L'usinabilité de la fonte ADI est influencée par ses caractéristiques mécaniques. En perçage, l'effort de poussée sur le foret est directement relié à la dureté et la résistance mécanique de la fonte. Lors de la phase d'austénisation, la température est plus influente que le temps du traitement. Une structure fortement ferritique, obtenue avec une faible température d'austénisation , engendre une formation de copeaux fortement cisaillés et adhérents, d'où une faible usinabilité.

- La morphologie des copeaux présente de fines lamelles pour les grandes vitesse de coupe (60, 90 m/min) quelque soit la vitesse d'avance. Le ratio de compression de la matière est inversement proportionnel à la vitesse d'avance. Les corrélations entre la micro-dureté des copeaux, le ratio de compression de la matière et les conditions de coupe ont été analysées. Un taux d'enlèvement de matière élevé est obtenu avec de faibles ratios de comperssion et d'énergie spécifiques de coupe.

- La micro-lubrification améliore considérablement l'usinabilité en perçage de la fonte ADI par rapport à l'usinage à sec, en améliorant l'évacaution des calories produites de la zone de coupe. En outre, la rugosité des surfaces obtenues est comparable à celle avec lubrification conventionnelle.

- Le revêtement d'outil multicouche (Ti,Al,Cr)N obtenu par dépôt en phase vapeur est le plus adapté en perçage à sec. Il montre de meilleures propriétés de résistance à l'adhérence dues à la formation de dépôts tribo-oxydes.

Perspectives

Sur la base de la présente étude, les perspectives pertinentes sont:

- Les morphologies de la structure métallurgique (en particulier les nodules de graphite) sont fonction de la coulée et du traitement thermique. L'influence de l'inoculation sur les nodules de graphite doit encore être analysée en corrélation avec le phénomène de surfusion et la nucléation du graphite pendant le processus de solidification.

- Le développement d'un outil de simulation numérique pour optimiser la formation du copeau et l'usure de l'outil au cours du processus d'usinage, notament la déformation plastique du matériau lors de l'usinage à sec et en micro-lubrification à haute température et vitesse de déformation élevée.

Chapter 1

Introduction

The use of iron and steel, in particular, in automotive and construction industries, is considerable and widespread. However, the production and processing technologies of these materials are energy intensive, and their subsequent environmental impacts are critical. Therefore, to maintain the use of these popular and versatile materials in the future will necessitate an increased attention to reductions in the energy consumption and greater sensitivity to the environment [1]. This requirement needs a sustainable development of either a suitable material or manufacturing process to improve the material efficiency and to reduce the environmental impacts. The introduction of new, or modified materials and processes for a given application is dependent on satisfying a lot of different parameters (production costs, recyclability and machinability, etc.) [2]. The present study thus attempts to explore the green manufacturing of the new class of cost and weight efficient materials known as Austempered Ductile Iron (ADI).

1.1   Historical Background

The commercial introduction of ductile iron casting in 1948 have proven to be a cost effective alternative to malleable iron castings, steel castings, and forgings. It emerged as an excellent material for structural applications due to its wide range of physical and mechanical properties. Moreover, it provides positive impacts on economic and environmental aspects by allowing production of high quality, low priced casting from recycled metal scrap. Furthermore, the considerable weight savings in ductile irons can be obtained using properly designed improved castings. The developments of these improved castings are possible through a more effective nucleation and growth of the graphite phase during solidification, often in combination with some additional heat treatment of the iron matrix [3].

The two-step heat treatment (austempering process) of the alloyed ductile iron produces ADI

with an excellent combination of strength, ductility and wear resistance [4, 5]. These remarkable properties of ADI make it suitable for a wide variety of applications in automotive and structural industries. The mechanical properties of ADI are primarily determined by the metal matrix and the relative proportions and morphologies of the different phases (retained austenite and acicular ferrite) which can be altered by the influence of heat treatment parameters. The properties of ADI are due to its unique matrix of acicular ferrite and carbon-enriched austenite called ausferrite [6]. The ADI was first commercially produced in 1972 and by 2010 its world-wide production was approaching 3×10^5 tonnes annually [7]. However, the austempering process was first applied to steel by Davenport and Bain in the 1930s and the resulting microstructure is known as bainite, named after Bain [8]. Bainite in steel consists of acicular ferrite and carbides and therefore, different from the ausferrite microstructure.

The presence of thermodynamically stable, carbon enriched austenite in ausferrite is responsible for its remarkable wear resistance. It can undergo a strain-induced transformation when exposed to high, normal forces. This transformation in ADI is more than mere work hardening. In addition to a significant increase in flow stress and hardness (typical in most metallic materials), this strain induced transformation also produces a localized increase in volume and creates high compressive stresses in the transformed areas. These compressive stresses inhibit crack formation and growth and produce significant improvements in the fatigue properties of ADI [8–10]. Moreover, ADI allows considerable weight (10 % lighter than steel) and cost reduction options as compared to steel. Furthermore, high vibration absorption capacity and damping capacity can be achieved in a gearbox using ADI material. These all properties together with high strength and ductility combinations predestine this material to act as a substitute for steel castings and forgings (crankshafts, gears and connecting rods) in automotive industries. With this high potential of ADI materials in various industrial applications, the demand of the ADI material is kept increasing. However, for the successful implementation of ADI material for a particular application on an industrial scale, further improvement requires in the casting and heat treatment practices. In addition, to improve the machinability of ADI, there is a need to correlate the machining characteristics of ADI with its microstructure and mechanical properties.

1.2   The significance of the research

The material selection for a particular engineering component depends on the correlation between the key properties of the material (density, strength, and wear resistance, etc.) and its function requirements [11]. These parameters for material selection are further constrained by

the energy consumption and its environmental impacts during material production and processing and the production cost of the final product. In the current global scenario, iron and steel are used across a broad range of applications, because of their good combination of properties. However, the environmental impacts of iron and steel production and processing are critical and keep increasing. It was revealed that the demand for iron and steel will grow by double in 2050 and at the same time there is a need to cut the environmental impacts due to iron and steel production and processing to no more than half present levels [12]. Therefore, to reduce the environmental impacts and to full-fill the current demands, there is a need to deliver more sustainable materials with improved material properties. For example in case of automotive industries, the environmental impacts can be reduced by using weight efficient and high-performance material components. This requires the materials with high specific stiffness and strength properties, which allow highly efficient light-weight load bearing structures to be produced. In addition, materials with enhanced processing capabilities, such as near net moulding allows greater design freedom in producing complex shapes and reducing machining costs [2]. The austempered ductile iron can be a solution in such circumstances.

The ADI material is produced by austempering of ductile iron casting. However, to get the optimum results, there is a need to develop a novel process route for ADI production. This requires the implementation of the controlled and efficient casting and heat treatment practices for ADI production. Moreover, the precise control of the spheroidization and inoculation practices of the melt are becoming more critical as the demand for the thinner section castings with improved mechanical properties grows. In addition, there is a need to understand the microstructure formations during the solidification and solid-state transformation of the castings. These phase transformations are, to a large extent, affected by nucleation and growth kinetics, which are dependent on, melt quality, alloying elements, spheroidization and inoculation practices, mould materials, pouring methods and many other factors. Many of these process factors and influence of their combinations on the final casting quality is still not fully understood today. Consequently, it is necessary to develop controlled foundry and heat treatment practices for the ADI casting production in order to achieve the optimum quality and mechanical properties of the final casting. To this end, a simulation tool is also required. First, to optimize the casting process at a low cost and second, to predict the filling and solidification behavior of melt for a particular mould material and correlate it with the evolution of microstructure and mechanical properties, as well as with the formation of defects in the final casting.

After the material production, the processing of end use product depends on the machining requirements and machining characteristics of the material. This processing step significantly influences the production cost of the final product. The growing demand in ADI materials

components require consistent ADI machinability at higher material removal rates to optimize the production rate and cost. However, machining at higher material removal rates requires ADI casting with uniform microstructures, improved mechanical properties and a minimum volume fraction of abrasive inclusions. This requires developing an approach of correlating the machinability of ADI castings with its production conditions (casting and heat treatment). Finally, the other aspects of the machining process from the environmental and economic point of view are the use of cutting fluids during machining. In these circumstances, the implementation of the dry or near-dry machining process can be a solution. However, the workpiece suitability for a dry cutting process depends on the machining operation and inherent properties of the workpiece material. For example, in case of drilling the use of cutting fluid is critical where chip transportation is enhanced using cutting fluid and responsible for the better surface quality of the machined surfaces. In such conditions, the introduction of near-dry machining or minimum quantity lubrication (MQL) and/or the tool's coatings significantly improve the machining conditions and led to the green manufacturing of the ADI components.

1.3   Originality of the research work

The present study is dedicated to the development of an innovative methodology for austempered ductile iron (ADI) manufacturing considering all production aspects such as melt treatment, casting, heat treatment and machining. The development of novel process route to reduce the environmental impacts and to produce a high-performance ADI material is essential for its mass exploitation in the current increasing demands. The continuing progress in the ADI manufacturing is being made by the three inter-related approaches.

First, depending on the detailed understanding of the production conditions and its combined influences on the microstructural characteristics and material performance, an innovative process design is introduced. It is based on the fundamental relationship between the microstructure characteristics and mechanical properties of ADI. It introduces the integrated approach towards casting and heat treatment practices for near-net shape light weight ADI casting production using a permanent mould. Both casting and heat treatment practices are then implemented efficiently in a control manner using thermal analysis adaptive system (melt quality) and fluidized bed (controlled and uniform heat treatment) respectively to enhance the foundry practice for ADI production.

Second, the present study introduces a correlative thermal methodology approach to understand the castability of ductile iron in a permanent mould for the novel ADI production. The approach utilizes the thermal characteristics of the melt to correlate the combined influences

of the heat transfer at melt/mould interface, and melt flow through the critical sections of the casting to produce a sound ductile iron casting and to predict the casting defects. The thermal characteristics of the melt were obtained using the thermal analysis system which further utilizes to enhance the melt quality.

Third, many studies have dealt with the machinability of ADI during turning and milling operations specifying the influence of cutting parameters and tool materials. However, not so much work has been done on the machining characteristics during drilling operation. Drilling is often carried out at the last stages of the material processing, and it almost compromising 22% of all metal-cutting operations and therefore, require special attention [13]. With this viewpoint, the present study investigates the drilling machining operation in correlation with the microstructural characteristics of ADI materials with variable austempering parameters. The key aspects of the novel ADI machinability were identified and highlighted with respect to tool wear mechanisms and chip formation characteristics. The dry and near-dry machining processes are later implemented for the green manufacturing of the novel ADI materials.

1.4 Organization of the thesis

This thesis is composed of seven chapters and their brief descriptions are listed below:

Chapter 1 Introduction

This chapter provides a brief description of the historical background of the ductile iron and evolution of ADI material. The chapter briefly highlighted the importance and motivation behind the current project. The originality of the research work is also highlighted briefly in relation with the major contributions of the thesis.

Chapter 2 Literature review

This chapter is dedicated to the background knowledge of the conventional ADI production and processing techniques, which help us to understand the current state of ADI in the global scenario. The background information mainly consists of two inter-related aspects of ADI. Firstly, the foundry work which includes the casting and heat treatment practices, responsible for the control and tailor of the ADI microstructures to get the desired mechanical properties. It highlights the impacts of the different casting and heat treatment parameters that can enhance the casting quality and material properties of ADI. Secondly, it presents the machinability of ADI, which is the function of the microstructural characteristics of ADI, including cutting conditions and tool material constraints. The influences of different tool materials under distinct cutting conditions are discussed with respect to the inherent properties of the ADI. It concluded

that with the advancement in the foundry and machining technologies, further works need to be done to implement the efficient and controlled approach during foundry and machining process to improve the material efficiency in combination with its machinability.

Chapter 3 Experimental techniques

This chapter is dedicated to the description of the main experimental techniques and methodology employed in this thesis. It starts with a brief overview of the controlled and efficient casting and heat treatment practices implemented for the novel ADI production using a sustainable processing technology. The chapter continues with a description of the various techniques used in the material characterization of the produced ADI samples. In the later section, the design of the performed machining experiments and their requirements are highlighted. Finally, the techniques used for the characterization of the machined part and tool materials are described.

Chapter 4 Innovative process route for ADI production

This chapter introduces the innovative process route for sustainable production of ADI materials by reducing energy consumption during its production cycle and improving material efficiency. The microstructure of the ADI materials is controlled and tailored to get the desired combination of mechanical properties by varying the austempering heat treatment parameters. It demonstrates the correlation between the microstructural characteristics and mechanical properties of the produced ADI samples. The variation in microstructural characteristics explained the variation in autempering kinetics during austempering process. In the later section, the influence of austempering parameters on the strain-hardening behavior of novel ADI materials is presented. As a result, good correlation is observed between microstructural characteristic and strain hardening behavior of ADI material.

Chapter 5 Correlative thermal methodology for novel ADI castability simulation

This chapter investigates the simulation analysis of simultaneous mould filling and solidification of ductile iron casting in a permanent mould by virtue of its thermal characteristics. It presents the thermal analysis system which is used to obtain the thermal characteristics of the melt during its solidification. This system further acts as a tool to control the metallurgical process for ADI production and to get a consistency during the foundry process. The thermal analysis system also revealed the nature of alloy depending upon the eutectic freezing and carbon equivalent of the melt. Based on the simulation tool, casting defects in the produced ADI materials are predicted.

Chapter 6 Ecological machining of novel ADI: Dry and near-dry machining

This chapter investigates the ecological machining of novel ADI materials during drilling machining operations. The influence of cutting parameters, cutting environment and coating materials are identified. It presents the correlation between the machiniability of ADI materials and their microstructures obtained by varying the heat treatment parameters. The machining characteristics of the produced ADI materials are identified with respect to the tool wear mechanisms, chip formation characteristics and the machined surface quality. In the later section, the near dry machining of ADI is introduced for the green manufacturing of ADI.

Chapter 7 Conclusions and future perspectives

Chapter 7 presents the main conclusions of this thesis and proposed future work, with the purpose of further assess the potential of novel ADI materials for increasing industrial demand.

Chapter 2

Literature review

2.1 Introduction

The term cast iron, present a large family of ferrous alloys. Cast irons are iron-carbon base alloys that contain major (carbon, silicon) and alloying elements. Depending primarily on composition, cooling rate, and melt treatment, cast iron can solidify according to the thermo-dynamically stable iron-graphite eutectic (gray cast iron) or metastable iron-carbide eutectic (white cast iron) [14, 15]. The cast irons show wide variations in mechanical properties that can be achieved by varying the carbon and silicon contents, by alloying with various metallic or non-metallic elements, and by varying melting, casting, and heat-treating practices. Therefore, the basic purpose of the metallurgical processing of cast iron is to manipulate the type, amount, and morphology of the eutectic in order to achieve the desired mechanical properties [14, 16].

Gray cast iron is the most common form of cast iron in which carbon exists in the flake form in a ferrite or ferrite/pearlite matrix [14, 17]. It can be suitable for a wide range of applications because of the property changes that can be produced by controlling the characteristics of its free graphite and matrix structure. The material properties and performance of gray cast iron can be further improved by the production of spheroidal graphite iron composed of a number of graphite crystals in spheroidal shape. The spheroidal shape of graphite in as-cast iron is promoted by the additions of small amounts of magnesium (Mg) to the molten metal into the ladle which changes the inter-facial energy between the graphite, and the melt [18].

The material properties of spheroidal graphite iron can be conveniently modified by using a wide range of heat treatments (HT), such as ferritizing, normalizing, quenching and tempering, and austempering, obtaining ferritic, pearlitic, martensitic and ausferritic matrices, respectively [19]. Recently, the introduction of austempered ductile iron (ADI) using the austempering process is one such example. In the current scenario, the ADI material is emerged out as an

opportunity to respond to the increasing industrial demand for the cost and weight efficient materials. Due to its remarkable combination of mechanical properties and wear resistance, predestine ADI material to act as a substitute for forged steel and cast iron components in many industrial sectors [20].

This chapter is thus devoted to an extensive review on the literature regarding foundry process and machining characteristics of ADI. In this regard, the available processing techniques for ductile iron are explained and their achievements, advantage and limitations are discussed. Due to the significant impact of heat treatment on the material properties of ADI, the heat treatment cycle and the correlation between heat treatment parameters and prevailed microstructure is explained and discussed. Later in this chapter, the machining characteristics of ADI and the recent advance in the machining process are presented and discussed to get a future direction in the manufacturing of ADI.

2.2 Ductile iron casting for ADI production

Figure 2.1 presents the mechanical properties of ductile iron family. Ductile iron is considered as a highly versatile material and is widely used in many engineering applications because of its wide range of mechanical properties [21]. It is also known as nodular graphite iron or spheroidal graphite iron. Unlike gray iron, which contains graphite as flakes, ductile iron has an as-cast structure containing graphite particles in the form of spheroidal nodules. Therefore, ductile iron possesses higher strength and elongation properties as compared to the gray cast iron [14]. The following section presents a study of techniques to produce ductile iron casting for ADI production and in the next section, the insights into the production process developed using these techniques will be reviewed.

2.2.1 Metallurgical control in ductile iron production

Conventionally ductile iron was produced by conducting melting of charge materials either in a coke-fired cupola or electric arc furnace or induction furnace. To maintain the consistency of the microstructure and to reduce the contamination of the castings due to certain alloying elements, the alloying elements in ductile iron casting for ADI production must be carefully selected [5, 16]. The recommended limits for the chemical composition of the cast unalloyed ductile iron is given in Table 2.1. Alloying elements should be controlled to the extent needed to obtain the required mechanical properties and/or microstructure in the critical sections of the castings [16]. However, all elements within the composition of ductile iron are needed to be controlled, the influence of most common alloying elements are as follows:
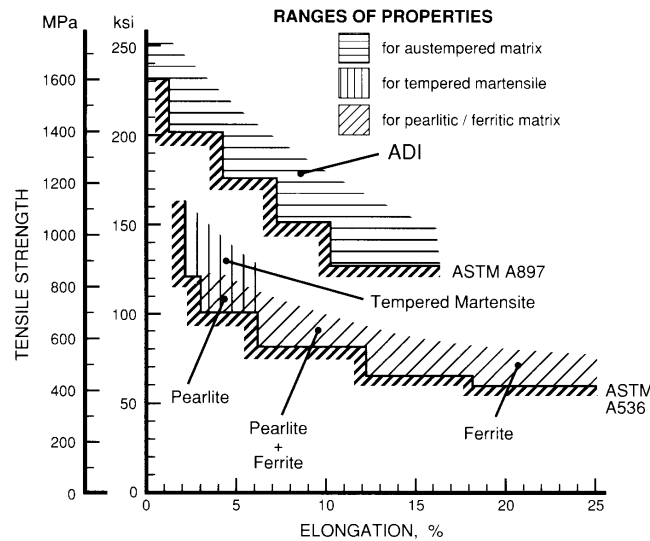
Figure 2.1: Ranges of mechanical properties for ductile iron (DI) family [5].

- Carbon (C) affects the fluidity of melt and the shrinkage characteristics of the casting during filling and solidification processes. The optimum range for carbon is usually 3.4 % to 3.8 %, depending on the silicon content. Excess carbon leads to a danger of graphite flotation, especially in heavy sections. It also increased the casting expansion during solidification, which can offset the casting shrinkage during transformation of melt from liquid to solid state. On the other hand, lower carbon content leads to the formation of carbides in the casting, particularly in thin sections [16, 22].

- Silicon (Si) is a powerful graphitizing agent. The preferred range for silicon is about 2.0 % to 2.8 %. The lower silicon levels lead to high ductility in heat-treated irons but to a danger of carbides in thin sections as-cast. On the other hand, high silicon accelerates annealing and helps to avoid carbides in thin sections. As the silicon content rises, the ductile-to-brittle transition temperature in ferritic iron increases. Hardness, proof stress, and tensile strength also increase with silicon content [16, 22].

- Manganese (Mn): The steel scrap used with the charge material is the main source of manganese. This element should be limited in order to obtain maximum ductility. In as-cast ferritic irons, it should be 0.2% or less. Manganese create the undesirable microsegregation. This is especially true in heavy sections, in which manganese encourages grain-boundary carbides, which promote low ductility and toughness values [16, 22].

- Magnesium (Mg): The magnesium content required to produce spheroidal graphite iron is usually ranged from 0.04 to 0.06%. If the initial sulphur content is below 0.015%, a lower magnesium content (in the range of 0.035 to 0.04%), may be satisfactory. Compacted

graphite structures with inferior properties may be produced if the magnesium content is too low, while high magnesium content may promote dross defects in the casting [16, 22].

- Sulphur (S) is derived from the charged metallic raw materials. Before magnesium treatment, the sulphur content should be as low as possible, preferably below 0.02%. Excessive final sulphur contents are usually associated with magnesium sulphide slag and dross [16, 22].

Element	Percentage (%)	Functions	Remarks
Carbon (C)	3-4	Constituent of the spheroids	Excess cause graphite location
Silicon (Si)	1.8-3	Graphitizer, ferritizer	Control as cast pearlite
Magnesium (Mg)	0.03-0.06	Spheroidizer	Excess promotes carbides
Cerium (Ce)	0.03 max	Promotes formation of spheroids in combination with Mg	Excess promotes carbides
Sulphur (S)	0.015 max	Combines with Mg	Sulphur removal is essential
Manganese (Mn)	0.2 max	Pearlite former	Excess promotes carbide
Phosphorus (P)	0.035 max	Embrittles structure	Pearlite stabilizer
Chromium (Cr)	0.04 max	Very potent carbide former	Retards annealing
Nickel (Ni)	0.04-2.0	Strength, hardness	Potent pearlite stabilizer
Copper (Cu)	0.03-1.0	Strength, hardness	Potent pearlite stabilizer

Table 2.1: Range of chemical composition of ductile iron casting for ADI production [5].

Other than this, Copper (Cu), Nickel (Ni), and Molybdenum (Mo) are also added as hard-enability enhancing elements during ADI production to provide sufficient hardenability to the matrix. The Mo and Mn are, however, potent carbide formers [5]. Therefore, their levels should be carefully controlled to avoid micro-segregation and the resultant degradation of mechanical properties. To obtain the desired hardenability, Cu and Ni should be added to the melt. Mo is usually preferred over Mn because of its stronger hardenability enhancement effect for an equivalent intercellular carbide forming tendency [25].

After the melting and alloy addition, spheroidization (magnesium treatment) is performed followed by or combined with the inoculation process to ensure a graphitic structure free from carbides [5]. Spheroidization, or magnesium treatment, of cast iron is a mean of modifying the solidification structure. It promotes the graphite phase precipitates to grow as spherical particles instead of flakes, thus resulting in a cast iron with significantly improved mechanical properties [26]. Figure 2.2 present the correlation between the residual Mg % and the obtained graphite shape in the cast iron metallic matrix. Depending upon the magnesium content, the shape of the graphite can be changed to either flake or compacted or spheroidal forms. The

(a)
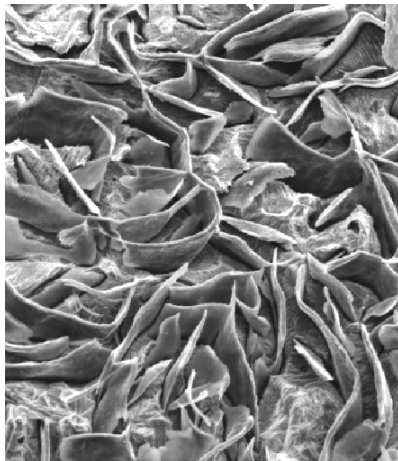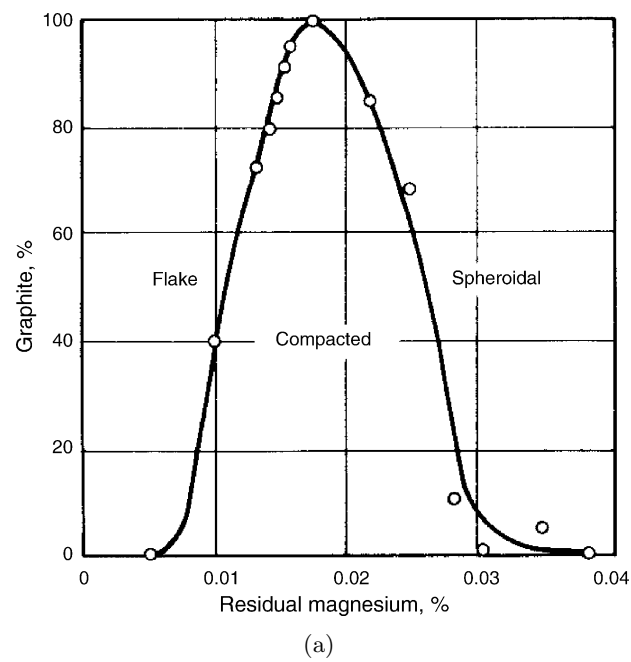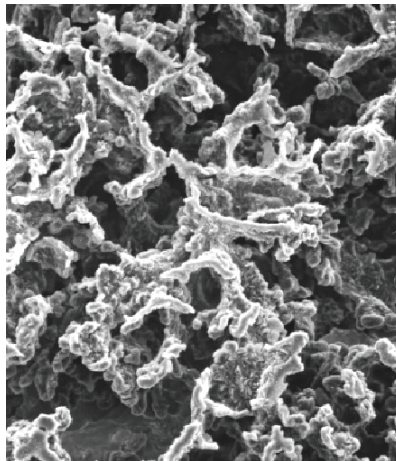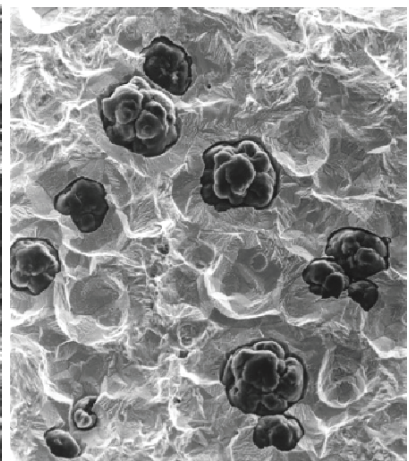
(b)　　　　　　　　　　(c)　　　　　　　　　　(d)

Figure 2.2: (a) Correlation between the Mg residual and graphite shape, (b) Flake graphite morphology, (c) Compacted graphite morphology and (d) Spheroidal graphite morphology [23, 24].

transition of graphite morphology from flake to compacted to spheroidal significantly influences the material properties of the microstructure [24]. Table 2.2 presents the comparison of ductile iron material properties with other cast irons. The Mg treatment can be regarded as desulphuring and deoxidizing treatment as it has strong affinity to both sulphur and oxygen. Therefore, it prevents unwanted slag to store as a mass, and promotes the dispersion of micro-particles, which act as potential sites for graphite nucleation during solidification [3, 21]. Hence, an effective spheroidization also gives a good basis for inoculation [21, 27]. Inoculation is the process of increasing the numbers of nucleating sites from which eutectic graphite grows during solidification. Most inoculants are based on ferrosilicon alloys that contain 70-75% silicon or ferrosilicon-graphite mixtures [28]. Inoculation reduces undercooling during solidification and helps to avoid the presence of carbides in the structure, especially in thin sections. It increases the number of graphite nodules, thus improving homogeneity, assisting in the formation of ferrite, and promoting ductility [3, 21].

Property	Ductile irons	Gray irons	CG irons
Tensile strength (N/mm^2)	400-700	160-320	300-600
Elongation(%)	6-25	nil	3-6
Modulus (GPa)	170-190	96-110	140-160
Charpy impact (J)	17	nil	3-7
Fatigue limit un-notched (N/mm^2)	185-280	108-123	230-310

Table 2.2: Comparison of ductile iron properties with gray and compacted graphite (CG) irons [24].

2.2.2   Casting and solidification

Ductile iron exhibits good fluidity and castability. However, special attention is required during its casting and solidification characteristics to produce sound, defect-free castings. The ductile iron normally contains magnesium, oxidation of this element, together with silicon, may give rise to small inclusions and dross both in the ladle and in the gating system [15, 22]. This dross must not enter the casting, where it can cause laps, rough surfaces, or pinholes. Other than this, the excessive temperature gradients in the casting and pouring of cold metal are undesirable and may promote carbide formation in thin sections and casting extremities. These can be avoided by pouring at not less than 1315 ℃ for castings of 25 mm section size and above up to 1425 ℃ for castings of 6 mm section size and by modifying the gating system to include such features as flow-off and runner bar extensions.
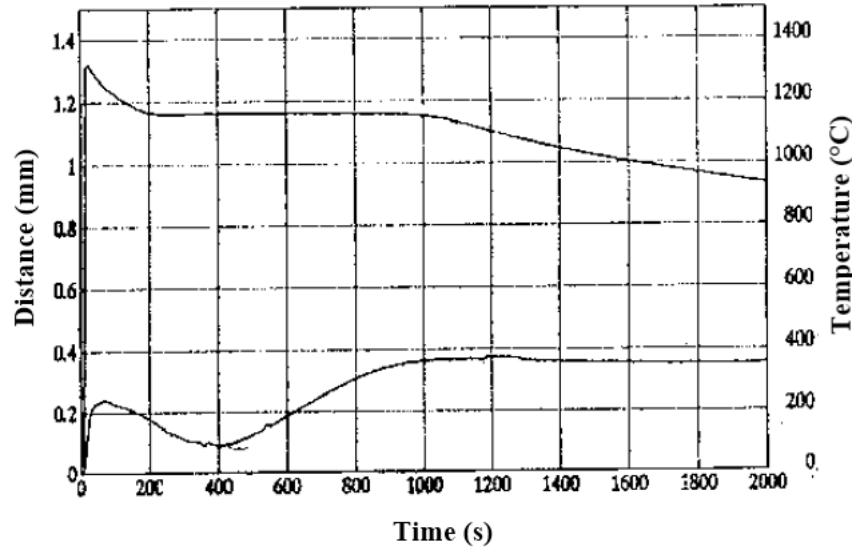
Figure 2.3: The upper curve temperature and lower curve outward dilatation curve in a green sand mould, casting of 50 mm plate, measured by thermocouple and dilatation transducer. [29].

The solidification of a ductile iron casting undergo three different stages of volume change as a result of cooling [22]:

- A volume decrease of the liquid metal as soon as it has been poured, while it cools to the temperature of eutectic solidification.

- A volume increase during eutectic solidification, when graphite nodules grow and exert considerable expansion pressure on the mould; depending on casting design and mould strength, this can lead to oversize castings.

- A volume decreases during the last stage of solidification (secondary shrinkage).

Figure 2.3 presents the influence of ductile iron volume change during solidification on the green sand mould wall. It can be seen that the eutectic expansion of ductile iron cannot be effectively utilized to compensate for earlier contraction and shrinkage in case of green sand mould as the mould wall dilates (move outward) when subject to the enormous expansion forces. Additionally at the end of solidification when the metal contracts the mould wall stays at its maximum dilated position leads to the shrinkage defect in the casting. It can be observed (Fig. 2.3) that the casting at the end of solidification in the green sand mould has increased in size by about 0.35 mm.

To reduce the shrinkage defects, the risers are used to achieve sound casting by taking advantage of the second-stage volume increase to reduce the amount of feed metal required.

This is done with pressure control, in which riser (feeder) necks are designed to freeze during solidification, causing the solidification volume increase to compensate for any casting expansion and late-stage volume decrease or secondary shrinkage [15, 22].

The green sand moulding is most widely used method for the production of ductile iron casting, which has its own limitations. First, it was found that the ductile iron expands slightly during eutectic solidification due to the formation of graphite [14, 22]. This expansion stresses the moulding material, causing an enlargement of the mould cavity if the sand is insufficiently compacted. This can lead to shrinkage defects as the eutectic expansion cannot be effectively utilized to compensate for earlier liquid contraction from the superheat temperature to liquidus temperature. Second, the limitations of the dimensional accuracy and surface finish of the final casing in the sand moulding process. Therefore, to reduce the casting defects and to obtain the near net shape casting, the mould should be rigid and its hardness is sufficient to withstand the eutectic expansion of the ductile iron and thus improving dimensional accuracy [22].

2.2.3 DI microstructure and ADI casting quality

The mechanical properties offered by ADI make it an attractive material for demanding applications in which distinct specifications must be met consistently. While greatly enhancing the properties of a conventional ductile iron casting, the ADI production process cannot compensate for casting defects that would impair mechanical properties. Therefore, ADI castings should be a sound defect free casting with the following microstructural parameters [5]:

- Nodularity: >80%;

- Nodule Count: $100/mm^2$ minimum;

- Consistent chemical composition;

- Essentially free of carbides, porosity and inclusions;

- Consistent pearlite/ferrite ratio.

Typical etched (Nital 2%) as-cast microstructure of spheroidal graphite iron is shown in the Fig. 2.4 in which graphite nodules are surrounded by a ferrite shell (light) and pearlite phase (dark) [30]. The typical nodule count is defined as the number of graphite nodules per square millimeter on a polished surface examined under a microscope at 100 magnifications (100X) [31]. The microstructure of ductile iron is characterized by the presence of spherical graphite particles (nodule counts) throughout the material. Nodule count has the following effects on the microstructure, can significantly influence the material properties of ductile iron [10, 32, 33]:
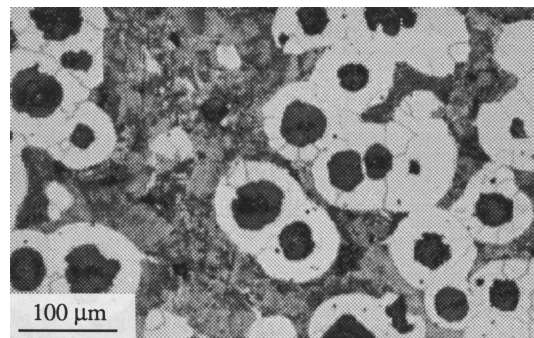
Figure 2.4: Typical spheroidal graphite iron microstructure [30].

- Increasing the nodule count decreases the pearlite content, decreasing strength and increasing elongation percentage.

- Nodule count affects carbide content. Increasing the nodule count improves yield strength, ductility and machinability by reducing the volume fractions of carbides.

- Increasing the nodule count produces a finer and more homogeneous microstructure. This refinement of the matrix structure reduces the segregation of the alloying elements, which might produce inter-cellular carbides.

- Nodule count affects graphite size and shape. Increasing nodule count results in a decrease in nodule size, which improves tensile, fatigue and fracture properties. Inoculation practices used to improve nodule count often make the nodules more spherical. Thus, high nodule count is generally associated with improved nodularity.

Therefore, the production of a high-quality DI casting is an essential step for the ADI production. However, it is not a sufficient condition to ensure optimum properties in ADI. The casting must be heat treated suitably by taking into account the interaction between casting dimensions, composition, microstructure and the desired properties in the required casting.

2.3   ADI castings characteristics

2.3.1   Heat treatment and ADI microstructure

The conventional heat treatment process for ADI production is shown in Fig. 2.5. The heat treatment process for ADI production consists of the austenitization and austempering processes [6, 20]. During austenitization, the casting is heated up to a temperature range of 850-950 °C to convert the ferrite/peralite metallic matrix into the austenite matrix. Isothermal heat

treatment at the austenitization temperature enriches the carbon content of austenite metallic matrix. The casting is then quenched down to an austempering temperature range (250-450 ℃) and holding for an appropriate time for isothermal transformation, and air cooling to room temperature.
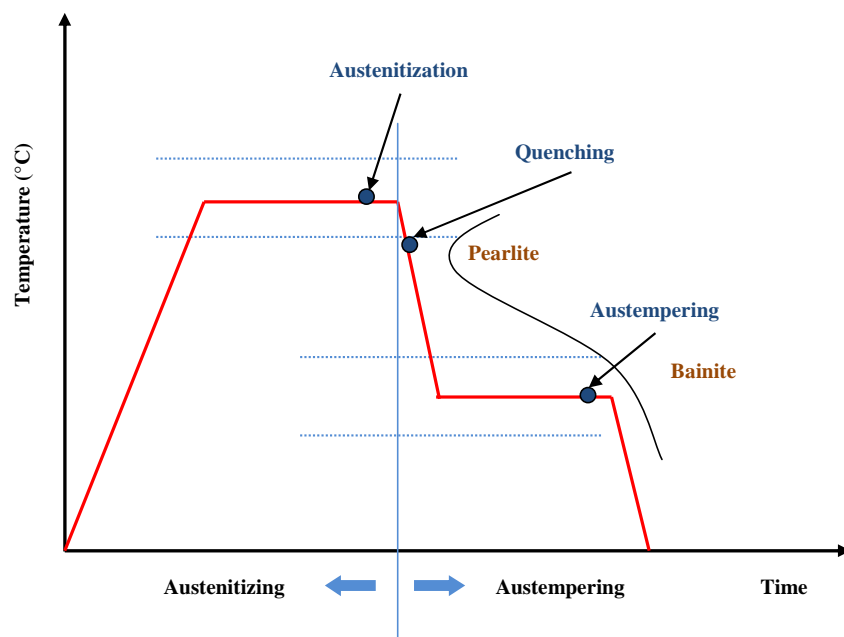
Figure 2.5: Conventional heat treatment process for ADI productions.

Depending upon the heat treatment parameters, ADI show versatile behavior in mechanical properties. The heat treatment parameters can provide insights into the detailed evolution and change in microstructure and mechanical properties of the ADI during its processing [34]. Austenitization is the first step of the ADI heat treatment. The austenitization temperature and time control the carbon content of austenite which in turn affects the structure and properties of ADI. Austenitization occurs by nucleation and growth [35, 36]. The austenite phase generally nucleates at the ferrite/graphite interface or ferrite/carbide interface if the matrix contains pearlite. The diffusion of carbon to austenite may take place by dissolution of graphite and cementite from nodules and pearlite, respectively [35]. Increasing the austenitization temperature accelerates the austenitization kinetics and increases the carbon content of resulting austenite. The higher carbon content of austenite increases its hardenability and stability. It also favours redistribution of segregated elements and decomposition of intercellular carbides if present. The optimum austenitization time is that at which austenite with maximum and uniform carbon has been achieved [5, 34]. Erdogan et al. [37] found that the carbon content of austenite increases with increasing the austenitization temperature during the austenitization process as shown in Fig. 2.6.
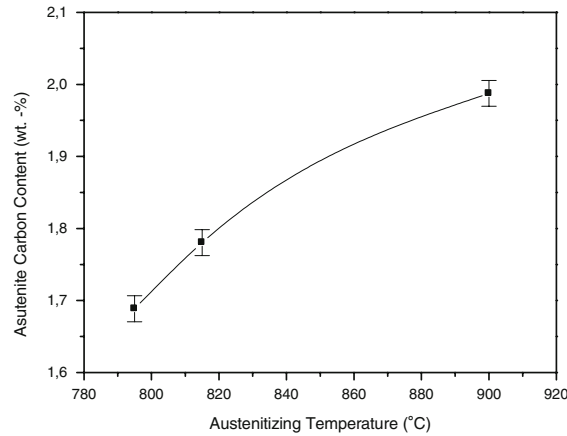
Figure 2.6: Variation of carbon content of austenite with austenitization temperature [37].
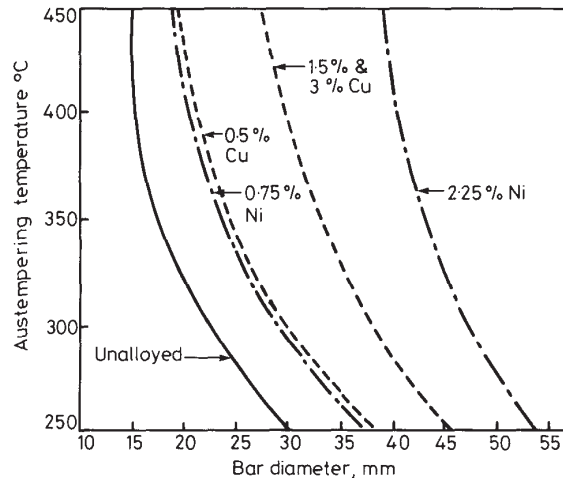
Figure 2.7: Effect of nickel and copper on the maximum bar diameter that can be austempered without pearlite formation (Base iron composition: 3.5% Carbon, 2% Silicon, and 0.25% Mn) [34].

The ductile iron casting is then quenched down to austempering temperature followed by austempering process. To obtain the optimized combination of mechanical properties, the prealite formation should be avoided during quenching. Blackmore and Hardning [34] illustrated that for unalloyed irons, the maximum diameter which could be transformed without pearlite formation increased from 15 mm at a temperature of 450 ℃ to 30 mm at a temperature of 250 ℃. Beyond these values, pearlite initially formed at the centre of sections associated with graphite nodule boundaries. Figure 2.7 illustrate the influence of Cu and Ni on the maximum bar diameter that can be austempered without pearlite formation. The presence of pearlite in the final ADI microstructure is detrimental to its mechanical properties.

Achieving optimal mechanical properties of ADI is a function of constituents of austempered
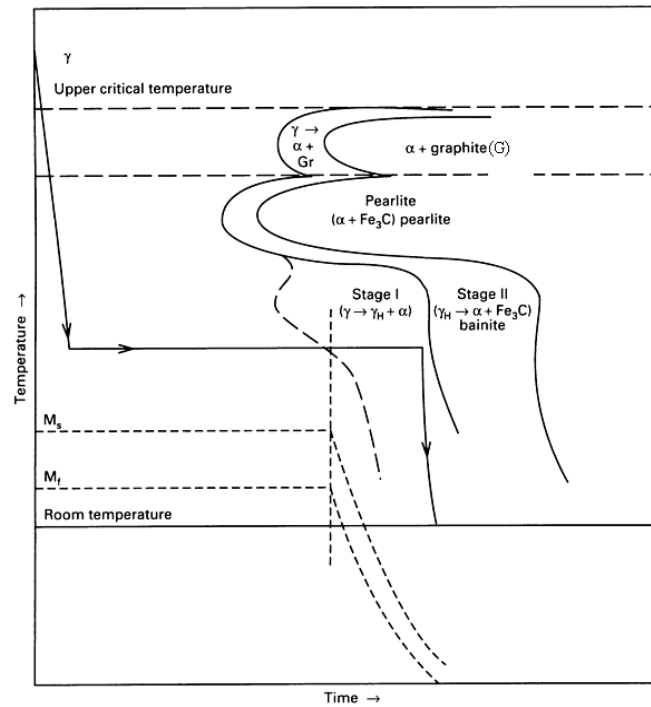
Figure 2.8: Isothermal transformation diagram of a processing sequence for austempering heat treatment [14]

microstructure, which in turn depends on the austempering temperature and time. Depending upon the austempering time two important stage reactions [36, 38, 39] occurred during austempering process as shown in Fig. 2.8. In the first stage, the primary austenite decomposes into ferrite (α) and high-carbon austenite (γ_{HC}), attaining a microstructure called ausferrite. The presence of 2 to 3 wt% silicon (Si) prevents the rapid formation of carbides during the austempering process. In addition, as the stage I reaction progress, the carbon enrichment of austenite decreases the martensite start temperature (M_s) and the martensite finish temperature (M_f) as shown in Fig. 2.8.

$$\gamma_0 = \alpha + \gamma_{HC} \tag{2.1}$$

$$\gamma_{HC} = \alpha + carbide \tag{2.2}$$

During austempering process the transformation kinetics is promoted by the nucleation and growth of ferrite needles by the rejection of the carbon atom to the surrounding austenite [40]. The rejection of carbon from ferrite enrich austenite with carbon and make it more stable. It was stated that the kinetics of the austempering process is governed by the variation in the volume

free energy which is proportional to the undercooling generated by the difference between the austenitizing and the austempering temperatures [41]. Moreover, for a particular austempering temperature, the nucleation and growth of ferrite needles influenced by the alloying elements and graphite morphology [42, 43]. As the austempering process proceeds the carbon content of austenite reached to its saturation values and then it show steady behavior with time, this stage is known as process window. At this stage the ADI material acquires its optimum mechanical properties. As the austempering time increases further, the high-carbon austenite further decomposes into ferrite and carbides and the stage II reaction starts. This reaction detriments the mechanical properties of the final casting, particularly ductility and toughness. The extent of processing window depends on many factors, including the percentage and segregation patterns of alloying elements, and the heat treatment parameters [40].

Processing window defines the austempering time interval, (t2-t1) over which the start of the processing window (time, t1) has been defined as the austempering time at which the amount of unreacted austenite, low carbon austenite has been reduced to 3%. The end of the processing window (time, t2) has been defined as the time at which the maximum retained austenite level has been reduced by 10% [44].
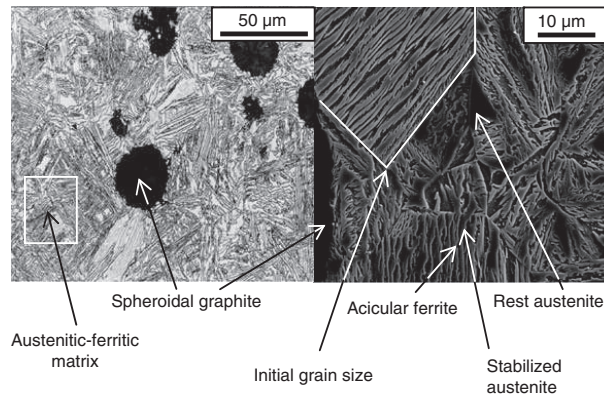
Figure 2.9: (a)SEM micrograph of ADI microstructure and (b) Ausferrite microstructure with acicular ferrite, carbon enriched austenite and graphite nodule [45]

The microstructure obtained by austempering heat treatment process is shown in Fig. 2.9. It consists of a mixture of acicular ferrite, high-carbon austenite and residual austenite with graphite nodules embedded in it, defining its unique mechanical properties [20]. Sidjanin et al. [46], suggested three different type of austenite in ADI based on its carbon percentages, which are as: (i) Un-reacted metastable austenite with carbon content less than 1.2 %, (ii) reacted metastable austenite with carbon content between 1.2-1.7%, and (iii) reacted stable austenite with carbon content between 1.8-2.2 %. Thus, the only desirable type of austenite in ADI, obtained after austempering is stable high carbon austenite as other forms of austenite may

be transformed into martensite at room temperature resulting in poor toughness and ductility. The term retained austenite includes all types of austenite.
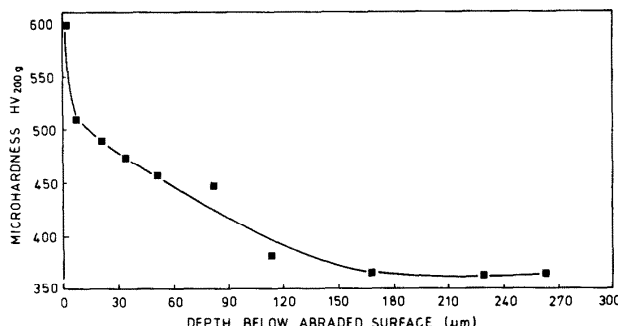
Figure 2.10: Micro-hardness survey of abraded surface layers in SG60 austempered at 350 ℃ for 22 min (Abraded length: 14.64 m; load: 31.38 N; Bulk hardness: 366 (HV 30)) [47].

2.3.2   ADI properties

The mechanical properties of ADI are related with its unique ausferrite microstructure. Not only, ADI is superior to other grades of DI (Fig. 2.1), it also replaced forged steels because of its equivalent strength. Moreover, the strength to weight ratio of the ADI is among the highest and its relative cost per unit of yield strength is among the lowest of all engineering materials, including aluminium [48]. It gives ADI economy in design without loss of performance. The yield strength of ADI is three times more than that of cast or forged aluminium. In addition, ADI weighs only 2.4 times more and 2.3 times stiffer as compared to aluminium. It is also 10% less dense than steel. For a typical component, it cost 20% less per unit weight than steel and half that of aluminium [49]. A significant advantage of ADI is its outstanding wear resistance. The enhanced wear resistance of ADI is due to the ability of unreacted high-carbon austenite to strain hardened when the surface of an ADI is subjected to deformation [50]. This transformation results in a significant increase of the surface hardness as shown in Fig. 2.10.

Shepperson and Allen [47] investigated the abrasive wear behavior of the ADI materials in correlation with its microstructural characteristics and then they compared it with the abrasion behavior of mild steels and abrasion-resistance alloys under similar experimental conditions. They observed that the ADI materials show superior wear resistance as compared to the mild steel and abrasion-resistant alloys at similar bulk hardness level. In additions, they found that the lower austempering temperatures results in better abrasion resistance at lower strain values and higher austempering temperatures results in higher toughness values. They concluded that at higher strain rates the wear resistance can be accommodated by the strain induced

transformation of austenite to martensite and the high work hardening rate of the resulting microstructure.

The material properties and microstructure of the ADI can be controlled and tailored by carefully controlling the heat treatment parameters, to get the desired combination of mechanical properties, e.g., high strength, high wear resistance or high fracture toughness. Table 2.3 lists the mechanical properties of different ASTM grades of ADI. The influence of the production parameters on the austempering kinetics and material properties of ADI are reviewed in the next section.

Property	ASTM A897 grades				
	1	2	3	4	5
Tensile Strength, min., MPa	900	1050	1200	1400	1600
Yield Strength, min., MPa	650	750	850	1100	1300
Elongation in 50 mm, min, %	9	7	4	2	1
Impact energy, J^1	100	80	60	35	20
Typical hardness, HBW, kg/mm^2	269-341	302-375	341-444	388-477	402-512

Table 2.3: Mechanical property requirements of different ASTM A897M grades of ADI [51].

2.4 Influence of production parameters on ADI characteristics

2.4.1 Role of alloying elements

The primary role of alloying elements in ADI production is to provide sufficient hardenability to the matrix to avoid the pearlite nose of the continuous cooling transformation (CCT) diagram (Fig. 2.8). The alloying elements also influence the processing window and the relative effectiveness of the austempering kinetics during stage I and stage II reactions. Manganese (Mn) and Molybdenum (Mo) delay the austempering kinetic reactions during stage I and stage II of the austempering process [25]. In case of mechanical properties, both tensile strength and ductility decreases with an increase in Mo content beyond a certain limit. This deterioration in properties is probably caused by the segregation of molybdenum to cell boundaries and the formation of carbides [10]. The level of molybdenum should be restricted to not more than 0.2% in heavy section castings. Copper (Cu) does not affect the carbon diffusion in austenite or the stability of austenite. However, it has been reported that Cu suppresses carbide formation

---

[1]Unnotched charpy bar tested at 22±4 ℃. The values in the table are a minimum for the average of the highest three test values of the four tested samples.

in lower bainite. Nickel (Ni) acts in a similar way to Cu. If Ni is present in excess of 0.5%, it slows down the stage I reaction, and thus, causes the formation of martensite at austenite cell boundaries on cooling [52]. The high carbon and silicon levels in ductile iron casting also play an important role in their response to heat treatment. The higher carbon levels in ductile iron increase hardenability, permitting heavier sections to be heat treated with lower requirements for expensive alloying or severe quenching media. It can also cause to quench cracking due to the formation of martensite, and/or the retention of metastable austenite. This undesirable phenomena make the control of composition, austenitizing temperature and quenching conditions more critical in ductile iron. Whereas, higher the silicon content in DI casting, lower the solubility of carbon in austenite and the more readily carbon is precipitated as graphite during slow cooling to produce a ferritic matrix [10].

The segregation of alloying elements in the intercellular region during solidification significantly influence the austempering kinetics together with mechanical properties as stated above. These segregations of alloying elements are not removed during the austenitization and produce heterogeneity in the structural matrix. Figure 2.11 present the segregation behavior of alloying elements between two graphite nodules. This segregation behavior of alloying elements is related to the eutectic cell that forms around the graphite nodule during solidification. It leads to a heterogeneous response towards austempering kinetics in the microstructure depending upon the position and amount of alloying elements. It show (Fig. 2.11) three different zones along the eutectic cell illustrating the the distribution of alloying elements in the ductile iron. Zone I is located along the graphite. In this zone the silicon, nickel and copper levels are high but the manganese is depleted. In zone II change in solute concentration is more gradual. Zone III is located at the solidification cell boundary, the silicon and copper levels are low but manganese, molybdenum, chromium and phosphorus are enriched. Bosnjak et al. [53] studied the influence of micro-alloying on the kinetics of bainitic reaction in austempered ductile iron. They concluded that the effect of Ni and Mo alloying elements on stage I kinetics is through their influence on the carbon content of the austenite. Alloying elements, Ni and Mo, show a strong influence on the stage II reaction through their effect on the nucleation and growth of the ferrite and carbide phases from high carbon austenite. According to them Ni and Mo delay the appearance of the processing window. Due to this, tight control of the alloying elements is imperative for ADI production if consistent properties have to be maintained.

2.4.2 Heat treatment parameters

The mechanical properties of ADI can be varied over a wide range by a suitable choice of heat treatment parameters. The properties achieved depend principally upon austempering
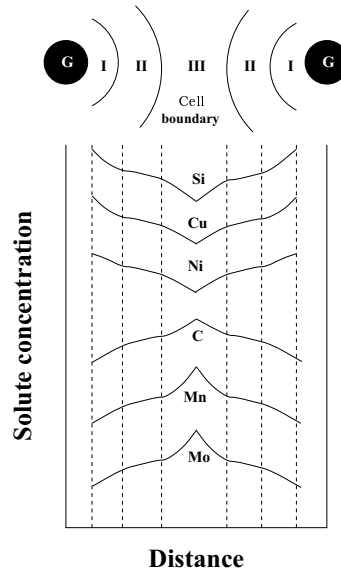
Figure 2.11: Schematic representation of the segregation zones between adjacent graphite nodules. [54].

temperature and time, but are modified by the austenitizing conditions and the composition of the iron. The carbon content of austenite is the function of austenitizing temperature and chemical composition. Avishan et al. [55] had found that at a constant austenitizing temperature, the lower austempering temperature makes the processing window wider. Furthermore, a lower austenitizing temperature shifts the beginning of the processing window to a shorter time and makes it wider. Lower austenitization time also results in the coarse austempered microstructure containing blocky austenite and martensite within it.

Blackmore and Harding [34] illustrated the influence of austempering and austenitization temperatures on the tensile properties of the ADI as shown in Fig. 2.12. According to them, the strength properties increases as the austenitizing temperature increases from 850 to 925 ℃. The effects of these properties were greatest at the lower austempering properties. However, no significant change was observed in elongation percentage. The variation in tensile properties with austenitizing temperature revealed that the strength properties are lower at lower austenitizing temperature. According to them, the carbon saturation and complete austenitization of the initial casting increase its strength properties. They stated that at higher austenitizing temperature, the austenitizing time has no significant effect on the tensile properties of ADI as the carbon saturation of austenite was reached relatively rapidly at higher austenitizing temperatures. They concluded that the longer treated time at higher austenitizing temperatures are not necessary, and the optimum mechanical properties in ADI can be achieved by the carbon saturation of initial casting using austenitizing temperatures between 900 and 925 ℃.
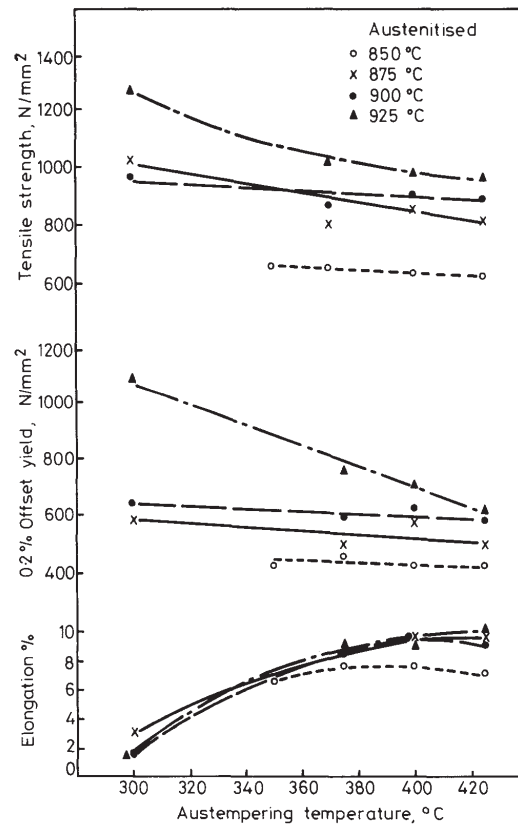
Figure 2.12: Variation of tensile properties with austenitizing and austempering temperatures (Austenitization time: 60 min and austempering time: 60 min) [34].
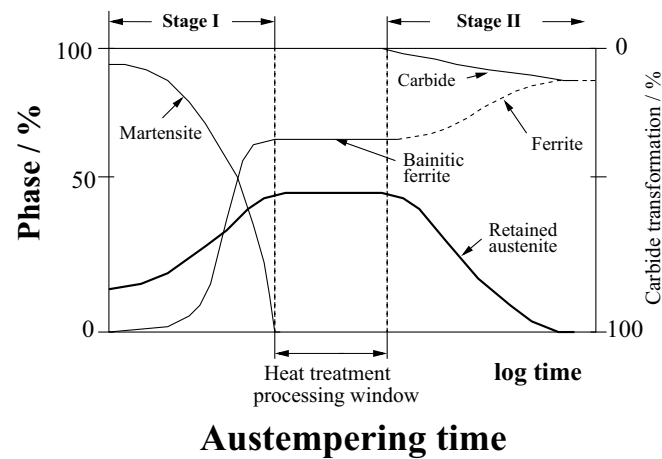
Figure 2.13: Schematic representation of the development of different phases in ADI during austempering process together with an illustration of the processing window [56].

The mechanical properties of ADI depend on the relative amounts of different phases (acicular ferrite and stabilized austenite, amount and morphology of retained austenite and the presence of martensite) in the metallic matrix which are the functions of the austempering heat treatment parameters [34]. Figure 2.13 show the variation in different phases of ADI during austempering process. It can be seen that the amount of acicular ferrite and retained austenite increase with austempering time and get optimized in the processing window range providing optimized material properties to ADI. The formation of martensite is favoured by low austempering temperatures and by short treated time. The presence of hard and brittle phase martensite in the final ADI microstructure causes machining problems and it is detrimental to the mechanical properties of ADI. In addition, the austempering parameters significantly influence the ferrite and austenite morphology. The higher austempering temperatures give rise to high volume fractions of carbon-enriched austenite and coarser acicular ferrite morphology in the ausferrite microstructure. This type of microstructure is responsible for the combination of lower strength and higher ductility properties in the ADI materials. On the other hand, austempering at lower temperatures produces a large-volume fraction of the acicular ferrite and lower amount of carbon enriched austenite, resulting in higher strength, lower ductility and increased wear resistance [57]. After selecting the austempering temperature, austempering time is chosen to optimize the mechanical properties of ADI. The short austempering time leads to the austenite transformation to martensite, resulting in poor toughness and ductility, while long austempering time will result in the austenite enrichment with carbon, give rise to the optimized mechanical properties. If the holding time is too long, austenite decomposes into ferrite and carbide, resulting in the loss of toughness and ductility.

2.4.3 Conclusions

While the unique ausferrite microstructure developed by the austempering heat treatment of ductile iron provides many remarkable engineering properties to ADI, certain characteristics impose limitations on its widespread use. These include (a) requirement of defects free ductile iron casting with a good dimensional accuracy and surface finish for ADI production, (b) optimization of heat treatment parameters, (c) saving energy and time during its large-scale industrial production, and (d) achieve better combinations of strength and ductility properties. Together with this, the opportunity for wide commercial exploitation of light weight ADI casting has arisen in response to pressure on engineering and automotive industries to produce components, which provide improved properties and performance at low manufacturing cost. However, to achieve full potential of ADI, there is a need for the development of controlled

and efficient casting and heat treatment practices to produce the desired properties and performance in ADI microstructure. The continuing progress in ADI processing technology should be made in twofold approaches. First, to understand the appropriate relationship between the microstructural characteristics of ADI and its influences on the mechanical properties. Second, is the implementation of the innovative process route to save energy and time during ADI production and to tailor the ADI microstructure to achieve the desired properties and performance.

The other aspect is to reduce the manufacturing cost of ADI by improving its machinability. ADI is considered as hard-to-machine material due to its inherent properties. In the current scenario, there is a growing demand of high material removal rates to increase throughput and minimize the overall manufacturing cost. However, machining at higher material removal rates requires parts with uniform microstructures, consistent properties, and a minimum volume fraction of abrasive inclusions. The ADI materials cause rapid tool wear, which leads to the loss of tolerances and surface quality, a loss in productivity, machine down time, and higher scrap rates. To solve this problem, there is a need of correlating the machining characteristics of ADI materials with its microstructures and production parameters. In the next section, the machining characteristics of ADI are reviewed.

2.5 The state of art in machining ADI

Machinability is a critical property controlling the product economy during the manufacturing of engineering components. It refers to the ease or difficulty with which a given material can be machined. Machinability of a material is generally defined in terms of three factors: forces and power consumption, tool wear and surface integrity. Thus, a material with good machinability is the one requiring low power consumption, with low tool wear and producing a good surface finish [58].

Understanding the microstructure and mechanical properties of the material is the key to understand the machinability of the material. In the machining of cast irons, tool life is influenced by the cutting parameters and the microstructure. The graphite in iron is important to its free-machining characteristics, but tool's life is dependent on the microstructure of the matrix metal around the graphite [14]. The graphite characteristics in cast irons determine the potential surface finish obtainable with a cutting process and the necessary cutting forces. Together with this, there are many other factors (different matrix phases, tool materials, and cutting environment etc.) that can influence the machinability of cast iron. One way to improve the machinability of hard to cut materials is to identify and rank by severity the influence of cutting parameters, cutting tool materials and conditions that have undesirable effects. The other approach is to correlate the metallurgical characteristics (chemical composition, microstructures and morphology of different phases) of material with its machinability. Therefore, a keen understanding is required for the interactions of microstructure, material properties, machining parameters, cutting tool's material and wear mechanisms for the optimization of the ADI machining process.

The other aspect of the machinability from the environmental and economical point of view is to reduce the use of lubricants during machining processes. To reduce the production costs and to make the machining processes environmentally safe, there is a need to move toward dry or near-dry machining by eliminating or minimizing the use of lubrication. To achieve the objective under these conditions there is a need for the development and the use of new materials for tools and coating. Therefore, in the following sections the machining characteristics of hard-to-machine ADI materials is reviewed and recent work and advances concerning machining of ADI materials are presented.

2.5.1 Machining characteristics of ADI

The material properties responsible for the poor machining characteristics of ADI are as follows:

- Austenite has higher work hardening rate than ferrite and this causes problems in machining of ADI. During plastic deformation of ADI, the austenite lattice show higher tendency to deform due to the greater number of sliding planes. At the same time it shows increase in strength and hardness during the deformation due to the transformation of metastable austenite [59].

- The lower thermal conductivity of austenite leads to the development of higher temperature at the cutting zone. Because of this, chips are formed on the basis on catastrophic failure in narrow shear surfaces and leads to the formations of unfavorable segmented chips during machining [59, 60].

- ADI has a coefficient of thermal expansion that is higher than that of carbon steel or ductile iron, so an increase in workpiece temperature will result in dimensional growth of workpiece during machining. This should be accounted for in operations such as deep-hole drilling [55, 60].

- ADI has a yield strength that is higher than most steels but its Youngs Modulus is 20% lower making it prone to vibrations in machining. Therefore, ADI requires an extremely rigid workpiece clamping device and similarly rigid tool holders with short tool bending moments. Failure to account for this reduced workpiece stiffness will result in undesirable vibrations during metal removal which accelerates tool wear, and results in an undesirable surface finish and an increased dimensional standard deviation [55].

During machining, these characteristics causes: the formation of built-up edges (BUEs) when carbide tools are used, breakage of ceramic inserts, and sudden falls in hardness of tools made from high-speed steels. Low values of tool life, increased cutting forces and the appearance of unfavourable tough chips are the main characteristics which rank ADI materials among the group of materials that are hard to machine [59].

2.5.2   ADI as hard to machine material

ADI is considered as hard to machine material due to its inherent properties, particularly the low thermal conductivity and high work hardening coefficient, which leads to high cutting forces and cutting temperature during machining and lead to a short tool life [61]. The primary objective of machining is to separate a certain layer from the rest of the work material with minimum possible plastic deformation and thus energy consumption [62]. Machining characteristics of ADI is influenced by a complex interplay of the graphite nodules and its surrounding ausferrite matrix. During machining the graphite nodules in the plastic zone undergo severe deformation

and become preferentially elongated in the shear plane direction, ahead of the cutting tool. Due to the presence of graphite in spheroidal forms, chip formation in ADI is characterized by more plastic deformation than fracture [63].
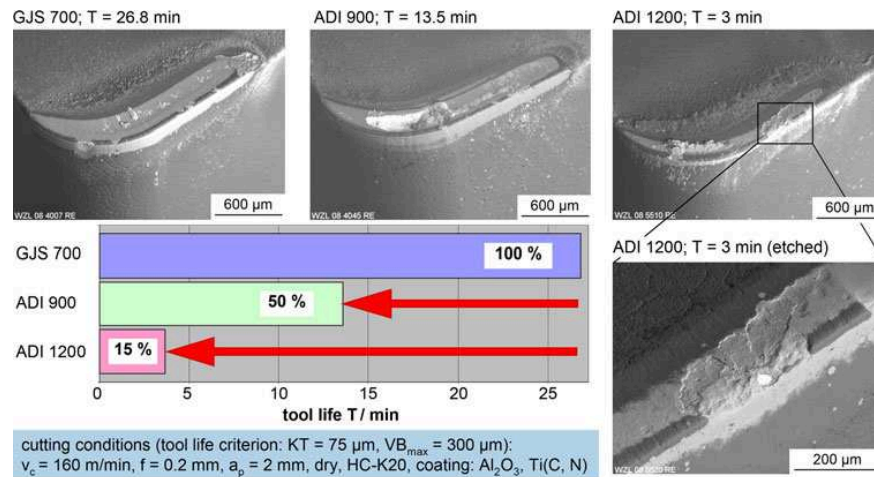
Figure 2.14: Wear mechanism and tool life in dry longitudinal turning [20].

Klocke et al. [64] stated that ADI exhibits low machinability as compared to conventional ductile iron materials and steels of similar strengths. They revealed the fundamental wear mechanisms when machining ADI. According to them the ausferrite microstructure of ADI has a tendency to adhere with tungsten-based carbide tools, which are commonly utilized for cutting cast irons. Besides adhesive, abrasive wear effects are also observed when machining ADI. They stated that abrasive wear is caused by the hardness of the ADI microstructure as well as by the segregation of alloying elements in the matrix. According to them during machining ADI, the cutting tools are exposed to a combination of both high abrasive and adhesive wear as well as to high specific loads on the cutting edge. As compared to other ductile irons the aptitude of ADI to segmented chip formation is even more which leads to the high dynamic proportion within the cutting forces and a deep crater wear close to the cutting edge can be detected. They concluded that the extreme crater wear near the cutting edge is a dominant typical tool wear mode in machining ADI. Therefore, there is a need to reveal the wear mechanisms being responsible for the poor machinability of ADI.

To better understand the machining characteristics of ADI, Klocke et al. [20] investigated the material related aspects of the machinability by varying the heat treatment parameters and alloying elements. They studied the tool wear behavior for different ADI grades (ADI 900 and ADI 1200) and pearlitic cast iron (GJS 700) for turning operation using the cutting tools (HC-K20, CNMA 120408)(Fig. 2.14). They found that in case of GJS 700, tool life was determined by abrasive flank wear (T = 27 min). On the other hand, in machining ADI 900,

strong crater wear close to the cutting edge was observed as mentioned above and tool life was reduced by 50% (13.5 min) in comparison to EN-GJS-700-2. However, in machining ADI 1200, delamination of the tool coating takes place, setting particularly the carbide substrate free, resulting finally in breakage of the cutting edge with tool life was reduced tremendously down to T = 3 min (Fig.15). According to them, the thermal load on the tool is high and the usage of coolant has to be preferred in order to suppress crater wear. They found that the flank wear is the major tool life criterion while using coolant as long as no plastic deformation of the cutting edge takes place. They found that the shape of the generated chips depends vitally on the material hardness. They stated that the machinability is influenced negatively and the tool life is reduced with a molybdenum content of more than 0.3%.

Therefore, for machining hard to machined ADI material, the cutting tool's materials should possess high hot hardness and strength together with excellent hot chemical inertia as well as high toughness. Moreover, the frictional characteristics at the tool-chip interface must be low for low heat production.

2.6   Cutting tool for machining ADI

The requirements for cutting tool material used for the machining ADI should include [65]:

- Cutting-tool substrate material must be very stable chemically and physically at high temperatures.

- Material hardness must be kept to the high temperatures suffered at the chip/tool interface.

- Tool material has to present a low wear ratio, both for the abrasion and adhesion mechanisms.

- Tool material must present enough toughness to avoid fracture, especially when operation to perform implies interrupted or intermittent cutting.

Figure 2.15 presents the cutting tool materials for the machining process. It includes tool steels, cemented carbides, cutting ceramics and super hard cutting tool materials made up of boron nitride and diamond. Matching the most suited cutting tool material and tool geometry with the workpiece material to be machined is important for trouble free and productive machining process. All of these factors added constraints on cutting tools. Cutting tool suppliers have responded with new tool materials, coatings, and geometries. Each of these components,
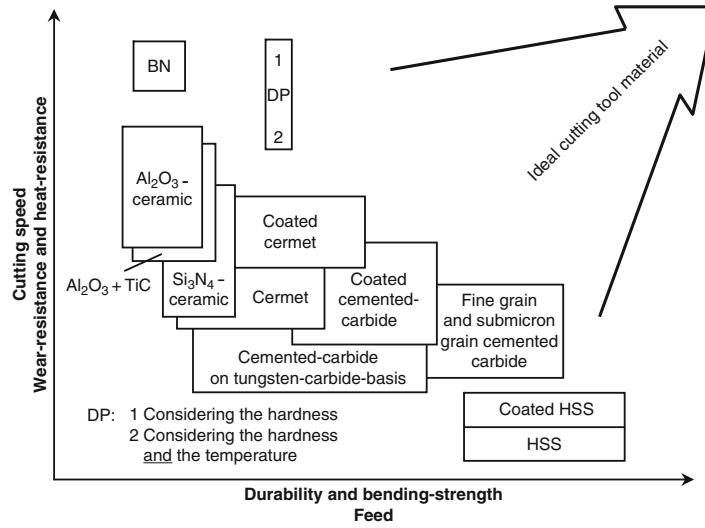
Figure 2.15: Schematic classification of several cutting tool materials [45].

separately and together, plays a critical role in achieving improved cutting performance and productivity. The following sections thus focus on the current state of cutting tool materials and coating technologies and outline their impact on ADI machining.

2.6.1 Machining ADI with carbide tools

Cemented carbide belongs to a class of hard, wear resistant, refractory materials in which the hard carbides of group IVB-VIB metals are bound together or cemented by a ductile metal binder, usually cobalt or nickel. Cemented carbides for metal cutting applications consist of more than 80% of hard phase tungsten carbide (WC). It is widely used for machining the ADI materials [66, 67].

Cakir et al. [57] investigated the machinability of different grades of ADI (ASTM grade 1, 2, 3 and 4) for dry turning operation using coated carbide inserts, ISO SNMG 120408 (K10). The machining conditions were as follows: (depth of cut: 1 mm; feed: 0.12 mm/rev; cutting speed: 96.7 m/min). They evaluated the machinability in terms of tool life, cutting forces and surface finish. They found that ADI material similar to ASTM Grade 1 appeared to cause the highest tool wear whereas ADI similar to ASTM Grade 3-4 appeared to cause the lowest tool wear. By reference to the as cast ductile iron, ADI similar to ASTM Grade 1 appeared to have the highest increase in the tangential cutting force (23%) whereas ADI similar to ASTM Grade 3-4 appeared to have the second highest increase (18%) in tangential cutting force. Surface roughness values (Ra) varied between 1.35 and 2.17 μm. ADI similar to ASTM Grade 1 seemed to have the best surface quality. However, these findings should be moderated because
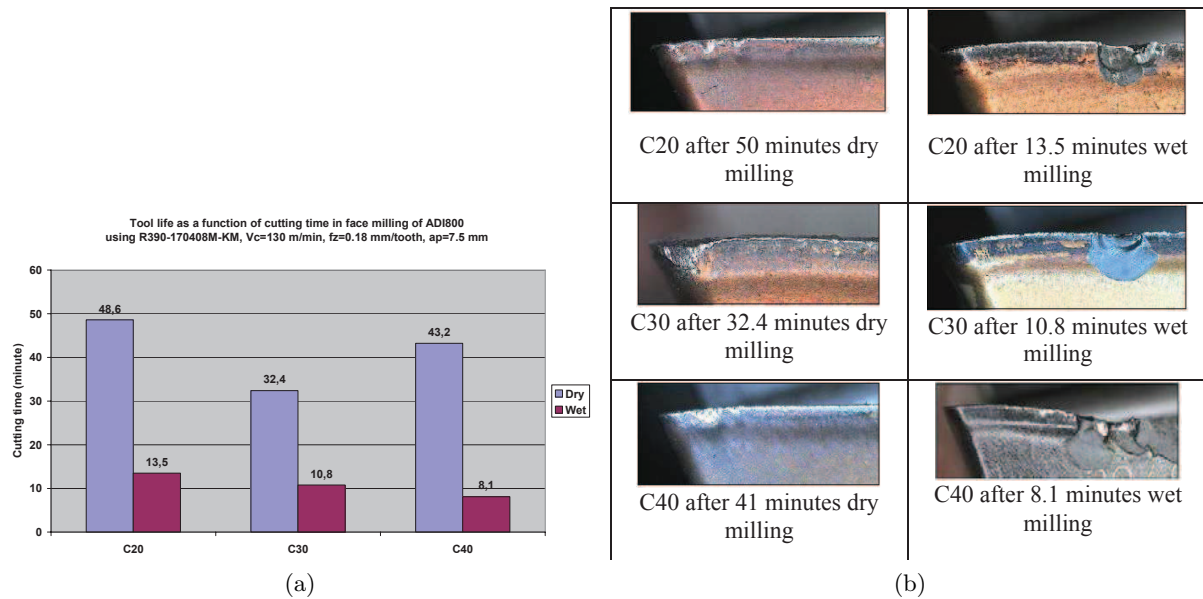
Figure 2.16: (a) The tool performance in dry and wet milling of ADI 800 and (b) The status of the inserts in the end of the tool life [68].

of the presence of martensite that was evident in these alloys.

Klocke and Klopper [69] investigated the turning of ADI material similar to ASTM Grade 1 using coated cemented carbide cutting tools (Al_2O_3-coated K10, Ti(C,N)-coated K10, TiN-Al_2O_3-coated P15), Al_2O_3 and Si_33N_4 ceramic cutting tools. They performed the machining test with or without the lubricant using a depth of cut of 1 mm, a feed of 0.2 mm/rev and a cutting speed in the range of 120-400 m/min. They found that the coated cemented carbide cutting tools could be successfully used at low cutting speeds. At high cutting speeds, Al_2O_3 ceramic cutting tools show better performance. The performance of Si_3N_4 ceramic cutting tools was very poor. The use of lubrication leads to the reduction of the flank and crater wear scars of cemented carbide tools, particularly at relatively high cutting speeds.

Sadik et al. [68] investigated the influence of cutting conditions on the tool life in milling of ADI 800 using the PVD (C20 and C30) and CVD (C40) coated carbide tools under the dry and wet conditions. They performed the machining experiment at a cutting speed of 130 m/min, feed: 0.18 mm/tooth, axial pass depth: 7.5 mm and radial engagement of the tool: 50 mm. They found that PVD coated C20 tool show best performance due to the presence of PVD coating with small grains and low compressive stresses, which leads to high abrasive wear resistance. They found that CVD coated grade (C40) provides better wear resistance under dry condition whereas the same coating shows poor performance under wet condition (Fig. 2.16a). They explained that the CVD coatings have tensile stresses and cooling cracks,

(a) $Al_2O_3 + ZrO_2$; Air

(b) $Al_2O_3 + ZrO_2$; Argon

(c) $Al_2O_3 + TiC$; Air

(d) $Al_2O_3 + TiC$; Argon
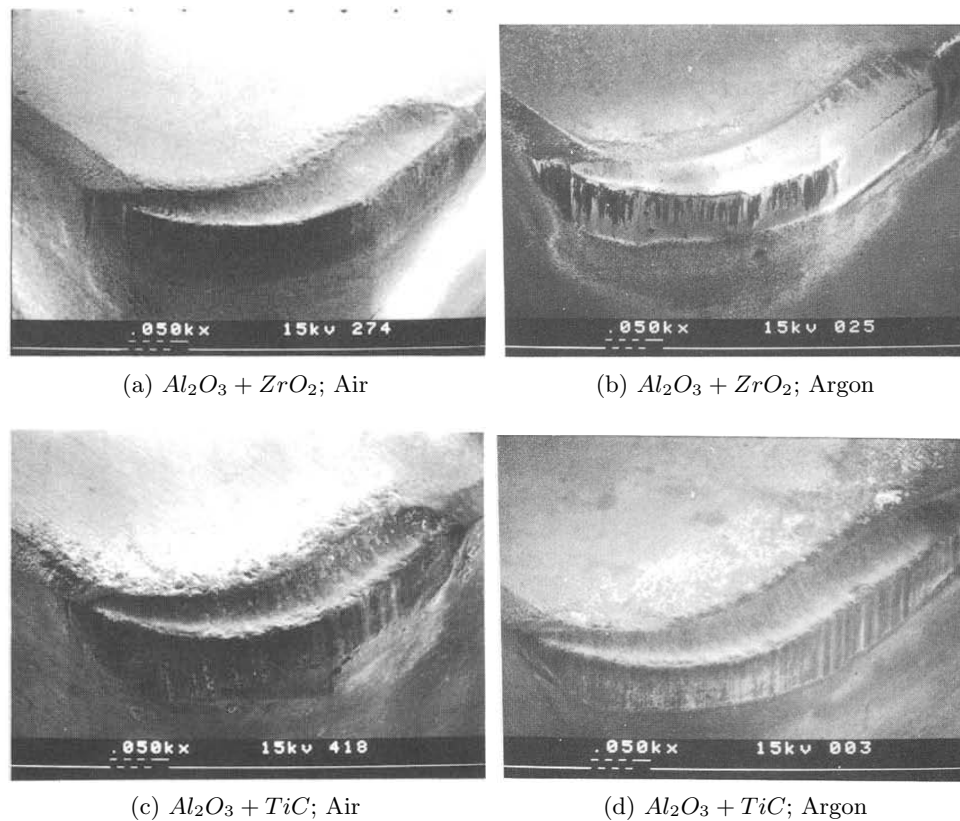
Figure 2.17: Tool wear pattern in argon and air cutting atmosphere [70].

which will grow continue under the thermal/mechanical loading. They found that under dry conditions chipping mechanism is the main wear mechanism whereas under wet condition notch wear is the determining wear mechanism while milling ADI (Fig. 2.16b).

The cemented carbide tools show stable behavior regarding chemical and thermal aspects of machining. However, they have their own limitations too. The high temperatures and stresses during machining can cause blunting from the plastic deformation of the tool tip, and high stresses may lead to catastrophic fracture.

2.6.2 Machining ADI with ceramics tools

Ceramics are inorganic, non-metallic materials, which are subjected to high temperature during synthesis or use [66]. Masuda et al. [70] investigated the cutting performance and wear mechanism of various commercial ceramic tools such as zirconia-toughened alumina ($Al_2O_3 + ZrO_2$), SiC whisker-reinforced alumina ($Al_2O_3 + SiCw$) and alumina containing TiC ($Al_2O_3 + TiC$) when turning ADI (UTS: 782 MPa and Elongation percentage: 3.8%) in air. In addition, to consider the difference in wear behavior between alumina inserts containing TiC and ZrO_2,
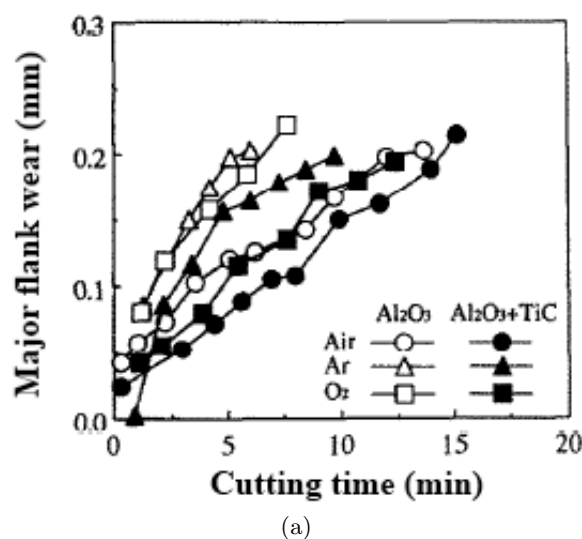
Figure 2.18: Effect of environmental atmosphere on major flank wear rate for ceramic insert during dry turning (cutting speed: 150 m/min; feed: 0.1 mm/rev; depth of cut: 1 mm) [70].

the effects of oxidation on tool wear were examined by performing the dry turning machining test under the influence of oxygen (O) and argon (Ar) environment. They observed that the cutting ADI in argon reduces the amount of adhesion on the flank and rake face (Fig. 2.17). However, they found that the wear rate of both inserts is more rapid in argon than in air (Fig. 2.18). They found similar results in case of oxygen as that of argon. They stated that the major flank wear of the alumina ceramics was more rapid in the argon or oxygen than in air because of the shorter tool-chip contact length. The shorter tool-chip contact implies that the high cutting temperature and the high stress are simultaneously concentrated near the cutting edge responsible for the increase in tool wear. They also found that zirconia added to alumina ceramic insert was transformed from the m-phase and/or t-phase to the t-phase only by elevated temperatures at higher cutting speeds. This transformation led to an increase in hardness, responsible for the increased wear resistance and tool life at higher cutting speeds. Cristino et al. [71] stated that the contact length (Lc) in steady-state cutting conditions is due to an energy compromise between the plastic work, a quantity inversely proportional to radius of curvature of the chip, and amount of frictional work, which is directly proportional to the contact length and, therefore, to radius of curvature of the chip. According to them, the cutting in the presence of inert gases such as Ar, decreases the friction coefficient, whereas cutting in the presence of active gases such as air increases the friction coefficient, it follows that frictional work will also increase with the formation of oxide films on the new freshly cut surfaces of material lead to the increase in the contact length.

Goldberg et al. [72] studied the dry interrupted facing of an ASTM Grade 3 ADI with Al_2O_3-

TiC and Al$_2$O$_3$-SiCw ceramic cutting tools under conditions close to light roughing (depth of cut: 2 mm; feed: 0.1-0.4 mm/rev; cutting speed: 425 m/min) and finishing (depth of cut: 0.5 mm, feed: 0.1-0.4 mm/rev; cutting speed: 700 m/min). Their results indicated that Al$_2$O$_3$-SiCw ceramic insert performed better than Al$_2$O$_3$-TiC ceramic insert for rough interrupted facing as well as finish interrupted facing at high cutting speeds. The lack of overwhelming performance for Al$_2$O$_3$-TiC ceramic inserts in this situation was linked to their poor thermal shock resistance. They reported that cutting tool wear was exclusively flank wear, which was a direct consequence of adhesion - abrasion wear mechanisms.

It can be concluded that ceramic tools show flank wear characteristics while machining ADI as a direct consequence of adhesion and abrasion wear mechanism. However, ceramics tools are suitable for machining the majority of ferrous materials, including super-alloys. Some of the disadvantage of ceramic materials is its cost and brittleness.

2.6.3 Machining ADI with PCBN tools

Polycrystalline cubic boron nitride (PCBN), is a polymorph boron-nitride-based material. Its high mechanical properties are due to its crystalline structure and its covalent link [67]. In addition, it exhibits good toughness and thermal shock resistance. In particular, PCBN tools provide the required thermal stability, hardness, and strength needed at elevated temperatures during machining. Modern PCBN grades are ceramic composites with a CBN content of 40-65%. The ceramic binder adds wear resistance to the CBN, which is otherwise prone to chemical wear. The PCBN grades are largely used for finish turning of hardened materials [66, 67].

Katuku et al. [73] investigated the wear mechanisms of PCBN cutting tools when dry turning ASTM grade 2 ADI under finishing conditions. They performed the machining test at cutting speeds ranging from 50 to 800 m/min. The depth of cut and the feed being constant at 0.2 mm and 0.05 mm/rev respectively. They observed a monotone decrease in the tool life with the cutting speed. They concluded that adhesion and abrasion were the main wear mechanism at cutting speeds lower than 150 m/min. They stated that the shearing of built-up edge (BUE) pressure welds after extensive strain hardening produced attrition that activated abrasion wear mechanisms. On the other hand, at cutting speeds greater than 150 m/min, wear occurred by a combination of chemical reaction, diffusion and abrasion. Subsurface cracking in the crater may have contributed to the wear. Additionally, at cutting speeds higher than 150 m/min, the high concentrations of Mg, Si, and O on the wear surfaces and the heat-affected zone of the tools indicated that wear through chemical reaction was the controlling wear mechanism (Fig. 2.19).

(a)

(b)
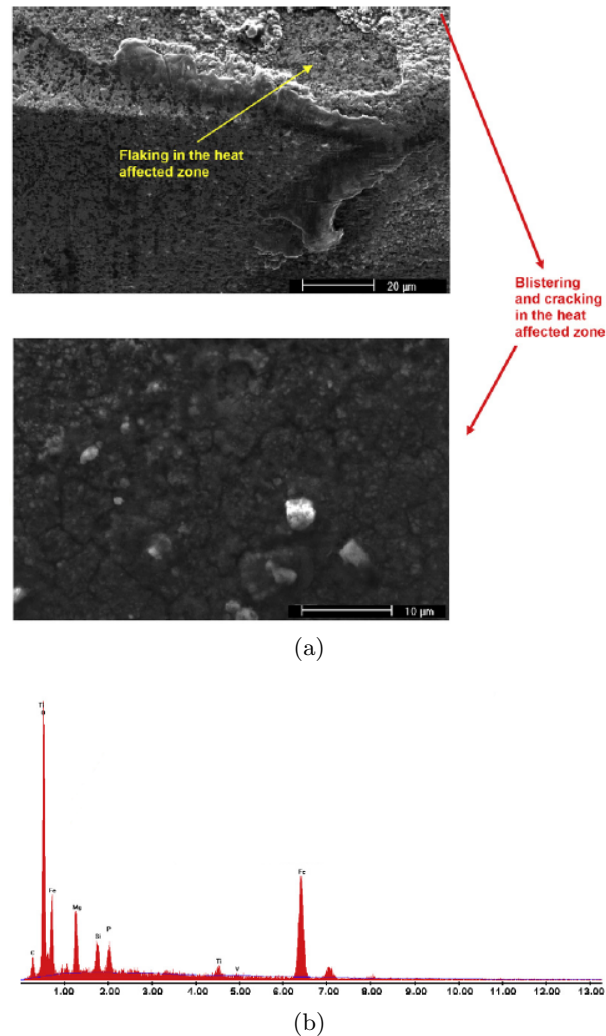
Figure 2.19: (a) Appearance of the heat-affected zone showing blistering, flaking and cracking (SEM micrographs) and (b) EDS spectrum of an area of the heat-affected zone [73].

Aslantas et al. [74] investigated the performance of CBN cutting tools when dry turning ADI material. The effects of the austempering process on the cutting forces and surface roughness were studied. They performed the machining test over three different work materials, namely, one as-cast and two austempered. Austenitizing of the latter work materials was carried out at 900 ℃ for 60 min and then quenched in salt bath at 250 ℃ and 325 ℃ for 60 min, respectively. They performed the machining test at four different cutting speeds V = 100 m/min, 200 m/min, 300 m/min and 400 m/min. The depth of cut and the feed being constant at 1 mm and 0.05 mm/rev respectively. According to them, a lower cutting speed would have been preferred in terms of cutting tool life. They concluded that for as cast material the lower cutting speed (<300 m/min) are not suitable while machining using CBN cutting inserts in terms of the obtained surface finish due to higher ferrite contents. In addition, they stated that at higher

cutting speed austenite undergoes a transformation to martensite due to a high strain rate and results in the formation of discontinuous chip during machining. According to them the friction coefficient at the tool-chip interface significantly increases with decreasing austempering temperature (250 ℃). As a result, the increasing friction coefficient causes significant wear on the tool rake face.

Due to the higher thermal stability and toughness of PCBN tools, the ADI machining process is improved by the better dissipation of heat from the cutting zone. The PCBN tools are more suitable for light cut and high speed machining of ADI.

In terms of the cutting tools, the main objective during machining is to get an optimized tool in all related aspects (cutting parameters, workpiece material properties, tool wear mechanisms, surface integrity etc.) for a particular machining operation. However, the economic and environmental impact of cutting and machining is kept increasing. These impacts can be minimized by the implementation of near to net shape technologies and dry or near dry machining process during the production line for a particular ADI component.

2.7 Ecological machining: Dry or near dry machining

In the metal cutting industry, cooling lubricants (CL) are used to achieve a prescribed result in terms of tool life, surface finish and accuracy-to-size, and make chip-breaking and chip-transport easier. However, the use of cutting fluids during machining creates problems in the immediate working environment and in waste disposal. These problems result in a large number of ecological problems and in a climate of increasingly strict work safety and environmental legislation [75]. Considering the threat to the environment and high cost associated with the use of cutting fluids, the removal of cutting fluids can be a significant economic incentive. To minimize the use of coolant and lubricant, new concepts of minimum quantity lubrication (MQL) application and coating technology have been developed in order to sustain high material removal rates. The coatings on the cutting tools are being used to improve the tribological characteristics of the cutting tool at the cutting zone. In the following sections, the dry and near dry machining processes are presented and discussed in relation with the different tool-coatings [65].

2.7.1 Near dry machining: MQL application

In this cutting fluid application, the tools are supplied with the smallest amounts of a coolant and/or lubricant. Usually, oils are used, but also emulsions, water or air. They are supplied to

the tool and/or cutting area in the smallest possible quantities. This is achieved either with or without a transport medium [45, 65]. Depending on the type and primary task of the added medium, we can draw a distinction between the lubrication function and cooling function of the medium. For example, when oils are used, then it is their good lubricating effect that is the primary function. Their task is to reduce friction and adhesion processes between the workpiece, chip and tool. By reducing friction, there is less frictional heat. The result is less heating of the tool and component in comparison to dry machining process (Fig. 2.20). Due to the low thermal capacity (C_p) of oil (C_p(oil): 1.92 kJ/kgK) and air (C_p(air): 1.04 kJ/kgK) and the small quantity applied, the direct cooling effect of the oil/air mixture is of only secondary importance [45]. Therefore, minimal quantity lubrication is a suitable alternative for economically and environmentally compatible production. It combines the functionality of cooling lubrication with an extremely low consumption of lubricant and therefore, it has the potential to close the gap between overflow lubrication and dry machining.
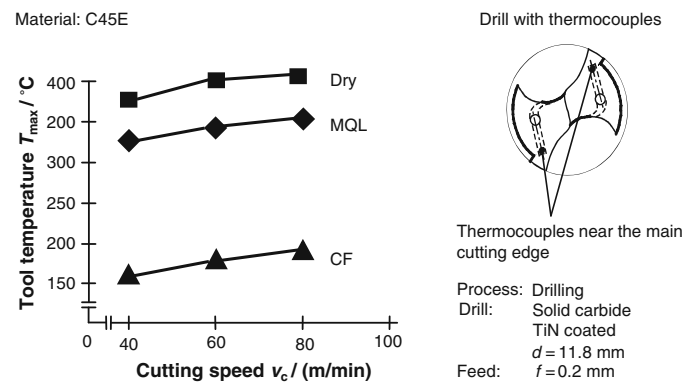
Figure 2.20: Influence of minimum quantity lubrication on the tool temperature [45].

Meena and Mansori [76] investigated the MQL drilling of ADI material similar to ASTM grade 2 ADI using the PVD-TiAlN coated tungsten carbide tools. They performed the machining experiments at a cutting speed of 60 m/min using a feed rate of 0.15 mm/rev. They also compared the MQL drilling performance with dry and wet drilling under the same experimental conditions. They concluded that crater wear at the outer cutting edge is the dominant wear mode in case of dry and MQL drilling.

No doubt that the near dry machining approach can be a partial solution for the ecological machining of the ADI material. However, proper steps must be taken to implement the near dry machining approach to make this technology reliable, environmentally friendly and cost efficient. Additionally, the cutting tool should be design in terms of the tool material, tool geometry and tool's coating as per the requirement of the near dry machining process.

2.7.2   Dry machining

The dry machining process can be another approach for the ecological machining of ADI by elimination of cutting fluids during machining. However, the basic functions of cutting fluid, cooling and lubrication are eliminated during dry machining. This elimination leads to the increase severity of the contact processes at the tool-chip and tool-workpiece interfaces and significantly affects the tribological conditions at these interfaces [65]. To adapt machining under such conditions, the heat removal from the cutting zone and better chip transportation conditions must be confirmed. Coating technology appears to be a good alternative under such conditions, which improves the tribological properties of the cutting tool. Therefore, the tool coatings can at least partially substitute the eliminated functions of the cutting fluids.

Tonshoff and Mohlfeld [77] investigated the wear mechanisms of different coated WC-cemented carbide and cermets tools during dry drilling of tempered steel. They stated that complex thermal and mechanical loads were developed at the cutting edge during the dry drilling machining process. Therefore, the cutting tool material requires high hot hardness and high toughness. They explained that the coating separate tools from the workpiece material in cutting and offers a possibility to replace coolants. The coating characteristics for dry machining should include reduced frictional heat at the tool-chip and tool-workpiece interfaces and enhanced tool life, and thus, improves the tribological characteristics of the cutting tool. The dry drilling process requires higher thermal stability and a certain toughness of the coating layer to prevent chipping. They stated that the (Ti,Al)N coating showed the lowest coefficient of thermal conduction and considerably increased oxidation stability compared with other hard coatings, particularly with TiN coating. The high hardness of (Ti,Al)N improves wear resistance and the low friction of (Ti,Al)N against steel reduces cutting forces as well as the heat generated in the process. Figure 2.21 shows the oxidation curves of $(Ti_{1-x}Al_x)$ coatings compared with a TiN coating. The oxidation of TiN coating starts at 550 ℃ in air while $(Ti_{1-x}Al_x)$ coatings with a cubic structure begin to oxidize at 750 ℃ for x = 0.25 and at 830 ℃ for x = 0.6. The weight gain in these coatings increases significantly at temperatures above 900 ℃. It was found that $(Ti_{1-x}Al_x)$ coatings upon oxidation formed two-phase mixtures of TiO_2 and Al_2O_3 at 1000 ℃ in air. The formation of a dense Al_2O_3 top layer increases diffusion and oxidation resistance of the (Ti,Al)N film. As compared to TiN, (Ti,Al)N has a high hardness even at elevated temperatures. For dry drilling operations, the ternary (Ti,Al)N system has remarkable advantages; as compared to uncoated and carbide and TiN coated tools, it has a superior wear behavior.

The main objective of the application of any coating during dry machining of hard to
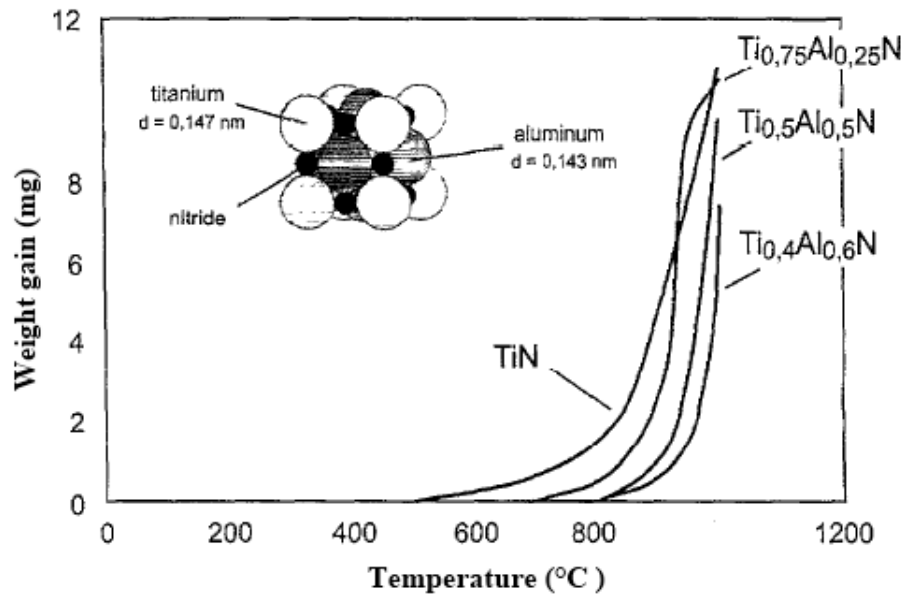
Figure 2.21: Oxidation curves for $(Ti_{1-x}Al_x)$ coatings as a function of temperature [77].

machine materials such as ADI, is to improve the tribological characteristics at the tool-chip and tool-workpiece interfaces. However, the major resource in improving tribological conditions in metal cutting (reduced tool wear and improved quality of machined surface), is in the inherent properties and structure of the work material. The machining characteristics of the work material can be improved by understanding the properties of the following surfaces [62]:

- Properties of the chip contact surface which is the counterpart of the tool rake face over the tool-chip contact length;

- Properties of the work material at the tool-workpiece interface (the flank surface), which define the contact conditions and tool wear over this interface.

Therefore, understanding the inherent properties of the ADI material and its subsequent influences on the above mentioned contact surfaces leads to the better understanding of the tool wear. This led to the application of suitable coating for ADI machining process capable of reducing the severity of this type of wear for the particular case.

2.8   Conclusions

The recent advance in casting and heat treating practices leads to the production of ADI materials, which offers a better combination of mechanical properties and enhanced wear resistance.

It comes out as an opportunity to respond to the increasing industrial demand for the cost and weight efficient materials. Due to its remarkable combinations of mechanical properties and high wear resistance, ADI act as a light weight (crankshaft, connecting rod, and gears, etc.) substitute for forged steel and cast iron components in automotive industries. However, as compared to standard grades of ductile cast irons, ADI is expensive and required high-quality ductile iron casting with consistent composition and microstructural characteristics. The composition for ADI production must be selected based on austempering response and not simply hardenability requirements. Moreover, the austempering heat treatment requirements are costly and more stringent as compared to other common heat treatments such as annealing, normalizing, quenching or tempering. All these factors acts as a technological barrier for the industrial exploitation of light weight ADI casting. The increasingly high-performance materials demanded by the high-tech industries requires development of new ADI processing technology and machining advance.

To advance in the innovative processing technology for ADI production, a more detailed understanding of the manufacturing process (casting, heat treatment, and machining) itself and of the behaviour of the ADI material during both processing and in-service performance is required. The innovative processing technology should be based on the knowledge of the appropriate relationship between the microstructure and its material properties. However, the applications and subsequent processing of ADI materials in many industrial sectors depend on the machining characteristics of the ADI microstructure. Therefore, there is a need to control and tailor the ADI microstructure to give the desired material properties and improve machining characteristics.

The manufacturability of ADI is controlled by the three important steps: Casting, heat treatment and machining practices. These three steps during the manufacturing cycle of ADI component are inter-related with each other. To implement a green manufacturing technology for ADI production, there is a need to consider simultaneously each production step and their influences. In addition, special attention must be paid to reduce to energy consumption and to improve the material efficiency of the final product. The production of near net shape, defect free sound light ductile iron casting is the first essential step. After that uniform heat treatment using the optimized heat treatment parameters must be required to get the optimize mechanical properties in ADI casting. Moreover, machining characteristics of the obtained ADI material must be improved using the proper tool material, cutting parameters and cutting environment. The dry and near dry machining should be promoted to make the machining process economic and environmentally safe. Therefore, the main objective of the present study is to implement

a sustainable innovative process design for ADI production and to integrate it with the dry or near-dry machining process for the green manufacturing of the light-weight ADI castings.

Chapter 3

Experimental techniques

The aim of this chapter is to introduce the applied experimental techniques and equipments used throughout this project for the correlation of the integrated casting-heat treatment route and machining for the sustainable ADI production. The present chapter is divided into the following sections:

- Casting and heat treatment practices: This section covers the experimental methods and equipments used to develop an integrated approach towards casting and heat treatment processes for ADI production. It includes a brief summary of spheroidization and inoculation process, thermal analysis tool, and heat treatment practice used in the present study.

- Material characterization: This section includes the details of the applied techniques and equipments used for the characterization of the produced ADI material.

- Machining experiments: This section includes the details of the machining practices carried out throughout the project and provided information regarding the cutting parameters, cutting tools, and cutting environments.

- Machinability characterization: This section includes the methodology performed after the machining test for the characterization of ADI machinability.

3.1 Casting and heat treatment practices

3.1.1 ADI processing cycle: Integrated casting-heat treatment route

The melting of charge materials was conducted in an induction furnace with a holding capacity of 100 kg, power of 120 kW and a frequency of 50 Hz. The charge materials were steel
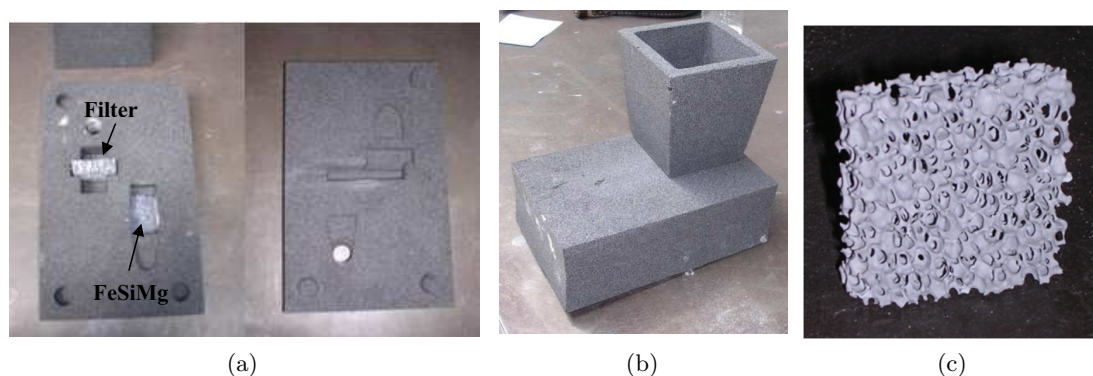
Figure 3.1: (a) Schematic representation of tundish ladle assembly, (b) Tundish ladle apparatus for spheroidization, and (c) Filter used in the tundish ladle assembly.

scraps, iron, carbon additive, and ferro-silicon. The metallic charge composition is based on the estimated losses and compositional requirements of ADI casting. Based on the chemical composition of the iron and steel scraps, a computational tool (Appendix A) was developed to calculate the amount of the charge materials to get the required chemical composition. The melt was initially superheated up to 1500℃ and alloying elements are added to the charge materials. Table 3.1 gives the recommended chemical composition ranges of the alloying elements for the ADI production.

Element	Recommended range (%)
Carbon (C)	3.60 ± 0.20
Silicon (Si)	2.50 ± 0.20
Magnesium (Mg)	(Sulphur(S)$\times$0.76)+0.025 $\pm$0.005
Manganese (Mn)	0.35 ± 0.05
Copper (Cu)	0.8 maximum, only as needed $\pm$ 0.05
Nickel (Ni)	2.0 maximum, only as needed $\pm$ 0.10
Molybdenum (Mo)	0.30 maximum, only as needed $\pm$ 0.03

Table 3.1: Control ranges for intentionally added elements (ASTM A897M-03) [51].

(i) Magnesium treatment (Spheroidization)

The magnesium treatment is a means of modifying the solidification structure so that the graphite phase precipitates and grows as spherical particles instead of flakes [21]. In the present study, the magnesium (magnesium ferro-silicon alloy) was added to the melt using a tundish cover treatment ladle (Fig.3.1a) to give a residual magnesium content of 0.030-0.040 % [24]. The typical alloy composition of the magnesium ferro-silicon alloy is provided in Table 3.2. The used tundish cover treatment ladle is a specially designed Mg treatment apparatus to

(a) (b)
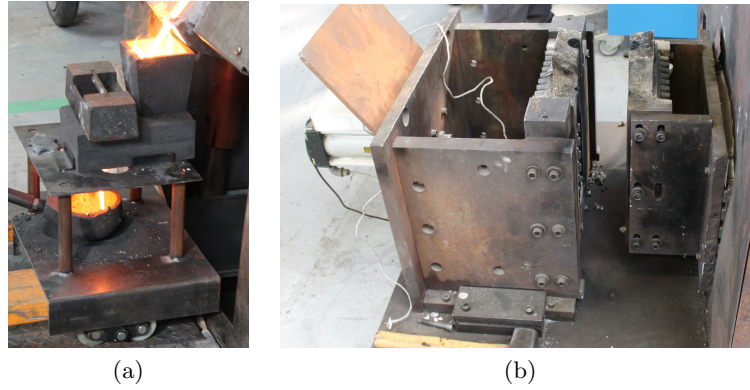
Figure 3.2: (a) Spheroidization process for the melt, and (b) Metallic mould.

improve Mg recovery. The spheroidization process (Fig 3.2a) was performed in the temperature range of 1450-1470 ℃. The temperature of the melt was measured by using platinum-platinum rhodium thermocouples. The filter (Fig.3.1c) was used during the Mg treatment to remove the non metallic inclusions from the melt, which are detrimental to the surface finish, mechanical properties, machining characteristics of the produced as cast material [78]. The details on the spheroidization techniques and the apparatus preparation is provided in Appendix A.

Element	Percentage (%)
Silicon (Si)	44.85
Magnesium (Mg)	6.13
Calcium (Ca)	2.94
Rare earth elements (RE)	0.90
Aluminium (Al)	0.94

Table 3.2: Chemical composition for ferrosilicon magnesium nodulant.

(ii) Inoculation process

The inoculation process was performed using the ferro-silicon based alloy just after magnesium treatment. The typical inoculant used in the present study has 0.7 wt% FeSi (75% Si). The primary objective of the inoculation process is to reduce under-cooling during solidification and helps to prevent carbides in the thin sections of the casting. It also increases the nucleating sites for the graphite nodules, thus improving homogeneity in the matrix structure [21].

(iii) Moulding process

After spheroidization and inoculation process the melt was poured into the permanent mould, and the casting process started. In the present study, the gravity die casting (permanent
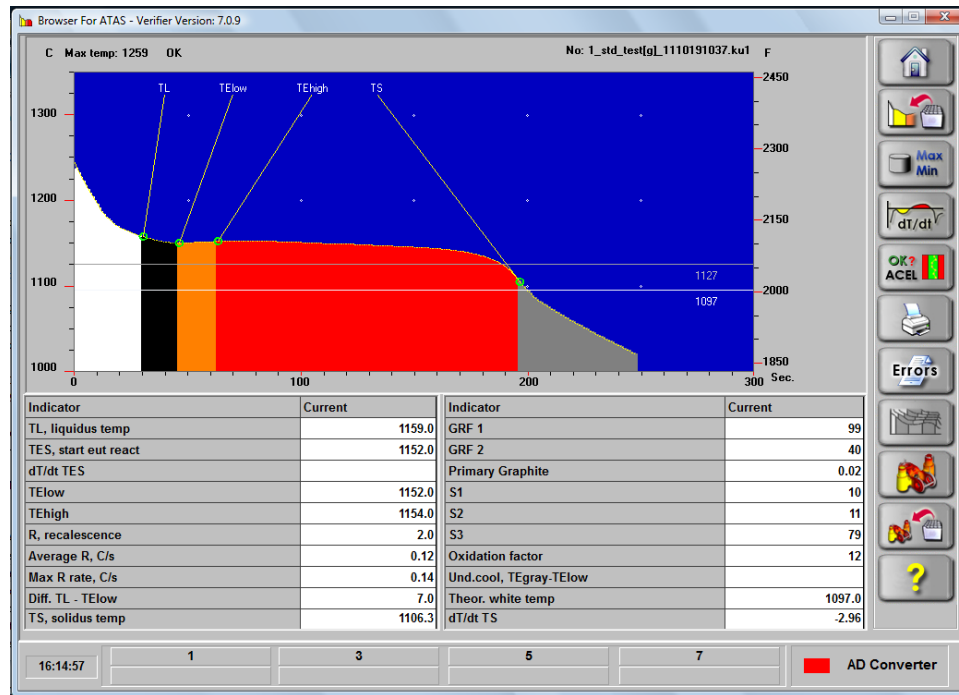
Figure 3.3: Typical solidification curve and thermal parameters obtained by using ATAS tool for ductile iron.

mould casting) process was used. The mould was preheated in temperature range of 175-225 ℃ to ease the melt flow during filling process and to prevent damage to the mould as a result of thermal expansion during pouring. The mould cavity is coated with a refractory material which prevents the casting from sticking to the mould and prolongs the mould life. The permanent mould (Fig. 3.2b) used in the present study is made up of gray cast iron because of its high thermal fatigue resistance [78]. It consists of two halves having dimensions of each 430 mm×280 mm×85 mm (Fig. 5.1a). The permanent mould was used to meet the challenges presented by the modern manufacturing industry: higher production rate of near net shape ADI castings and the in-situ heat treatment for austempering [22]. The near net shape casting processes leads to the reduction in the machining and finishing costs [15]. The mould cavity consists of two specimens and riser as shown in Fig. 5.1b. Each specimen is in the shape of rectangular block with size of 182 mm×29 mm×16 mm. The production process was performed by maintaining a regular time interval for each production cycle (one cycle produce two specimens) including casting and ejection processes. The temperature of the mould and ejected casting was measured by using K-type thermocouples fitted to the mould at selected locations. The mould temperature is controlled by using forced-air cooling method.

3.1.2 Thermal analysis

The thermal analysis of the melt was carried out by using a commercial thermal analysis tool known as adaptive thermal analysis system (ATAS). It is a system for measuring and controlling liquid iron metallurgy by monitoring the temperature-time curve of the melt. The temperature time curve of the melt is influenced by the metallurgical conditions of the melt [79]. During melt cooling, the latent heat released by the solidification of different phases causes changes in the cooling curve and its derivative. These changes are linked with the development and characteristics of the microstructure observed in the cast product. The correlation among the changes observed in the cooling curve and its derivative and the microstructure present in the cast by statistically based models has allowed the foundryman to monitor and control the melt quality before pouring [80]. In addition, it provides, information on nucleation, growth, graphite expansion, graphite shape and thermal conductivity [81]. Typical temperature time curve and thermal parameters obtained by using ATAS are shown in Fig. 3.3. The ATAS parameters range and their functions for the optimization of ductile iron casting are summarized in Table 3.3.

Parameter	Optimal values and functions
TElow (T_{El})	Low eutectic temperature. A high value is normally better, >1145 ℃. It reflects the nucleation status of the melt.
R	Recalescence=TEhigh-TElow. A low value is often the best, <5. R indicates how fast the eutectic growth is initially.
GRF1 (G_1)	Graphite Factor 1. G_1 indicates the amount of eutectic graphite during the second phase of freezing. For ductile iron G_1 >90 is preferred. High value means a high nodule count.
GRF2 (G_2)	Graphite Factor 2. G_2 indicates indirectly the heat conductivity and amount of eutectic at the very end of freezing. For ductile iron $30<G_2<50$ is preferred.
TS (T_S)	Solidus temperature: It is lowered with addition of Mg. Too low values are not good as they indicate too much Mg or high levels of tramp elements. For ductile iron TS should be 1080 ℃$<T_S<$1105 ℃.

Table 3.3: The ATAS parameters range and their functions for evaluating ductile iron casting [79].

3.1.3 Heat treatment

The heat treatment was performed just after the casting process to develop the innovative integrated approach towards casting and heat treatment. In this process, the ductile iron samples ejected from the permanent metallic mould are first austenized immediately after solidification process followed by austempering heat treatment in fluidized bed and then air cooled at room

temperature to produce the ADI materials. The austenitization treatment was carried out in a muffle furnace at 930 ℃ for 90 min. A muffle furnace from Nabertherm model no. N161 was used for the austenitization of the produced samples. After austenitization, the specimens were quenched down to the austempering temperature in the first fluidized bed furnace (at room temperature). The specimens were then austempered in another fluidized bed for different austempering conditions (temperature and time). An average quenching rate of 7℃/s (Fig. 3.5) was obtained by using the fluidized bed at room temperature. The quenching experiment was performed in the riser of the produced sample (diameter: 32 mm) using the K-type thermocouple. The quenching experiment was performed under the same experimental conditions as that used for the ADI production. The conventional CCT curve for ductile iron showing different cooling rates to obtain the combination of the different metallic matrix is shown in Fig. 3.4. According to this figure, the minimum cooling rate required to avoid the pearlite region in the temperature range of 700-500 ℃ is 3 ℃/s. However, the characteristics of the CCT curve can be changed by the alloying elements.

Figure 3.5 showing the schematic presentation of the integrated casting-heat treatment process for ADI production. It presents the controlled correlative approach towards casting and heat treatment process by implementing thermal analysis system (melt quality) and fluidized bed heat treatment (controlled cooling heat treatment) to improve ADI foundry process.

3.2   Material characterization

3.2.1   Metallographic analysis

The microstructural characterization of the samples was carried out at three different sections (bottom, middle and top) of the samples as shown in Fig. 3.6a. The obtained samples were sectioned using wet abrasive cutting method at different sections and mounted in resin (Fig. 3.6b) for wet grinding and polishing to prepare the samples for metallographic analysis. Grit reductions of 180, 400, 600, 800, and 1200 silicon carbide are used. A final surface polish of 3 μm and 1 μm grain size was also performed. The polished surfaces are then etched with 4% Nital (96-98 mL ethanol and 2-4 mL nitric acid (HNO_3)) for 2-5 seconds at room temperature. Microstructures were observed by optical microscope (OM) and scanning electron microscope (SEM). The graphite nodule counts at different zones (centre and outer zones) were determined on the un-etched sample surface by taking the average of five different regions (100X) at each section (bottom, middle and top) of the samples using an optical microscope.
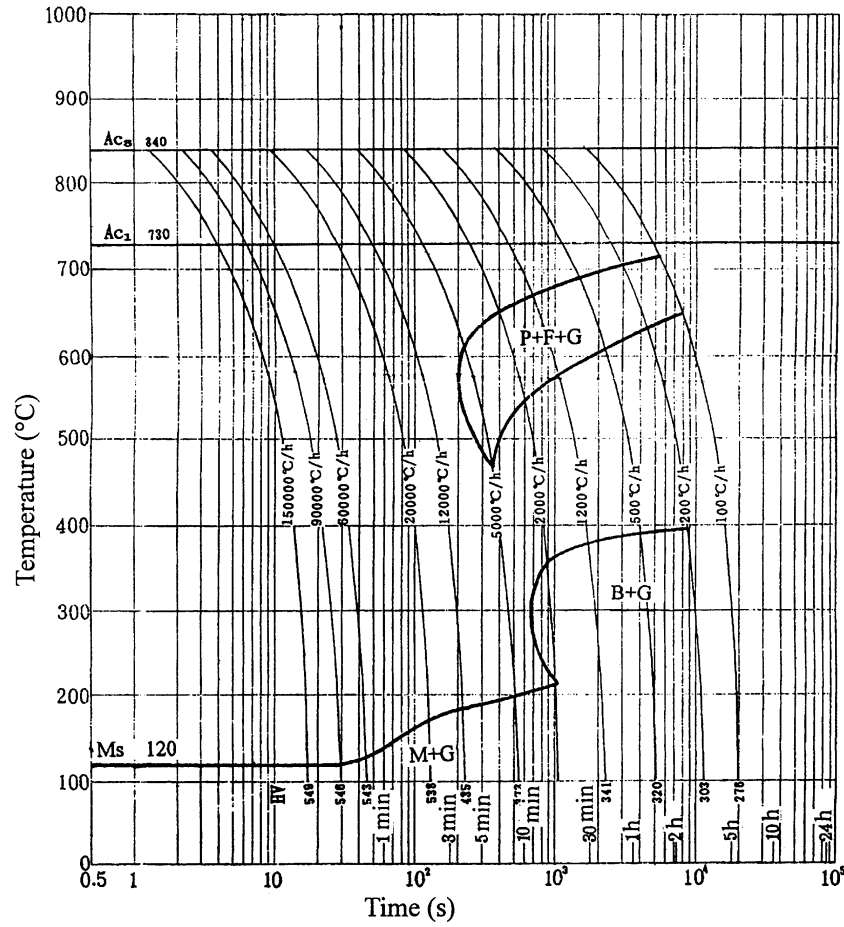
Figure 3.4: The CCT curve for ductile iron with cooling rates [82].

3.2.2 Mechanical properties and strain hardening analysis

Tensile test was conducted according to ISO 6892-1:2009 standard [83]. The tests were carried out at a cross head speed of 10 mm/min on an MTS (material testing system) servo-hydraulic machine (MTS810) at room temperature in an ambient atmosphere. Load and displacement plots were obtained on an X-Y recorder and from these load-displacement diagrams 0.2% yield strength, ultimate tensile strength and percentage elongation values were calculated. Samples for the tensile tests were taken from the centre zone (Fig. 3.7) of the material. Hardness test was performed using a Buehler MacroVickers 5112 tester with an applied load of 196.13 N (20 kgf). The hardness value is the average of five different values taken in the various zones for each sample. The values of mechanical properties presented are the averages of testing at least four samples.

The strain hardening behavior of the produced ADI samples were determined using the
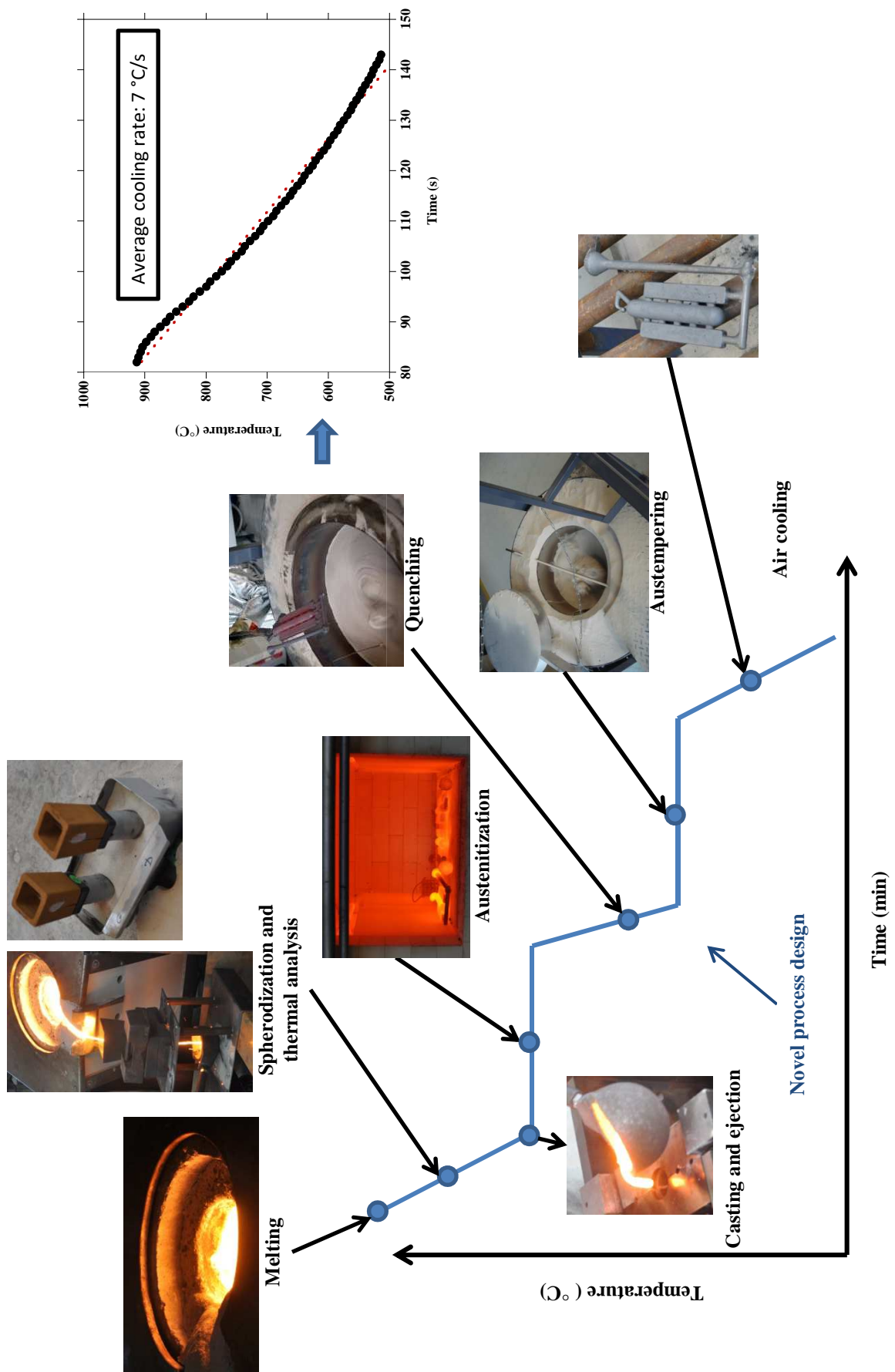
Figure 3.5: Schematic representation of novel process route for ADI production.

(a)   (b)
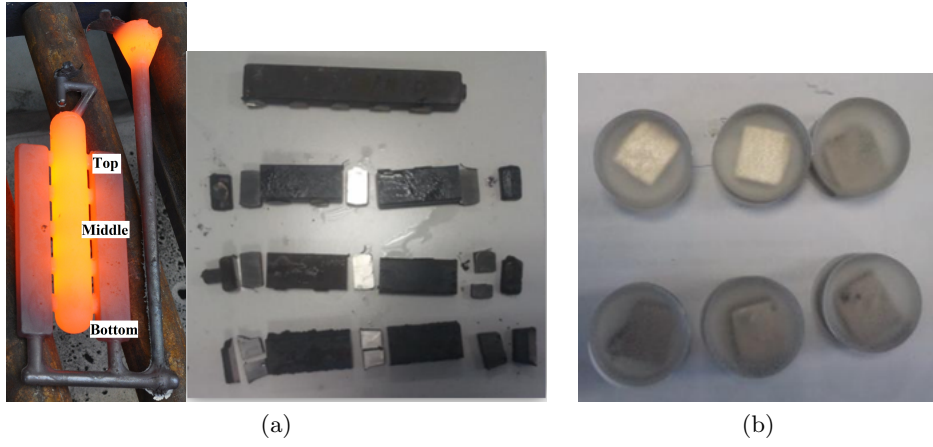
Figure 3.6: (a) Different sections (bottom, middle and top) for the microstructural characterization of the obtained ADI samples, and (b) Samples in resin.
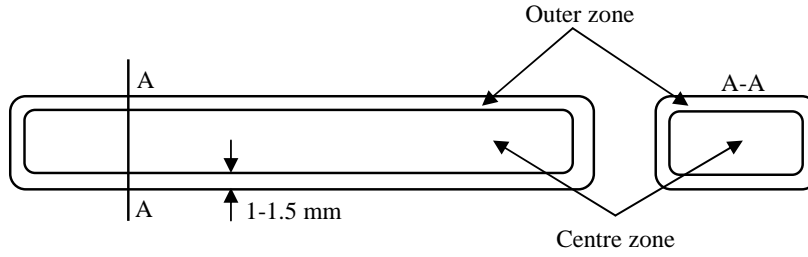
Figure 3.7: Samples for the tensile test (centre zone).

stress-strain data obtained in a uniaxial tension test. The strength hardening exponent (n) and strength coefficient (K) were determined using the Hollomon Equation 3.1 [9, 84, 85] presented as follows:

$$\sigma = K\epsilon^n \tag{3.1}$$

where: σ = true stress; ϵ = true plastic strain; K = strength coefficient and n = strain hardening exponent

$$log\sigma = logK + nlog\epsilon \tag{3.2}$$

The logarithms (Equation 3.2) of the Hollomon's equation ((Equation 3.1)) are calculated within the plastic range. From these paired sets of (log σ, log ϵ), calculate, via linear regression analysis of log σ versus log ϵ, the slope, n, the y-intercept (K) and the standard error of the

slope are calculated. The Equation 3.3 for the slope of the linear regression line provides the strain-hardening exponent as follows:

$$n = \frac{N \sum xy - \sum x \sum y}{N \sum x^2 - (\sum x)^2} \tag{3.3}$$

The equations for the strength coefficient are as follows:

$$K = \exp(b) \tag{3.4}$$

$$b = \frac{\sum y - n \sum x}{N} \tag{3.5}$$

The calculation of the standard deviation (SD) of the n-value is based upon the variance of the slope of the regression line. This measure of variability contains the computed n-value and the computed strength coefficient.

$$SD = (\frac{\sum(y - b - nx)^2}{N \sum x^2 - (\sum x)^2} \times \frac{N}{N - 2})^{1/2} \tag{3.6}$$

where $y = log\sigma$; $x = log\epsilon$; $b = logK$

N = Number of data pairs (N=150 for the present study);

SD = Standard deviation of the n value;

n = Strain hardening exponent

The typical relationship between $log\sigma$ and $log\epsilon$ is shown in Fig. 3.8 The values of n and b computed via linear regression analysis are 0.180 and 3.164 respectively. The values of K and SD are 1460 MPa and 0.0037 respectively.

3.2.3   X-ray diffraction (XRD) analysis

The X-ray diffraction analysis was used to determine the retained austenite volume fraction in the produced ADI by comparing the integrated cobalt (Co) X-ray diffraction intensity of ferrite (body centered cubic, BCC) and austenite (face centered cubic, FCC) phases with theoretical intensities. The X-ray diffraction studies were carried out on an INEL X-ray diffractometer equipped with CPS 120 wide-angle curved proportional counter. The analysis was performed using a monochromatic Co Kα radiation at 30 kV and 30 mA. The X-ray diffraction patterns were fitted using a WINDIF software. Integrated intensities of the (2 0 0) peaks of ferrite and the (2 0 0) peaks of austenite were used for the calculation of the amount of retained austenite
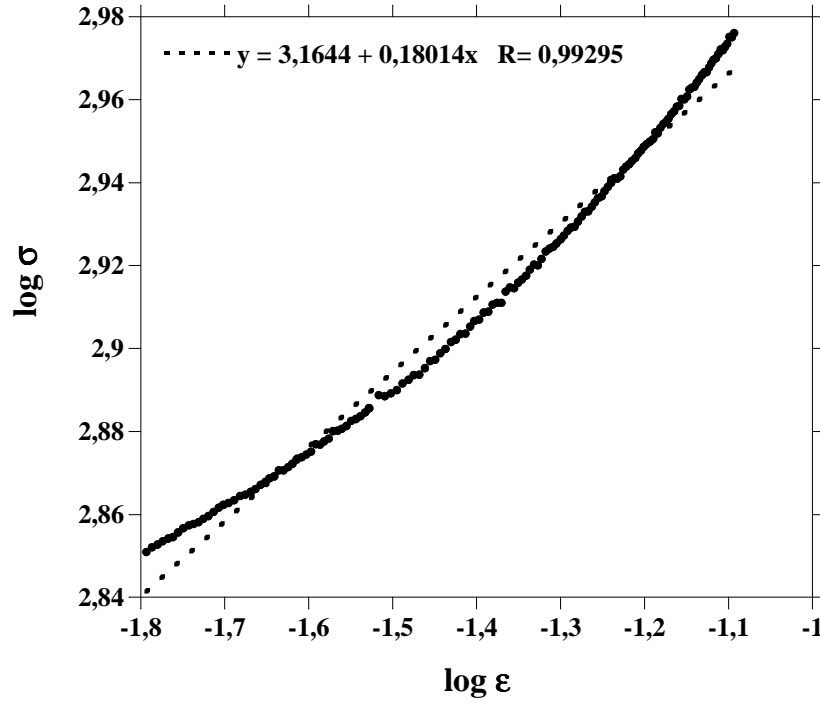
Figure 3.8: Log true stress vs log true strain (Austempering temp.: 380℃; Austempering time: 120 min).

(γ) and ferrite(α) in the microstructure by using Equation 3.7 [4, 86]. Schematic representation of X-ray spectrum as a function of wavelength is shown in Fig. 3.9.

$$\frac{I_\gamma(hkl)}{I_\alpha(hkl)} = \frac{R_\gamma(hkl)X_\gamma}{R_\alpha(hkl)X_\alpha} \tag{3.7}$$

Where, $I_\gamma(hkl)$ is the integrated intensity from a given plane (hkl) of austenite (γ) phase; $I_\alpha(hkl)$ is the integrated intensity from a given plane (hkl) of ferrite (α) phase and $R_\gamma(hkl)$ and $R_\alpha(hkl)$ are constants, where

$$R = (1/v^2)(|F|^2 pL)e^{-2m} \tag{3.8}$$

Where,

v is the atomic volume of unit cell;

F is the structure factor;

p is the multiplicity factor of the (hkl) reflection;

L is the Lorentz-polarization factor (LP) factor;

e^{-2m} is the Debye-Waller or temperature factor.
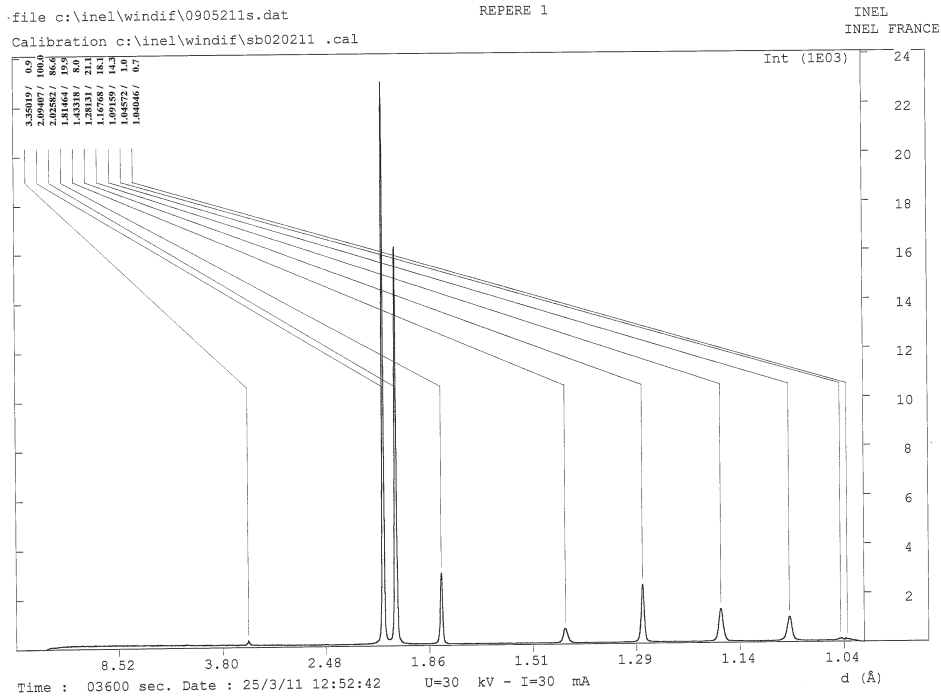
Figure 3.9: Schematic representation of X-ray spectrum as a function of wavelength.

The carbon content of austenite was determined by the following Equation 3.9 [4, 87]:

$$a_\gamma = 0.3548 + 0.0044C_\gamma \tag{3.9}$$

Where a_γ is the lattice parameter of austenite in nanometre and C_γ is the carbon content of austenite in wt%. The (1 1 1), (2 0 0) and (2 2 0) planes of austenite were used for the calculation of lattice parameter. The ferritic cell size (d) was calculated by using $B_{1/2}$ of FWHM (full width at half its maximum intensity) at (1 1 0) planes of ferrite. The following Scherrer Equation 3.10 [4, 86] was used for the calculation of ferritic cell size (d).

$$d = \frac{0.9\lambda}{B_{1/2}cos\theta_B} \tag{3.10}$$

Where λ is the wave length, $B_{1/2}$ is the FWHM (full width at half its maximum intensity) at (1 1 0) peak of ferrite and θ_B is the Bragg angle.
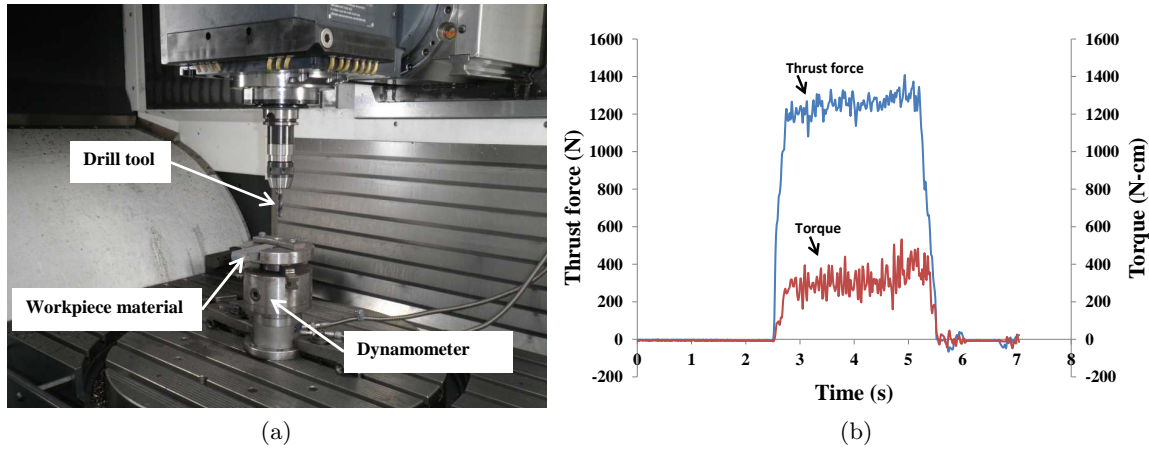
Figure 3.10: (a) The experimental setup for dry and wet drilling, and (b) Typical thrust force and torque during dry drilling of ADI (Cutting speed: 60 m/min; Feed rate: 0.15 mm/rev).

3.3 Machining experiments

3.3.1 Instrumented test and data collection

The produced ADI material in the form of a rectangular box of size 182 mm×29 mm×16 mm was used as the workpiece. The dry drilling tests were carried out on a Deckel Maho five axis machining centre (DMU 80 P). The machining experiments were carried out at three different cutting speeds (30, 60 and 90 m/min) and three different feed rates (0.05, 0.10 and 0.15 mm/rev) in an ambient atmosphere. A single drill tool was used for each set of experiments. The drilling depth for each hole is 16 mm. The cutting parameters, tool diameter and drilling depth were chosen based on the industrial drilling application. The machining tests were conducted using different PVD-coated carbide tools of diameter 8 mm. Thrust and torque components generated during drilling of each hole were measured simultaneously with a two-component dynamometer of type 9271A made by Kistler. The experimental set-up is shown in Fig. 3.10a.

The average torque (N-cm) and thrust force (N) generated during drilling for each individual hole was calculated within the time period corresponding to the drills first contact with the workpiece surface and its complete retraction at the end of the drill cycle, as shown in Fig. 3.10b(cutting speed 60 m/min and feed rate 0.15 mm/rev).

3.3.2 MQL and wet drilling

The MQL drilling experiments were carried out on the Mikron HSM 700 machining centre equipped with an external MQL system. The experimental set-up for the MQL drilling is

<table>
<tr><td>(a)</td><td>(b)</td></tr>
</table>
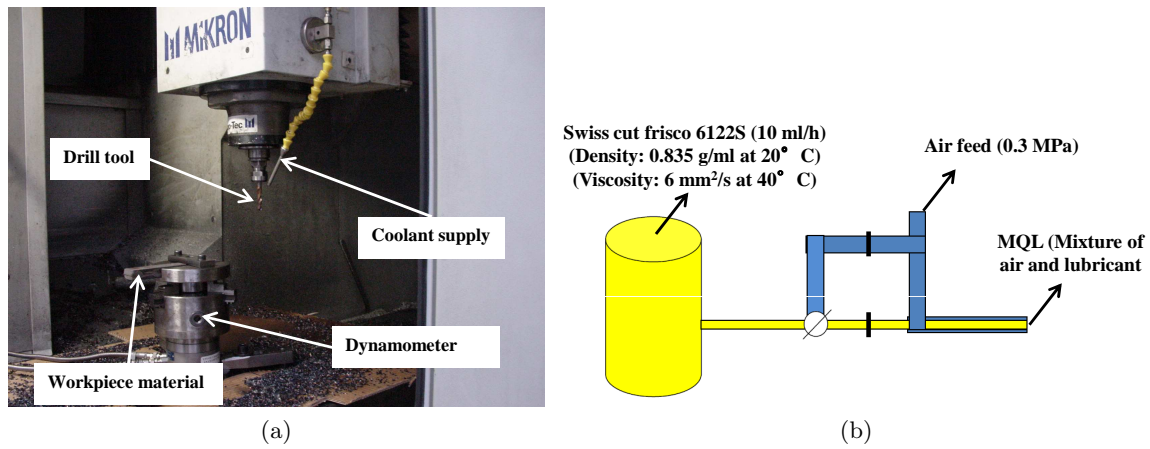
Figure 3.11: (a) The experimental setup for MQL drilling, and (b) Schematic diagram of the external MQL supply system.

shown in Fig. 3.11a. For MQL drilling, Swiss cut frisco 6122 S lubricant was used, having a density of 0.835 g/ml at 20℃ and a viscosity of 6 mm^2/s measured at 40℃. In MQL drilling, the MQL is applied to the drill tip at a flow rate of 10 ml/h for oil and air at a pressure of 0.3 MPa. For wet drilling condition, lubricant, eco-cool cat+ has been used with a viscosity of 35 mm^2/s at 40℃. The dry drilling tests were carried out on a Deckel Maho five axis machining centre of the model DMU 80 P.

(a) Tool 1   (b) Tool 2   (c) Tool 3
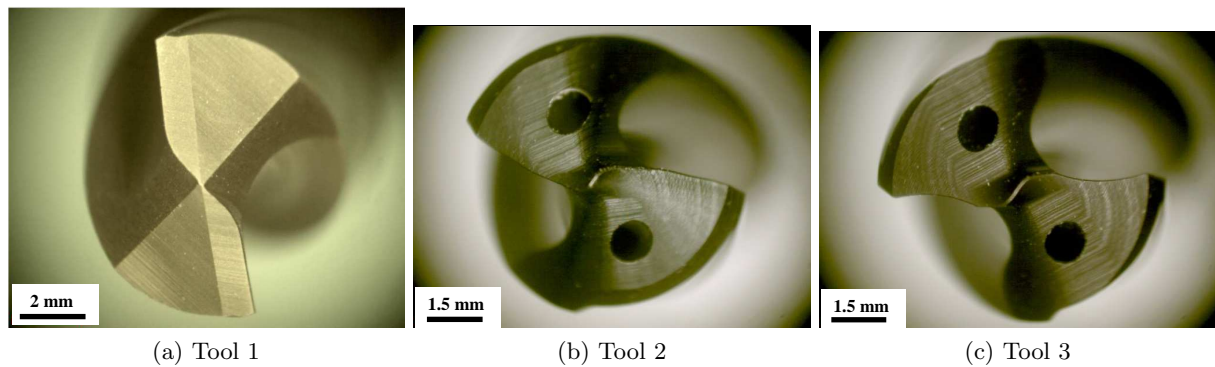
Figure 3.12: The tool geometries used in the present study.
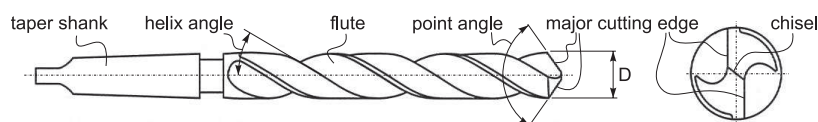
Figure 3.13: Standard geometry of the twist drill tool.

3.3.3 Cutting tools

In the present study, the machining tests were conducted using three different PVD-coated carbide tools of diameter 8 mm. The tool tips of the drill tools are shown in Fig. 3.12. The tool specifications and coating details are provided in Table 3.4. A schematic representation of the drill and the terms used in describing its geometry are shown in Fig. 3.13. The dry, MQL and wet drilling experiments were conducted using tool 1 whereas, the cutting performance of the PVD based coatings during the dry drilling machining process was conducted using tool 2 and tool 3.

Specifications	Tool 1	Tool 2	Tool 3
Reference	R840-0800-30-A0A 1220	B254A08000YPC	B254A08000HPC
Company	Sandvik Coromant	Kennametal	Kennametal
Coating type	PVD	PVD	PVD
Coating structure	Multilayer	Multilayer	Monolayer
Coating material	TiN/TiAlN	(Ti,Al,Cr)N	TiAlN
Point angle (°)	140	135	135
Helix angle (°)	30	30	30

Table 3.4: Tool specifications and coating details used in the present study.

3.4 Machinability characterization

3.4.1 Chip morphology

Chips generated from the different cutting conditions were collected to study the chip morphology and its characteristics. Free and back surfaces of the chips were examined using the scanning electron microscope (JEOL JSM-5510 LV model). The top surfaces of the chips were observed after mounting it in cold resin. The specimens were then ground, polished, and subsequently etched with 4% Nital (96-98 mL ethanol and 2-4 mL nitric acid (HNO_3)) for 2-5 seconds at room temperature for metallographic preparation. An image analyser software was also used to measure the geometrical parameters of the chip cross-section. The chip micro-hardness measurements were conducted using a 1600-5101 MicroMet analog micro indentation hardness tester. A load of 50 gf and a dwell time of 10 s were used in each measurement. The average micro-hardness value is corresponded to a series of four measurements for each value.

3.4.2   Tool wear analysis

(i) Optical and scanning electron microscopy

Tool wear was measured using Scanning Electron Microscope (SEM) and Optical Microscope (OM). The microscope consists of a telescope binocular Nikon SMZ-2T magnification 10 to 120 times. It is equipped with a Sony SSC-DC38P camera. This equipment is coupled to an image analysis software CLEMEX Vision. The SEM used was a JEOL JSM-5510 LV model. Its main features are:

- Magnification of 18 to 300,000;

- Maximum size of specimens: diameter = 32 mm;

- Modes of operation: HV (high vacuum) and LV (low vacuum);

- SEI detector (secondary electrons) and BEI (backscattered electrons);

- Accelerating voltage: 0.5 to 30 kV.

(ii) Energy dispersive spectroscopy (EDS)

The local chemical analysis of the drill flutes and the worn surfaces of the drill tool materials were performed by using the Energy Dispersive Spectroscopy (EDS) analysis. The EDS analysis was carried out with using the scanning electronic microscope (JEOL, model JSM 5510-LV) and energy dispersion spectrometry (EDS) (Oxford Instrument, INCA).

Y: Profile curve
X: Profile direction
Z: Average roughness height
L: Samling length
H: Profile herght
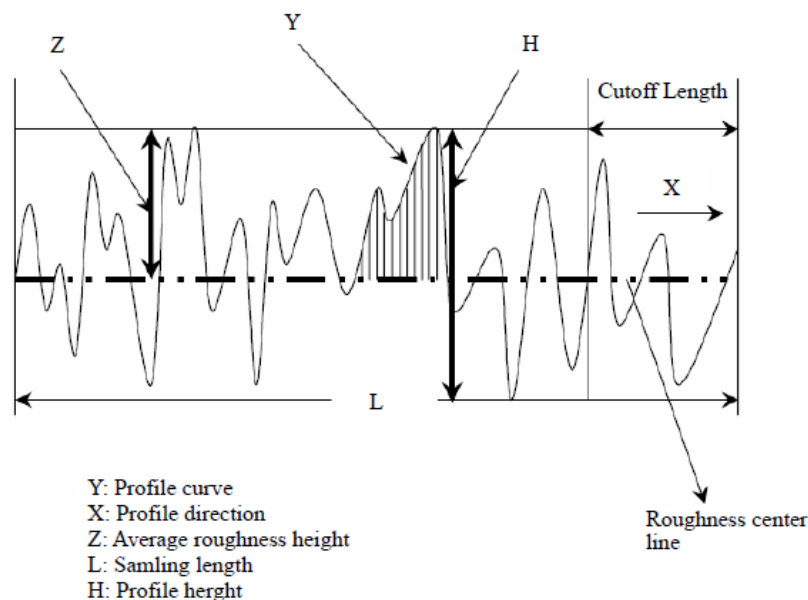
Figure 3.14: Surface roughness profile.

3.4.3   Surface roughness measurements

Surface roughness values were measured using a stylus based instrument (Hommel wave) having an accuracy of 0.5 μm with a cut off length of 0.8 mm. The average values correspond to a series of four measurements for each value. The surface parameter used to evaluate surface roughness, in this study, is the roughness average, Ra. This parameter is also known as the arithmetic mean roughness value, arithmetic average (AA) or centerline average (CLA). The average roughness (Ra) is the area between the roughness profile and its center line, or the integral of the absolute value of the roughness profile height over the evaluation length (Figure 3.14). Therefore, the Ra is specified by the following equation:

$$R_a = \frac{1}{L} \int_0^L |Y(x)| dx, \tag{3.11}$$

when evaluated from the digital data the integral is normally approximated by the trapezoidal rule:

$$R_a = \frac{1}{n} \sum_1^n |Y_i| \tag{3.12}$$

where R_a is the arithmetic average deviation from the mean line, L is sampling length and Y represent the ordinate of the profile curve.

3.5   Conclusions

The experimental approach developed throughout this chapter helps to implement the controlled innovative process design for ADI production. It led towards the correlative approach towards foundry practices (casting and heat treatment) for ADI production and its microstructural characteristics. This correlative approach should be investigated within the interest of interaction between the inherent process conditions and prevailed ADI microstructure. With this viewpoint, the microstructural and mechanical characteristic of produced ADI was investigated in the next chapter in correlation with the foundry practices.

Chapter 4

Innovative process route for ADI production

4.1 Introduction

Recently, the environmental impacts of material production and processing, particularly those related to energy, are rapidly increasing [88, 89]. These impacts can be reduced, to some extent, by implementing innovative processing technologies and/or by improving material efficiency [12]. By implementing innovative processing technologies for material production we mean to control and tailor the microstructure of materials to get the desired properties at low cost. On the other hand, material efficiency means providing improved material services with less energy consumption and material production [11]. Both of these factors are interrelated and can be put in a single term known as green manufacturing of the product. Thus, the growing demand of engineering materials in construction and automotive industries required either a new material with improved material properties and/or an optimum manufacturing route to yield the desired material and performance.

The recent emergence of near net shape ADI casting can be considered as a significant economic advantage in terms of the material efficiency options. The material efficiency options provided by light weight ADI castings are the upgraded combination of material properties and enhanced component life through increased wear resistance [4, 50]. However, due to limited resources and the growing environmental impacts of material production, the ADI production process needs an innovative processing technology. The present chapter thus attempts to explore the innovative process route for the production of near-net shape light weight ADI casting in a permanent mould. It is based on the integrated approach towards casting and heat treatment process within the framework of correlation between microstructure and mechanical properties of ADI. In the following sections, the recent technologies for ADI production will

63

be discussed. Then, the results related with the novel process route for ADI production are presented and discussed in terms of the microstructural characteristics, mechanical properties and strain hardening behavior of the resultant ADI materials.

4.2   Background

The first part of this section will elaborate upon the recent advance in the optimization of ADI microstructure by applying various processing technologies to acquire better combination of mechanical properties. These technologies include ausforming, cold rolling, controlled cooling, two-step austempering, and dual phase ADI production. The second section provides a brief summary of the innovative process route developed in the present study for ADI production.

4.2.1   Existing technologies

During the last few years, industrial applications of ADI have grown enormously. This fact can be accredited to the improvement achieved in casting technology as well as in the heat treatment technology. Many researchers [4, 7, 38, 90] in the past try to optimize the ausferrite microstructure by applying various processing technologies. Achary [38] investigated a new processing method for improving the strength and elongation percentage of ADI by grain refinement of parent austenite using thermo-mechanical treatment. They deformed the material at the austenitization temperature by single and multipass rolling before the austempering heat treatment. They choose three different austenitization temperature 900, 950 and 1000 ℃ with an austenitization time of 90 min. They performed austempering heat treatment at different austempering temperatures between 260 ℃ and 340 ℃ and austempering times between 30 and 100 min. They found an increase in tensile properties with increasing austenite deformation up to 40%, and then it starts to decrease. They obtained tensile properties (Tensile strength/Yield strength/Elongation %) in the range of 1790 MPa/1275 MPa/5 % and 1355 MPa/ 920 MPa/15 % with thermo-mechanical treatment of ADI. They concluded that higher ductility and lower strength values can be obtained at higher austempering temperature due to the higher volume fraction and higher carbon content in saturated austenite.

Janowak and Gundlach [90], investigated controlled cooling experiment for the production of ADI. Their test involved a 25 mm Y-block casting poured from a ductile iron containing 3.3% C, 2.3% Si, 0.32% Mn, 1.5% Ni, 1.0% Cu and 0.5% Mo. They performed the casting shake out from the oil-bonded sand mould at 870 ℃ and allowed it to air cool down to 370 ℃. The casting was then placed into a container of insulating material (Sil-O-Cel). In 2 hours the temperature had declined to 345 ℃ and the casting was removed and allowed to air cool. They

found that mechanical properties of the obtained samples show good combination of strength and elongation properties (Tensile strength: 876 MPa, Yield strength: 504 MPa and Elongation percentage: 7.9%). They concluded that control cooling options are more feasible to achieve high strength and toughness.

Yang and Putatunda [4] investigated the influence of two-step austempering process on microstructure and mechanical properties of ADI. They performed the austenitization of samples at 927 ℃ for 120 min. According to their two step austempering process, the samples were initially quenched for 5 min in a salt bath maintained at 260 ℃ and then austempered for 120 min at the different austempering temperatures. They found that the volume fraction of austenite and carbon content of austenite increases with an increase in austempering temperature. The tensile properties of the obtained ADI samples processed by the two-step austempering process was in the range of 900-1300 MPa for yield strength, 1200-1500 MPa for ultimate tensile strength and 2-10% for elongation percentage. In addition, they found that strength properties decrease with austempering temperatures and elongation properties increases with austempering temperatures. They concluded that two-step austempering process resulted in higher yield strength, tensile strength and fracture toughness as compared to the conventional single step austempering process.

Recently, a new grade of ADI known as dual phase ADI consists of pro-eutectoid ferrite and ausferrite or martensite was found to be validated for the suspension parts of the automotive owing to its greater ductility than the conventionally heat treated ADI [37]. From the literature [19, 37], it was found that the dual phase ADI was obtained by the partial austenitization of ductile iron within the single phase (austenite) region followed by austempering or quenching the material at room temperature. Basso et al. [19] investigated the fatigue and mechanical properties of dual phase ADI. They obtained three different dual phase ADI by partial austenitization of ferritic samples at temperatures of 800, 820, and 835 ℃ for 60 min, followed by austempering process at 350 ℃ for 90 min (for each sample). They found that the tensile properties of the dual phase ADI is in the range of 521-728 MPa for ultimate tensile strength, 354-410 MPa for yield strength and 18-24% for elongation percentage. They concluded that dual phase ADI could provide a wide range of mechanical properties based on the relative percentage of different phases in the matrix.

The recent advance in the ADI processing technology significantly enhances the mechanical properties of ADI. However, still there is a need to improve the material efficiency of ADI in correlation with its environmental impacts and microstructural characteristics. Therefore, in the coming sections, a novel processing route was investigated for the sustainable ADI production.
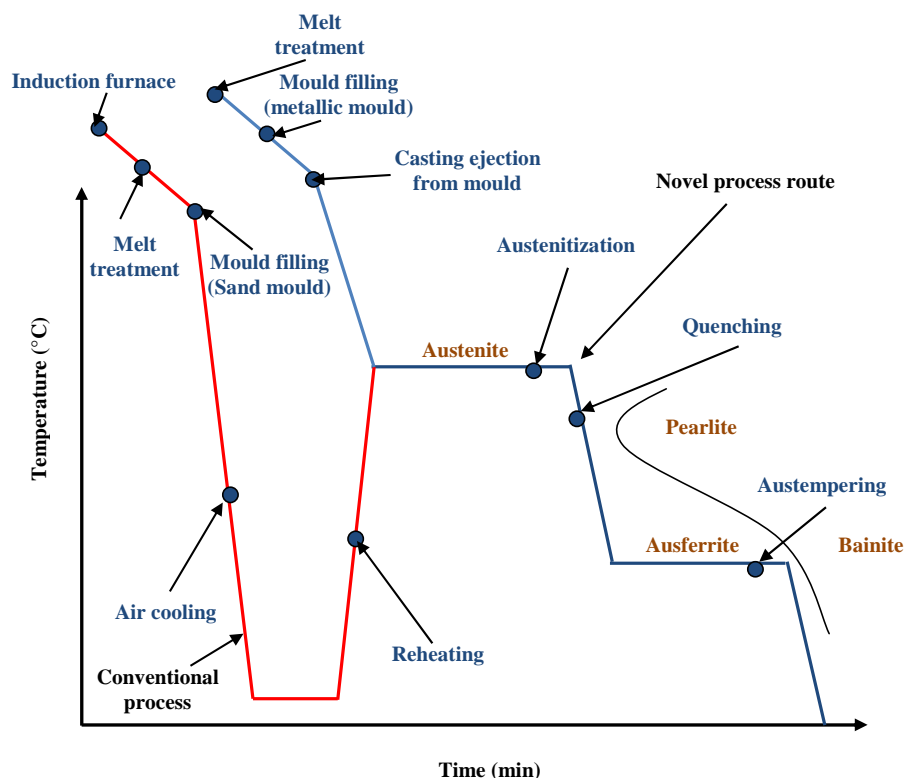
Figure 4.1: Schematic representation of the conventional and innovative processing technology for ADI production.

4.2.2 Integrated continuous casting-heat treatment technology

Figure 4.1 shows the schematic representation of the conventional and developed innovative process route for ADI production. In this innovative processing technology, the ductile iron samples obtained using the permanent mould are first austenized immediately after solidification process followed by austempering heat treatment in the fluidized bed and then air cooled at room temperature to get ADI material [76, 91]. The permanent mould was used to meet the challenges presented by the modern manufacturing industry: higher production rate of near-net shape ADI castings and the in-situ heat treatment for austempering [22]. The near-net shape casting process leads to the reduction in the machining and finishing costs [15]. The ductile iron samples are first austenitized at 930 ℃ for 90 min. The obtained specimen were then quenched down to austempering temperature in first fuidized bed at room temperature and then austempered in another fluidized bed for different austempering temperature (320, 350 and 380 ℃) and time (60, 90, 120 and 150 min). Fluidized bed technology is being increasingly used in the heat treatment industry, due to the increased energy efficiency, more uniform and controlled heat treatment option [92]. The detail procedure regarding the foundry and heat treatment practices of the novel process route for ADI production is provided in Chapter 3.
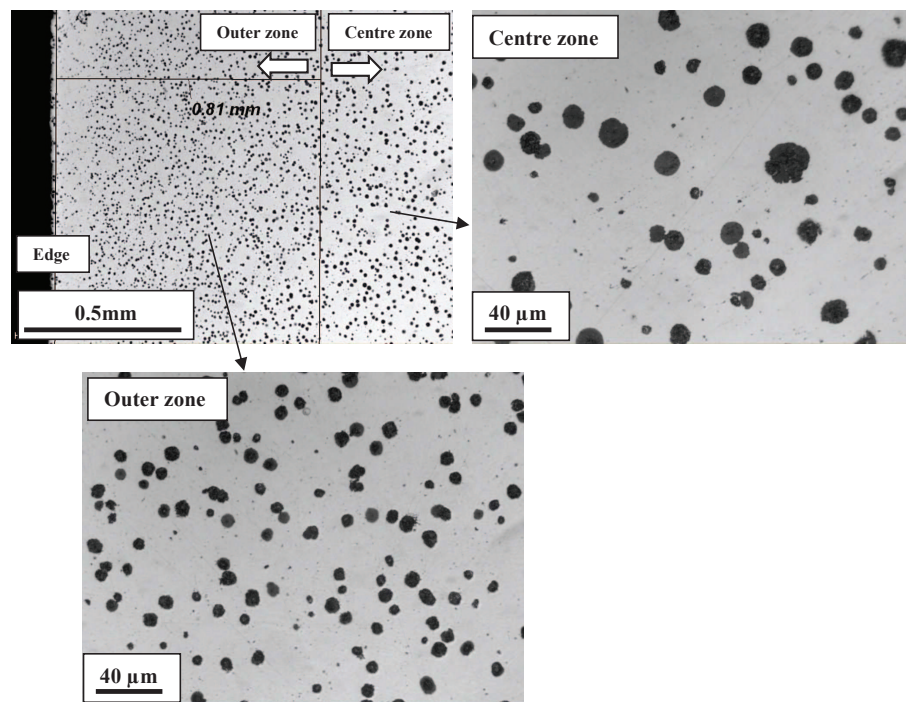
Figure 4.2: Typical unetched microstructure of resulting ADI sample (produced by the innovative processing technology) at outer and centre zones (Austempered at 380 °C for 90 min).

4.3 Results and discussion

4.3.1 Typical green ADI microstructure

The chemical composition of the ductile iron used in the present chapter is shown in Table 4.1. The typical un-etched microstructure of the produced ADI sample is shown in Fig 4.2. Based on average graphite nodule counts and average graphite nodule size, two different zones exhibiting slightly different microstructures were observed. First is the outer zone at the outer surface which is approximately 0.5-1 mm thick and second is the centre zone which is at the interior of the samples. Image analysis of optical micrographs of un-etched samples at different sections (bottom, middle and top) gave an average graphite nodule density in the range of 900 ± 150 nodules/mm^2 at centre zone with a mean graphite nodule size in the range of 13-17 μm whereas average graphite nodule density at the outer zone is in the range of 1300 ± 160 nodules/mm^2 with a mean graphite nodule size in the range of 5-10 μm. The variations in the average graphite nodule counts and its average size in the resultant microstructure can be explained due to the distinctly different cooling rates during solidification at the centre and outer zones. The outer zone is in contact with the metallic mould, solidified rapidly resulting in higher nodule counts with smaller size compared with those in the interior zone of the casting. Salazar et al. [93] explained the relationship between cooling rate and graphite nodule count and its

size. They stated that the nucleation of graphite nodule and its size increases due to the higher under-cooling which can be achieved by larger cooling rates.

Element	Percentage (%)
Carbon (C)	3.50-3.60
Silicon (Si)	2.70-2.80
Manganese (Mn)	0.23-0.25
Molybdenum (Mo)	0.19-0.21
Copper (Cu)	0.75-0.80
Nickel (Ni)	0.55-0.63
Sulphur (S)	0.017-0.022
Magnesium (Mg)	0.030-0.038

Table 4.1: Chemical composition range for the resultant ADI samples.
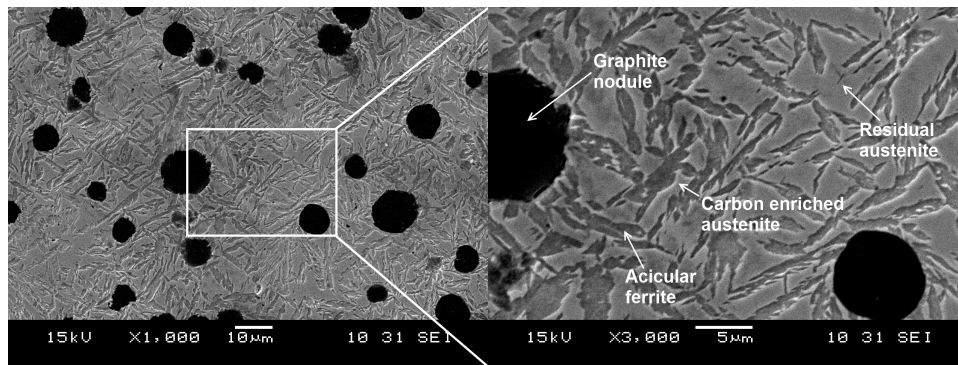
Figure 4.3: SEM micrograph of resultant ADI microstructure (Austenitized at 930 ℃ for 90 min; Austempered at 380 ℃ for 120 min).

Figure 4.3 shows the SEM micrograph of the typical ADI microstructure produced by using an integrated continuous casting heat treatment process route. Due to the in-situ heat treatment of ductile iron samples, the obtained microstructure consists of a matrix having dark needle-shaped ferrite and bright austenite with graphite nodules embedded in it. The dark needle-shaped ferrite and bright austenite between the needles in the micrograph constitute an ausferrite matrix, and the bright bulky region is untransformed austenite volume [20, 94]. The austempering temperature and time during the austempering heat treatment process of ductile irons play a critical role in the development of microstructural characteristics of ADI and its mechanical properties. The combined effect of austempering temperatures (320, 350 and 380 ℃) and times (60, 90, 120, and 150 min) on the resultant ADI microstructures are shown in Fig. 4.4. At a constant austempering time and lower austempering temperature (320 ℃), fine needles of acicular ferrite were observed with only a small amount of retained austen-
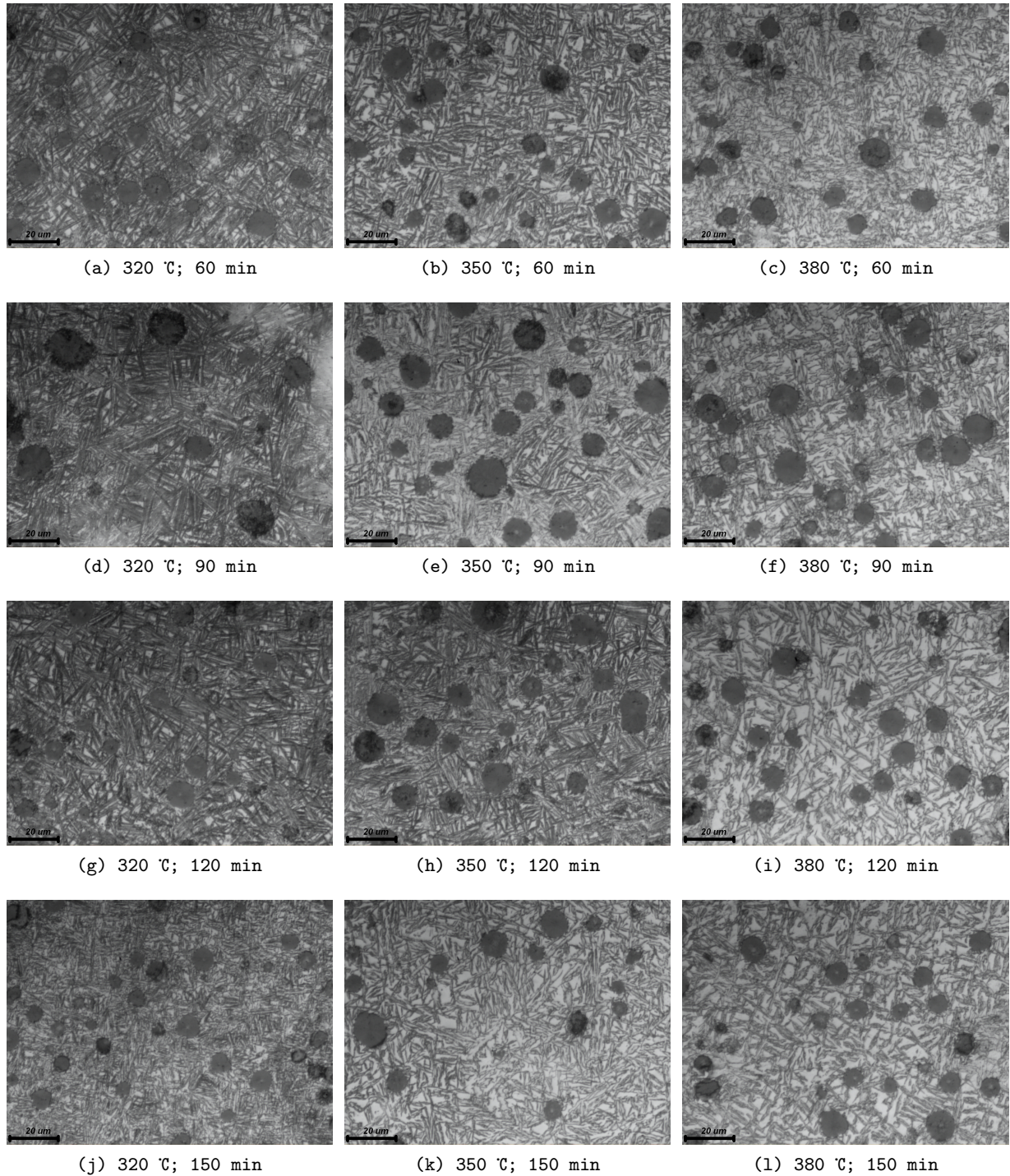
Figure 4.4: Typical ADI microstructure obtained by integrated continuous casting heat treatment process for different austempering conditions (Austenitizing temperature: 930 ℃; Austenitizing time: 90 min), scale: 20 μm.

ite in between. As the austempering temperature is raised from 320 ℃ to 380 ℃ the amount of bright austenite between ferrite needles increases. At higher austempering time, increased austempering temperature leads to the coarsening of the ferrite needles. This can be explained due to the fact that at lower austempering temperatures, due to high supercooling, a high nucleation rate results in a large number of fine ferrite needles [87, 95]. On the other hand, at higher austempering temperatures, the lower nucleation rate results in fewer ferrite needles, each growing to a larger size. Thus at 380 ℃ coarse feathery ferrite characteristic was observed. It can be also observed that on increasing the austempering time at a constant austempering temperature the white retained austenite region between ferrite needles first increases and then show decreasing behavior.
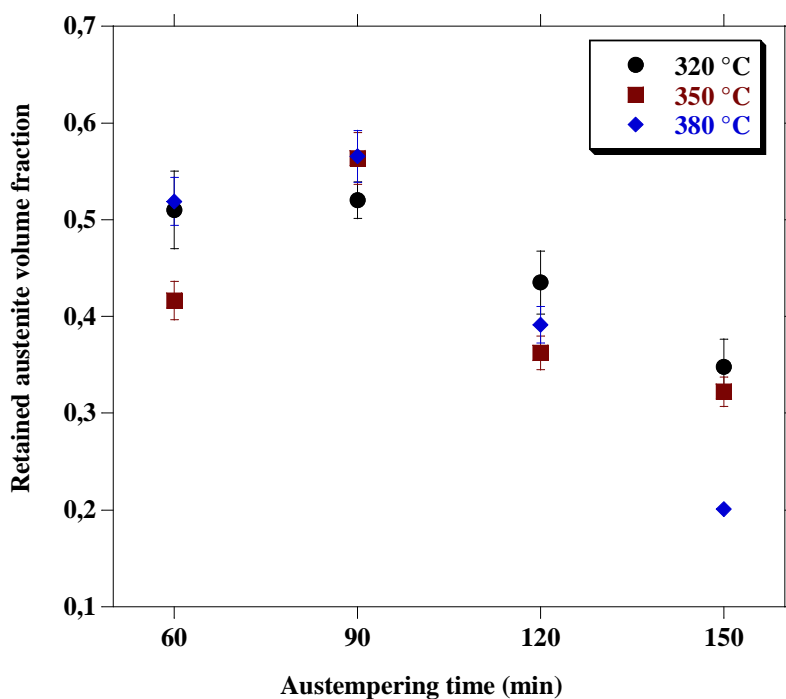
Figure 4.5: Variations in the retained austenite volume fraction with the austempering conditions.

The quantitative estimation of the resultant ADI samples was obtained by the XRD analysis. The austempering temperature and time has a significant influence on the relative amount of the acicular ferrite and retained austenite produced during the austempering process. The volume fraction of retained austenite varying with austempering conditions is shown in Fig. 4.5. It can be observed that for higher austempering temperatures (350 and 380 ℃), retained austenite volume fraction show increasing behavior with austempering time in the range of 60-90 min and then it starts to decrease with austempering time in the range of 90-150 min. On the other hand, at lower austempering temperature (320 ℃), the retained austenite volume fraction shows
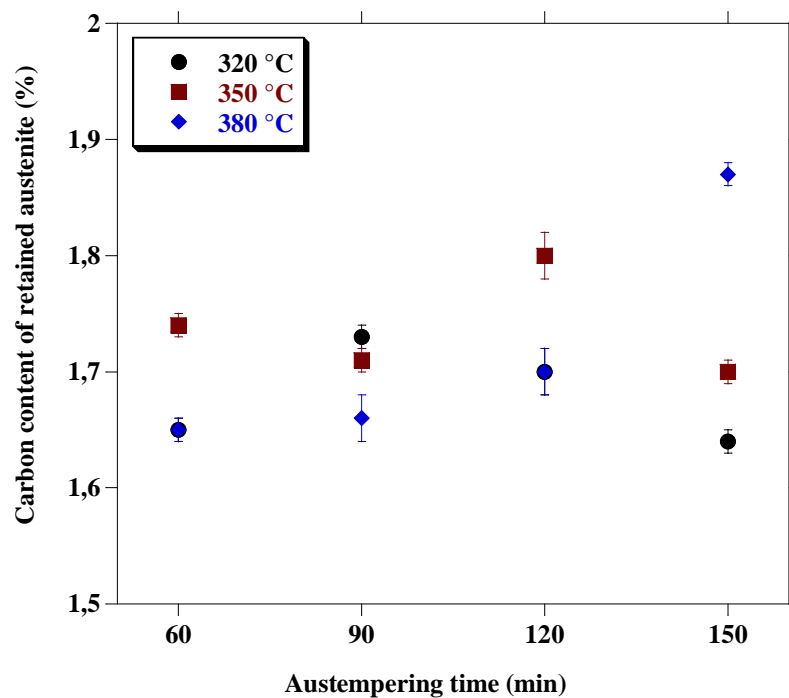
Figure 4.6: Influence of austempering temperature and time on the carbon content of the retained austenite (wt%).

constant behavior in the austempering time range of 60-90 min and then it shows decreasing behavior with austempering time in the range of 90-150 min. It was also observed that the decreasing rate of retained austenite volume fractions at higher austempering time is directly proportional to the austempering temperature. The difference in the retained austenite volume fraction generated at higher and lower austempering temperature have an important influence on the spatial distribution of this phase, as can be seen in Fig. 4.4. The ferrite growth during austempering process depend on the carbon diffusion from the ferrite to the surrounding. Since the carbon diffusion during austempering process is directly proportional to the austempering temperature, the carbon diffusion from the ferrite to the surrounding region is higher at higher austempering temperature than that of lower austempering temperature [95]. The variation of the retained austenite volume fraction with austempering time can also be understood from the initiation of stage I reaction in the range of 60-90 min. During this reaction, the austenite volume gets enriched with carbon and improves its stability [87]. However, on increasing the austempering time further from 90 min to 150 min there is a decrease in the retained austenite volume fraction due to the execution of stage II reaction.

Figure 4.6 shows the variation of carbon content of retained austenite as a function of austempering time in the lower and higher ausferritic temperature ranges. It can be observed that at lower austempering temperature (320 ℃), the carbon content of retained austenite rises
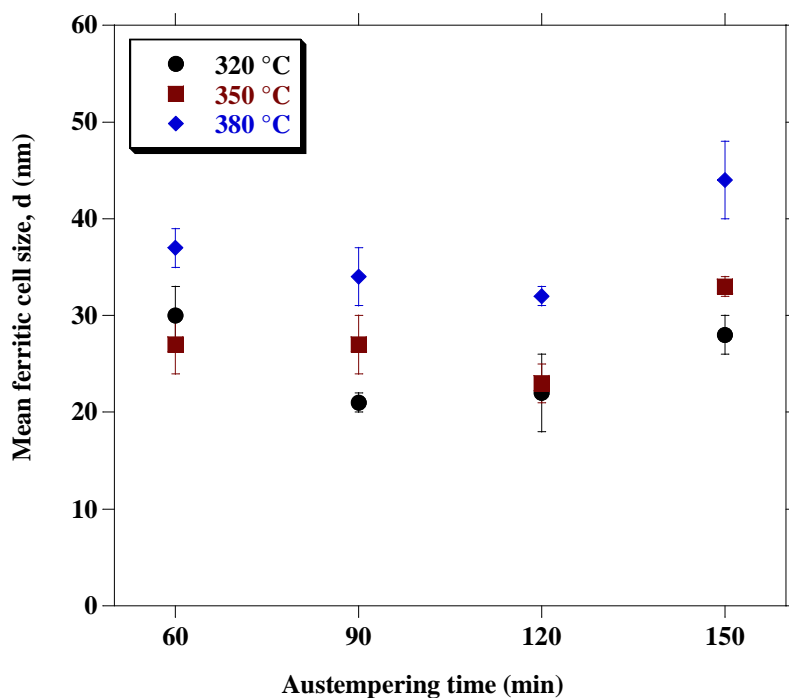
Figure 4.7: Influence of austempering time on the mean ferritic cell size (d).

gradually from a low value of 1.65 wt.% at 60 min to 1.73 wt.% at 90 min. After that it show decreasing behavior with an increase in austempering time. On the other hand, at 350 ℃ the carbon content of retained austenite shows a constant behavior (1.7 wt.%) with austempering time in the range of 60-90 min. However, it found to be increases to a value of 1.8 wt.% at the austempering time of 120 min. On further increasing the austempering time to 150 min, the carbon content of retained austenite reaches to its constant values of 1.7 wt.% at 350 ℃. At higher austempering temperature (380 ℃), the carbon content of retained austenite shows a gradually increasing behavior with austempering time in the range of 60-120 min and then it increased to 1.9 wt.% at the austempering time of 150 min. It can also observe that in the austempering time range of 60-120 min, the higher values of carbon content of retained austenite were found at the austempering temperature of 350 ℃. The low carbon content of retained austenite at lower austempering temperature (320 ℃) is due to the low diffusion rate of carbon and fast kinetics of ferrite formation, little carbon diffuses into the austenite. As the austempering temperature increases more carbon will diffuse to the surrounding austenite and leads to the carbon enrichment of the austenite.

Figure 4.7 shows the variation of ferritic cell size (d) with austempering time at different austempering temperatures. It can be observed that the lower values of mean ferritic cell size was obtained at lower austempering temperature (320 ℃). For higher austempering temperatures the mean ferritic cell size shows constant behavior with austempering time in the range

of 60-120 min. The d values increases significantly with an increase in austempering time in the range 120-150 min. The increase in d values at higher temperatures and time is indicative of rapid grain coarsening of ferrite.
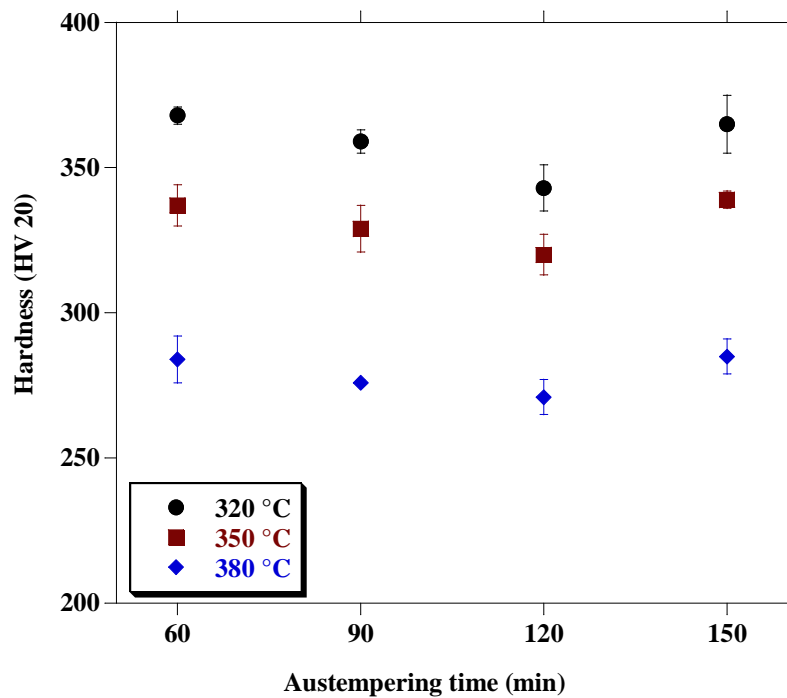
Figure 4.8: Influence of austempering time on the hardness values (HV 20)

4.3.2 Austempering kinetics

The austempering temperature and time have a marked influence on the retained austenite volume fraction and its carbon content. All these microstructural characteristics can be further used to gain information regarding the kinetics of stage I and stage II reactions during austempering process. The change in measured properties (retained austenite volume content, carbon content of retained austenite, ferrite cell size, etc.) during the austempering process reflects the progress of stage I and II reactions [53].

The austempering kinetics were also followed by observing the hardness modification of the resultant ADI microstructures as a function of austempering time. The influence of austempering time on the hardness values of resulting ADI samples are shown in Fig. 4.8. The austempering temperature show a significant influence on the hardness values as compared to the austempering time. The hardness values decrease with an increase in austempering temperature. Lower hardness values are obtained at the higher austempering temperatures. It can be observed that the hardness values show constant behavior with austempering time in the

range of 60-120 min for all austempering temperature. However, a significant rise was observed in hardness values for longer treated time (120-150 min) for all austempering temperatures. This behavior can be explained by the fact that as the austempering time increases, more of the softer phase of high-carbon austenite formed and the average matrix hardness decreases. This continues until the onset of stage II of the reaction, after which the hardness is expected to rise slightly due to the formation of carbides during stage II reaction. Thus, the progress of stage I reaction during austempering kinetics can be explained by an increase in retained austenite volume fraction and by a decrease in hardness values. On the other hand, the stage II reaction during austempering process is accompanied by an increase in hardness and a decrease in retained austenite volume fraction.
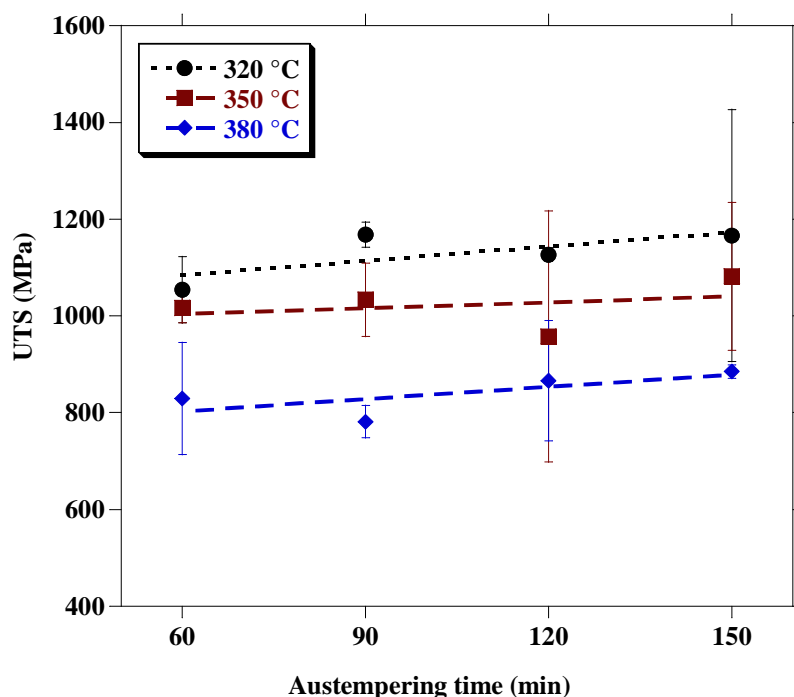
Figure 4.9: Influence of austempering time on the ultimate tensile strength (MPa).

4.3.3 Tensile properties

Figure 4.9 shows the influence of austempering time on the ultimate tensile strength (UTS) for different austempering temperatures. It can be seen that austempering temperature play a critical role in the evolution of UTS as compared to the austempering time. It can be also observed that UTS decrease gradually with an increase in austempering temperature for all austempering time. Austempering time did not show significant influence over the UTS values in the range of 60-150 min. However, higher UTS values are obtained at higher austempering time (150 min).
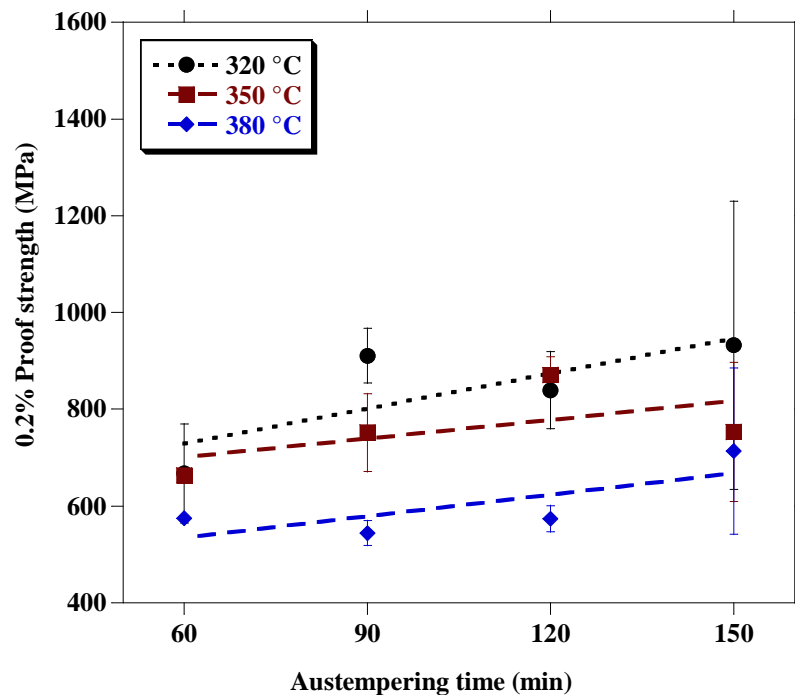
Figure 4.10: Influence of austempering time on the 0.2% yield strength (MPa)

The variation of 0.2% yield strength of the resultant ADI samples with austempering time for different austempering temperature is shown in Fig. 4.10. It shows similar behavior with respect to austempering time as that of UTS. However, significant influence of austempering time was observed in case of yield strength. It can be seen that at lower austempering temperature (320 ℃), the yield strength values increases initially with austempering time in the range of 60-90 min and then attains constant values at higher austempering time. On the other hand, at higher austempering temperatures (350 and 380 ℃), the yield strength values show constant behavior with austempering time. Figure 4.11 shows the evolution of ductility behavior of the resultant ADI samples as a function of austempering time for different austempering temperature. It can be seen that the ductility behavior is significantly influenced by both temperature and time parameters during austempering process. It was found that at lower austempering temperature (320 ℃) the ductility of the resultant ADI samples show constant behavior at higher austempering time. However, at 380 ℃ the ductility increases with austempering time and attains its maximum value at 120 min. On further increasing the austempering time it shows decreasing behavior. On the other hand, at 350 ℃ the ductility of the samples are higher in an intermediate time interval (90-120 min).

The variation in mechanical properties with austempering parameters (temperature and time) depends on the change in the evolution of microstructural variables, particularly, the ferrite morphology, the retained austenite volume fraction and the carbon content of retained
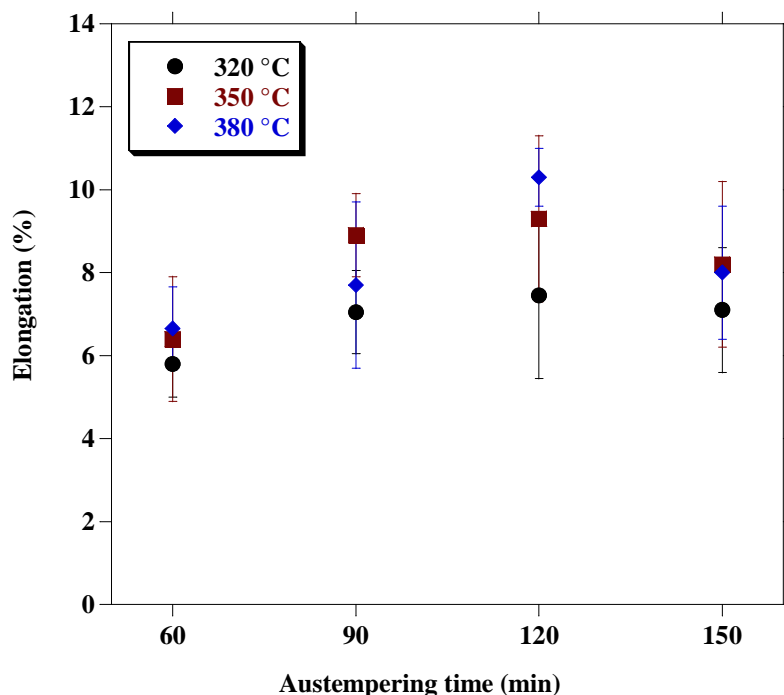
Figure 4.11: Influence of austempering time on the ductility of the resultant ADI.

austenite. The decrease in strength properties with an increase in austempering temperature can be explained due to the change in the ferrite morphology and amount of the retained austenite volume fractions with austempering temperature. At lower austempering tempera-ture, the ferrite has fine acicular ferritic characteristics. The fine ferrite morphology provides higher strength to the ADI microstructure by providing greater resistance to dislocation mo-tion [87]. Other than this, on increasing the austempering temperature the retained austenite volume fraction increases resulting in a decrease in strength properties. In additions, at lower austempering temperatures the carbon precipitation within the ferrite is high due to low dif-fusion rate of carbon, which increases its stability. On the other hand, at higher austempering temperature, coarsening of ferrite together with higher retained austenite volume fraction de-creases its strength values. The high retained austenite volume fraction at higher austempering temperature is also responsible for the increased ductility of resultant ADI samples. The ductil-ity of ADI samples improves with an increase in the carbon content of retained austenite with austempering time. However, at higher austempering time, the ductility values are lower due to the occurrence of stage II reaction. It can be also observed that the variation in strength properties with austempering temperature show decreasing behavior with respect to the mean ferritic cell size (d). This behavior is well supported by the Putatunda et al. [95]. They stated that to obtain high strength values, ADI microstructure must have simultaneously the following microstructural characteristics:

- The fine ferrite and austenite morphology;

- The high carbon content of austenite;

- The lower values of mean particle ferritic size (d).
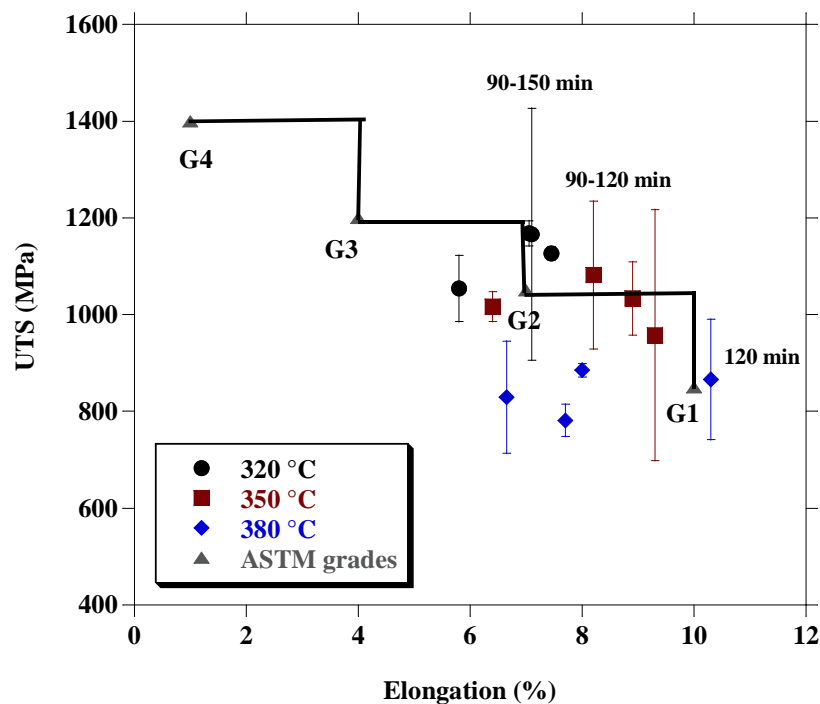
Figure 4.12: The UTS-elongation % comparison of resultant ADI samples with ASTM ADI grades.

Figure 4.12 shows the strength properties plotted in the form of UTS-elongation percentage relationship. The minimum properties defined for the ASTM grade 1, grade 2, grade 3 and grade 4 ADI are denoted by the points G1, G2, G3 and G4 respectively. It can be seen that the resultant ADI produced at the austempering temperature of 380 ℃ and austemering time of 120 min is comparable to ASTM grade 1 ADI. On the other hand, the resultant ADI produced at the selection of treatments 350 ℃/90-120 min and 320 ℃/90-150 min are comparable to ASTM grade 2 ADI.

4.4 Interpretation of tensile stress-strain curve

Figure 4.13 compares the stress-strain curves of resultant ADI at the different austempering time. The stress-strain curve was analysed to understand the elastic and plastic behavior of the material. In addition, the area under the stress-strain curve signifies as strain energy
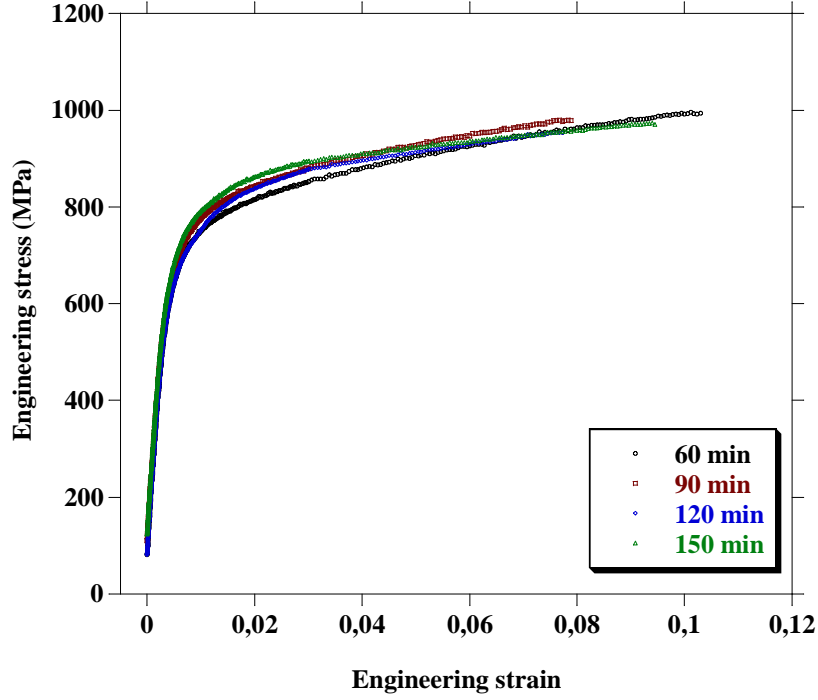
Figure 4.13: Tensile test curves of the novel ADI samples for different austempering time (Austempered at 350 ℃).

required to shear the metal during the machining process. It is the combined function of the strength, modulus, strain hardening coefficient and strain to failure of the material. The stress-strain curve is divided into two parts. First part in which, the deformation of the material is proportional to the applied stress. This deformation is known as elastic deformation and it is reversible. The proportional relation between the stress and elastic strain is described by Hookes law (Equation 4.1). The elastic deformation can be explained by the reversible displacements of atoms from their equilibrium positions [84]. Plastic deformation of material started as soon as the stress applied exceeds its elastic limit, it imparts permanent non-recoverable deformation in the material. Plastic deformation involves breaking of the original atomic bonds, movements of atoms and the restoration of bonds. In the present study, the plastic behavior of the material was described using the Hollomon equation (Equation 4.2) [84, 85].

$$\sigma = E\epsilon_e \tag{4.1}$$

$$\sigma = K\epsilon_p^n \tag{4.2}$$

Where, σ is the true stress, E is the Youngs modulus (Pa), ϵ_e is the true elastic strain, K is

the strength coefficient (Pa), ϵ_p is the true plastic strain and n is the strain hardening exponent. The shape and size of the engineering stress-strain curve depends on material properties, heat treatment, prior history of plastic deformation, strain rate, temperature and state of stress imposed on specimen during the test.

In literature [84, 85], the dislocation processes are considered as the dominant deformation mechanism for plastic deformation of metals at room temperature. The dislocation is the defect responsible for the phenomenon of slip, by which most metals deform plastically. During the plastic deformation of metals, the shear stress required to produce slip continuously increases with increasing shear strain. The increase in the stress required to cause slip because of previous plastic deformation is known as strain hardening. It is caused by dislocations interacting with each other and with barriers, which impede their motion through the crystal lattice. In Hollomon equation (Equation 4.2), the strength coefficient (K) determines the strength potential of the material whereas the strain hardening exponent (n) determines the strain hardening capacity of the material. The constants n and K are determined by evaluating data from the tensile test curves.

The n values determined the strain hardening capacity of the material when it is plastically deformed. A high n value indicates a more uniform strain distribution which results in a greater resistance to deformation. A lower n values indicate lower work hardening rate, which is preferred from a machining point of view. As stated earlier that ADI microstructure consists of austenite and ferrite phase with austenite has a higher work hardening rate than ferrite. Thus, the machinability of the material will highly depend on the amount and morphology of retained austenite which in turn depend on the austempering temperature and time. Therefore, the present chapter also investigates the strain hardening behavior of ADI material with respect to the amount of retained austenite.

4.4.1 Strain hardening behavior

The strain hardening exponent (n) and strength coefficient (K) are determined from the logarithmic form (Equation 4.3) of the Equation 4.2, representation of the true stress versus true strain curve within the plastic range.

$$log\sigma = logK + nlog\epsilon_p \tag{4.3}$$

The true stress (σ) and true strain (ϵ) values are calculated from the following equations:
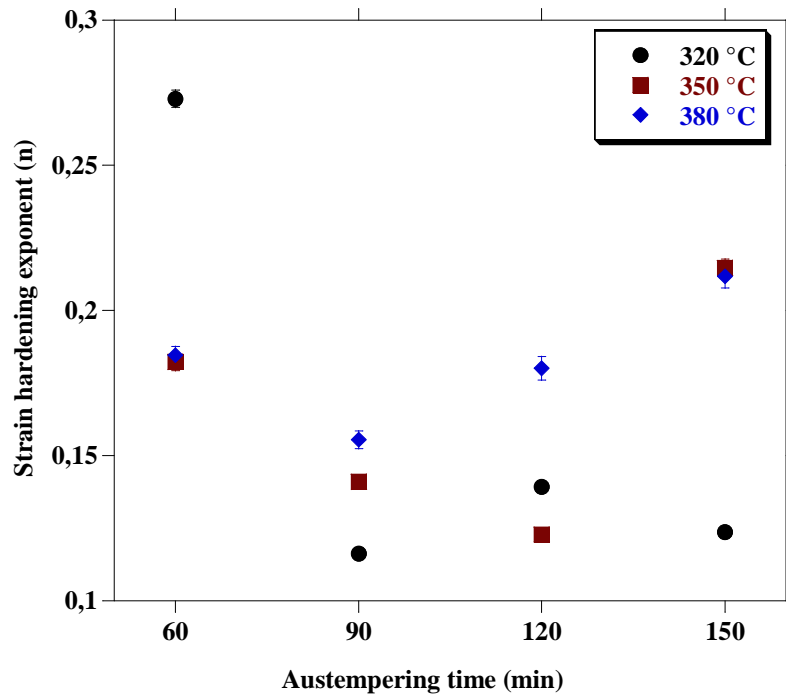
Figure 4.14: Influence of austempering time on the strain hardening exponent (n)

$$\sigma = S(1 + e) \tag{4.4}$$

$$\epsilon = ln(1 + e) \tag{4.5}$$

Where:

S=Engineering stress and,

e=Engineering strain.

4.4.2 Strain hardening exponent

Figure 4.14 shows the influence of austempering time on the strain hardening exponent of the resultant ADI samples for different austempering time. It can be observed that for all austempering temperature, strain hardening exponent show decreasing behavior for shorter treated time (60-90 min). On further increasing the austempering time, strain hardening exponent show different behavior for each austempering temperature. At lower austempering temperature (320 ℃) the property showed approximately constant behavior. However, at 350 ℃ the property attains its minimum value 0.12 at 120 min and then it reaches to its maximum value
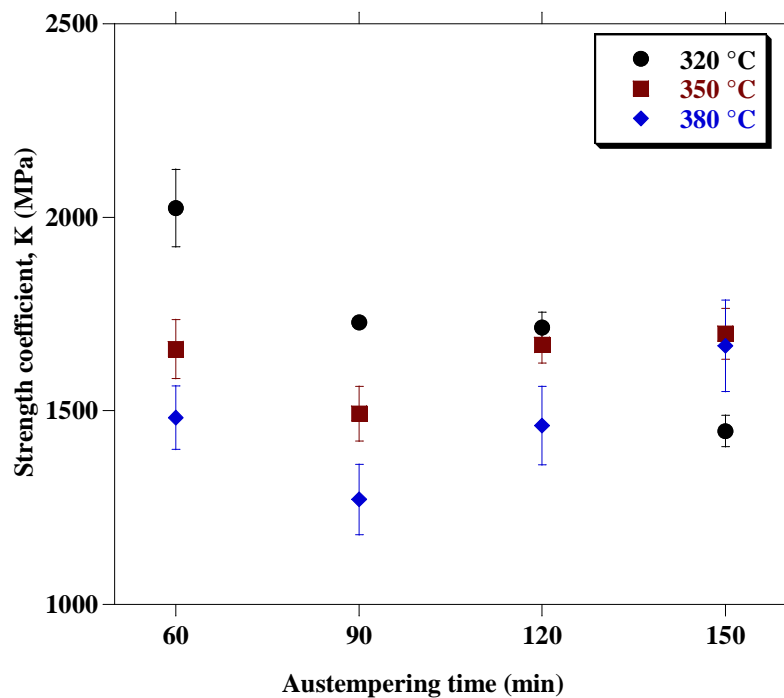
Figure 4.15: Influence of austempering time on the strength coefficient

of 0.21 at 150 min. On the other hand, for higher austempering temperature (380 ℃), the property gradually increases with austempering time > 90 min and attains maximum value of 0.21 at 150 min.

The variation in strain hardening exponent with different austempering conditions can be understood from variations of the austenite and ferrite volume fractions in the ADI microstructure. The austenite shows higher strain hardening characteristics as compared to the ferrite [60]. Together with this, the carbon content of retained austenite plays a critical role in its strain hardening characteristics [95–97]. The carbon content of retained austenite increases its stability at room temperature. The strain hardening behavior of resultant ADI samples with austempering temperature can be explained due to the change in the ferrite morphology and its content with austempering temperature. On increasing the austempering temperature, the ferrite morphology changes from fine to coarser. This leads to the fewer interface areas and weaker interactions between dislocation and carbon atoms, resulting in a lower strain hardening exponent. It can be seen that the maximum strain hardening exponent value of 0.27 was obtained from the combination of lower austempering temperature (320 ℃) and time (60 min). This can be explained due to the lower diffusion rate of carbon at lower austempering temperature. This can lead to the high volume of untransformed austenite in ADI microstructure, which can be transformed to martensite at room temperature. The presence of martensite significantly increases the strain hardening exponent. The variation in strain hardening expo-

nent with austempering time can be understood from the fact that during the initial phase of austempering process the growth of ferrite needles was higher. This leads to the decrease in strain hardening exponent values. However, on further increasing the austempering time, strain hardening exponent values increases for higher austempering temperature due to the higher diffusion rate of carbon from ferrite to austenite, which improves the strain hardening behavior of austenite.

4.4.3 Strength coefficient

Figure 4.15 shows the influence of austempering time on the strength coefficient of the resultant ADI samples for different austempering temperature. It can be seen that the strength coefficient values decrease with austempering time in the range of 60-90 min for all austempering temperatures. On further increasing the austempering time, the property shows different behavior with respect to austempering temperature. At 320 ℃ the property show constant behavior and then reaches to its minimum values at 150 min. On the other hand, at 350 ℃ the strength coefficient increase slightly and reaches a plateau. However, at 380 ℃ the strength coefficient show increasing behavior with austempering time > 90 min.

The higher values of the strength coefficient at lower austempering temperature in the austempering time range of 60-120 min can be explained due to the fine ferritic morphology in ADI microstructure resulting in higher strength values. The gradual decrease in strength coefficient values with initial austempering phase (60-90 min) indicate the progress of stage I reaction and the increase in the retained austenite volume fraction. However, the further increase in strength coefficient values with austempering time indicate the occurrence of stage II reaction and decrease in retained austenite volume fraction. The higher value of strength coefficient at the combination of low austempering temperature (320 ℃) and low treated time (60 min) indicate the transformation of austenite to martensite at room temperature due to the lack of carbon enrichment. The formation of martensite in the resultant ADI microstructure leads to the high strength coefficient.

4.5 Conclusions

An innovative process route was developed for the light-weight ADI casting production using an integrated casting-heat treatment route. The microstructural characteristics of the produced ADI samples were investigated in correlation with its mechanical properties and strain hardening behavior. Based on the results obtained, the following conclusions can be drawn:

1. The integrated casting-heat treatment process route leads to the production of light weight ADI casting with ausferrite microstructure (needle-shaped ferrite and high-carbon austenite) and high graphite nodule counts. The high nodule counts are associated with the increased cooling rates due to the thin wall ADI casting. This innovative process route leads to save energy and time during ADI production.

2. The quantitative estimation of resultant ADI revealed an increase in ferritic cell size with austempering temperature due to rapid grain coarsening of ferrite.

3. The lower values of retained austenite volume fraction and ferritic cell size at lower austempering temperature give rise to high strength ADI samples with lower ductility. The ductility of ADI samples improved with an increase in retained austenite volume fraction and its carbon content.

4. The selection of austempering parameters of 380 ℃/120 min leads to the production of ADI casting having tensile strength of 866 MPa and ductility of 10.3%, which is higher as compared to ASTM grade 1 ADI.

5. The strain hardening behavior of the resultant ADI samples are influenced by the microstructural characteristics of produced ADI. The low strain hardening values are obtained in the austempering time range of 90-120 min.

It was revealed that the innovative process route is capable for the production of ADI casting having combination of strength and ductility comparable to ASTM grades of ADI. In addition, the present study significantly elaborate the correlation of strain hardening behavior and mechanical properties of ADI with its microstructural characteristics. However, in order to get a sound ductile iron casting and to develop a controlled casting process for ADI production, there is a need to develop a simulation tool to predict the castability of ductile iron in permanent mould. The correlative thermal methodology for novel ADI castability simulation is introduced in the next chapter.

Chapter 5

Correlative thermal methodology for novel ADI castability simulation

5.1 Introduction

The use of simulation technologies to simulate mould filling and solidification processes during casting has expended greatly in recent years. The advance in simulation technology has been driven by the inherent complexity of the process involved, namely, interrelated fluid flow and thermal effects coupled with phase change [98]. The numerical simulations provide a means of understanding the combined effects of chemical composition, heat transfer, fluid transport phenomena, and their relationships to microstructure and the formation of defects during mould filling and solidification processes. Thus, the numerical simulation process can be used as a vital tool for the optimization of the overall casting process at a moderate cost.

However, numerical simulation of mould filling and solidification during casting is a challenging task. It involves various phenomena such as fluid mechanics with phase change, inter-facial heat transfer between the melt and the mould, solidification mechanisms, microstructure evolution and mechanical stress, which make the overall casting process more complex [99]. Moreover, the heat transfer between the different contacts interfaces (melt, mould and air) and thermal resistances to heat flow from the interior of casting due to air gap at melt/mould interface leads to change in the melt castability and thus final casting quality [100, 101]. Therefore, there is a need to correlate and understand the combined effect of melt thermal characteristics, heat transfer at melt/mould interface, and melt flow through the critical sections of the casting to produce a sound defect-free ductile iron casting for ADI production.

The present chapter, explores the recent advances in the simulation analysis of simultaneous mould filling and solidification during casting. In this regard, the simulation of mould filling and

solidification is performed considering a permanent mould for ductile iron casting by virtue of its thermal characteristics. The thermal characteristics of the melt are obtained by using thermal analysis. This thermal analysis system acts as a tool to control the metallurgical process for ADI production and to get a consistency in the foundry process. Due to the significant impact of the filling and solidification on the melt castability (i.e. property of melt, which determine the ease of forming a quality casting depends upon interactions of the alloy and/or addition elements and part design) and final casting quality, an effort has been made to analyse the influence of process parameters on the formation of casting defects. The present chapter thus focus on the implementation of the correlative thermal methodology for ADI castability simulation in a permanent mould to develop the novel process deign for ADI production.

5.2   Background

Casting involves two important steps. First step is the filling of melt in a mould, and second step is the solidification of melt by withdrawal of heat. In literature [102, 103] it was stated that mould filling affects the heat transfer, and solidification characteristics of the melt which in turn influences the fluidity of the melt. Han and Xu [104] defined the fluidity of the melt as an empirical measure of the distance that the melt can flow in a specific channel before being stopped by solidification. Ravi et al. [105] described that during mould filling, the fluidity of the melt is affected by the thermal characteristics of the melt and mould, pouring conditions, reinforcement characteristics and solidification mechanisms. The next step is the solidification of the melt by virtue of heat transfer. The heat transfer during solidification in a permanent metallic mould plays a significant role in determining the mechanical properties and the quality of the final casting [99]. In past many researchers [100, 101, 106], tried to understand the heat-transfer mechanisms at the melt-mould interfaces during solidification and tried to optimize the casting quality. They stated that during casting in a permanent mould the heat transfer at the melt/mould interfaces varies due to the formation of an air gap and due to the relative expansion and contraction of mould and casting during solidification. The formation of the air gap significantly reduces the heat transfer at the melt-mould interfaces. Additionally, temperature gradients are influenced by the geometry of the casting. These factors influence the quality of the final casting by generation of tensile thermal stresses at the solidification front that can ultimately lead to the appearance of hot tears/cracks in the final casting [107].

Recently, numerical simulation of casting processes has received huge attention because of its potential in increasing productivity and improving casting quality in metal casting industry. Vijayaram et al. [108] stated the significance of the use of accurate thermo-physical data,

boundary conditions and elimination of few uncertainties to get realistic descriptions of the casting process. The heat transfer and the air gap formation at the melt/mould interface and thermal characteristics of melt are some such uncertainties, which affect the dissipation of heat flow at melt/mould interfaces and also affect the overall solidification process. The thermal characteristics of the melt can be obtained by using the thermal analysis, i.e. by monitoring the changes in cooling curves and its derivative curves during solidification. These changes occurred as the latent heat released by the solidifying micro-constituents and enables the identification of important parameters (liquidus, eutectic, and solidus temperatures, etc.) which are linked with the development and characteristics of the microstructure observed in the final casting [80]. The thermal characteristics of the melt is influenced by the metallurgical conditions of the melt which in turn influence the fluidity of the melt [80, 109]. The correlation between the changes observed in the cooling curve and its first derivative using thermal analysis has allowed foundries to monitor and control the melt and treatment procedures with higher precision.

There are mainly two methods, FEM (finite-element method) and FDM (finite-difference method) for numerical simulation of casting [108]. Kermanpur et al. [110] illustrated the difference between the FEM and FDM. According to them, the FEM uses body fitted computational grids leading to a more accurate representation of melt/mould interface as compared to FDM. The FEM has its ability to handle complicated geometries (and boundaries) with relative ease. However, FEM requires higher memory resources for calculations and the usage of special generators for building 3D meshes. On the other hand, FDM offers ease of mesh generation due to the structured nature of the mesh and use fewer memory resources as compared to FEM. In contrast, FDM often requires fine grids to describe complicated geometry to reduce errors associated with the stair-step representation of curved boundaries. The latter introduces inaccuracies when computing liquid metal flow along the wall and heat fluxes normal to wall. In the present study, CVM (control volume meshing) is used instead of FDM and FEM. In CVM the domain is partitioned into small control volumes, and the approximation is derived using the conservation properties over each control volume. The CVM associates to each interior mesh point a volume. Miller (1998) defined these volumes as non-overlapping regions which union approximates the domain [111]. As compared to FE/FD methods, it reduces the simulation time and gives higher accuracy.

5.3 Numerical simulation procedure

Mould filling and solidification during casting in a permanent metallic mould were simulated using commercial CVM casting simulation software, NovaFlow&Solid CV. In the present study,

(a)

(b)
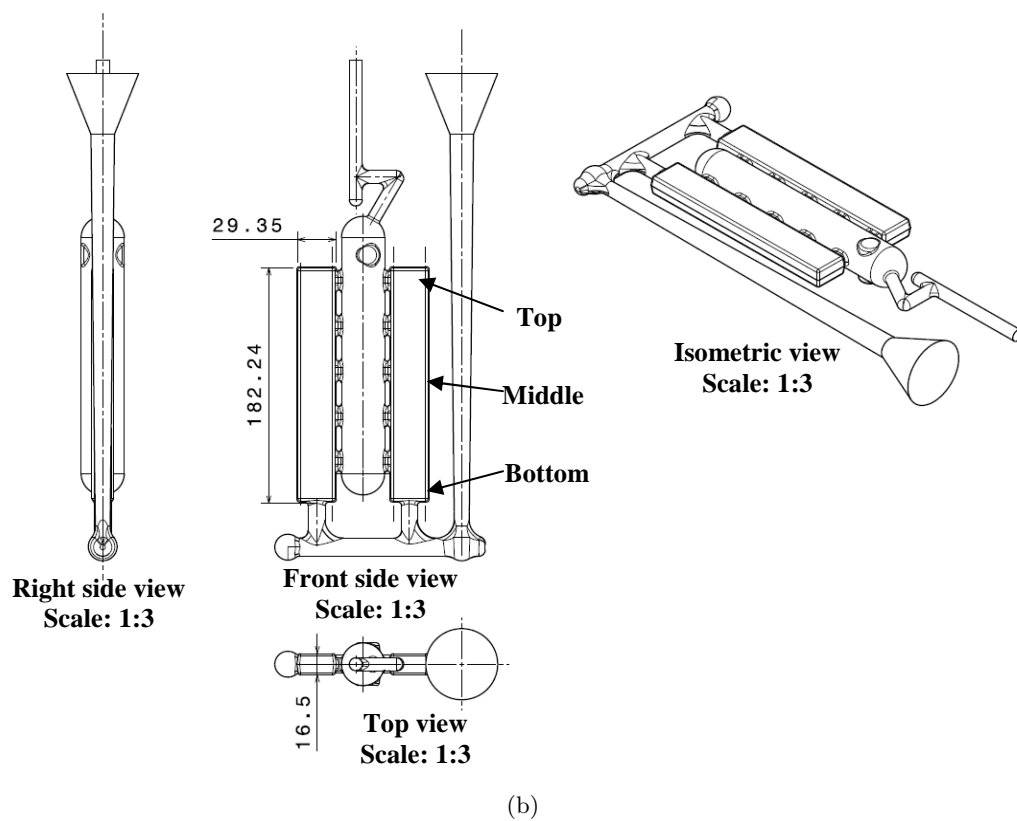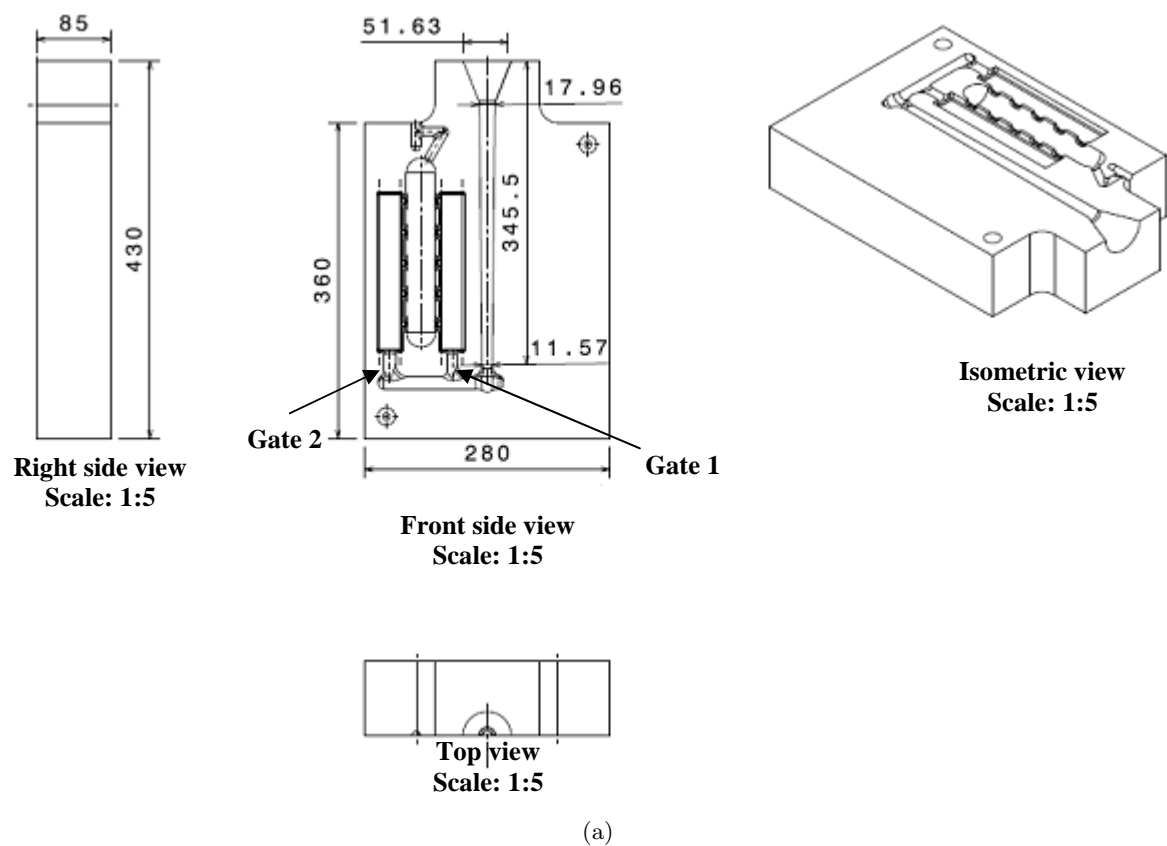
Figure 5.1: All dimensions are in (mm)(a) Permanent mould design and (b) Casting design.

Element	Percentage (%)
Carbon (C)	3.39-3.44
Silicon (Si)	2.44-2.48
Manganese (Mn)	0.23-0.25
Molybdenum (Mo)	0.20-0.21
Copper (Cu)	0.84-0.87
Nickel (Ni)	0.7-0.71
Sulphur (S)	0.014-0.018
Magnesium (Mg)	0.036-0.038

Table 5.1: Chemical composition range for the obtained ADI samples.

the simulation model adopts the quasi-equilibrium theory of the two-phase zone for alloy crystallization. In contrast to pure metal alloys, crystallize in the temperature interval from liquidus temperature to solidus temperature. This zone is named as two-phase as both liquid and solid phases are present. In literature [112–114], it was stated that during casting solidification, supercooling of melt occurs ahead of the crystallization front due to concentration changes, which cause the formation of a region where the melt temperature is lower than the equilibrium temperature of the phase transition. This physical transition of the melt leads to the appearance of a metastable zone between solid and liquid phases, known as two-phase zone, which is also referred as quasi-equilibrium zone.

The chemical composition of the melt is provided in Table 5.1. The permanent metallic mould design is shown in Fig. 5.1. It is made up of gray cast iron. It consists of two rectangular blocks each having dimensions of 430 mm×280 mm×85 mm. The sprue is 345.5 mm in length with an average diameter of 17.96 mm at top and 11.57 mm at bottom. The mould cavity consists of two specimens and riser as shown in Fig. 5.1. Each specimen has the shape of rectangular block with size of 182 mm×29 mm×16 mm. The mould cavity was coated with thick silica coating to gain a good insulation effect for the casting.

The present simulation software adopts the heat-transfer model, which calculates the interfacial heat transfer coefficient by considering the variation in interfacial air gap size. The interfacial air gap size usually develops at the metal-mould interface during the solidification. Griffiths [115] suggested that initially a thin skin of solidified metal formed in contact with the mould surface, and that heat transfer occurred by conduction through the peaks of the rough surface of the casting. However, as solidification proceeds, a thin air gap is formed by a relative movement of the solidifying melt and mould, caused by the thermal expansion of the mould and solidification shrinkage of the melt. Conduction is thus gradually reduced, and the heat transfer can be described by a simple superposition of conduction and radiation terms.

Figure 5.2: Schematic representation of standard non-tellurium cups for thermal analysis.

5.4 Results

5.4.1 Thermal analysis

Thermal analysis is an important tool for characterizing the melt preparation and to evaluate its solidification [80]. By virtue of thermal characteristics of melt and its solidification behavior; it provides information regarding nucleation potential of graphite and its morphology [81]. In the present study, thermal analysis of the melt was performed using the adaptive thermal analysis system (ATAS). At the time of pouring the standard non-tellurium (Te) cups were simultaneously filled (Fig.5.2) to get the thermal characteristics and thermo-physical parameters of the melt by recording the cooling curves using the commercial ATAS tool. The cooling curves were subsequently analyzed for determining the solidification behavior and eutectic point of alloy during its solidification. The obtained thermo-physical parameters and pouring parameters used in the simulation process are summarized in Table 5.2.

Figure 5.3 presents the typical cooling curves recorded using the thermal analysis tool. It describes the balance between evolution of heat in the samples, and heat released from the samples during solidification. Chaudhari et al. [116] described the cooling curve for the solidification of ductile iron in three successive steps: (i) primary formation of either austenite or graphite, (ii) initial and limited growth of eutectic, and (iii) bulk eutectic growth. However, the recorded cooling curves provide four arrest points during solidification, which are described as follows:

Property	Value
Liquidus temperature	1156 ℃
Solidus temperature	1104 ℃
Mould temperature	200 ℃
Pouring temperature	1360 ℃
Thermal conductivity (1140 ℃)	71.4 W/m-℃
Thermal conductivity (500 ℃)	34 W/m-℃
Density (1156 ℃)	7003 kg/m^3
Density (1104 ℃)	6932 kg/m^3

Table 5.2: Thermophysical properties of ductile iron and other parameters used in the simulation.
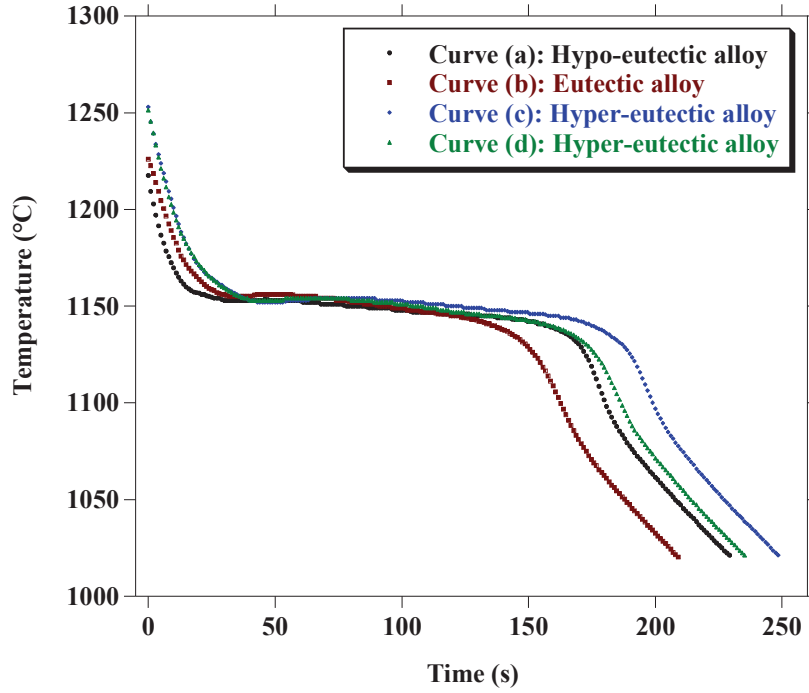
Figure 5.3: The typical cooling curves obtained from thermal analysis tool for different experiments.

- T_L: (Liquidus temperature): Starts precipitation, usually as pro-eutectic austenite.

- T_{El}: The lowest eutectic temperature, the minimal point from where the temperature is increasing.

- T_{Eh}: The highest eutectic temperature, the maximum temperature after the increase in temperature.

- T_S: The solidus temperature

The cooling curve (Fig. 5.3) gives us information about the solidification behavior of the melt. T_L (liquidus temperature), is the first temperature arrest during the solidification of the melt. It represents the beginning of the solidification process. At this stage, the austenite nucleates and the liquid iron gets enriched with carbon. The lowest eutectic temperature T_{El}, is second thermal arrest during solidification. At this stage, the heat generated from released specific heat and latent heat during the phase precipitation give rise in the temperature, and the temperature reaches to T_{Eh}, known as highest eutectic temperature. The difference between the highest eutectic temperature and lowest eutectic temperature is known as recalescence (R). After that the sample continues cooling until solidus temperature T_S is reached and all metal has solidified. The cooling curve analysis further provides parameters such as graphite factor 1 (G_1), which is an indication of overall eutectic graphite precipitation during eutectic freezing after TEh. The other parameter is (G_2), which is the angle of the first derivative of the cooling curve at the end of freezing.
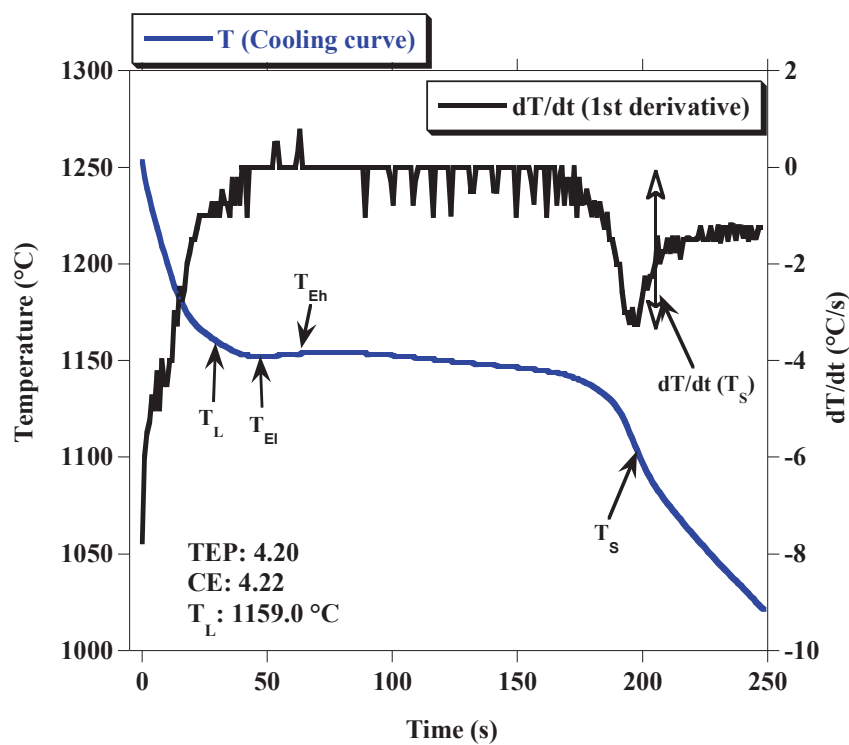
Figure 5.4: Cooling curve and its first derivative curve, with arrest points labelled for the curve (c).

The cooling curve and its time derivative are presented in Fig. 5.4. The derivative (dT/dt) of the cooling curve provides information about the cooling rate of the samples. It can be observed that at the beginning of solidification the derivative values increases, and then it decreases at the end of solidification. The obtained thermal characteristics and thermal parameters of the

melt during its solidification for all cooling curves are listed in Table 5.3. Graphite factor 1 (G_1) indicates the amount of eutectic graphite precipitation occurs between T_{Eh} and T_S. A high value of (G_1) shows high graphite precipitation during solidification which further improves casting quality by reducing the micro shrinkage defects in the casting. Thus high value of (G_1) reflects the high shrinkage resistant of the casting. The thermal parameter, Graphite factor 2 (G_2) is inversely proportional to the thermal conductivity of the obtained material and thus reflects graphite shape. The low values of (G_2) indicate higher precipitation of graphite at the end of the freezing. The thermal parameter, recalescence (R) reflects the increase in temperature during eutectic reaction. The rise in temperature depends on the precipitation of austenite and graphite during the first part of eutectic freezing. Therefore, it indirectly represents the amount of graphite that precipitates during eutectic reaction and the time span for the reaction. High values of recalescence (R) show high volume expansion of the casting which leads to the high probability for microshrinkage and porosity defects in the casting. Table 3.3 provides the ATAS parameters range and their functions for the optimization of ductile iron casting.

Parameters	Curve (a)	Curve (b)	Curve (c)	Curve (d)
T_{El}	1151.0 °C	1155.0 °C	1152.0 °C	1153.0 °C
T_{Eh}	1149.5 °C	1156.0 °C	1154.0 °C	1154.0 °C
R	0	1.0	2.0	1.0
G_1	98	94	99	101
G_2	34	51	40	46
T_S	1107.2 °C	1099.9 °C	1106.3 °C	1103.6 °C
T_L	1153.0 °C	1155.0 °C	1159.0 °C	1158.8 °C
Alloy nature	Hypo eutectic	Eutectic	Hyper eutectic	Hyper eutectic
TEP	4.21	4.17	4.20	4.19
CE	4.19	4.17	4.22	4.20

Table 5.3: Thermal parameters for different curves obtained from the thermal analysis of ductile iron.

5.4.2 Casting simulation

Figure 5.5 shows the temperature profile of the melt at different stages of mould filling. At first, the melt is poured in pouring basin from a ladle and then the melt passes through a sprue at the top of the mould. The melt flows then through a runner system and enters into the mould cavity through the gate 2 of the casting at 0.5 s with an average temperature of 1244 ℃. The melt then starts filling the casting through the gate 1 at 0.7 s with an average temperature of 1260 ℃. The melt then reaches the middle section of the casting at 2.4 s with an average temperature of about 1222 ℃. At 4.0 s the molten metal reaches the top of casting with an

Figure 5.5: The temperature profile of the melt at different stages of mould filling: (a) 0.5 s, (b) 0.7 s, (c) 2.4 s, and (d) 4.9 s.

average temperature of about 1179 ℃. The simulated filling time is about 4.9 s, that is close to the experimentally measured one, 5.1 s. The numerical simulation has been carried out at a filling rate of 0.666 kg/s.

For a given, alloy melt, the velocity profile usually determines the filling behavior of the mould under the gravitational field. Figure 5.6 shows the velocity profile of the melt at different stages of mould filling. The melt was poured in pouring basin at the filling rate of 0.666 kg/s, which gives melt the velocity of 1.46 m/s at the top cross-section of sprue at 0.06 s. The melt falls through the sprue to reach the lowest level of casting with a velocity of 2.04 m/s at 0.3 s. The melt then flowed through a runner system and enters to the mould cavity through the gate 2 of the casting at 0.5 s with a velocity of 0.42 m/s. The melt then started filling the casting through the gate 1 at 0.7 s with a velocity of 0.31 m/s.

Liquid phase analysis shows the presence of 92.9 % liquid phase by volume at 100 % filling. Figure 5.7 shows the solidification time profile of the casting at different solidification stages. The melt solidification was started at the top of sprue and riser at 7.4 s with the solidification

Figure 5.6: The velocity profile of the melt at different stages of mould filling: (a) 0.06 s, (b) 0.3 s, (c) 0.5 s, and (d) 0.7 s.

time of 2.06 s. The gates are completely solidified at 9.6 s with the solidification time of 3.67 s and 3.09 s for gate 1 and gate 2 respectively. The solidification patterns show a progressive solidification behavior starts from outer sides of the casting and move towards the casting centre. At 18.9 s the only liquid fraction present is within the riser and in the pouring basin. The whole casting was finally solidified at 29.7 s. The simulation results show the presence of the last solidification zone (Fig. 5.7c) in the riser, which prevent cavities due to shrinkage in the casting.

Property	Top		Middle		Bottom	
	Centre	Outer	Centre	Outer	Centre	Outer
Nodule counts	1304±83	1704±23	1368±72	1764±51	1440±72	1896±83
Nodule size (μm)	11±2	7±1	11±2	7±1	9±1	6±1

Table 5.4: Variation in graphite nodule counts and graphite nodule size at different sections and zones.
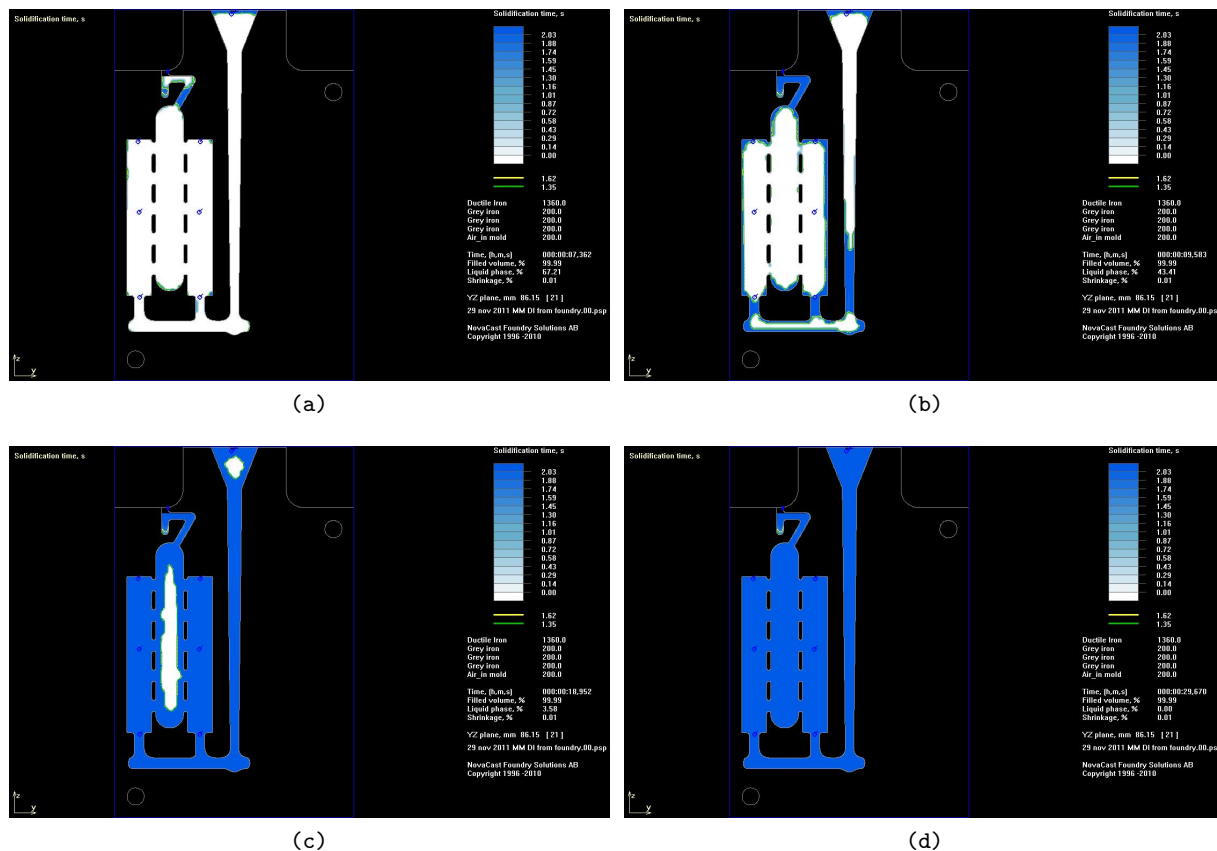
Figure 5.7: The solidification time profile of the melt at different stages of melt solidification: (a) 7.4 s, (b) 9.6 s, (c) 18.9 s and (d) 29.7 s.

5.4.3 Microstructure observation at different sections

The microstructure of the produced ADI samples is observed at different positions with respect to the metal/mould interface. As stated previously, two distinct zones (centre and outer zones) were observed in the un-etched micrograph based on average graphite nodule counts and average graphite nodule size (Fig 4.2). Figure 5.8 show the un-etched micrographs of the different zones at different sections (bottom, middle and top). The average graphite nodule counts and average graphite nodule size for different zones and different sections are summarized in Table 5.4. It can be observed that the centre zone has lower average graphite nodule density as compared to the outer zone whereas the average graphite nodule size is higher at centre zone as compared to the outer zone of the matrix.

Figure 5.9 shows the hardness variations of the ADI samples at different sections (bottom, middle and top) of the casting for centre and outer zones. It can be observed that the hardness values at the outer zones are higher as compared to the centre zones for all sections.

(a) Top section; Centre zone   (b) Top section; Outer zone

(c) Middle section; Centre zone   (d) Middle section; Outer zone

(e) Bottom section; Centre zone   (f) Bottom section; Outer zone
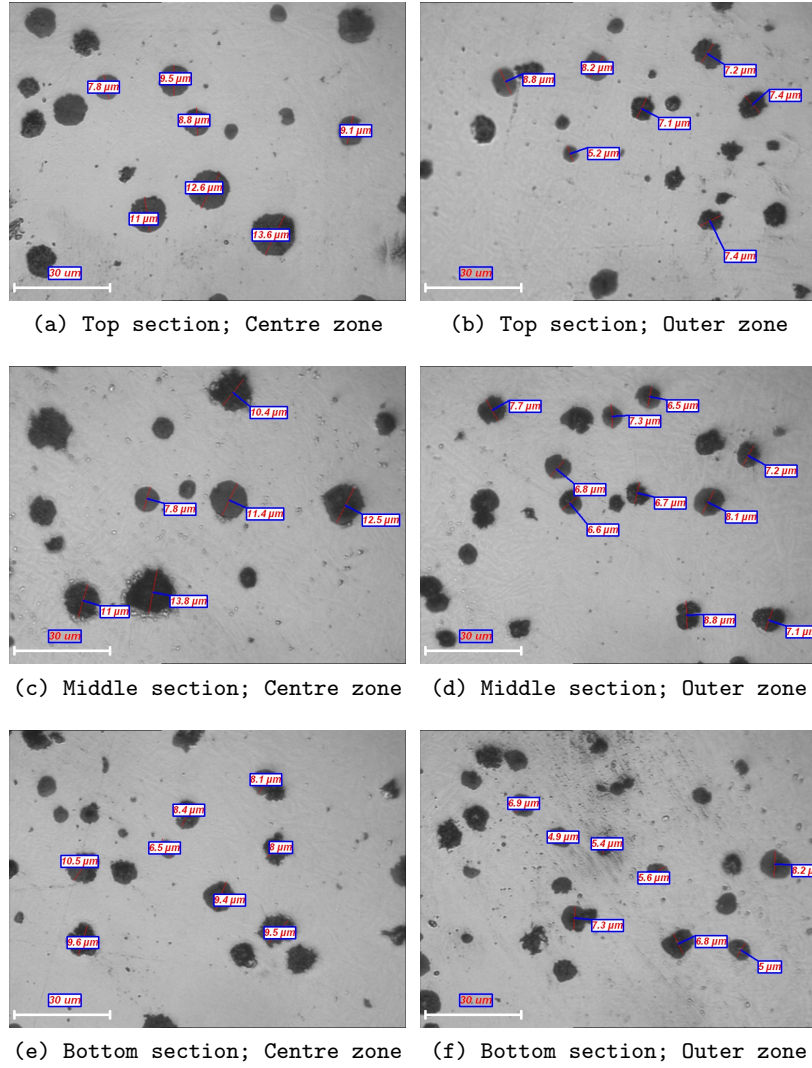
Figure 5.8: Unetched optical micrograph of the novel ADI sample at different sections (top, middle and bottom) and at different zones (centre and outer zones).

5.5 Discussion

The carbon is dissolved in the melt above liquidus temperature. In case of hypo eutectic alloys, the carbon first dissolves in the initially precipitated austenite during solidification. The remaining carbon is then ideally precipitated as graphite at the eutectic temperature. For hypereutectic alloys, graphite is precipitated instead of austenite when liquidus is reached. The variation in the nature of alloy is based on the variation of carbon equivalent (CE) with respect to the true eutectic point (TEP) of the alloy. True eutectic point is defined as the point where the horizontal eutectic line crosses the liquidus line. The liquidus line is mainly dependent on the chemical composition of the alloy whereas, the horizontal eutectic line is a function not only
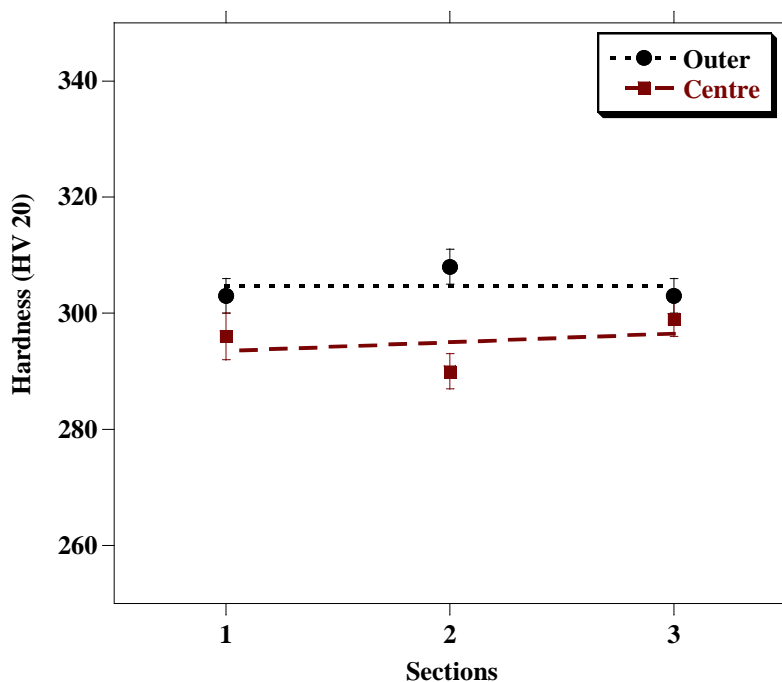
Figure 5.9: Variation in the micro-hardness at centre and outer zones for different sections (1: Bottom section, 2: Middle section and 3: Top section).

of the chemical composition but also of nucleation and cooling rate.

According to Campbell [117], the mould filling simulation helps us to predict how running and gating design affects surface turbulence in the mould which may trap oxidation products and cause potential defects. There is a critical velocity below which a liquid metal should enter the mould cavity to minimize the surface turbulence during mould filling [117, 118]. In addition, there is a risk that the surface of the liquid metal may be folded over by surface turbulence if the liquid velocity exceeds the critical velocity. The liquid velocity above its critical velocity, give rise to sessile drop in the melt, which is no longer supported by its surface tension. It will therefore, fall back under gravity and may thus entrain its own surface in an enfolding action and give rise to the risk of entrainment leading to defect creation. The critical velocity for iron alloys is 0.45 m/s [118]. From the simulation results, it was found that at gate 1 the melt velocity is around 0.31 m/s and at gate 2 the melt velocity is around 0.42 m/s, both of which are under critical velocity.

The solidification time of any casting is controlled by a parameter known as the modulus, m (cm). The modulus for a given casting is defined as the ratio of a solid volume to its surface area; for a section, it is defined as the ratio of section area to its perimeter [118–120]. In addition, Campbell [118] also illustrated that for a given mould material the modulus of a casting is directly proportional to the fluidity of the melt. Higher modulus values show higher
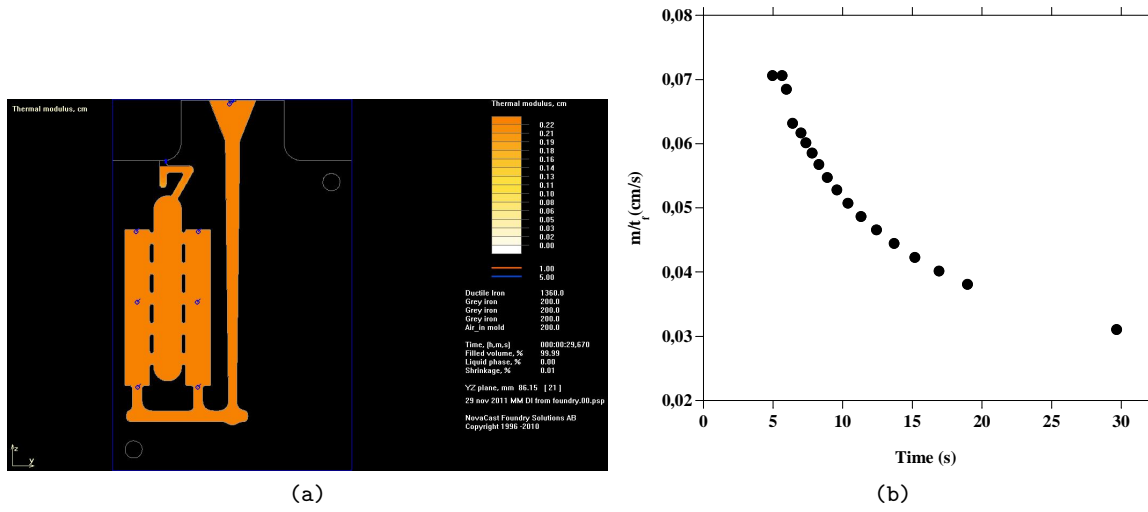
Figure 5.10: (a) Modulus values of casting at 29.7 s and (b) Variations of m/t_f (proportional to (Heat transfer coefficient (h)/Proportionality constant (k)) with time during solidification process (m: modulus (cm); t_f: solidification time (s)).
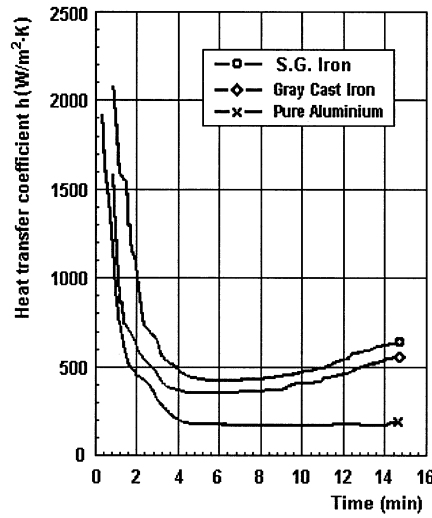
Figure 5.11: Evolution of the interfacial heat transfer coefficient for different types of alloys [100].

fluidity of melt for a given mould material and improve filling. The modulus values for the given casting are in the range of 0.19-0.22 cm at the end of solidification as shown in Fig. 5.10a. Campbell [118] described the relation between solidification time and modulus of the casting, in case where interfacial heat transfer dominates heat flow, by (Equation 5.1):

$$t_f = k * \frac{m}{h} \tag{5.1}$$

Where, t_f (s) is the maximum solidification time of the casting at the particular instant, k is

(a)

(b)

(c)
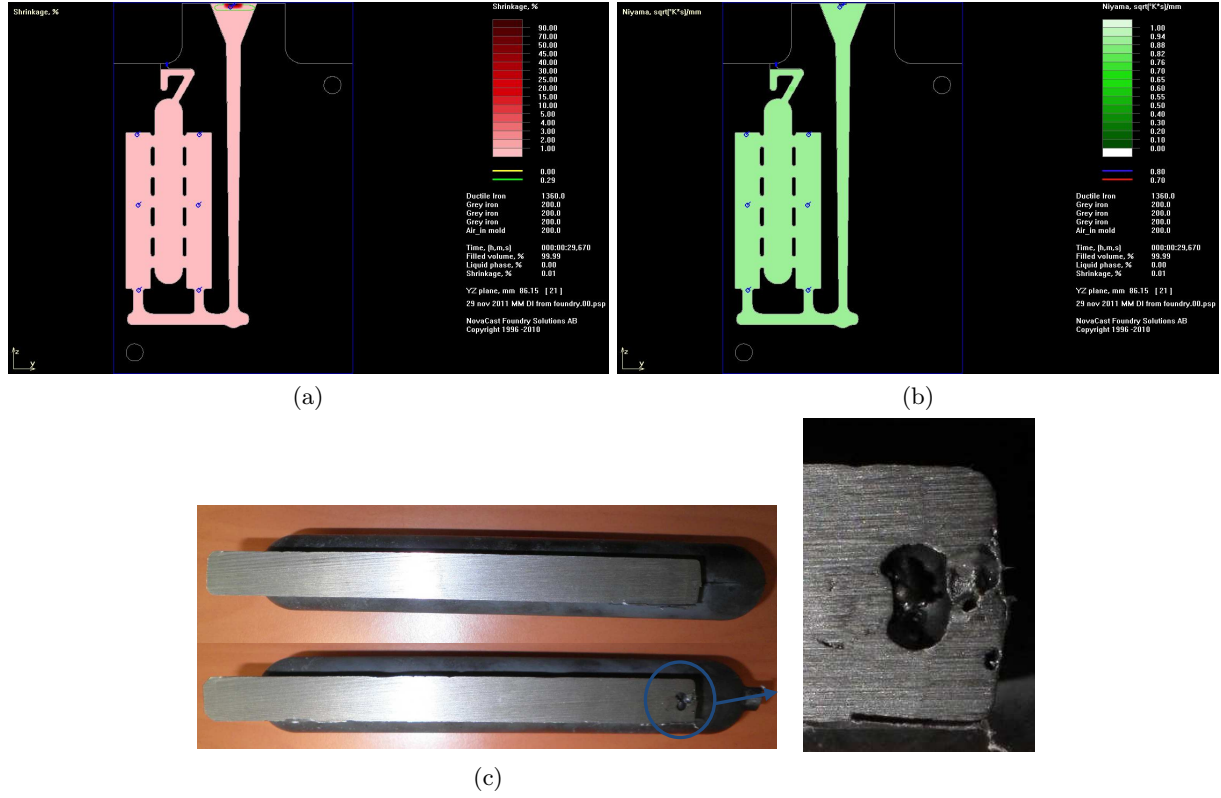
Figure 5.12: (a) The shrinkage % at 29.670 s, (b) The Niyama criterion at 29.670 s and (c) Porosity defects at the top section of the casting.

proportionality constant, m (cm) is the maximum modulus of casting at the particular instant and h ($Wm^{-2}K^{-1}$) is the coefficient of heat transfer.

Figure 5.10b shows the variation of m/t_f with respect to time during the solidification. It can be observed that the ratio m/t_f decreases with time during the solidification. It means that heat transfer coefficient decreases with time during the solidification as the ratio m/t_f is directly proportional to the heat transfer coefficient. The decrease in the interfacial heat transfer coefficient with solidification time can be explained due to the formation of the air gap at the melt/mould interface, which acts as a thermal resistance to heat flow during the solidification.

The similar behavior in the heat transfer coefficient has been reported in the literature [100, 101, 121]. Lau et al. [100] noted that the interfacial heat transfer coefficients (h) between the metallic mold and spheroidal graphite (SG) iron (Fig. 5.11) drops rapidly as a result of air gap formation at the initial stage of solidification, but then h values reach a steady state for a short period of time. They found that with the progress of the solidification, the heat transfer coefficient increases slightly due to the expansion of the ductile iron which reduces the

(a) Bottom section

(b) Middle section

(c) Top section
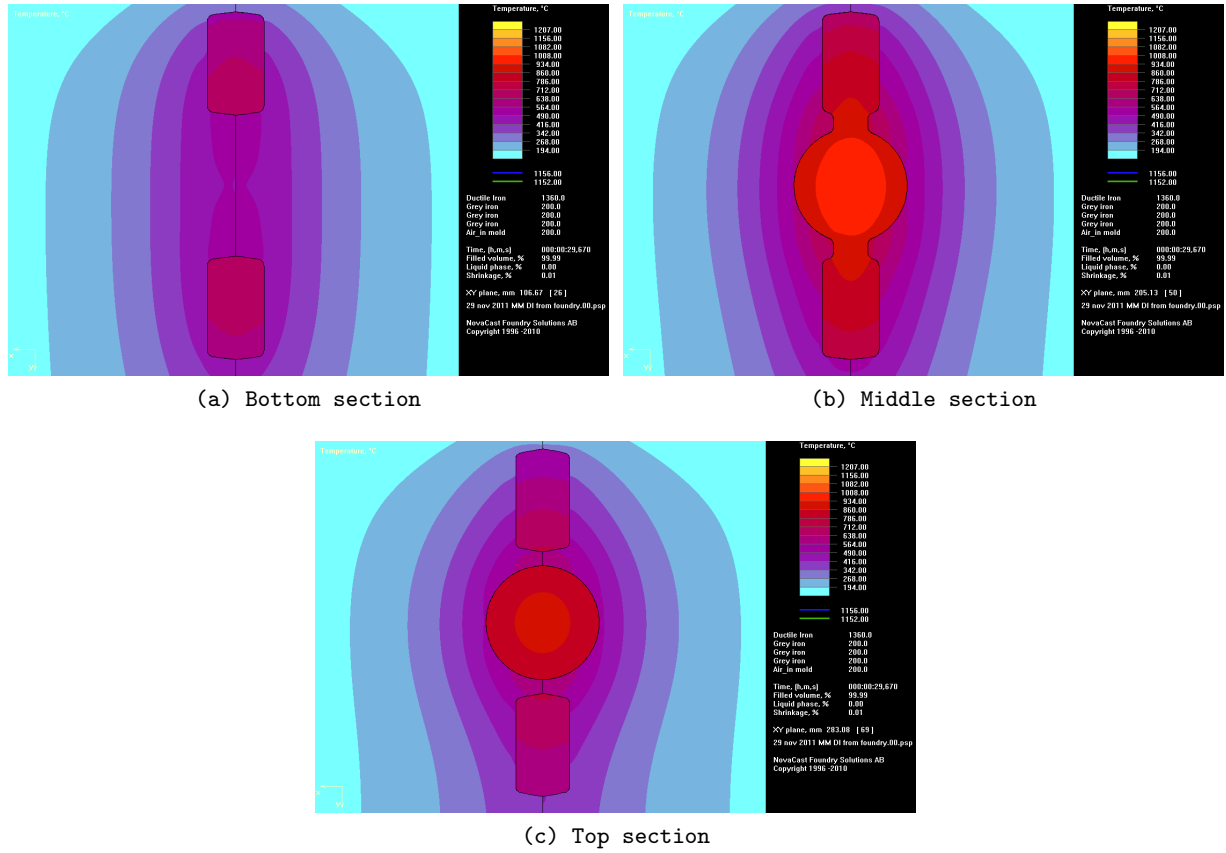
Figure 5.13: The variation in temperature at different sections.

air gap size at the melt/mould interface. According to Ho et al. [121], interfacial heat transfer conductance is subjected to a variation caused by the change of interfacial gap width with time. Santos et al. [101] illustrated that the interfacial heat transfer coefficient shows a high value at the initial stage of solidification. However, as solidification progresses, air gap forms due to the expansion of the mould. Once the air gap forms, the heat transfer across the interface decreases rapidly and a relatively constant value of the heat transfer coefficient is attained. They also stated that the mode of heat transfer across the melt/mould interface has been suggested to be due to both conduction through isolated melt/mould contacts and through gases present in the gap and radiation between the surfaces.

The influence of solidification time and thermal modulus (both of which are depended on mould geometry and casting cooling rate) on the casting defects can be better understood by knowing the variation of the local thermal parameters known as "Niyama criterion".

Niyama criterion [122] is a local thermal parameter defined as:

$$N_y = \frac{G}{\sqrt{\dot{T}}} \tag{5.2}$$

Where G is the temperature gradient in K/mm at the solidus temperature and $\sqrt{\dot{T}}$ is the cooling rate in K/s. Carlson et al. [123], suggests a critical value of 0.775 $K^{1/2}s^{1/2}mm^{-1}$ below which shrinkage defects occur according to Niyama criterion for iron and steel alloys. Niyama criterion was evaluated at the end of solidification. Physically, the criterion was justified by Darcy's law, which relates the inter-dendritic feeding flow velocity to the pressure drop across the mushy zone. It shows the difficulty of providing liquid feeding in the later stages of solidification when inter-dendritic liquid channels are almost closed [124]. It takes into account the effect of casting shape and size, but also can evaluate the loss of flowing pressure more accurately. According to Niyama criterion, the shrinkage porosity increases with an increase in cooling rate, because the feeding flow velocities and the resulting pressure drop across the mushy zone are higher for higher solidification rates [122]. Therefore, the chances of obtaining shrinkage defects at the thin section of casting are more pronounced. The simulation result show 0.9 $K^{1/2}s^{1/2}mm^{-1}$ Niyama criterion values at different locations of the casting at 29.7 s which is higher than the critical value. The simulation results (Fig. 5.12a) show no shrinkage defects at the end of solidification, which show good correlation with the Niyama criterion values along the center-line of the casting at 29.7 s (Fig. 5.12b). However, the experimental results show porosity defects at the top section of the casting (Fig. 5.12c), which can be explained due to entrainment defects caused by the folding action of the (oxidized) liquid surface during filling [117, 118]. These types of defects are common in gravity poured casting. Figure 5.13 shows the temperature field at different positions (bottom, middle and top) for the casting at 22.0 s. It can be seen that the temperature drop at outer zone is faster as compared to the centre zone of the casting which gives rise to the different nodule counts and hardness values at outer and centre zones of casting.

5.6 Conclusions

The simulation analysis of mould filling and solidification of ADI casting in a permanent mould by virtue of its thermal characteristics was investigated in the present chapter. Thermal analysis of the melt was performed using the commercial adaptive thermal analysis system (ATAS). Thermal analysis of the melt showed four different temperature arrests during solidification. It revealed the variation in the eutectic nature of alloy for different solidification curves due to the variations in true eutectic point and carbon equivalent of the melt. The numerical simulation results show filling time of 4.9 s at a filling velocity of 0.666 kg/s. The simulation

results showed the average melt velocities at gate 1 and gate 2 of the casting as 0.31 m/s and 0.42 m/s respectively, which are well below the critical velocity of 0.45 m/s for cast iron to avoid the surface turbulence during the mould filling. The solidification patterns show a progressive solidification behavior starts from all outer sides of the casting and move towards the casting centre. The whole casting was solidified at 29.7 s. The ratio of thermal modulus and solidification time is directly proportional to heat transfer coefficient and decreases with time during the solidification. This behavior can be explained by the formation of thin air film at the melt/mould interface, which decreases the heat transfer from the melt to the surrounding. The simulation analysis revealed the absence of porosity and shrinkage defects at the end of solidification. However, experimental results show porosity defects at the top section of the casting, which are considered as common defects in the gravity die casting process and can be explained due to entrainment defects caused by the folding action of the (oxidized) liquid surface during filling. Thus thermal analysis and simulation tools helps in improving the overall casting process during ADI production by providing the realistic thermal description of the melt and by predicting the porosity and shrinkage defects.

The introduction of novel process route and foundry simulation tool build up a system to set-up the optimal process parameters for ADI production. This system can be used as a iteration tool to optimize the ADI casting in correlation with its microstructural and machining characteristics. Therefore, there is a need to understand machining characteristics of the novel ADI. The machining characteristics of ADI within the framework of green manufacturing in introduced in the next chapter.

Chapter 6

Ecological machining of ADI: Dry and near dry machining

This chapter presents the results obtained from the dry drilling machining process of the novel ADI material. The main objective of this chapter is to evaluate the machinability of ADI materials under various cutting conditions by investigating the specific cutting forces, surface roughness of the machined surface and tool wear behavior. In the later section, influences of austempering parameters on the machinability of ADI are addressed and discussed with respect to the cutting forces and tool wear mechanism. The chip morphology characteristics were then introduced to evaluate the ADI machiniability during dry drilling. To improve the ADI machinability in relation with ecological machining, the near dry machining process was also introduced. Finally, dry drilling of ADI was investigated using different PVD-coated tools.

6.1 Characterization of ADI machining: Dry drilling

This section shows the influence of cutting parameters on the machinability of produced ADI during dry drilling in terms of cutting forces, surface roughness and tool wear behavior. The dry drilling experiments were carried out using the Deckel Maho five axis machining center (DMU 80 P). The drilling tests were performed at three different cutting speeds (30, 60, and 90 m/min) and three different feed rates (0.05, 0.10, and 0.15 mm/rev). The machining tests were conducted using the PVD TiAlN-coated tungsten carbide tools of diameter 8 mm. The tool was produced by Sandvik Coromant with tool reference R840-0800-30-A0A 1220 (helix angle:30, point angle:140). The chemical composition and mechanical properties of the the work piece are summarized in Table 6.1 and 6.2 respectively.

Element	Percentage (%)
Carbon (C)	3.65-3.75
Silicon (Si)	2.60-2.70
Manganese (Mn)	0.23-0.25
Molybdenum (Mo)	0.19-0.21
Copper (Cu)	0.75-0.80
Nickel (Ni)	0.55-0.63
Sulphur (S)	0.017-0.022
Magnesium (Mg)	0.030-0.038

Table 6.1: Chemical composition of the workpiece material (ADI).

Property	Range
Ultimate tensile strength (MPa)	890-1000
0.2 % yield strength (MPa)	573-696
Elongation (%)	7.2-10.4

Table 6.2: Tensile properties of the workpiece material (Austempering temperature: 350℃; Austempering time: 90 min).

6.1.1 Specific Cutting force and specific cutting energy

In machining, for a given chip section any variation of cutting force with cutting speed can be attributed to variation in the specific cutting force. The specific cutting force K_c (MPa) [125, 126] is calculated by the following equation (Equation 6.1).

$$K_c = \frac{8 \times M_z \times 1000}{f \times d^2} \tag{6.1}$$

where M_z is the cutting torque in N-m, f is the feed in mm/rev, and d is the diameter of the drill in mm.

Variation of specific cutting force (K_c) during dry drilling of ADI for different feed rates as a function of cutting speed is shown in Fig. 6.1. It can be observed that at higher feed rate (0.15 mm/rev), the specific cutting force shows steady behavior with cutting speed. However, at lower feed rate (0.05 mm/rev), the specific cutting force first decrease with an increase in cutting speed from 30 to 60 m/min and then it attains its maximum value at a cutting speed of 90 m/min. On the other hand, at a feed rate of 0.10 mm/rev, the specific cutting force increases with an increase in cutting speed from 30 to 60 m/min and then it show constant behavior at higher cutting speed. It is also noteworthy that the combined effect of cutting speed at its
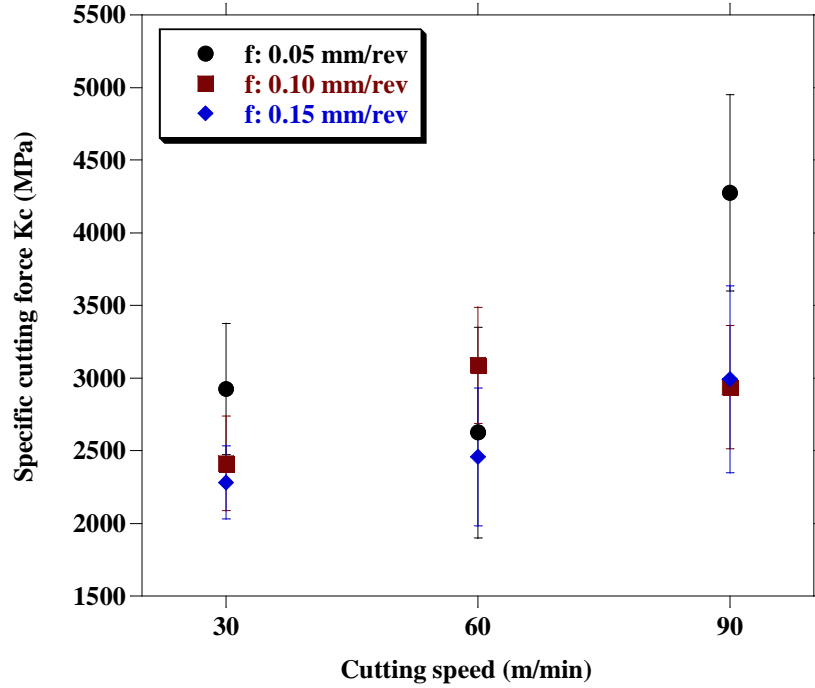
Figure 6.1: Influence of cutting conditions on the average specific cutting force.

higher value (90 m/min) and feed rate at its lower value (0.05 mm/rev) give significant rise in the specific cutting force value.

The specific cutting force signifies the cutting force per unit area of chip removed. The change in the evolution of specific cutting force with cutting parameters is dependent on the tool-workpiece material properties. Together with this, the specific cutting force is largely influenced by the cutting temperature [125–127]. Therefore, it can be concluded that the combination of high cutting speed and low feed rates give rise to high temperature at cutting zone, which can be detrimental to the tool life and resulting in the higher values of specific cutting force.

Figure 6.2 shows the variation of specific cutting energy (u) with respect to feed rate for different cutting conditions. The specific cutting energy, u (J/mm^3) was calculated by (Equation 6.2):

$$u = \frac{M_z \times \omega}{MRR} \tag{6.2}$$

where M_z is cutting torque in N-m, ω is rotation speed in rad/s, and MRR is material removal rate in mm^3/s.

The specific cutting energy is defined as the amount of energy required to remove a unit
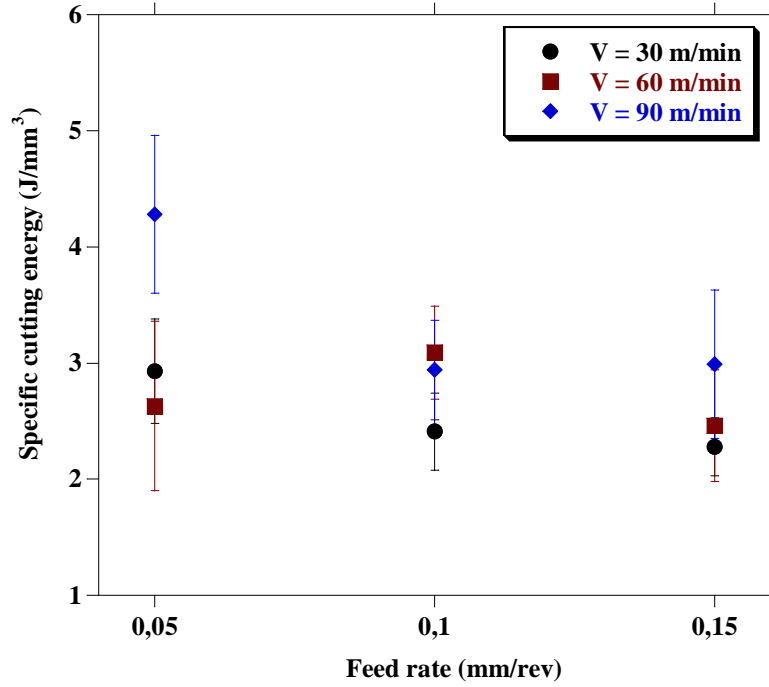
Figure 6.2: Influence of cutting conditions on the specific cutting energy (u).

volume of workpiece material during the machining process. It can be used as a parameter to quantitatively measure the machinability of material under the particular machining conditions [128]. The specific cutting energy is a function of inherent properties of work material, cutting conditions, and tool material and geometry. It can be observed that (Fig. 6.2), at higher cutting speed (90 m/min), specific cutting energy decreases with an increase in feed rate from 0.05 to 0.10 mm/rev. On further increasing the feed rate, it shows constant behavior. On the other hand, for lower cutting speeds (30 m/min and 60 m/min), the specific cutting energy shows constant behavior with an increase in feed rate. This behavior can be understood from the well known phenomenon known as size effect, which states that there is a substantial increase in the specific energy with a decrease in chip size. The increase in specific cutting energy at a small feed rate has been explained by specific mechanisms such as material strengthening due to lack of defects, strain rate hardening, and lack of thermal softening [129]. This behavior is in good correlation with the variation in specific cutting pressure with different cutting conditions.

6.1.2 Surface roughness

Figure 6.3 shows the variation of average surface roughness values (Ra) as a function of cutting speed for different feed rates. Analyzing the obtained roughness values, one can observe that the
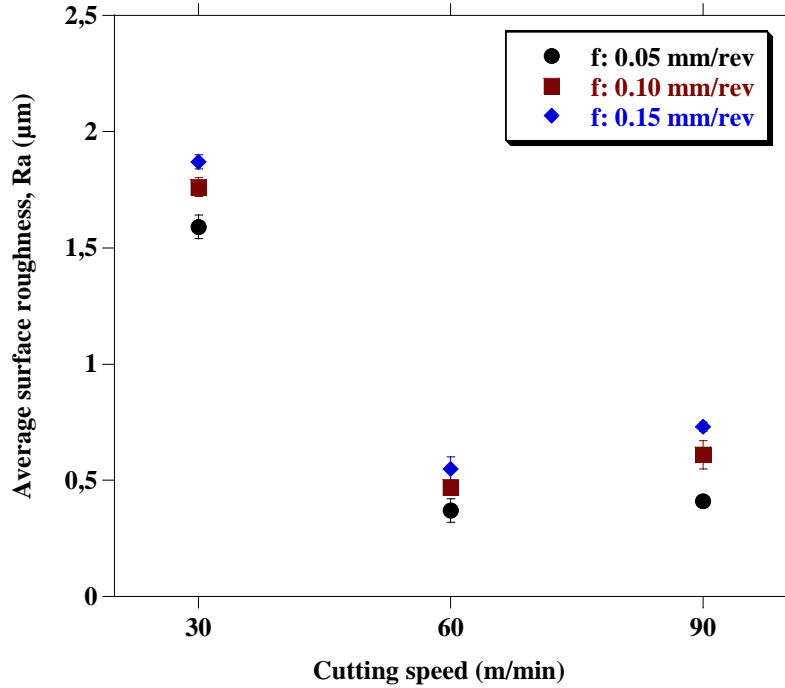
Figure 6.3: Influence of different cutting conditions on the average surface roughness values.

Ra values are within the range of 0.29 and 1.87 μm. The obtained results show clear tendency towards the reduction in Ra values as the cutting speed increases in the range of 30-60 m/min. However, on further increasing the cutting speed to 90 m/min, Ra values show no significant difference. It can be observed that the Ra values show gradual decreasing behavior with an increase in feed rate. The increase in surface roughness values with an increase in feed rate can be explained due to an increase in the chip section size. The improvement in the surface quality with an increase in the cutting speed from 30 to 60 m/min can be explained due to the influence of thermal softening, which gives rise to easy plastic deformation of the workpiece material and improves the surface quality. From the obtained results, it can be observed that influence of cutting speed is higher than feed rate on the Ra values. Therefore, to optimize the surface roughness values during dry drilling of ADI, there is a need of proper combination of cutting parameters.

6.1.3   Tool wear analysis

Figures 6.4 presents the SEM micrographs of the failure mode of the drill tools for different cutting parameters. It can be seen that at lower cutting speed (30 m/min) abrasion of the coating was observed near the cutting edge irrespective of the feed rates. However, at higher cutting speeds (60 and 90 m/min), crater wear close to the outer corner of the drill tool was
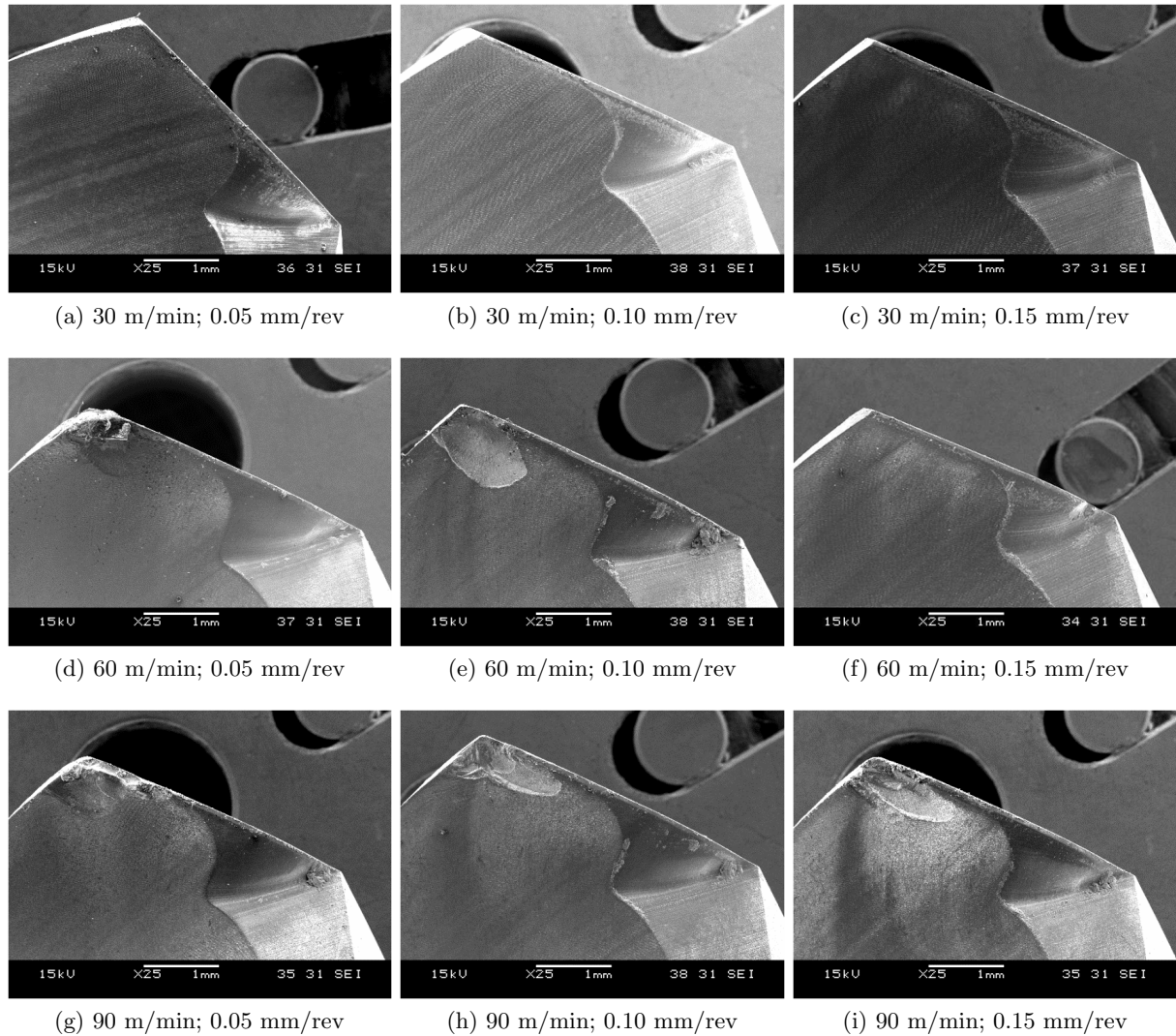
Figure 6.4: SEM micrographs of the failure mode of the PVD-coated carbide tools for different cutting parameters.

observed. The deep crater wear located near to the cutting edge is the characteristic tool wear phenomena while machining ADI is already mentioned in literature as a major tool failure [20, 45]. In addition, it was found that the tool performance was reduced significantly at higher cutting speed. On increasing the cutting speed from 60 to 90 m/min at a lower feed rate (0.05 mm/rev), tool performance was reduced by 60%. On the other hand, at higher feed rates (0.10 and 0.15 mm/rev) tool performance was reduced by 40% on increasing the cutting speed from 60 m/min to 90 m/min. The tool performance and its wear resistance is significantly influenced by the substrate and coating properties, which further influenced by workpiece material properties (ausferrite microstructure). At lower cutting speed the ausferrite microstructure tends to show abrasion of the tool material due to the presence of inherent carbide particles. However, on

increasing the cutting speed the specific thermal and mechanical load on the cutting edge increases due to the transformation of metastable austenite to martensite. The formation of deep crater wear at the outer cornet of the drill tool signifies the presence of adhesion and abrasion wear mechanisms at higher cutting parameters. To better understand the tool wear mechanisms in relation with the cutting parameters, SEM micrographs and EDS spectra of the wear surface morphologies are further discussed.
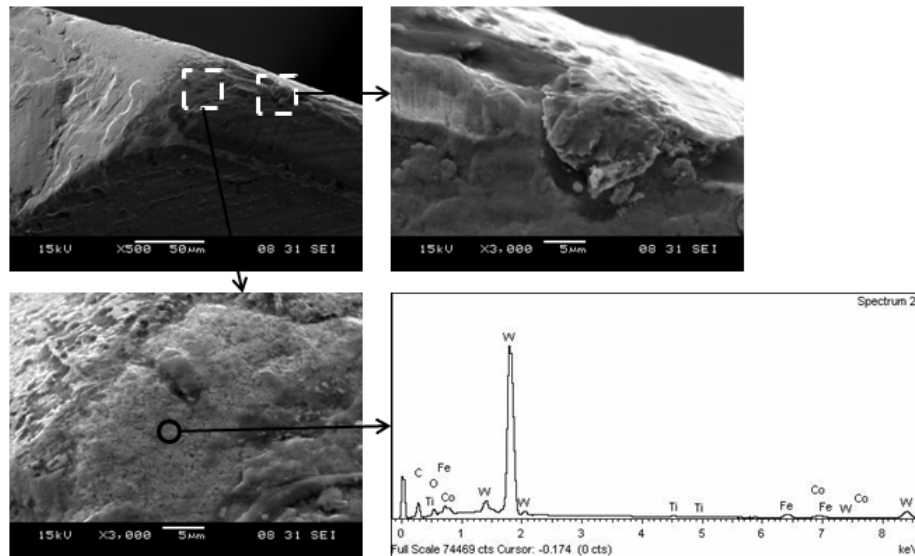
Figure 6.5: SEM micrographs and EDS spectra of the wear surfaces of drill tool (V: 30 m/min and f: 0.05 mm/rev).

Figures 6.5 shows SEM micrographs and EDS spectra of the wear surfaces of the tool used to machined ADI at the combination of low cutting speed (30 m/min) and low feed rate (0.05 mm/rev). Examinations of the wear surfaces revealed the abrasion of the coating material at the outer corner of the drill tool and show the presence of built up edge (BUE) at the cutting edge. The occurrence of small BUE at the cutting edge indicate the adhesion of workpiece material at the cutting edge. The EDS spectra of the grain like structure revealed the presence of tungsten (W) showing exposure of the substrate material due to removal of the coating material. This behaviour suggest that at the combination of low cutting speed and low feed rate the wear mechanism of abrasion was more dominant as compared to adhesion.

Figures 6.6 shows SEM micrographs and EDS spectra of the wear surfaces of the tool used to machined ADI at the combination of higher cutting speed (90 m/min) and low feed rate (0.05 mm/rev). The deep crater wear at the outer corner of the drill tool was observed. In addition, edge chipping was also observed which indicate the removal of large fragments of cutting edge due to the BUE formation. The adhered workpiece material at the cutting edge supports the formation of BUE. This morphology of the wear surfaces obtained at higher cutting speed were
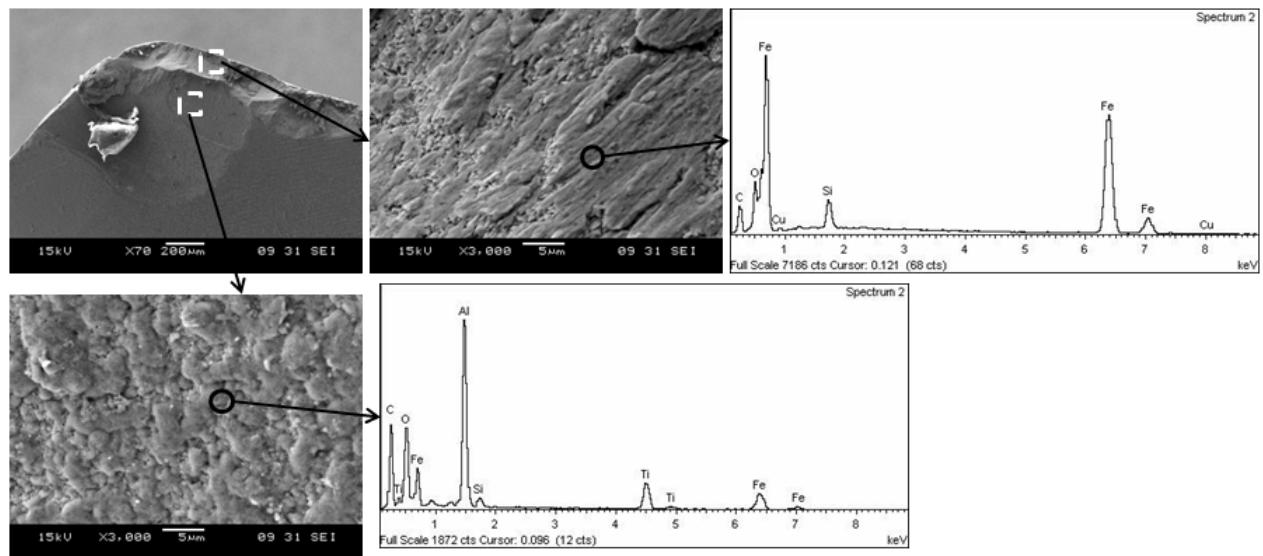
Figure 6.6: SEM micrographs and EDS spectra of the wear surfaces of drill tool (V: 90 m/min and f: 0.05 mm/rev).

different as compared to those obtained at lower cutting speed. The EDS spectra of the crater wear surface in the chipping zone near to the cutting edge revealed the presence of adhered fragments of oxidized workpiece material (Fe, Si and high O content). On the other hand at the bottom of the crater wear the oxidation of the coating material clearly evident due to the presence of aluminium (Al) and titanium (Ti) (with high O content). This behaviour clearly indicate that the combination of low feed rate and high cutting speed leads to an increase in specific thermal and mechanical load on the cutting edge which subsequently favours adhesion wear mechanism resulting in crater wear at the outer corner of the drill tool.

Figures 6.7 shows SEM micrographs and EDS spectra of the wear surfaces of the tool used to machined ADI at the combination of high cutting speed (90 m/min) and high feed rate (0.15 mm/rev). It revealed that at higher material removal rate cracks appears on the wear surfaces which leads to sudden fracture of the drill tool at the outer edge. The SEM micrographs clearly show the presence of smooth fracture zone. The presence of cracks on the tool wear surfaces indicate the high compressive stresses and temperature at the cutting edge which further lead to the plastic deformation of the cutting edge. EDS spectra of the fracture part revealed the presence of oxidized coating material (Al, Ti with high content of O). The fracture part also revealed the exposure of the substrate material and adhesion of the workpiece material near the tool cutting edge (due to the presence of Fe, Si and high content of O).
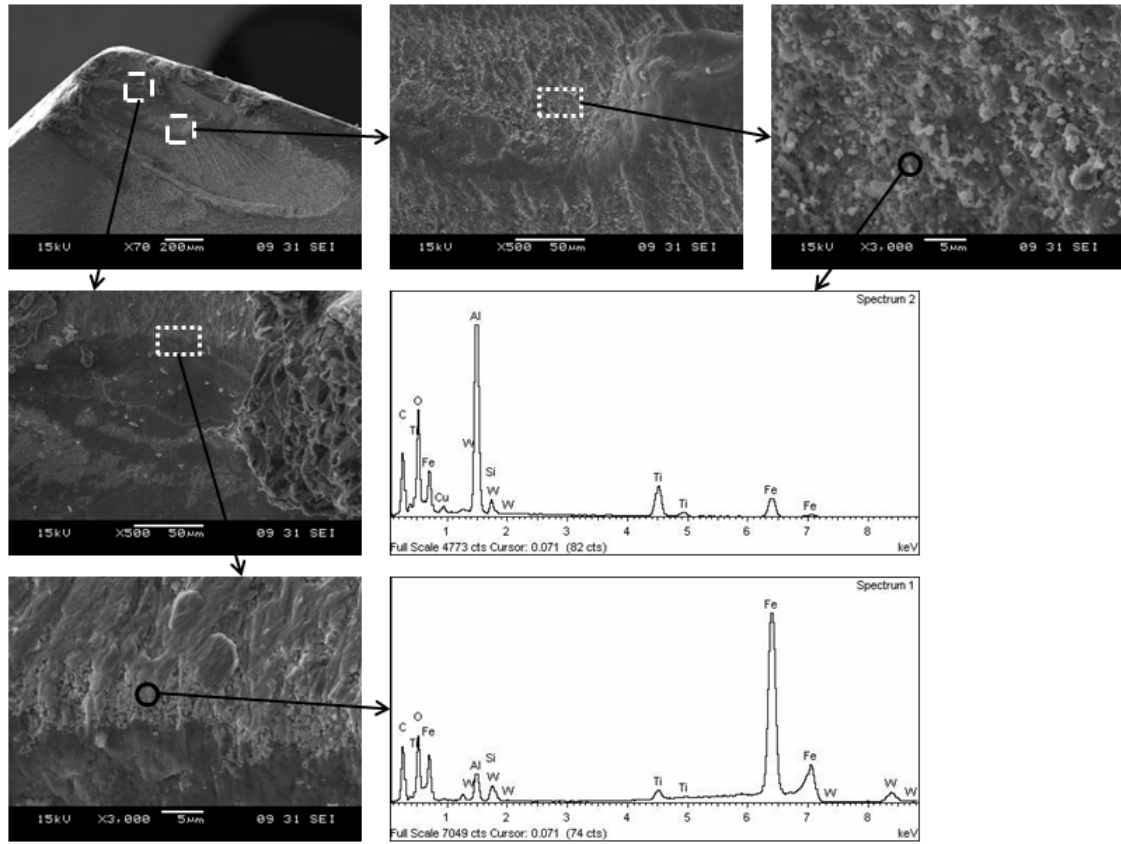
Figure 6.7: SEM micrographs and EDS spectra of the wear surfaces of drill tool (V: 90 m/min and f: 0.15 mm/rev).

6.1.4   Influence of austempering parameters

The influence of the austempering parameters on ADI machinability was investigated by machining (dry drilling) different ADI samples austempered for different temperature (320, 350 and 380℃) and time (60, 90, 120 and 150 min). The machining tests were conducted under the same cutting conditions (cutting speed: 60 m/min and feed rate: 0.15 mm/rev) using the same cutting tool (ref: R840-0800-30-A0A 1220). Figure 6.8 show the evolution of cutting forces for different austempering temperatures as a function of austempering time. The austempering parameters did not show any significant change in the average cutting torque. The average cutting torque attains its maximum value at the austempering time of 120 min and austempering temperature of 320 ℃. However, average thrust force varies significantly with austempering parameters. It can be seen that at higher austempering temperature (380 ℃), average thrust force show gradually increasing behavior with austempering time and attains its maximum values at 150 min. At 350 ℃ the average thrust force increases with an increase in austempering time from 60 to 90 min, after that it shows constant behavior in the austempering time range of 90-120 min and then attains its maximum value at 150 min. On the other hand,
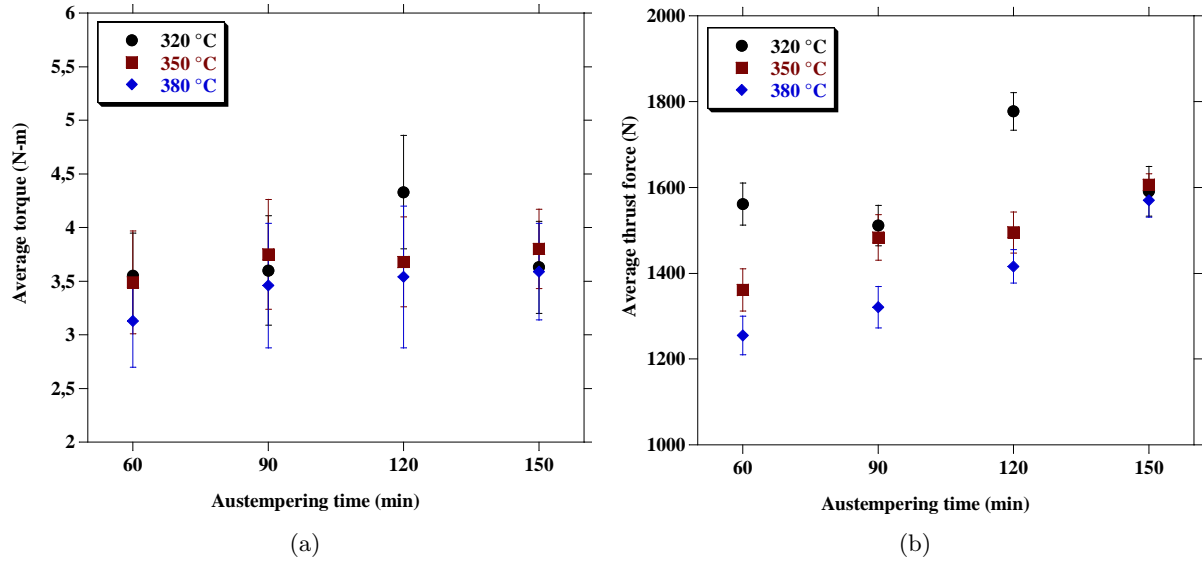
Figure 6.8: Influence of austempering parameters on the (a) Average torque (N-m), and (b) Average thrust force (N) (Cutting speed: 60 m/min; Feed rate: 0.15 mm/rev).
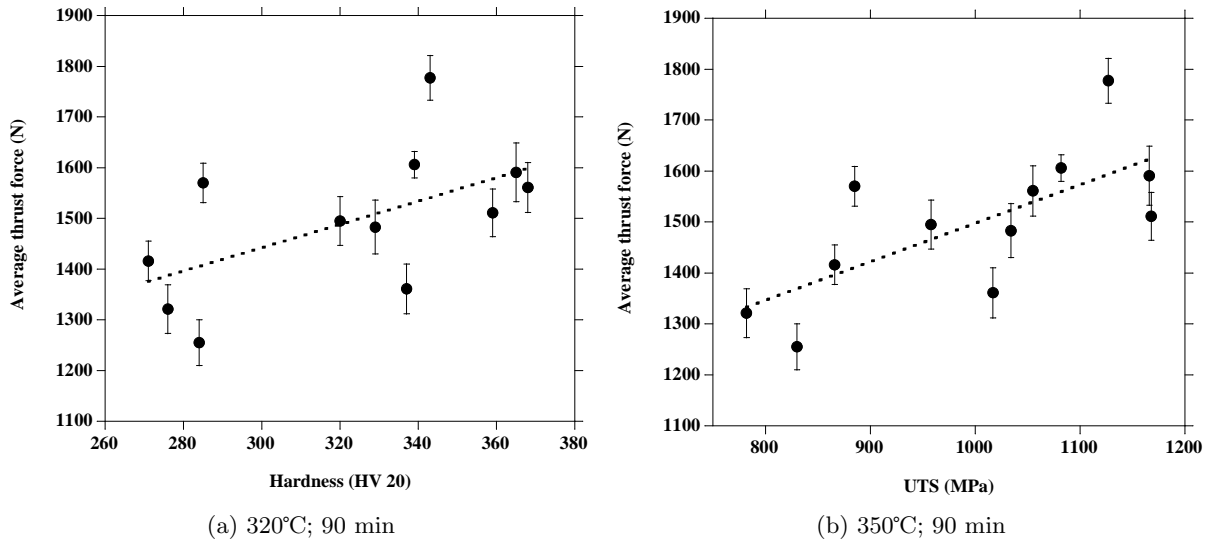
Figure 6.9: The variation of average thrust force as a function of (a) Average hardness values, and (b) Ultimate tensile strength of ADI material produced at different austempering conditions.

at lower austempering temperature (320 ℃), the thrust force shows constant behavior at the low austempering time (60 and 90 min). It attains its maximum value at austempering time of 120 min and then it shows decreasing behavior in the austempering time range of 120-150 min. It was also observed that in the austempering time range of 60-120 min, the thrust values show decreasing behavior with an increase in austempering temperature. However, at the

higher austempering time (150 min), the thrust values for all austempering temperature show constant values.

(a) 380 ℃; 90 min

(b) 350 ℃; 90 min

(c) 320 ℃; 90 min

Figure 6.10: SEM micrographs of the failure mode of the PVD-TiAlN coated tungsten carbide drills at the end of tool life for different austempering temperatures (Cutting speed: 60 m/min; Feed rate: 0.15 mm/rev)

The machinability of a material is controlled by the complex interplay between the inherent properties of the workpiece, cutting tool material, cutting parameters and cutting environment. However, the inherent properties of the ADI material is controlled by the alloying elements and heat treatment parameters, which further tailored the prevailed microstructure and its mechanical properties. With this viewpoint, Fig. 6.9 show the variation of the average thrust force with respect to the hardness and ultimate tensile strength of ADI material. It can be seen that there is a linear relation between thrust force and hardness as well as between the thrust

force and UTS. The high hardness and high UTS values lead to the higher thrust force values. Asthakhov [62] stated that in metal cutting the combined stress at the tool-chip interface that causes the fracture of the layer being removed depends primarily on the mechanical properties of the work material. It was also stated that the mean shear strength at the tool-chip interface increases with an increase in the tensile strength of the material. Moreover, the normal shear stress at the tool-chip interface increases with an increase in hardness value of the material [62]. Therefore, it can be concluded that mechanical properties of workpiece material particularly, hardness and tensile strength have significant influence over the shear stress at the tool-chip contact interface, which can further influence the cutting forces. It was also observed that low cutting force values are obtained at low hardness and tensile strength, which lead to improve machining characteristics of the material.

The tool wear behavior and tool life was also investigated to understand the influence of austempering parameters on machining characteristics of ADI. Figures 6.10 showed the SEM micrographs of the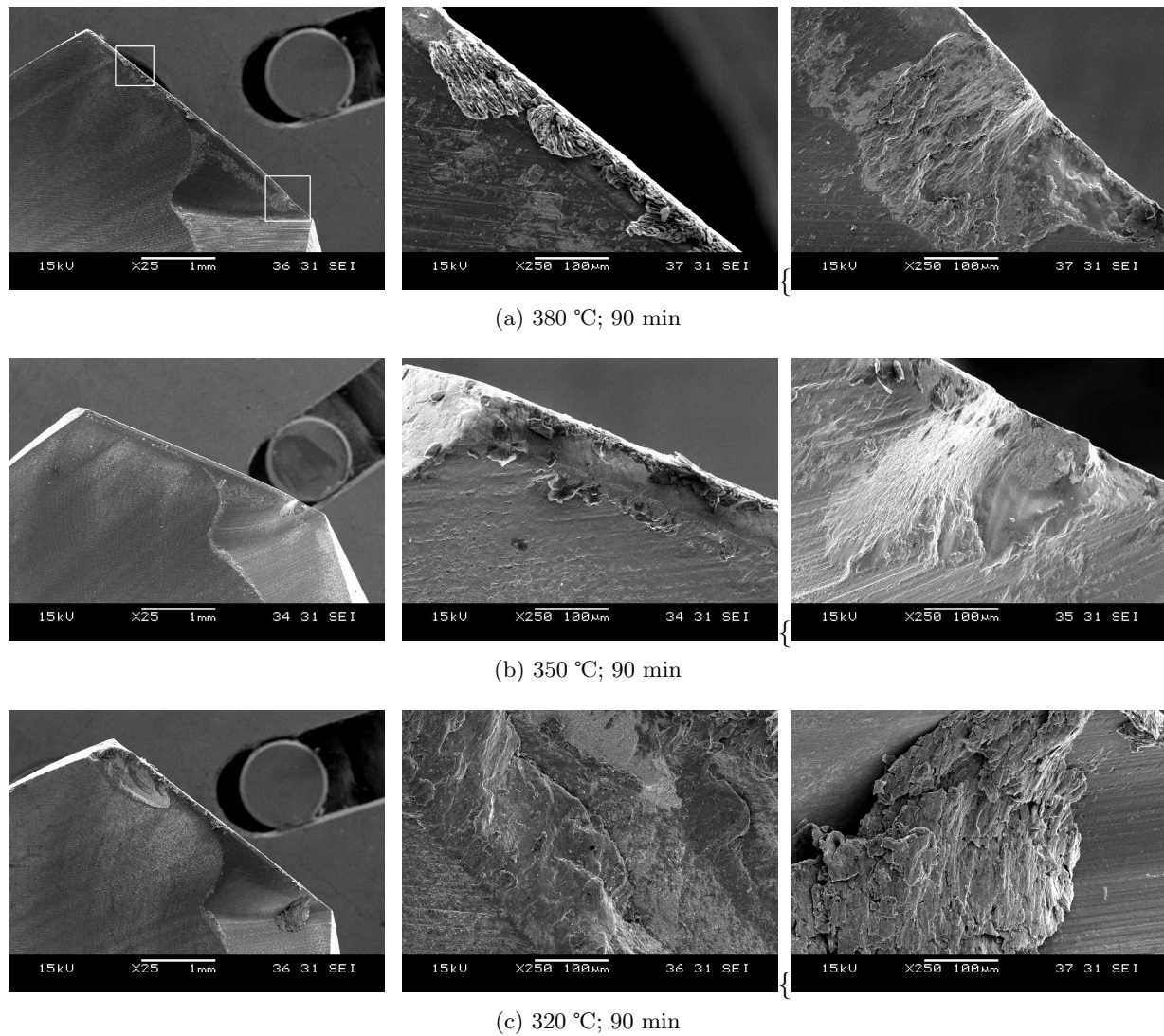 failure mode of the PVD-TiAlN coated carbide drills at the end of tool life for different austempering conditions. It can be seen that at the higher austempering temperature (380 ℃), adhesion of the work material was observed at the cutting edge, and significant abrasion of coating and chipping of the cutting tool was observed near the drill point. At the austempering temperature of 350 ℃ the tool wear behavior is same as that at 380 ℃. However, at lower austempering temperature (320 ℃), deep crater wear was observed at the outer corner of the cutting edge. The micro-cracks were observed in the substrate material. The adhesion of work material was also observed near to the drill point. At a constant austempering time (90 min), the tool life decreases by 70% on decreasing the austempering temperature from 350 to 320 ℃. However, at higher austempering temperature (350 and 380 ℃), tool life shows constant behavior. The poor machinability of ADI at lower austempering temperature (320℃) can be explained due to the increase in the acicular ferrite content. The higher ferrite content leads to the increasing chipping behavior during machining due to its strong tendency to adhere, which favours material smearing on the tool and the formation of built-up edges and built-up edge fragments [45]. It can be concluded that the austempering temperature has higher influence on the machinability of ADI as compared to the austempering time.

6.1.5 Conclusions

The influence of cutting parameters on machinability of ADI was investigated in the present section. The dry drilling experiments were performed at various cutting conditions using PVD coated tungsten carbide tool. The machinability was evaluated using specific cutting forces, surface roughness of the machined surface and the tool wear behavior. It was found that the

combination of the low feed rate and higher cutting speed leads to the higher mechanical and thermal loads on the tool's cutting edge, resulting in higher values of specific cutting force. The cutting speed shows more effective influence on the surface quality of the machined surface than feed rates. The tool wear behavior under various cutting conditions revealed that the crater wear at the outer cutting edge is the main wear mode under the influence of abrasive and adhesive wear. Examinations of the wear surfaces at low material removal rate (30 m/min and 0.05 mm/rev) revealed the abrasion of the coating material at the outer corner of the drill tool and show the presence of built-up edge (BUE) at the cutting edge. The occurrence of small BUE at the cutting edge indicates the adhesion of workpiece material at the cutting edge. However, at higher material removal rate (90 m/min and 0.15 mm/rev), cracks appear on the wear surfaces which lead to sudden fracture of the drill tool at the outer edge. The presence of cracks on the tool wear surfaces indicates the high compressive stresses and temperature at the cutting edge which further lead to the plastic deformation of the cutting edge. EDS spectra of the fracture part revealed the presence of oxidized coating material (Al, Ti with high content of O). The fracture part also revealed the exposure of the substrate material and adhesion of the workpiece material near the tool cutting edge (due to the presence of Fe, Si and high content of O).

The influence of austempering parameters on machinability of ADI was also investigated during the dry drilling process. Austempering temperature shows significant influence on machinability of ADI than austempering time. It was found that ADI material produced at lower austempering temperature shows poor machinability due to the higher ferrite content. The ferrite content leads to increase in chipping behavior and formation of built-up edges due to its higher tendency to adhere during machining.

It revealed that the machinability of ADI relates specifically to its microstructure and relative amount of different phases. These key aspects are controlled and tailored by the specific casting (metallurgical) and heat treatment (austempering parameters) practices. These practices controlled the specific inherent properties of ADI and hence machinability of ADI. The whole process cycle gives a foundation to the development of a new iteration cycle for the development of ADI machinability.

6.2   Chip morphology characteristics

The chip formation in drilling machining is different and more complicated as compared to the orthogonal cutting process. The orthogonal cutting models assume the existence of a primary shear zone, which has the aspect of a thin band where the chip is formed by intense shearing of the work material [130]. Olson et al. [131], explained that in drilling the chip formation process get more complicated due to the radial change in cutting velocity, which increases linearly from the drill centre to the outer edge of the drill. Second, as compared to the shearing in planar shear zone for chip formation in orthogonal models, drilling has two distinct chip formation processes: the first is an extrusion process caused by the wedge point of drill tool and second a shearing operation caused by the cutting edge of the drill tool. Third, the breakage and transportation of chips in flute before ejection, are considered as important factors, which make drilling more complicated cutting process as compared to orthogonal cutting process.

The chip formation process in drilling has been widely studied by many researchers [131–136]. The shear angle during machining, chip thickness, shape and size of the chips formed are greatly influenced by the cutting parameters during drilling [136]. In drilling, well broken chips are more desirable as compared to long chip due to ease in transportation and low torque requirements [133, 135]. Meena and Mansori [91], classified the generated chip forms in wet drilling of ADI according to their morphology (needle shaped, conical, and amorphous) and gave descriptions for each one. Generally, the generated chip forms, their morphology and characteristics are the result of different cutting conditions, which mainly depend on mechanical, thermal and thermo-mechanical characteristics of the work material; the geometry of the cutting tool and the changes in the tribological circumstances at the tool-chip interfaces [137]. The thermo-mechanical characteristics of the work material can influence the chip formation and chip breaking process, through a phenomenon known as the adiabatic shear instability. During the plastic deformation process, strains are initiated near defects thus achieving localized stress concentrations. If the strain rate is high enough, the process is adiabatic and overheating of these areas involve a localized softening, increasing the local strain and so on until an instantaneous shearing [138].

During machining, the primary objective is to separate a certain layer from the rest of the work material with minimum possible plastic deformation and thus energy consumption [62]. In literature [139], the chip compression ratio (CCR) which is determined as the ratio of the chip thickness to the uncut chip thickness, was used as a measure of plastic deformation of work material in metal cutting. Therefore, CCR is determined in the present study to measure the plastic deformation of the ADI in its transformation into the chip during dry drilling. In

the present section, the influence of cutting parameters on chip morphology characteristics, chip compression ratio and its micro-hardness during dry drilling of ADI are presented and discussed.
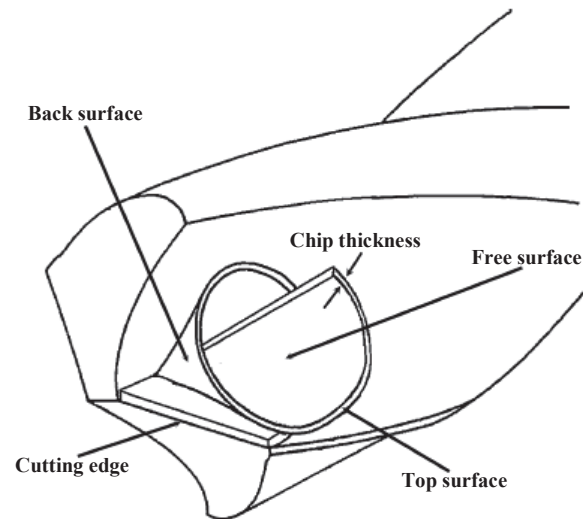
Figure 6.11: Schematic representation of chip formation in drilling [136].

6.2.1 Chip morphology

During machining, the rake angle of the drill decreases from the periphery towards the centre of the drill. Since the cutting speed also drops from the periphery towards the centre, the cutting edge will work inefficiently at the point of drill. At the drill point, tool presses and scrapes the material rather than cuts it, which leads to the plastic deformation of the material where the rake angle is negative and cutting speed is low. Moreover, the variations in cutting speed and rake angle leads to the variations of the chip shape and thickness along the cutting edge during machining. The three-dimensional view of chip formation is shown in Fig.6.11. Three surfaces of the chip, i.e., the free surface, the back surface and the top surface have been defined. The free and back surfaces are formed due to the action of the cutting edge whereas; top surface is generated by the out-most point of the cutting edge. As per the representation, these surfaces are analysed in the following sections.

Figure 6.12 shows the influence of cutting speed and feed rates on the shape and size of the ADI chips. It was noted that well broken cone shaped chips are formed at lower cutting speed (30 m/min) with cone diameter increasing with an increase in feed rate. It was also observed that at lower feed rate (0.05 mm/rev), the increase in cutting speed leads to the formation of continuous chips with the chip color getting blue. At higher cutting speed (90 m/min), with an

<table>
<tr><td>(a) 30 m/min; 0.05 mm/rev</td><td>(b) 60 m/min; 0.05 mm/rev</td><td>(c) 90 m/min; 0.05 mm/rev</td></tr>
<tr><td>(d) 30 m/min; 0.10 mm/rev</td><td>(e) 60 m/min; 0.10 mm/rev</td><td>(f) 90 m/min; 0.10 mm/rev</td></tr>
<tr><td>(g) 30 m/min; 0.15 mm/rev</td><td>(h) 60 m/min; 0.15 mm/rev</td><td>(i) 90 m/min; 0.15 mm/rev</td></tr>
</table>
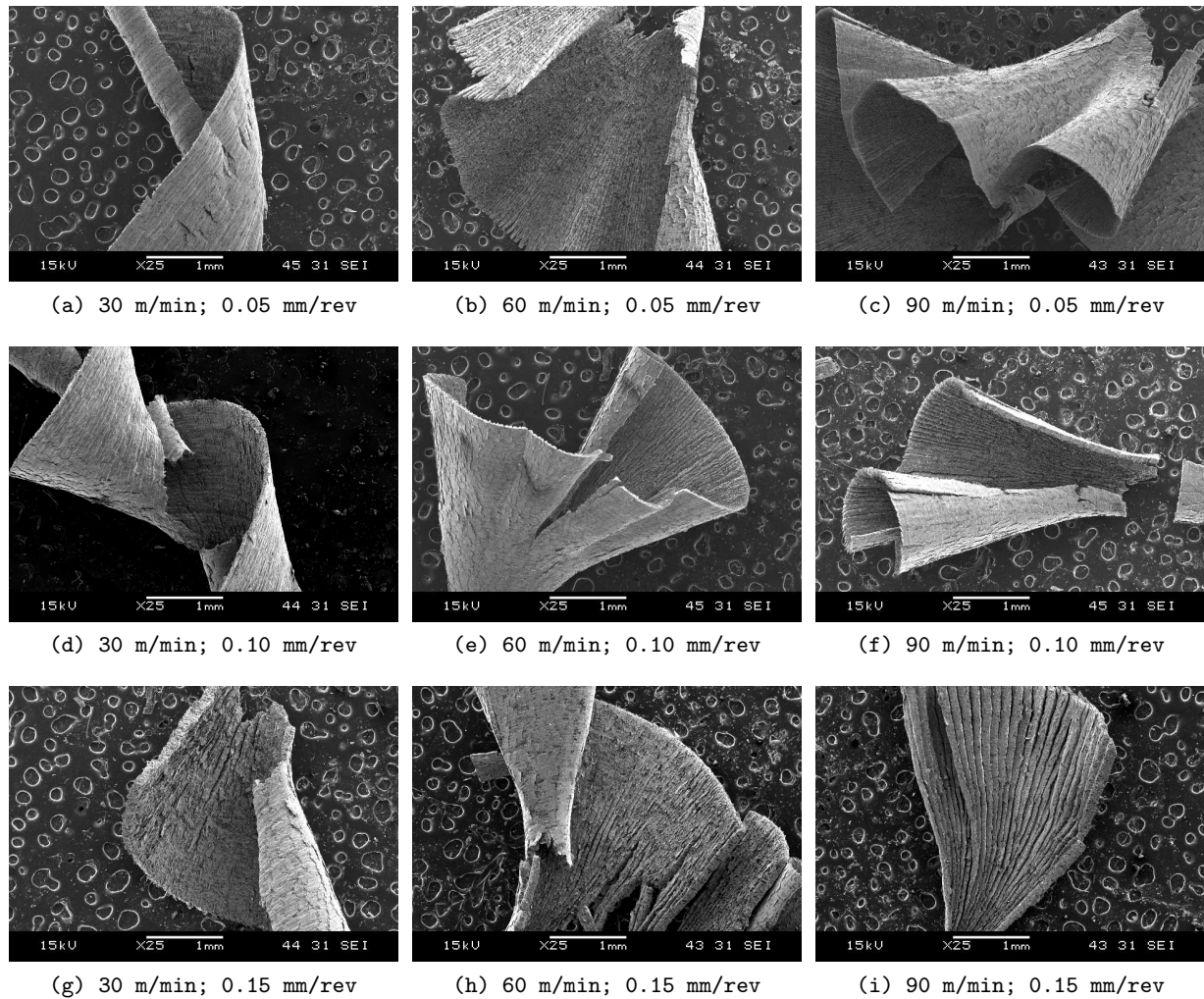
Figure 6.12: SEM micrographs of the obtained chip forms for different cutting conditions.

increase in feed rate the chip transformed from continuous chip (at 0.05 mm/rev) to amorphous chips (the cone-shaped chips broken at the bottom of the cone).

6.2.2   Chip-free surface

Figure 6.13 shows SEM micrographs of the chip-free surface for all cutting conditions. The fine lamella structures were observed at higher cutting speeds (60, 90 m/min) for all feed rates whereas, at lower cutting speed (30 m/min) a rough lamella structure was observed. The lamella structure on the free surface signifies the shearing morphology on the free surface [140]. The lamella structure was observed to form across the width of chip and normal to the direction of chip flow. Barry and Byrne [141], explained that the transformation in the lamella structure at the chip-free surface favored by an increase in cutting speed and un-deformed chip thickness.
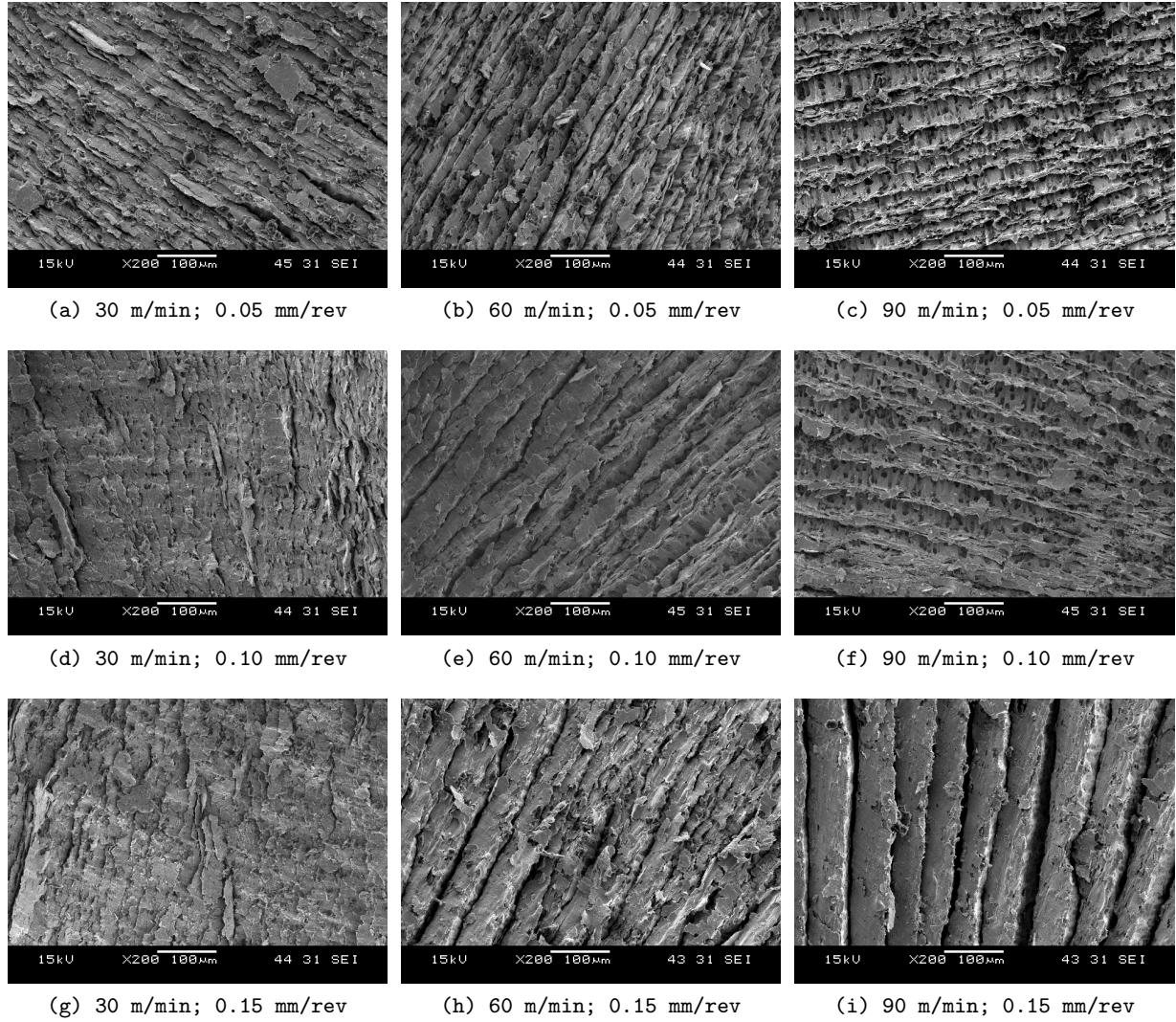
Figure 6.13: SEM micrographs of the chip free surfaces for different cutting conditions.

At lower cutting speed (30 m/min) the obtained lamella structures have a low width with higher frequency. On the other hand, it was observed (Fig. 6.13) that the width and depth of the lamella structure increase with an increase in feed rate and cutting speed showing the formation of fragmentary chips with the saw tooth. This behavior can be explained due to the increase in strain rate at the primary shear zone with an increase in cutting speed. Under the influence of large strain characteristics at primary shear zone shear instability occurs. At this stage, the flow stress decrement caused by thermal softening exceeds the increment in flow stress caused by strain and strain hardening rate [142]. This leads to the formation of shear localized chip morphology.

(a) 30 m/min; 0.05 mm/rev   (b) 60 m/min; 0.05 mm/rev   (c) 90 m/min; 0.05 mm/rev

(d) 30 m/min; 0.10 mm/rev   (e) 60 m/min; 0.10 mm/rev   (f) 90 m/min; 0.10 mm/rev

(g) 30 m/min; 0.15 mm/rev   (h) 60 m/min; 0.15 mm/rev   (i) 90 m/min; 0.15 mm/rev
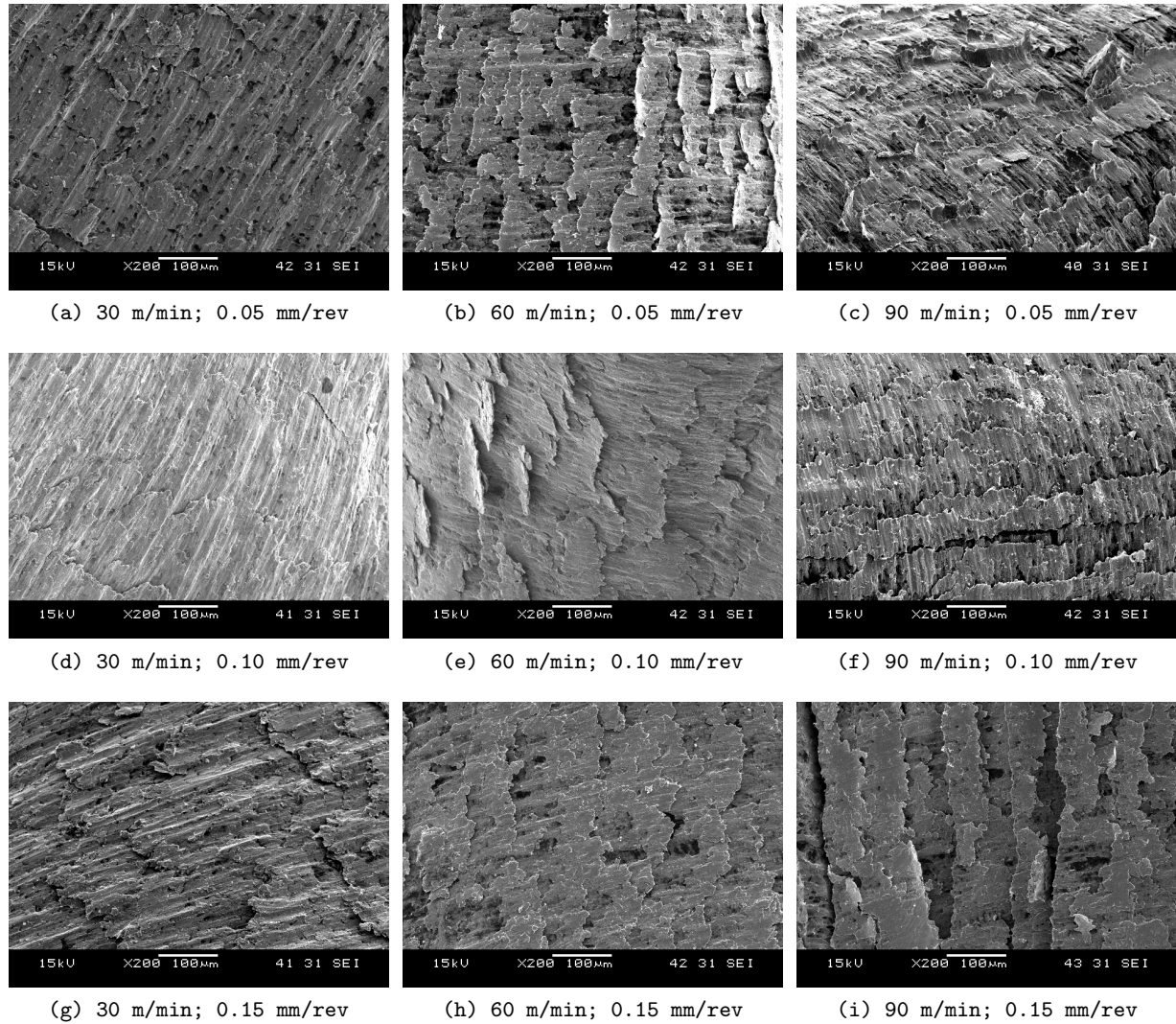
Figure 6.14: SEM micrographs of the chip back surface for different cutting conditions.

6.2.3   Chip-back surface

Figure 6.14 shows the scanning electron micrographs of the chip-back surface for different cutting conditions. At low cutting speed the smooth back surface suggested a ductile fracture with graphite micro-pores emerged, grow and coalesce during shear deformation. However, at higher cutting speed fold-type patterns are observed on the back surface which further increases with an increase in feed rate. Barry and Byrne [143], suggested the formation of fold-type structure due to the evolution of thermally softened micro-shear zones within the lower region of primary shear zones, which may initiate adiabatic shear at the tool tip.

(a) 30 m/min; 0.05 mm/rev   (b) 90 m/min; 0.05 mm/rev

(c) 30 m/min; 0.15 mm/rev   (d) 90 m/min; 0.15 mm/rev
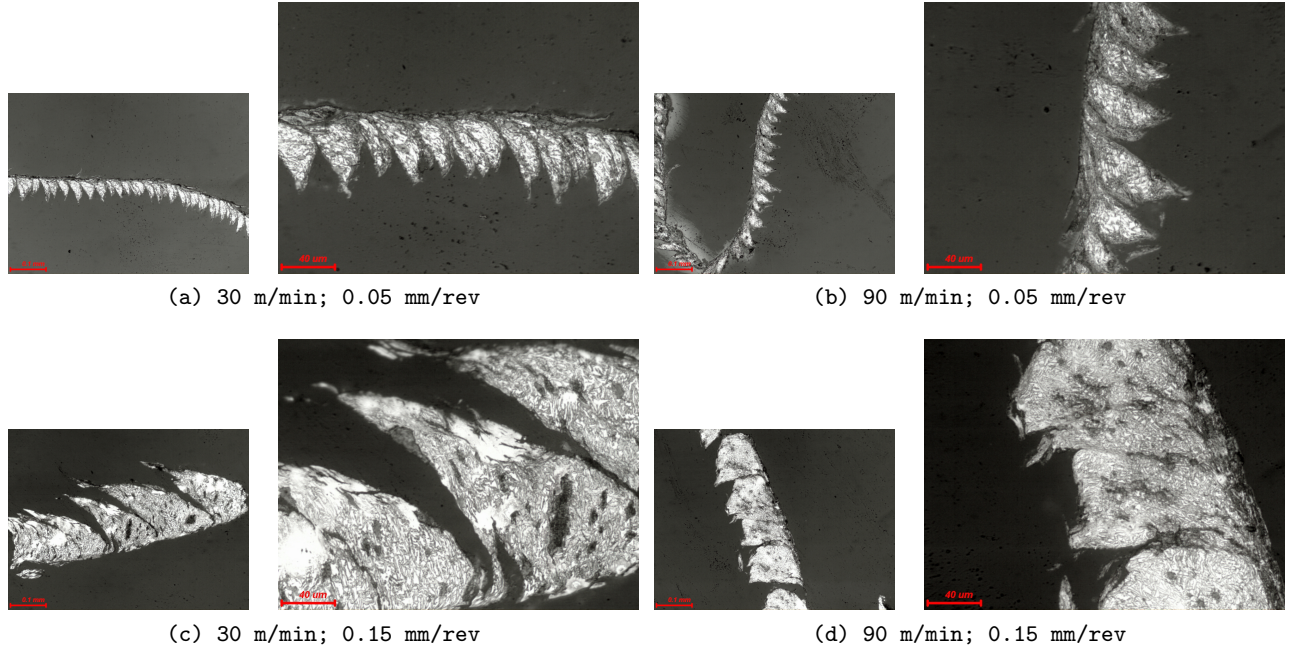
Figure 6.15: SEM micrographs of the chip top surface for different cutting conditions.

6.2.4 Cross section of top surface

Figure 6.15 shows the cross-sectional images of chip top surface for different cutting conditions. The typical saw tooth continuous fragmentary chips were observed for all cutting conditions. It can be clearly seen that the feed effect is more dominant as compared to cutting speed effect over the shape and size of the cross-section of chips. The frequency of saw tooth was observed to be decreased with an increase in feed rate. The decrease in the frequency of saw tooth with an increase in feed rate can be correlated with a size effect exist in metal cutting, where the specific energy increases with decrease in deformation size.

The chip compression ratio (CCR) ζ (Equation 6.3) which is defined as the ratio of the chip thickness (t2) the uncut chip thickness (t1), was used as a measure of plastic deformation in metal cutting in previous studies [62, 139]. However, many researchers [143, 144] did not consider CCR as a parameter to provide qualitative support to plastic deformation in metal cutting.

$$CCR(\zeta) = \frac{t_2}{t_1} \tag{6.3}$$

To measure the uncut chip thickness Astakhov [145] suggested the following equation (Equation 6.4).

$$t_1 = \frac{f}{2}\left(\frac{1}{\sqrt{1 + (cotk_r/cosu_r)^2}}\right) \tag{6.4}$$
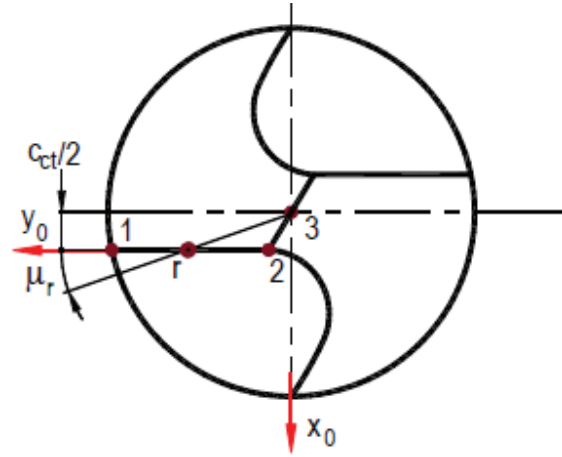
Figure 6.16: Geometrical representation of angle u_r [145].

Where f is feed rate, and k_r is equal to half of point angle. Figure 6.16 shows the geometrical representation of angle u_r and it depends on the location of desired point on the cutting edge. In this study the value of u_r is equal to 11.30 degree for the out-most cutting edge of the drill tool.
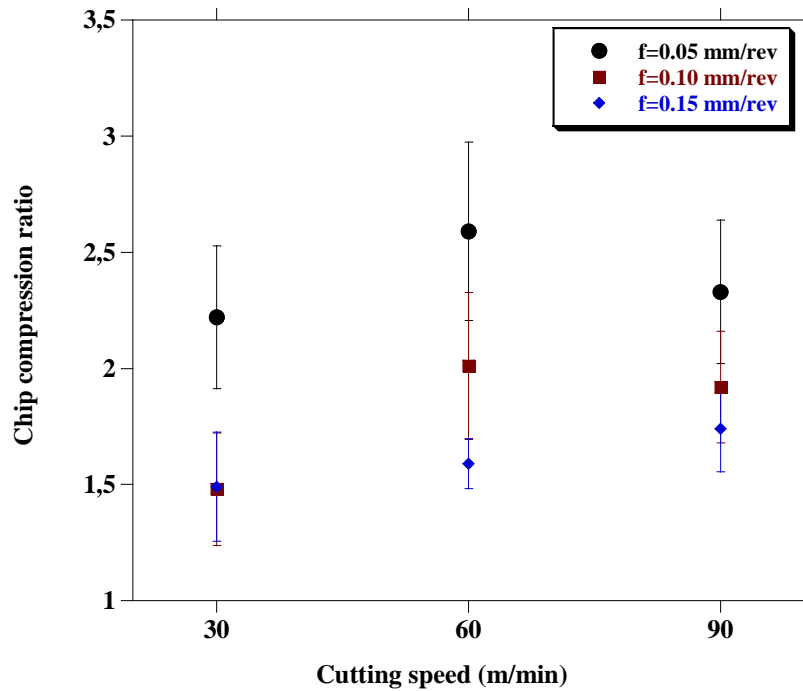
Figure 6.17: Variations in the mean chip compression ratio (CCR) with respect to cutting speed.

Figure 6.17 shows the variation of mean chip compression ratio with respect to different cutting parameters. The CCR observed to decrease with an increase in feed rate for all cutting speeds. However, a different behavior can be seen in CCR with respect to cutting speed. At lower feed rates (0.05 and 0.10 mm/rev), a significant increase in the CCR values was observed with cutting speed in the range of 30 m/min and 60 m/min, after which the CCR values show decreasing behavior with cutting speed. On the other hand, higher feed rate (0.15 mm/rev), the CCR values show linearly increasing behavior with cutting speed. This indicates that the work done in plastic deformation during metal-cutting increases with cutting speed in the range of 30 m/min and 60 m/min for all feed rates which means that strain hardening rate exceeds the thermal softening rate for the above conditions. However, on a further increase in the cutting speed at lower feed rates (0.05 and 0.10 mm/rev) the thermal softening behavior dominates over strain hardening behavior of material as CCR decreases. The increase in work done (plastic deformation) during machining with cutting speed at 0.15 mm/rev indicate the change in material properties of workpiece due to thermal softening.
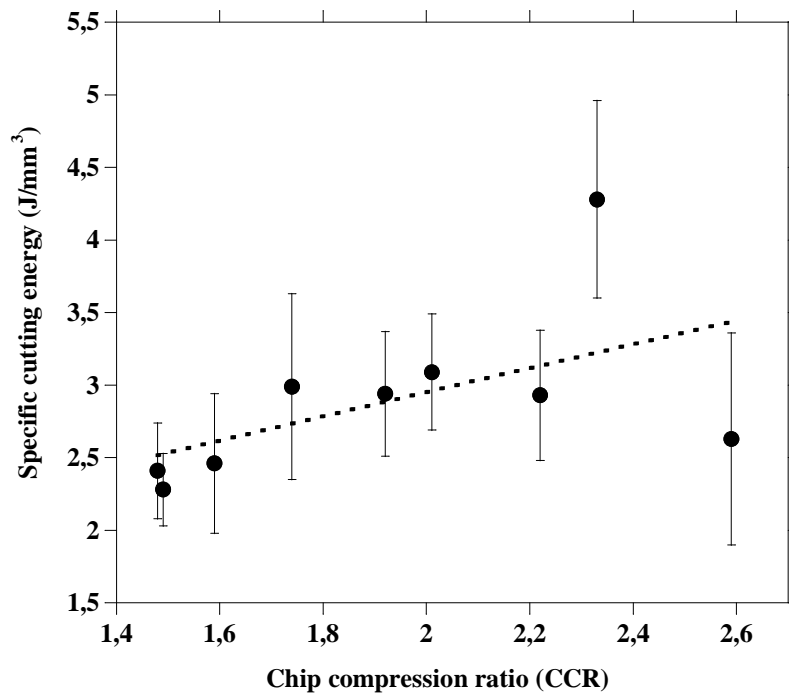
Figure 6.18: Variation in the specific cutting energy (u) with respect to the chip compression ration (CCR).

Figure 6.18 illustrates the variation in specific cutting energy with respect to the chip compression ratio. It can be seen that in the range of 1.4-2.4 (CCR values) the specific cutting energy show increasing behavior with CCR values. However, on further increasing the CCR value, specific cutting energy decreases. As the CCR values increases, the work done during the

plastic deformation of the workpiece increases which further led to the development of material strengthening characteristics. This material strengthening behavior gives rise to an increase in the specific cutting energy.
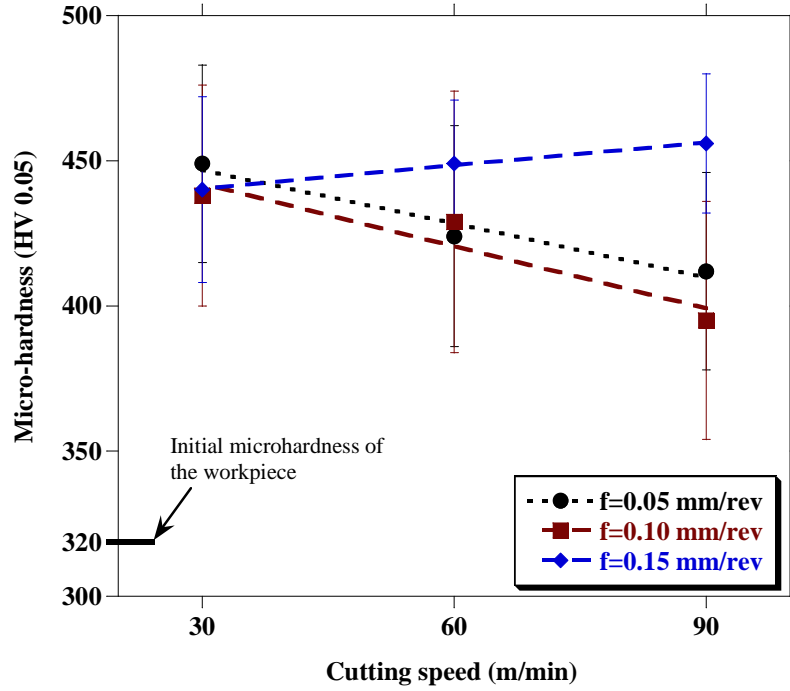
Figure 6.19: Variation in the chip micro-hardness with respect to cutting speed.

6.2.5   Chip micro-hardness

Astakhov [62] illustrated the effects of cutting speed on chip formation in two major ways. First, it changes the strain rate in the deformation zone and thus affects the resistance of the work material, and the thermal energy generated in its deformation. Second, it affects the tool-chip relative speed and the natural length of the tool-chip interface and thus affects the tribological conditions at this interface. Both factors lead to the change in mechanical properties of the chip. Chip micro-hardness values for chips are measured under different cutting conditions to understand these changes.

Figure 6.19 shows the variation of chip micro-hardness with respect to different cutting conditions. It was observed that the average micro-hardness values of chips are much higher than that of average micro-hardness of the work material reflecting the plastic deformation of chips during the chip formation process. At higher feed rate (0.15 mm/rev), the chip microhardness values show increasing behavior with cutting speed whereas, at lower feed rates (0.05, 0.10 mm/rev), chip's micro-hardness values were observed to decrease with an increase in cutting
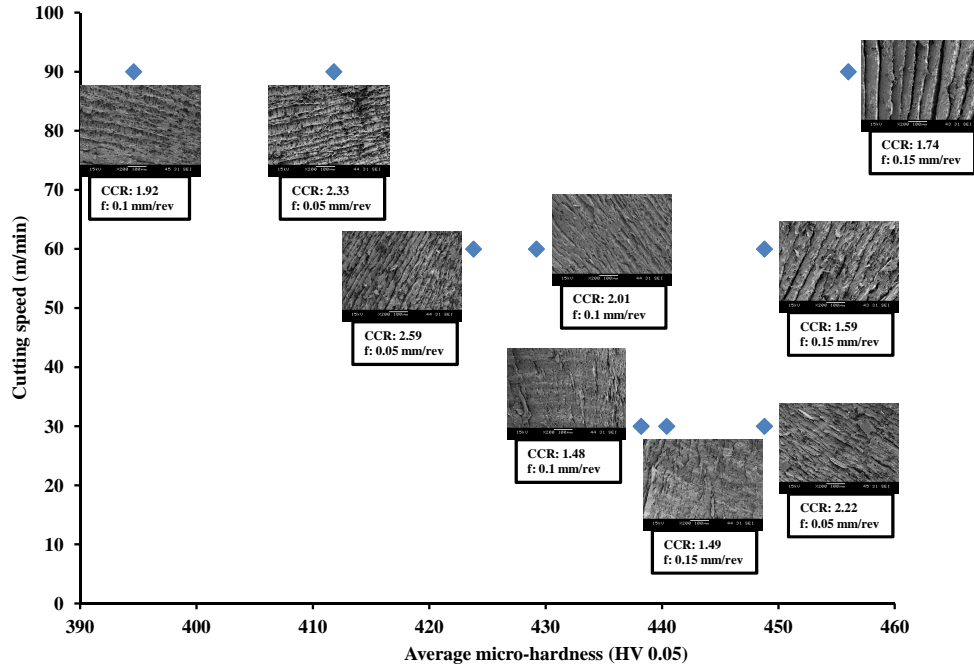
Figure 6.20: Relationship between the chip micro-hardness, CCR, cutting parameters and chip morphology.

speed. The decrease in chip microhardness with cutting speed at lower feed rates (0.05 and 0.10 mm/rev) can be explained due to the influence of thermal softening, which leads to the recrystallization in the deformed chips. Figure 6.20 illustrates the relationship between the chip micro-hardness, CCR, cutting parameters and chip morphology. It allows to understand the machinability of ADI within the framework of the chip formation process. The chip formation process is a complex interplay between tool materials, workpiece material and cutting parameters, which is hard to define for the optimized condition. The possible solutions for the machining problems of ADI can be solved by understanding the transition of chip morphology with respect to the specific cutting energy, CCR values under the influence of different cutting conditions. The choice of low CCR values and low specific cutting energy at the higher material removal rates can be the ideal one to improve the machinability of ADI.

6.2.6 Conclusions

The dry drilling experiments were conducted on ADI produced by the integrated casting-heat treatment process. The experimental investigation of chip morphology characteristics, chip compression ratio and its micro-hardness were presented. Based on the experimental results following conclusions can be summarized.

1. The well broken cone shaped chips are formed at lower cutting speed (30 m/min) with cone diameter increasing with an increase in feed rate. The increase in cutting speed at lower feed rate (0.05 mm/rev) leads to the formation of continuous chips.

2. The fine lamella structures were observed at higher cutting speeds (60, 90 m/min) for all feed rates whereas, at lower cutting speed (30 m/min) a rough lamella structure was observed for all feed rates. The width and depth of lamella structure increases with an increase in feed rate and cutting speed, which leads to the formation of fragmentary chips with the saw-tooth.

3. At lower feed rates (0.05 and 0.10 mm/rev), a significant increase in the CCR was observed with cutting speed in the range of 30 m/min and 60 m/min, after which the CCR show decreasing behavior with cutting speed. On the other hand, at higher feed rate (0.15 mm/rev), the CCR values show linearly increasing behavior with cutting speed.

4. At higher feed rate (0.15 mm/rev), the chip micro-hardness values show increasing behavior with cutting speed whereas, at lower feed rates (0.05, 0.10 mm/rev), chip's micro-hardness values were observed to decrease with an increase in cutting speed.

5. Under the influence of dry drilling condition, the higher productivity within the range of good machinability for novel ADI can be achieved by the choice of low CCR values and low specific cutting energy at the higher material removal rates. However, further enhancement is possible by the use of cutting fluid during the machining process to improve the tribological characteristics at the cutting zone. With this viewpoint, the minimum quantity lubrication (MQL) drilling is investigated in the next section.

6.3   Minimum quantity lubrication (MQL) drilling

Coolants and lubricants for machining can improve the machinability of the workpiece, increase productivity, and extend tool life by reducing tool wear [76]. However, for environmental and economic reasons, recent research in industry and academia has sought ways to reduce the use of machining fluids. This section thus reports the near-dry machining characteristics of ADI for ecological machining of ADI. The ADI material for machining is produced by the integrated casting-heat treatment process. The chemical composition of the workpiece material is as follows: 3.54% carbon, 2.51% silicon, 0.27% manganese, 0.27% molybdenum, 1.23% copper, 0.66% nickel and 0.012% sulphur. The mechanical properties of the workpiece material are provided in Table 6.3. The present section focused on the influence of MQL drilling on the machinability of ADI material with respect to the cutting forces, surface roughness and tool wear behavior. The MQL drilling, performance is then compared with the dry and wet drilling conditions process under the same experimental conditions. The machining experiment was conducted using the TiAlN-coated tungsten carbide tool (reference: R840-0800-30-A0A 1220) of diameter 8 mm. A single drill tool of the same reference was used for each set of experiments. The machining experiments were carried out at a cutting speed of 60 m/min and feed rate of 0.15 mm/rev.

Property	Range
Ultimate tensile strength (MPa)	698-725
0.2 % yield strength (MPa)	610-640
Elongation (%)	4.5-6

Table 6.3: Tensile properties of the workpiece material (Austempering temperature: 380℃; Austempering time: 120 min).

6.3.1   Results and discussion

(i) Torque and thrust force

Figure 6.21 shows the variation in the average cutting torque with respect to the number of holes drilled under the influence of dry, MQL and flooded (wet) drilling conditions. It can be seen that cutting torque values show constant behavior until 10 holes. However, after that significant variation in cutting torque was observed for different cutting environment. In case of dry drilling cutting torque show a monotonic increase with respect to the number of holes drilled and show a tool life of 80 holes. On the other hand, for MQL drilling the cutting torque values show constant behavior until 40 holes, and then it starts to increase with the number of

holes drilled and show the tool life of 110 holes. However, in case of wet drilling, no significant change was observed in cutting torque until 90 holes. The variation in average thrust forces with respect to the number of holes drilled under the influence of dry, MQL and wet drilling conditions are shown in Fig. 6.22. In case of MQL drilling, no significant change was observed in thrust force with the number of holes drilled. However, in case of dry and wet drilling, thrust force show increasing behavior with the number of holes drilled after 40 and 60 holes respectively. It was revealed that the reduction in maximum average torques obtained in case of MQL and flooded drilling as compared to dry drilling was 6%, and 24%, respectively, whereas the reduction obtained in case of maximum average thrust forces for MQL and wet machining conditions were 10%, and 13% respectively as compared to dry machining condition. It can be observed that MQL machining show a considerable reduction in torque and thrust forces as compared to dry machining. In addition, MQL machining until 40 holes are comparable to the wet machining conditions with respect to the cutting torque values.

Figure 6.21: A comparison of average torques with number of holes drilled under dry, MQL and flooded (wet) drilling conditions (Cutting speed: 60 m/min; Feed rate: 0.15 mm/rev)

(ii) Surface roughness

Surface finish is considered as an important industrial production parameter for the evaluation of machinability for a particular workpiece-tool combination [65]. It indicates the performance and service life of the machined component. Figure 6.23 shows the variation in surface roughness (Ra) values with the number of holes drilled for different cutting environment. The
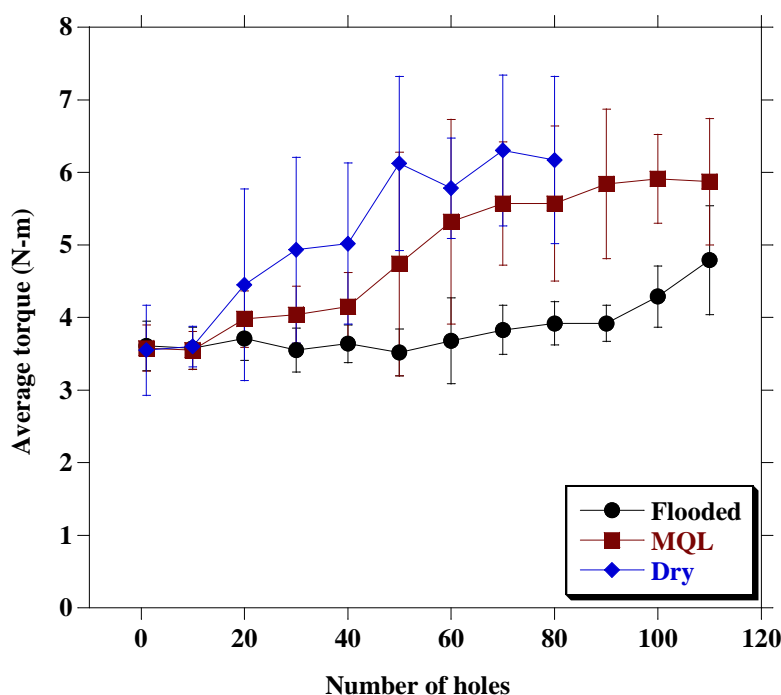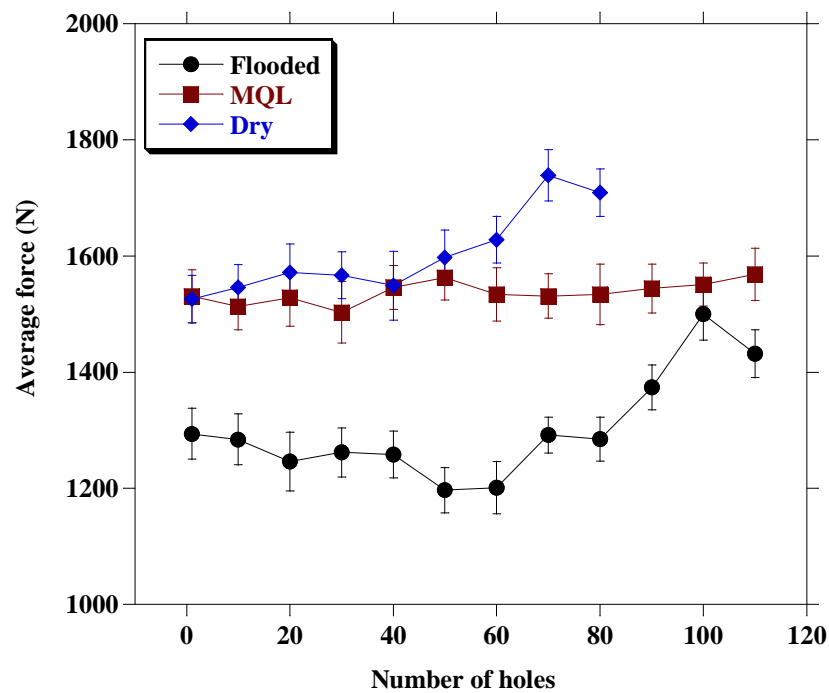
Figure 6.22: A comparison of average thrust forces with number of holes drilled under dry, MQL and flooded (wet) drilling conditions (Cutting speed: 60 m/min; Feed rate: 0.15 mm/rev
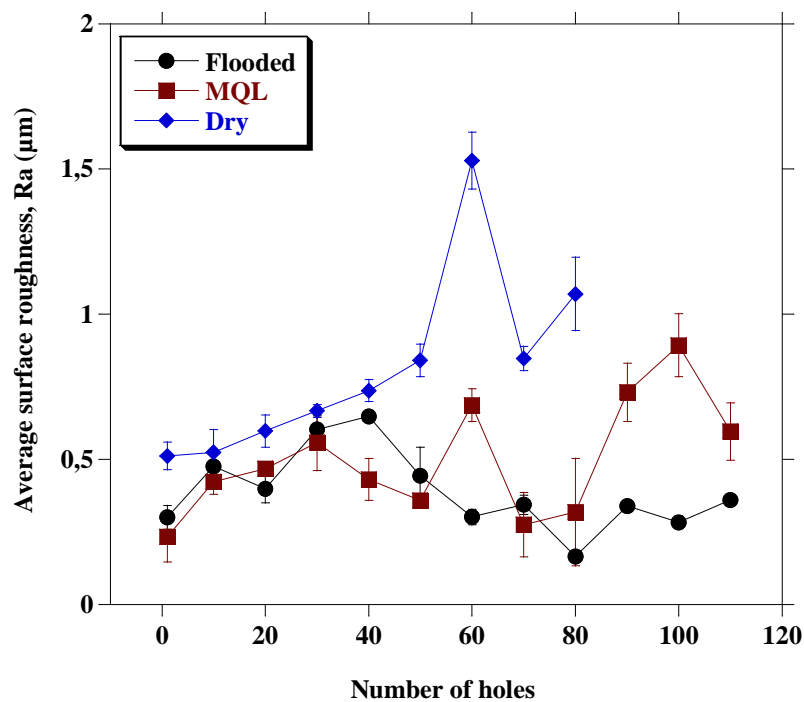

Figure 6.23: Variation in the surface roughness values with number of holes drilled for different cutting environment (dry, MQL and wet cutting environment)

surface roughness measurements were made inside the holes. It can be seen that the Ra values increases rapidly with the number of holes drilled in case of dry machining as compared to the MQL and wet machining conditions. The Ra values are within the range of 0.389±0.136 μm and 0.498±0.2 μm for wet and MQL machining conditions respectively. The highest Ra value recorded was 1.529±0.098 μm at the onset of drill failure during dry machining condition. The higher Ra values during dry machining conditions indicate the evolution of tool wear with the number of holes drilled. With an increase in the number of holes drilled the adhesion of the material particles on the rake face take place, which lead to the growth of built-up edge. During machining, these adhesion particles degrade the machined surface quality. However, in case of MQL machining, significant reduction in surface roughness was found as compared to the dry machining condition. The MQL machining improves surface quality of the machined surface depending on the workpiece-tool combination by providing the sufficient lubrication condition at the workpiece-tool interfaces and through controlling the controlling the deterioration of the cutting edge by abrasion, chipping and built-up edge formation.

(iii) Tool wear

The measured values of flank wear width at the end of machining experiments were 0.41 mm, 0.25 mm and 0.12 mm for dry, MQL and wet machining conditions respectively. It was revealed that as compared to the dry machining the tool life was increased by 25%, and tool wear was reduced by 40% in case of MQL machining. Fig. 6.24 shows the SEM and optical micrographs of the drill tools wear at the end of machining experiments for different cutting environments. It can be seen from the micrographs that tool wear mainly takes place at the cutting edge near to the periphery for all cutting environments. It was found that at the initial stage of drilling, the coated layer is abraded off from the cutting edge (near to the periphery) of the drill tool material. After that as the number of drilled holes increases, the friction force increases continuously due to the abrasion of coating. This lead to the formation of BUE (built-up edge) at the outer corner of drill tools, which further leads to the chipping of the cutting tool material. The chipping together with flank and crater wear causes the failure of drill eventually. The non uniform flank wear, chipping and material adhesion is observed at the outer cutting edge of the tool in case of dry and MQL machining conditions which under the influence of higher cutting forces leads to the crater wear at the outer corner of the drill tool.

Dry drilling
(after 80 holes)
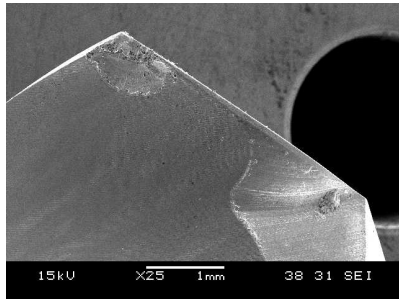
MQL drilling
(after 110 holes)
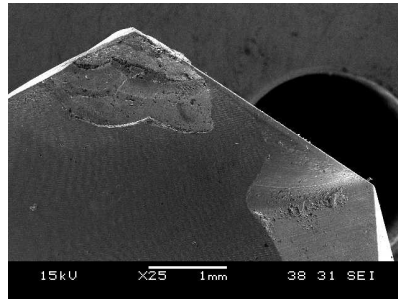
Flooded drilling
(after 110 holes)

(a)

(b)
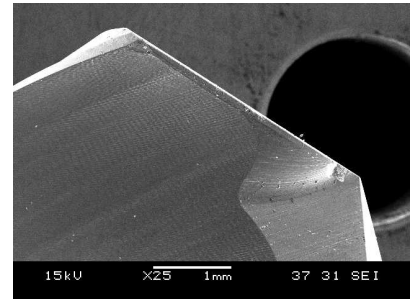
(c)
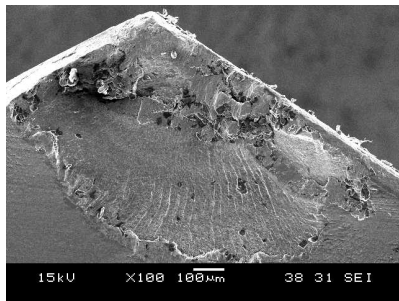
(d)
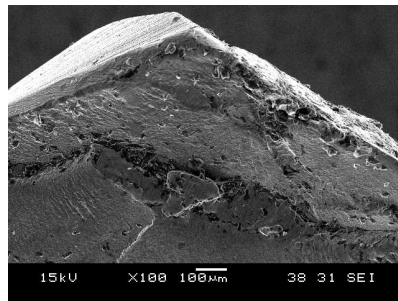
(e)
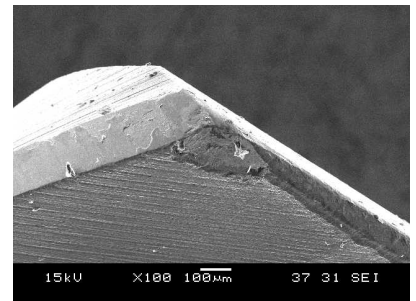
(f)
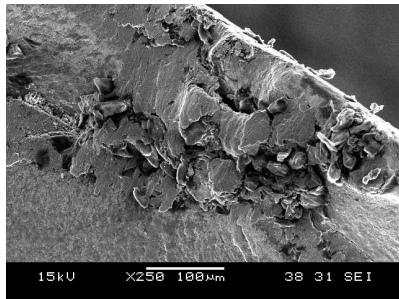
(g)
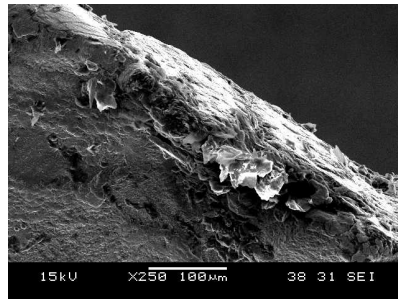
(h)
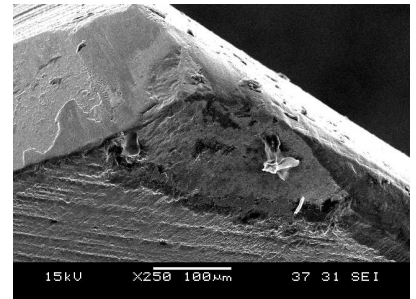
(i)
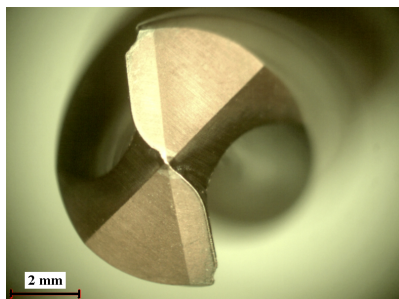
(j)
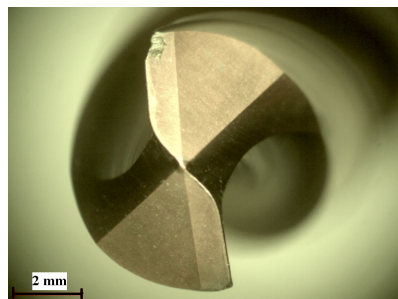
(k)
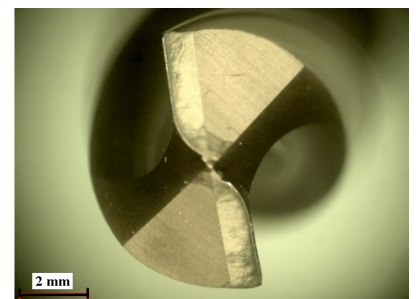
(l)

Figure 6.24: SEM and optical micrographs of tool wear (TiAlN-coated tungsten carbide tool) for dry, MQL and flooded drilling conditions at the end of machining experiments.

6.3.2   Conclusions

The MQL drilling performance using the PVD-TiN/TiAlN multilayer coated tungsten carbide tools were investigated in the present study for the ecological machining of ADI. The MQL drilling performance of ADI is also compared with the wet and dry machining process under the same experimental condition. Based on the results obtained, the following conclusions can be drawn:

1. The MQL machining condition gives rise to the reduction of 6 % and 10 % in average cutting torque and average thrust force receptively as compared to the dry machining condition. On the other hand, the MQL machining shows comparable behavior with the wet machining in terms of the thrust force generated.

2. The MQL machining appeared to be effective in reducing the surface roughness of the machined surfaces as compared to the dry machining and comparable to the wet machining.

3. It was revealed that as compared to the dry machining the tool life was increased by 25% and tool wear was reduced by 40% in case of MQL machining.

4. Crater wear at the outer corner of the drill tools was the dominant wear mode in case of dry and MQL machining. The crater wear is the consequence of the higher frictional and adhesive characteristics at the tool-workpiece interface which further leads to the chipping of the cutting edge followed by damage at the outer corner of the drill tool. However, the limited of machinability of ADI under the dry condition can be improved using advanced coating material and tool geometry. Therefore, the cutting performance of different PVD coated tools are investigated in the next section.

6.4 Cutting performance of PVD coated tools

6.4.1 Specific cutting energy and Tool wear mechanisms

Two different tool geometries coated with different PVD-coating materials were used for the dry drilling tests in the present section. The tool 1 (B254A08000YPC) is coated with PVD-multilayer coating of (Ti,Al,Cr)N and tool 2 (B254A08000HPC) is coated with PVD-monolayer TiAlN coating. Figure 6.25 shows the variations of the specific cutting energy with the number of drilled holes for tool 1 and 2. It can be observed that tool 1 show steady behavior with the number of holes drilled. However, tool 2 shows linearly increasing behavior with the number of drilled holes. The results (Fig. 6.25) can be analyzed according to the cutting performance of different PVD coatings. The average maximum specific cutting energy was calculated to be 2.80 J/mm^3 in case of tool 1 and 3.73 J/mm^3 in case of tool 2, corresponding to an increase of the 33% as compared to the tool 1. The specific cutting energy which is also known as cutting energy per unit volume is responsible for the temperature increase at the tool-chip interface during the machining process. Astakhov [62] stated that only 30-50 % of the cutting energy spent for the separation of the layer being removed from the workpiece. The rest is spent on the tribological interaction between tool-chip and tool-workpiece interfaces, which is converted into heat and give rise to temperature at the cutting zone during machining operations. Therefore, the specific cutting energy is the relevant indicator of the temperature in the deformation zone. The use of cutting tool coating can further enhance the heat dissipation and reduce friction, and thus reduce the temperature at the tool-chip interface. The change in the specific cutting energy with the number of drilled holes for different tools can be explained with the improved tribological characteristics at the tool-chip interface using the tool 1.

The surface characteristics of the PVD coated tools were analyzed to determine the nature of tools wear using the SEM and EDS techniques. SEM images of the worn drill tools (cutting edge) are shown in Fig. 6.26. It can be observed that adherence of the workpiece material occurs in tool 2, mainly at the cutting-edge, near the periphery, and coating layer abraded off and cutting-edge damage occurs near the drill point. However, large abrasion of coating was found at the outer edge of tool 1. A quantitative element analysis was carried out using EDS analysis (Fig. 6.26), identifying the elements at the worn surfaces. EDS analysis of tool 1 (region 1) near to the cutting edge reveals the presence of iron (Fe) and carbon (C) indicating the transfer of the workpiece material to the drill tool during the machining process. High peaks of titanium (Ti) and chromium (Cr) are observed at region 1, indicating the wear resistance of the coating near to the cutting edge. EDS analysis of wear surface at region 2 reveals the abrasion of coating (low peaks of Ti and Cr). High peaks of aluminum (Al) and oxygen (O) are
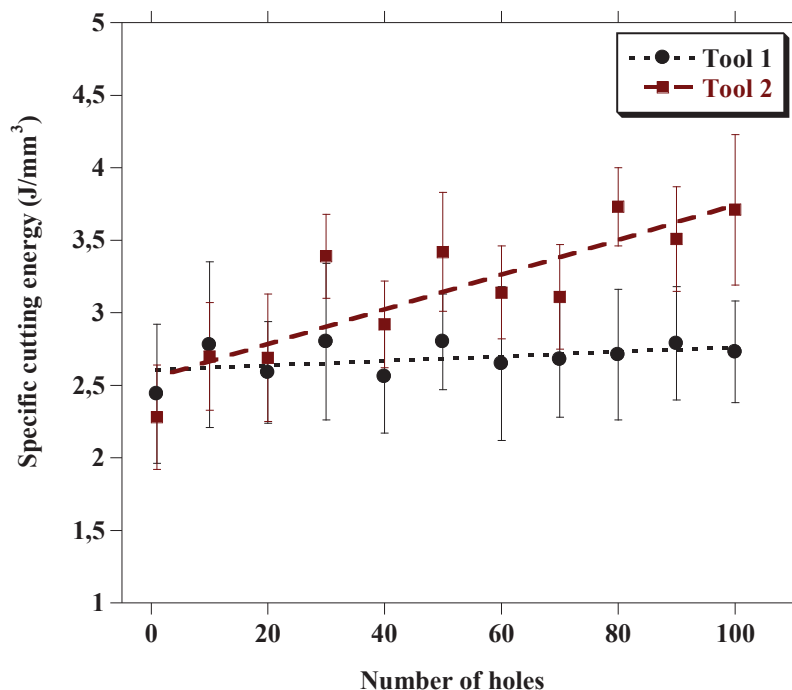
Figure 6.25: The variations of average specific cutting energy with number of drilled holes for different PVD coatings.

observed at the tool surface (region 3) indicating the formation of protective aluminum oxide layer on the rake face of the tool. In case of tool 2, EDS analysis at the cutting edge (region 4) reveals the presence of silicon (Si), in addition to Fe and C. The high content of O reveals the possibility of oxidation of adhered workpiece material at the cutting edge. The oxidation of adhered workpiece material at the cutting edge indicates the significant rise in temperature at the cutting zone. Peaks of tungsten (W) and cobalt (Co) in EDS analysis (region 5) indicates the entire removal of the coating and leads to the exposure of the substrate material. EDS analysis at region 6 showing peaks of Al and O indicates the presence of protective aluminum oxide layer.

The tool wear behavior provides an insight into the sequence of events leading to the cutting-edge failure. From the results, it was observed that tool 1 show better wear resistance as compared to the tool 2. Tool 1 consists of PVD multi-layers (Ti,Al,Cr)N coating. Due to the presence of chromium (Cr), it shows higher thermal stability [62]. Holmberg and Matthews [146] stated that in chromium coatings, the formation of chromium oxide layers on the tool surface during machining leads to the low tool wear. The chromium oxide further acts as a barrier layer preventing contact between the workpiece and tool surface and suppressing adhesive wear. The formation of protective oxide (layers of alumina and chromia) at higher cutting temperature reduces the adherence of workpiece material to the cutting tool surface.
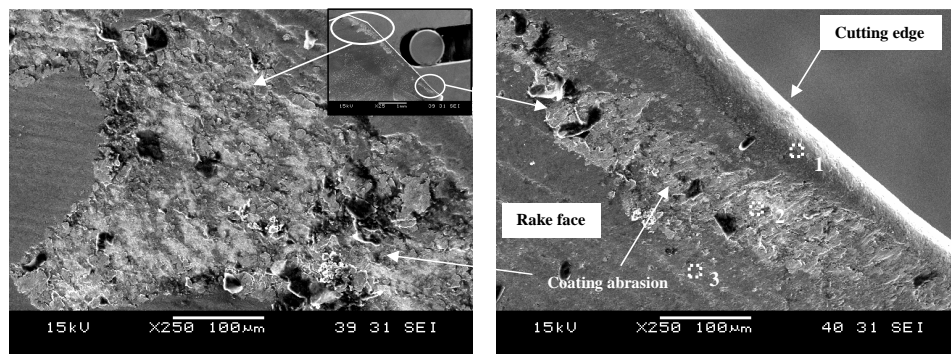
(a) Tool 1 after 100 holes
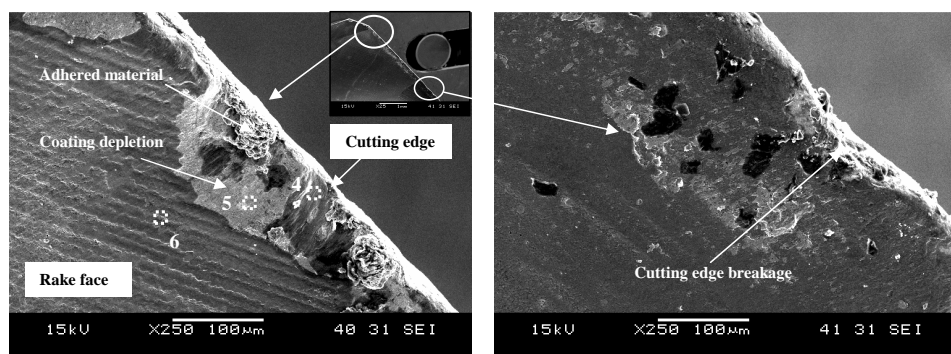
(b) Tool 2 after 100 holes
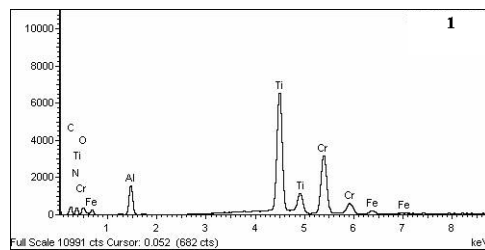
(c) Region 1
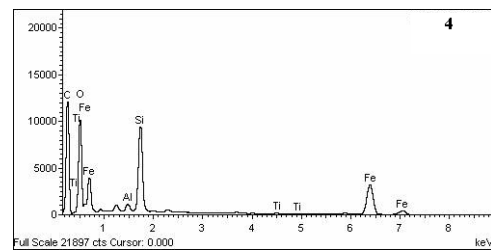
(d) Region 4
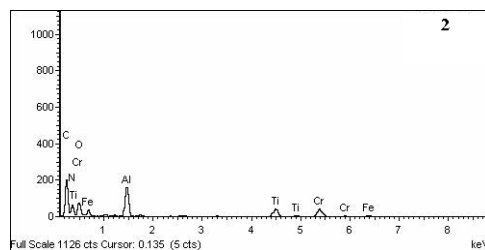
(e) Region 2
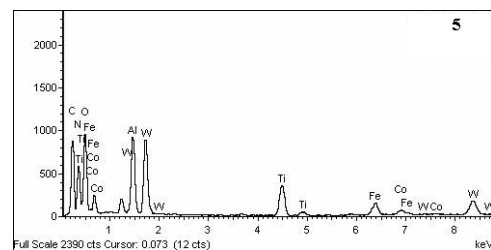
(f) Region 5
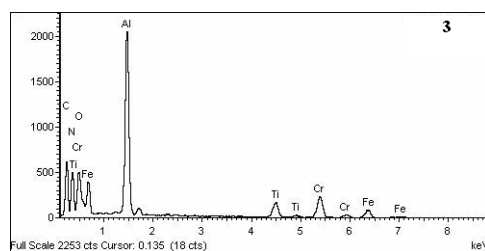
(g) Region 3
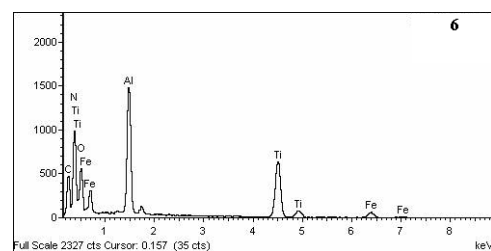
(h) Region 6

Figure 6.26: SEM micrographs and EDS spectra of the wear surfaces on tool 1 and 2 after machining 100 drilled holes.

6.4.2 Surface roughness and micro-hardness profile

Figure 6.27 shows the variation of average surface roughness (Ra) of the machined surfaces as a function of specific cutting energy for both tools. It can be observed that for tool 2, the Ra values show linearly increasing behavior with the specific cutting energy. However, in case of tool 1 the majority of Ra values obtained is in the range of lower specific cutting energy. The Ra values are within the range of 0.62-1.12 m and 0.69-1.61 m for the tool 1 and 2 respectively. The tool 1 appears to produce better surface finish and keeping the specific cutting energy low as compared to tool 2. Rodrigues and Coelho [147] stated that the specific cutting energy increases during machining due to the increase in chip-tool friction and increase in cutting zone temperatures, which are influenced by the tool coating and its wear. The presence of adhered workpiece material and the exposure of substrate material (tool 2) during machining leads to the increase in surface roughness and specific cutting energy during the machining process.
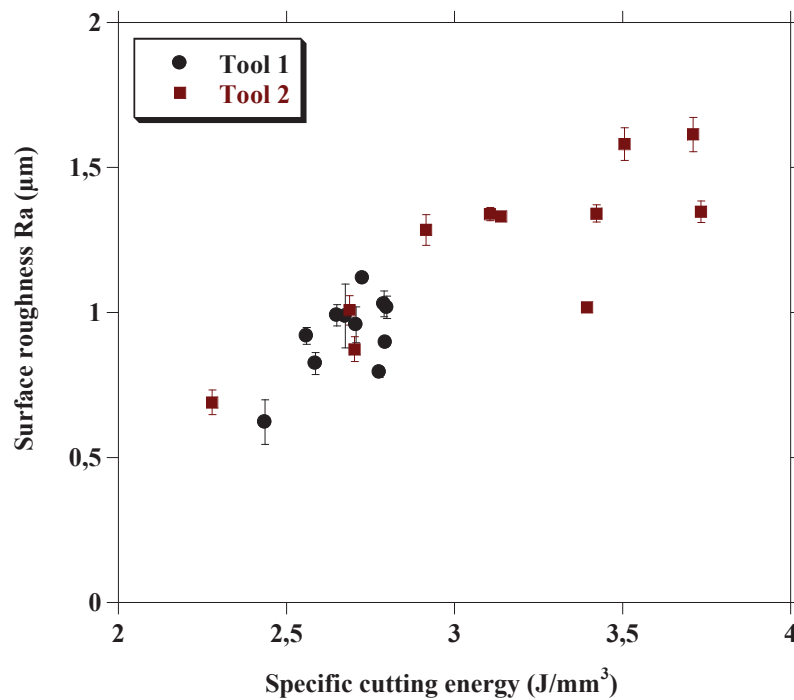
Figure 6.27: Surface roughness parameter, Ra (μm) as a function of average specific cutting energy for tool 1 and 2.

The surface behavior of the workpiece material during machining can be understood by examining the hardness profile of the workpiece subsurface beneath the drilled surface. For this purpose, Vickers microhardness variation at the machined subsurface in a direction normal to the edge of the drilled surface is shown in Fig. 6.28. For each distance, three measurements were taken. It can be observed that the workpiece was hardened near to the machined surface
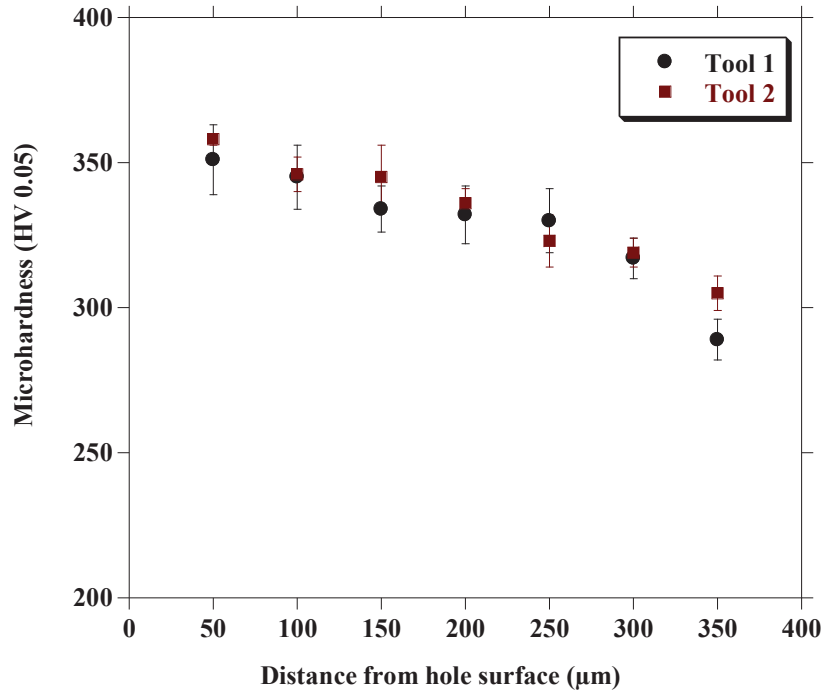
Figure 6.28: Microhardness profile of the machined subsurface for the tool 1 and 2.

(50 m) by 351 HV and 358 HV for drill tool 1 and 2 respectively. The microhardness variation gradually returns to the material bulk microhardness (290-310 HV 0.05) at about 350 m beneath the machined surface. Abrao et al. [67] stated that the surface alterations induced by machining are typically of mechanical, metallurgical and thermal nature. Pawade et al. [148] studied the microhardness variation on the machined surface of high speed turned Inconel 718. They found that the microhardness near the machined surface is approximately 50% higher than those of bulk material. According to them, the microhardness profile indicated that a significant amount of plastic deformation was induced by machining at a maximum depth of 200 m beneath the machined surface. In the present study, the both tools are showing similar microhardness variation at the machined subsurface indicating the surface alteration of the workpiece material during dry drilling.

6.4.3 Chip morphology

The morphological analysis of obtained chips from new sharp edge tools (tool 1 and 2) was carried out for studying the influence of PVD coatings on chip morphology. The obtained chips were analyzed by scanning electron microscopy as shown in Fig. 6.29. For both tools, cone-shaped chips were formed. The free and back surfaces of chips, which are formed due to the action of cutting edge during machining, were analyzed. For both tools, lamella structure was

(a) Chip form (Tool 1)

(b) Chip form (Tool 2)

(c) Chip free surface (Tool 1)

(d) Chip free surface (Tool 2)

(e) Chip back surface (Tool 1)

(f) Chip back surface (Tool 2)
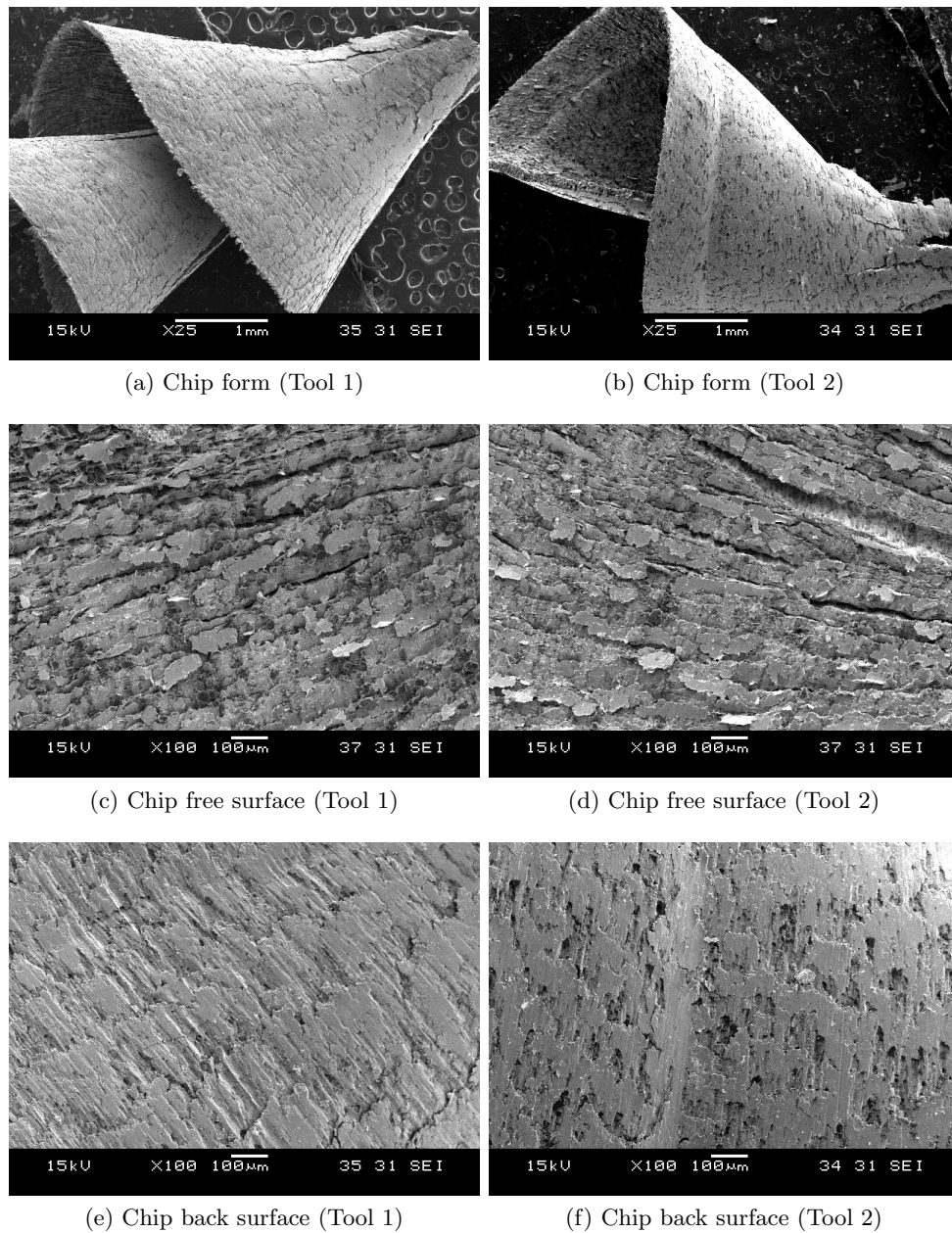
Figure 6.29: SEM micrographs of the obtained chip forms, chip free surfaces and chip back surfaces for tool 1 and 2.

observed at the chip-free surface. The lamella structure signifies the shearing morphology of the free surface [140]. It formed across the width of chip and normal to the direction of chip flow. However, different chip patterns were observed at the chip back surface using tool 1 and 2. For the tool 1, smooth fold type patterns are observed and for the tool 2, graphite micro-pores emerged at the back surface which, grow and coalesce during shear deformation. The obtained lamella pattern at the chip-free surface indicates high pressure and friction forces on the tool rake face and on the flute during its transportation, which causes high cutting temperature in cutting zone [149].

(a) Tool 1   (b) Tool 2

(c) Tool 1   (d) Tool 2
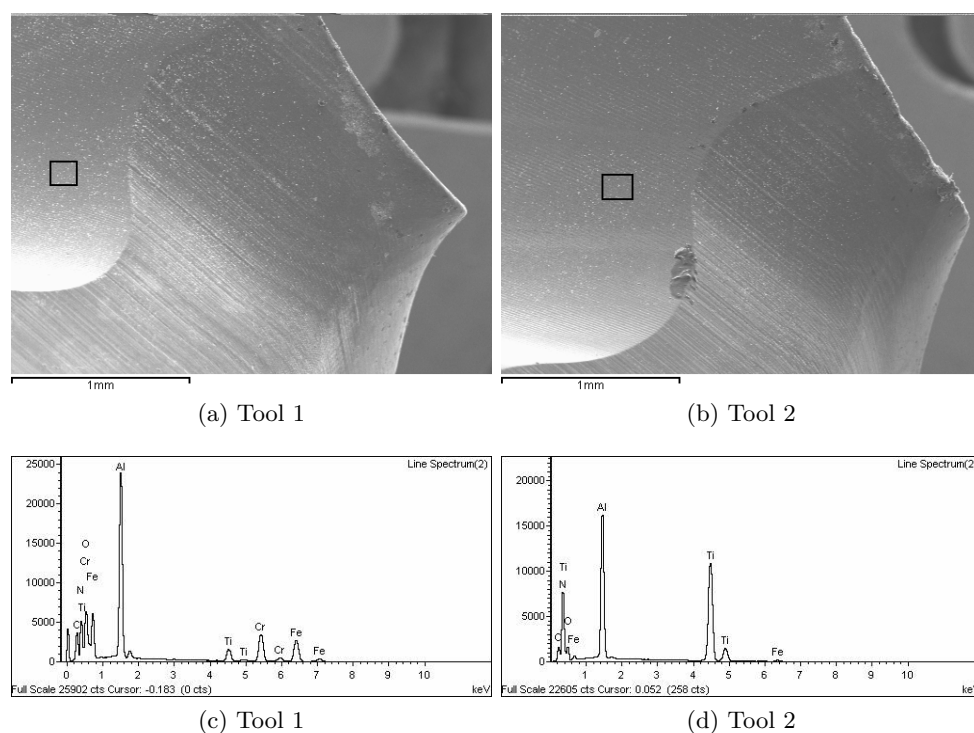
Figure 6.30: SEM micrographs and EDS spectra of the chip sliding surfaces on the drill flute for tool 1 and 2.

The drill flute surfaces (chip sliding surfaces) were investigated for both tools using the EDS analysis (Fig. 6.30) after the machining tests to observe the influence of chip transportation on the sliding surfaces of the flute during machining. The presence of the Fe and C in the EDS analysis indicates the transfer of the workpiece material to the drill flute durng chip transportation. Tool 1 show higher peaks of Al as compared to the tool 2. The effectiveness of the drill tool 1, may thus attributed to the formation of protective layer of aluminium oxide and chromium oxide on the drill surfaces which further improve the chip transportation.

6.4.4   Conclusions

The cutting performance of two different geometries and PVD coatings, multilayer (Ti,Al,Cr)N (Tool 1) and monolayer TiAlN (Tool 2), coated on tungsten carbide tools was investigated during dry drilling of sustainable ADI material with strength properties similar to ASTM grade 1 ADI. The cutting performance was analyzed by tool wear analysis, specific cutting energy, surface roughness profile and chip morphology. Based on the results obtained, the following conclusions can be drawn:

1. Tool geometry and coating significantly influence the evolution of specific cutting energy and tool wear. The adhesion mechanism can be avoided using better geometry (enhanced chip transportation) and better wear resistant coating material. In case of tool 1, the combined influence of coating and geometry is responsible for the steady behavior of specific cutting energy with respect to number of drilled holes.

2. The tool 1 revealed significant resistance to the adhesion wear as compared to tool 2 due to the formation of aluminium and chromium oxides. The adhesion of workpiece material was observed in tool 2, mainly at the cutting edge; near the periphery and coating layer abraded off in case of tool 1.

3. In case of tool 1, at the chip back surfaces smooth fold type patterns are observed. On the other hand, for the tool 2, graphite micro-pores emerged at the back surface which, grow and coalesce during shear deformation reflects poor surface quality of the machined parts.

The multilayer (Ti,Al,Cr)N PVD coating seems to be suitable option for dry drilling machining process of novel ADI. It shows better adhesion resistance properties due to the formation of tribo-oxides films. The enhanced cutting performance of these coatings can be observed by the absence of deep crater wear at the outer corner of the cutting tool.

6.5   Conclusions

The dry machining characteristic of novel ADI was investigated for different cutting conditions in correlation with its microstructure and production parameters. It was found that the combination of the low feed rate and higher cutting speed leads to the higher mechanical and thermal loads on the tool's cutting edge, resulting in higher values of specific cutting force and specific cutting energy. The surface quality of machined surfaces significantly influenced by cutting speed as compared to the feed rate. The tool wear behavior under various cutting conditions revealed that the crater wear at the outer corner of the drill tool is the main wear mode under the influence of abrasive and adhesive wear during dry drilling of ADI. It was also found that mechanical properties of workpiece material, particularly, hardness and tensile strength have significant influence over the shear stress at the tool-chip contact interface which can further influence the cutting forces. It was observed that the austempering temperature significantly influence the machining characteristics of ADI as compared to the austempering time by changing the ferrite morphology in the ADI microstructure. The chip morphology characteristic was investigated for different cutting conditions during dry drilling of ADI. The fine lamella structures were observed at higher cutting speeds (60 and 90 m/min) for all feed rates. On the other hand, at lower cutting speed (30 m/min) a rough lamella structure was observed for all feed rates. The width and depth of lamella structure increases with an increase in feed rate and cutting speed, which leads to the formation of fragmentary chips with the saw-tooth. The obtained CCR values were found to be inversely proportional to the feed rate and directly proportional to the specific cutting energy. The relationship between specific cutting energy and CCR can be explained by the phenomenon known as size effect. The correlation between the chip micro-hardness, CCR values and cutting conditions were made to obtain the optimal cutting parameters for dry drilling of novel ADI. It can be seen that the higher productivity within the range of good machinability for novel ADI can be achieved by the choice of low CCR values and low specific cutting energy at the higher material removal rates.

The green manufacturing of ADI was promoted by the implementation of MQL drilling on ADI. The MQL machining condition appeared to be effective in reducing the surface roughness of the machined surfaces as compared to the dry machining conditions and comparable to the wet machining condition. In addition, the tool life was increased by 25%, and tool wear was reduced by 40% in case of MQL machining as compared to dry machining. In case of tool wear, the crater wear at the outer corner of the drill tool was the dominant wear mode in case of dry and MQL machining condition. The crater wear is the consequence of the higher frictional and adhesive characteristics at the tool-workpiece interface which further leads to the chipping of the cutting edge followed by damage at the outer corner of the drill tool. The dry drilling

process was further enhanced by use of multilayer (Ti,Al,Cr)N PVD coating, which provides significant resistance to the adhesion wear due to the formation of aluminium and chromium oxides.

Chapter 7

Main conclusions and perspectives

Main conclusions

The main objective of the thesis is to develop an innovative methodology for austempered ductile iron (ADI) manufacturing considering all production aspects such as melt treatment, casting, heat treatment and machining. Over the past decade, ADI emerged out as an excellent material due to its wide range of physical and mechanical properties. However, there are possibilities to further control and tailor ADI microstructure to get the desired mechanical properties and performance. Moreover, there is a need to reduce the environmental impacts of material production and processing, particularly those related to energy. Therefore, attention is required to develop an energy and material efficient approach for ADI manufacturing. With this viewpoint, an integrated casting-heat treatment process route is developed for near-net shape ADI casting production. The casting process is further optimized in correlation with the melt thermal characteristics. Finally, dry and near-dry machining of ADI is performed to adopt ecological machining. The following main conclusions can be drawn based on the research conducted in this thesis.

- The innovative process route led to the production of light weight near-net shape ADI casting having ausferrite microstructure (carbon enriched austenite and acicular ferrite) with high graphite nodule counts. High density of fine ferrite needles was observed at lower austempering temperature, whereas a coarse feathery ferrite characteristic was observed at higher austempering temperature. The quantitative estimation of the resultant ADI revealed an increase in ferritic cell size with austempering temperature due to rapid grain coarsening of ferrite. The lower values of retained austenite volume fraction and ferritic cell size at lower austempering temperature give rise to high strength ADI samples with lower ductility. The strain hardening behavior of the resultant ADI sample is influenced by its microstructural characteristics.

- Thermal analysis of the melt revealed the different temperature arrests depending on the evolution of different phases and graphite precipitation during solidification. The variation in the nature of alloy was found due to the variations in true eutectic point and carbon equivalent of the melt. Thermal characteristics of the melt are further used to perform the simulation analysis of mould filling and solidification. The simulation results show a progressive solidification behavior. The ratio of thermal modulus and solidification time which is directly proportional to heat transfer coefficient was found to decrease with time during solidification. This behavior can be explained by the formation of thin air film at the melt/mould interface, which decreases the heat transfer from the melt to the surrounding. The simulation analysis revealed the absence of porosity and shrinkage defects at the end of solidification. However, experimental results show porosity defects at the top section of the casting, which are considered as common defects in the gravity die casting process and can be explained due to entrainment defects caused by the folding action of the (oxidized) liquid surface during filling. Thus thermal analysis and simulation tools helps in improving the overall casting process during ADI production by providing the realistic thermal description of the melt and by predicting the porosity and shrinkage defects.

- The dry machining characteristics of novel ADI was investigated for different cutting conditions in correlation with its microstructure and production parameters. It was found that the combination of the low feed rate and higher cutting speed leads to the higher mechanical and thermal loads on the tool's cutting edge, resulting in higher values of specific cutting force and specific cutting energy. The surface quality of machined surfaces significantly influenced by cutting speed as compared to the feed rate. The tool wear behavior at various cutting condition revealed that the crater wear at the outer cutting edge is the main wear mode under the influence of abrasive and adhesive wear mechanism. Examinations of the wear surfaces at low material removal rate (30 m/min and 0.05 mm/rev) revealed the abrasion of the coating material at the outer corner of the drill tool and show the presence of built-up edge (BUE) at the cutting edge. The occurrence of small BUE at the cutting edge indicates the adhesion of workpiece material at the cutting edge. However, at higher material removal rate (90 m/min and 0.15 mm/rev), cracks appear on the wear surfaces which lead to sudden fracture of the drill tool at the outer edge. The presence of cracks on the tool wear surfaces indicates the high compressive stresses and temperature at the cutting edge which further lead to the plastic deformation of the cutting edge. EDS spectra of the fracture part revealed the presence of oxidized coating material (Al, Ti with high content of O). The fracture part also revealed the exposure of

the substrate material and adhesion of the workpiece material near the tool cutting edge (due to the presence of Fe, Si and high content of O).

- Designing the ADI microstructure to get the desired properties and performance significantly influences its machinability. The thesis demonstrated that machinability of ADI is strongly influenced by its austempering parameters (temperature and time). The correlation between cutting forces and material properties is established. Higher hardness and strength values results in higher thrust force values during machining. Moreover, it was found that ADI material produced at lower austempering temperature show poor machinability due to the higher ferrite content. The ferrite content leads to increase in chipping behavior and formation of built-up edges due to its higher tendency to adhere during machining.

- The chip morphology characteristics revealing fine lamella structures were observed at higher cutting speeds (60, 90 m/min) for all feed rates. The width and depth of the lamella structure increase with an increase in feed rate and cutting speed, which leads to the formation of fragmentary chips with the saw-tooth. The CCR values were found to be inversely proportional to the feed rate and directly proportional to the specific cutting energy. The correlation between the chip micro-hardness, CCR values and cutting conditions was made to obtain the optimal cutting parameters for dry drilling of novel ADI. It can be seen that higher productivity within the range of good machinability for novel ADI can be achieved by the choice of low CCR values and low specific cutting energy at higher material removal rates.

- The MQL machining significantly enhance the machinability of ADI compared to dry condition in terms of tool life and tool wear by providing the effective cooling and lubrication functions at the cutting zone. Moreover, it appeared to be effective in reducing the surface roughness of the machined surfaces as compared to the dry machining and comparable to the wet machining.

- The multilayer (Ti,Al,Cr)N PVD coating seems to be a suitable option for dry drilling of novel ADI. It shows better adhesion resistance properties due to the formation of tribo-oxides films. The enhanced cutting performance of coating can be observed by the absence of deep crater wear at the outer corner of the cutting tool.

Perspectives

The main objective of the present study has been accomplished. However, further steps are required for the optimization of ADI manufacturability. Therefore, based on the present study, suggestions are provided for future work and research regarding ADI manufacturing mainly focused on the melt treatment practices (spheroidization and inoculation), heat treatment and machining.

- The evolution of graphite morphology in a casting is the functions of casting section size and melt treatment practices. The melt control for ductile iron includes spheroidization and inoculation practices responsible for the production of sound ductile iron casting with the desired structure and required properties. However, the influence of inoculation on the graphite nodularity still needs to be addressed properly in correlation with under-cooling and graphite nucleation during solidification.

- Scaling of the ADI production is required using the innovative integrated casting-heat treatment route for mass exploitation of ADI materials. However, this step requires effective melt treatment practices. The melt treatment practices are critical and their effects faded over time, which depends on the melt and inoculant compositions, pouring temperature and melt velocity. This step further controls the solidification characteristic of the melt. Therefore, in order to achieve the effectiveness of the melt treatment practices at large-scale production, the melt treatment equipment must be reliable under the extreme operating conditions found during the melt treatment and pouring.

- ADI is considered as hard to machine material due to its microstructure induced inherent properties. In order to understand the machining characteristic of ADI materials, there is a need to develop FEM based simulation tool taking into account the microstructural characteristics (ausferrite matrix and graphite nodule) of ADI. This tool can be used to determine the chip formation mechanisms as well as stress and temperature distribution. Moreover, it can be further utilized to understand the influence of tool's geometry, tool wear behavior and cutting conditions to optimize the ADI machining process.

Appendix A

Foundry procedure for ADI production

Step 1: Primary data

1. Reference and date of casting.

Date of casting:	DD-MM-YYYY		Casting reference:	Austempered Ductile Iron (ADI)

Melt Quantity:	80	kg

2. The required chemical composition of the final obtained casting.

Required composition:

	C	Si	Mn	Cu	Ni	Mo	S	P	Cr	Al
wt%	3.55	2.7	0.23	0.75	0.55	0.2	0.01	0.05	0.03	0.01

3. The charge materials and their respective compositions.

Charge materials:

	Name/Source	Date
Iron alloy 1	Grade TF10 / Fonderie Nicolas	
Steel	Fonderie Abilly	
Iron alloy 2	Fonte ADI Bielles	
Iron alloy 3	Fonte ADI UCOFAM / ADJ	
Re-carburizer	Desulco®	
FeSi	F.G. Ferrosilicium (Elkem)	
Cu	Fil de cuivre	
Ni		
Fe-Mo	Fe-Mo 70 %	

Charge materials composition:

	C	Si	Mn	Cu	Ni	Mo	S	P	Cr	Al
Iron alloy 1	4.1	1.58	0.049				0.01	0.045		
Steel	0.061	0.036	0.275	0.055	0.034	0.004	0.005	0.012	0.022	0.036
Iron alloy 2	3.54	2.5	0.27	1.23	0.66	0.27	0.01	0.06	0.06	0.01
Iron alloy 3	3.61	2.45	0.26	1.2	0.7	0.3	0.01	0.07	0.07	0.015
Re-carburizer	99.6						0.08			
FeSi	0.05	75					0.08	0.019		0.1
Cu				99.9						
Ni					99.9					
Fe-Mo						68				

4. The melt treatment practice.

Melt treatment:

Mould reference:	1					

Ref. Spheroidisers	FeSiMg Mg/63 3-25 mm					
Composition %	Fe	Si	Mg	Al	Ca	TR
	44.24	44.85	6.13	0.94	2.94	0.9

Casting mass	3	kg
% Mg	0.035	

Step 2: Calculation

1. The yield % of charge materials and alloying elements.

Yield table (%)

	C	Si	Mn	Cu	Ni	Mo	S	P	Cr	Al
Iron alloy 1	90%	92%	98%				90%	98%		
Steel	90%	92%	98%	98%	98%	98%	90%	98%	98%	90%
Iron alloy 2	92%	92%	98%	98%	98%	98%	90%	98%	98%	90%
Iron alloy 3	92%	92%	98%	98%	98%	98%	90%	98%	98%	90%
Re-carburizer	85%						90%			
FeSi	95%	90%					95%	98%		90%
Cu				99.9%						
Ni					99.9%					
Fe-Mo						90%				

2. The distribution of the charge materials to get the required composition.

First approach:

Data:

M1	32	kg	Iron alloy 1
M2	16	kg	Steel
M3	16	kg	Iron alloy 2
M4	16	kg	Iron alloy 3
	80		

3. The chemical composition control calculation and the amount of the required materials to get the theoretical chemical composition.

M5	0.804	kg	Re-carburizer
M6	0.955	kg	FeSi
M7	0.228	kg	Cu
M8	0.235	kg	Ni
M9	0.122	kg	FeMo

M_{tot}	82.344	kg

Calculate

4. The detail compositions list before (Initial composition) and after (Final composition) the addition of alloying elements to get the required chemical composition.

	C	Si	Mn	Cu	0	Mo	S	P	Cr	Al
Initial composition	2.72	1.92	0.17	0.47	0.27	0.11	0.01	0.04	0.03	0.01
Final composition	3.55	2.70	0.17	0.75	0.55	0.20	0.01	0.04	0.03	0.01
Required composition	3.55	2.7	0.23	0.75	0.55	0.2	0.01	0.05	0.03	0.01

5. The final list of the charge materials and alloying elements to get the required chemical composition for ADI foundry.

Iron alloy 1	32 kg
Steel	16 kg
Iron alloy 2	16 kg
Iron alloy 3	16 kg
Re-carburizer	0.804 kg
FeSi	0.955 kg
Cu	0.228 kg
Ni	0.235 kg
FeMo	0.122 kg

masse totale	82.344 kg

Print

	C	Si	Mn	Cu	0	Mo	S	P	Cr	Al
Final composition	3.55	2.70	0.17	0.75	0.55	0.20	0.01	0.04	0.03	0.01
Required composition	3.55	2.7	0.23	0.75	0.55	0.2	0.01	0.05	0.03	0.01

Step 3: Magnesium treatment of ductile iron using tundish ladle apparatus

1. Measure the Mg quantity required for the spherodization process.

2. Tundish ladle apparatus assembly
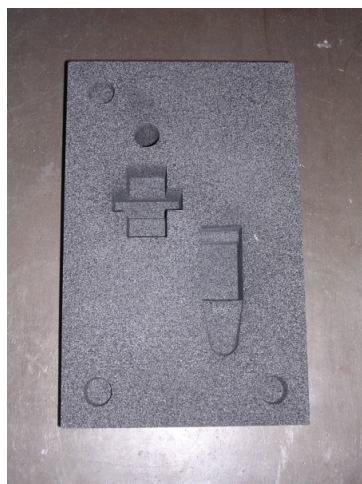
(a) Bottom part
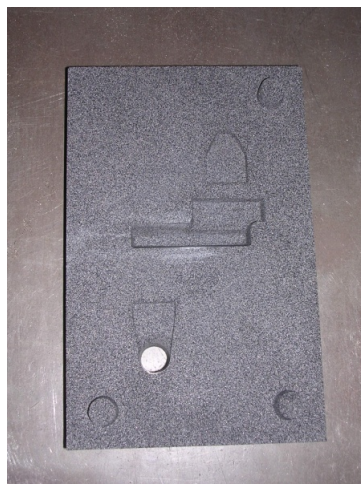
(b) Top part
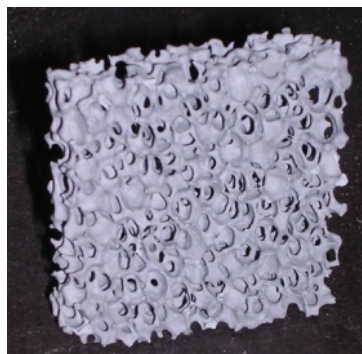
(c) Filter

(d) Pouring cup

3. Preparation of tundish ladle apparatus.
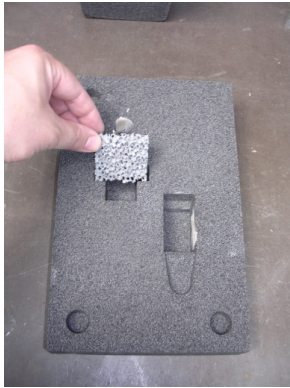
(a)
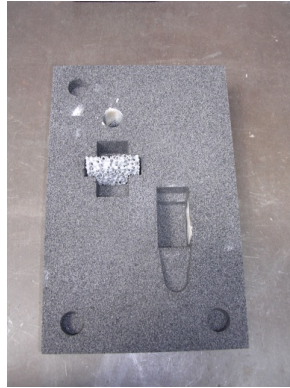
(b)
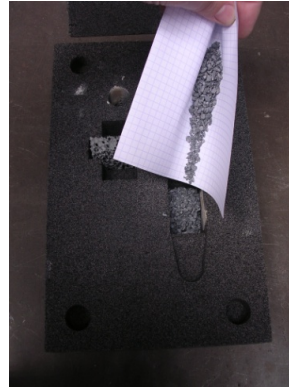
(c)

(d)

(e)
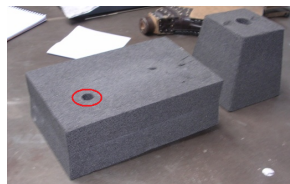
(f)

(g)
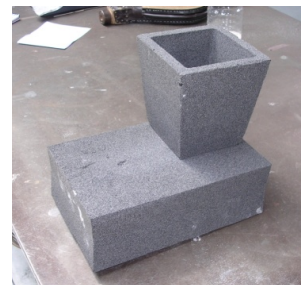
(h)

Appendix B

Publications and Scientific communications

Refereed journal publications

1. **Meena, A.**, Mansori, M.El, 2012. Material characterization of Austempered Ductile Iron (ADI) produced by a sustainable continuous casting-heat treatment process. Metallurgical and Materials Transactions A: vol. 43(12), pp. 4755-4766.

2. **Meena, A.**, Mansori, M.El, 2012. Correlative thermal methodology for castability simulation of ductile iron in ADI production. Journal of Materials Processing and Technology: vol. 212(11), pp. 2484-2495.

3. **Meena, A.**, Mansori, M.El, 2012. Drilling performance of green Austempered Ductile Iron (ADI) grade produced by novel manufacturing technology. International Journal of Advanced Manufacturing Technology: vol. 59(1), pp. 9-19.

4. **Meena, A.**, Mansori, M.El, 2011. Study of dry and minimum quantity lubrication drilling of novel austempered ductile iron (ADI) for automotive applications. Wear: vol. 271(9-10), pp. 2412-2416.

Refereed conference proceedings

1. **Meena, A.**, Mansori, M.El, 2012. Chip morphology characteristics during dry drilling of austempered ductile iron (ADI). Transactions of the North American Manufacturing Research Institute of SME 40 (NAMRC 40), Indiana, USA, pp. 414-422.

2. **Meena, A.**, Mansori, M.El, Ghidossi, P., Mkaddem, A., 2011. Anti-friction coating for drilling of green Austempered Ductile Iron (ADI) grade. AIP Conference Proceedings of ESAFORM (1353), Belfast, UK, pp. 1800-1805.

3. **Meena, A.**, Mansori, M.El, Ghidossi, P., 2010. Machinability of austempered ductile iron (ADI) produced by integrated green technology of continuous casting and heat treatment processes. AIP Conference Proceedings of AMPT (1315), Paris, France, pp. 1521-1526.

International conference oral presentations

1. **Meena, A.**, Mansori, M.El., 2012. Chip morphology characteristics during dry drilling of austempered ductile iron (ADI). Transactions of the North American Manufacturing Research Institute of SME 40 (NAMRC 40), Indiana, USA.

2. **Meena, A.**, Mansori, M.El., 2012. Cutting performance of PVD coatings during dry drilling of sustainable austempered ductile iron (ADI). ICMCTF 2012, San Diego, USA.

3. **Meena, A.**, Mansori, M.El., 2012. Study of dry and minimum quantity lubrication drilling of novel austempered ductile iron (ADI) for automotive applications. WOM 2011, Philadelphia, USA.

4. **Meena, A.**, Mansori, M.El., Ghidossi, P., Mkaddem, A., 2011. Anti-friction coating for drilling of green Austempered Ductile Iron (ADI) grade. ESAFORM 2011, Belfast, UK.

5. **Meena, A.**, Mansori, M.El., Ghidossi, P., 2010. Machinability of austempered ductile iron (ADI) produced by integrated green technology of continuous casting and heat treatment processes. AMPT 2010, Paris, France.

Patent

1. **Meena, A.**, Mansori, M.El., A novel process route for light weight austempered ductile iron (ADI) casting production using integrated casting-heat treatment technology (Under examination).

Bibliography

[1] K. Marukawa and K. L. Edwards, "Development of iron and steel into eco-material," *Materials and Design*, vol. 22, no. 2, pp. 133–136, 2000.

[2] K. L. Edwards, "Strategic substitution of new materials for old: Applications in automotive product development," *Materials and Design*, vol. 25, no. 6, pp. 529–533, 2004.

[3] M. I. Onsoien, O. Grong, O. Gundersen, and T. Skaland, "A process model for the microstructure evolution in ductile cast iron: Part I. the model," *Metallurgical and Materials Transactions A*, vol. 30, no. 4, pp. 1053–1068, 1999.

[4] J. Yang and S. K. Putatunda, "Improvement in strength and toughness of austempered ductile cast iron by a novel two-step austempering process," *Materials and Design*, vol. 25 (3), pp. 219–230, 2004.

[5] A. Trudel and M. Gagne, "Effect of composition and heat treatment parameters on the characteristics of austempered ductile irons," *Canadian Metallugical Quarterly*, vol. 36 (5), pp. 289–298., 1997.

[6] L. C. Chang, "Carbon content of austenite in austempered ductile iron," *Scripta Materialia*, vol. 39, no. 1, pp. 35–38, 1998.

[7] A. A. Nofal and L. Jekova, "Novel processing techniques and applications of austempered ductile iron (review)," *Journal of the University of Chemical Technology and Metallurgy*, vol. 44(3), pp. 213–228, 2009.

[8] J. Zimba, D. J. Simbi, and E. Navara, "Austempered ductile iron: An alternative material for earth moving components," *Cement and Concrete Composites*, vol. 25 (6), pp. 643–649, 2003.

[9] U. R. Kumari and P. P. Rao, "Study of wear behaviour of austempered ductile iron," *Journal of Materials Science*, vol. 44(4), pp. 1082–1093, 2009.

[10] I. Rio Tinto Iron & Titanium, "Ductile iron data for design engineers," tech. rep., Soremetal, 1998.

[11] M. F. Ashby, *Materials Selection in Mechanical Design, Third edition.* Butterworth-Heinemann, Oxford, UK, 2005.

[12] J. M. Allwood and M. C. Jonathan, *Sustainable Materials - with both eyes open.* UIT Cambridge Ltd., Cambridge, England, 2012.

[13] H. K. Tonshoff, W. Spintig, W. Konig, and A. Neises, "Machining of holes developments in drilling technology," *CIRP Annals - Manufacturing Technology*, vol. 43, no. 2, pp. 551–561, 1994.

[14] J. R. Davis, ed., *Cast Irons: ASM specialty handbook.* ASM International, 1996.

[15] S. Lampman, ed., *Casting Design and Performance.* ASM International, 2009.

[16] J. R. Davis, ed., *Alloying: Understanding the Basics.* ASM International, 2001.

[17] W. D. Callister, *Fundamentals of Materials Science and Engineering (5th Edition).* John Wiley & Sons, Inc., 2001.

[18] R. E. Smallman and R. J. Bishop, *Modern Physical Metallurgy and Materials Engineering-Science, Process, Applications (6th Edition).* Butterworth-Heinemann, Woburn, MA, 1999.

[19] A. Basso, M. Caldera, M. Chapetti, and J. Sikora, "Mechanical characterization of dual phase austempered ductile iron," *ISIJ International*, vol. 50, no. 2, pp. 302–306, 2010.

[20] F. Klocke, M. Arft, and D. Lung, "Material-related aspects of the machinability of austempered ductile iron," *Production Engineering*, vol. 4 (5), pp. 433–441, 2010.

[21] T. Skaland, O. Grong, and T. Grong, "A model for the graphite formation in ductile cast iron: Part i. inoculation mechanisms," *Metallurgical and Materials Transactions A*, vol. 24A, pp. 2321–2345, 1993.

[22] D. M. Stefanescu, ed., *ASM handbook (Volume 15: Casting).* ASM International, 1998.

[23] D. M. Stefanescu, "Solidification and modeling of castiron-a short history of the defining moments," *Materials Science and Engineering: A*, vol. 413-414, pp. 322–333, 2005.

[24] J. R. Brown, ed., *Foseco Ferrous Foundrymans Handbook.* Butterworth-Heinemann, Woburn, MA, 2000.

[25] B. Y. Lin, E. T. Chen, and T. S. Lei, "The effect of alloy elements on the microstructure and properties of austempered ductile irons," *Scripta Metallurgica et Materiala*, vol. 32 (9), pp. 1363–1367, 1995.

[26] J. O. Choi, J. Y. Kim, C. O. Choi, J. K. Kim, and P. K. Rohatgi, "Effect of rare earth element on microstructure formation and mechanical properties of thin wall ductile iron castings," *Materials Science and Engineering A*, vol. 383, no. 2, pp. 323–333, 2004.

[27] S. Bockus and A. Dobrovolskis, "Effect of melting techniques on ductile iron castings properties," *Metalurgija*, vol. 45, no. 1, pp. 13–16, 2006.

[28] M. H. Jacobs, T. J. Law, D. A. Melford, and M. J. Stowell, "Basic processes controlling the nucleation of graphite nodules in chill cast iron," *Met Technol*, vol. 1 (2), pp. 490–500, 1974.

[29] M. Wessen and I. L. Svesson, *Handbook of Mechanical Alloy Design*. Marcel Dekker, Inc., New York, 2004.

[30] A. Boudot, V. Gerval, D. Oquab, J. Lacaze, and H. Santos, "The role of manganese and copper in the eutectoid transformation of spheroidal graphite cast iron," *Metallurgical and Materials Transactions A*, vol. 28, pp. 2015–2025, 1997.

[31] C. V. White, R. A. Flinn, and P. K. Trojan, "An investigation of three different methods of nodularity evaluation in ductile cast iron," *American Foundrymen's Society, Transactions*, vol. 89, pp. 639–644, 1981.

[32] I. Riposan, M. Chisamera, S. Stan, T. Skaland, and M. Onsoien, "Analysis of possible nucleation sites in Ca/Sr over-inoculated grey irons," *AFS Transactions*, vol. 109, pp. 1151–1162, 2001.

[33] K. M. Pedersen and N. S. Tiedje, "Graphite nodule count and size distribution in thin-walled ductile cast iron," *Materials Characterization*, vol. 59 (8), pp. 1111–1121, 2008.

[34] P. A. Blackmore and R. A. Hardning, "The effects of metallurgical process variables on the properties of austempered ductile irons," *Journal of Heat Treating*, vol. 3 (4), pp. 310–325., 1984.

[35] U. Batra, S. Ray, and S. R. Prabhakar, "Mathematical model for austenitization kinetics of ductile iron," *Journal of Materials Engineering and Performance*, vol. 14 (5), pp. 574–581, 2005.

[36] U. Batra, S. Ray, and S. R. Prabhakar, "Effect of austenitization on austempering of copper alloyed ductile iron," *Journal of Materials Engineering and Performance*, vol. 12 (5), pp. 597–601, 2003.

[37] M. Erdogan, V. Kilicli, and B. Demir, "Transformation characteristics of ductile iron austempered from intercritical austenitizing temperature ranges," *Journal of Materials Science*, vol. 44(5), pp. 1394–1403, 2009.

[38] J. Achary and D. Venugopalan, "Microstructural development and austempering kinetics of ductile iron during thermomechanical processing," *Metallurgical and Materials Transactions A*, vol. 31 (10), pp. 2575–2585, 2000.

[39] Y. Amran, A. Katsman, P. Schaaf, and M. Bamberger, "Influence of copper addition and temperature on the kinetics of austempering in ductile iron," *Metallurgical and Materials Transactions B*, vol. 41 (5), pp. 1052–1058., 2010.

[40] R. Gregorutti, K. Laneri, J. Desimoni, and R. C. Mercader, "Study of the austempering transformation kinetics in compacted graphite cast irons," *Metallurgical and Materials Transactions A*, vol. 35 A, no. 1, pp. 103–110, 2004.

[41] R. W. Cahn and P. Haansen, eds., *Physical Metallurgy (Fourth Edition)*. North-Holland, Amsterdam, 1996.

[42] N. Darwish and R. Elliott, "Austempering of low manganese ductile irons," *Materials Science and Technology*, vol. 9, no. 7, pp. 572–585, 1993.

[43] N. Darwish and R. Elliott, "Austempering of low manganese ductile irons Part 2 Influence of austenitising temperature," *Materials Science and Technology*, vol. 9, no. 7, pp. 586–602, 1993.

[44] M. Bahmani, R. Elliott, and N. Varahram, "The austempering kinetics and mechanical properties of an austempered Cu-Ni-Mo-Mn alloyed ductile iron," *Journal of Materials Science*, vol. 32 (18), pp. 4783–4791, 1997.

[45] F. Klocke, *Manufacturing Processes 1: Cutting (RWTH Edition)*. Springer-Verlag Berlin Heidelberg, 2011.

[46] L. Sidjanin, M. Novovic, and R. E. Smallman, "Metallographic investigations of adi materials," *Practical Metallography*, vol. 33(1), pp. 2–16, 1996.

[47] S. Shepperson and C. Allen, "The abrasive wear behaviour of austempered spheroidal cast irons," *Wear*, vol. 121, no. 3, pp. 271–287, 1988.

[48] P. Dhanapal and S. S. Mohamed Nazirudeen, "Multi-response optimization of carbidic austempered ductile iron production parameters using taguchi technique," *Journal of Scientific and Industrial Research*, vol. 70 (4), pp. 284–288, 2011.

[49] B. V. Kovacs, "Austempered ductile iron: Fact and fiction," *Modern Casting*, pp. 38–41, 1990.

[50] R. Castillo, V. Bermont, and V. Martinez, "Relationships between microstructure and mechanical properties in ductile cast irons: A review.," *Revista de Metalurgia (Madrid)*, vol. 35 (5), pp. 329–334, 1999.

[51] *Standard specification for austempered ductile iron castings.* ASTM Standard A897/A 897M, ASTM International, West Conshohocken, PA, United States, 2003.

[52] U. Batra, S. Ray, and S. R. Prabhakar, "The influence of nickel and copper on the austempering of ductile iron," *Journal of Materials Engineering and Performance*, vol. 13, no. 1, pp. 64–68, 2004.

[53] B. Bosnjak, V. Asanovic, B. Radulovic, and K. Pop-Tonev, "Influence of microalloying and heat treatment on the kinetics of bainitic reaction in austempered ductile iron," *Journal of Materials Engineering and Performance*, vol. 10, pp. 203–211, 2001.

[54] J. Schissler and J. Saverna, "The effect of segregation on the formation of austempered ductile iron," *Journal of Heat Treating*, vol. 4, pp. 167–176, 1985.

[55] B. Avishan, S. Yazdani, and D. Jalali-Vahid, "The influence of depth of cut on the machinability of an alloyed austempered ductile iron," *Materials Science and Engineering A*, vol. 523 (1-2), pp. 93–98, 2009.

[56] M. A. Yescas, H. K. D. H. Bhadeshia, and D. J. MacKay, "Estimation of the amount of retained austenite in austempered ductile irons using neural networks," *Materials Science and Engineering: A*, vol. 311, no. 12, pp. 162–173, 2001.

[57] M. C. Cakir, A. Bayram, Y. Isik, and B. Salar, "The effects of austempering temperature and time onto the machinability of austempered ductile iron," *Materials Science and Engineering A*, vol. 407 (1-2), pp. 147–153, 2005.

[58] Y. Isik, "Investigating the machinability of tool steels in turning operations," *Materials and Design*, vol. 28 (5), pp. 1417–1424, 2007.

[59] S. Dolinsek, "Work-hardening in the drilling of austenitic stainless steels," *Journal of Materials Processing Technology*, vol. 133, no. 1-2, pp. 63–70, 2003.

[60] S. K. Putatunda, S. Kesani, R. Tackett, and G. Lawes, "Development of austenite free ADI (austempered ductile cast iron)," *Materials Science and Engineering A*, vol. 435-436, pp. 112–122, 2006.

[61] K. Katuku, A. Koursaris, and I. Sigalas, "Wear, cutting forces and chip characteristics when dry turning ASTM Grade 2 austempered ductile iron with PcBN cutting tools under finishing conditions," *Journal of Materials Processing Technology*, vol. 209, no. 5, pp. 2412–2420, 2009.

[62] V. P. Astakhov, *Tribology of metal Cutting.* Elsevier Ltd, London, UK., 2006.

[63] R. O. Marwanga, R. C. Voigt, and P. H. Cohen, "Influence of graphite morphology and matrix structure on chip formation during machining of gray irons," *AFS Transactions*, vol. 107, pp. 595–607, 1999.

[64] D. F. Klocke, C. Klopper, D. Lung, and C. Essig, "Fundamental wear mechanisms when machining austempered ductile iron (ADI)," *CIRP Annals - Manufacturing Technology*, vol. 56, no. 1, pp. 73–76, 2007.

[65] J. P. Davim, ed., *Machining: Fundamentals and Recent Advances.* Springer-Verlag, London, 2008.

[66] A. M. Bayer, B. A. Becherer, and T. Vasco, *ASM handbook (Volume 16: Machining).* ASM International, 1998.

[67] J. P. Davim, ed., *Machining of Hard Materials.* Springer-Verlag London Limited, 2011.

[68] M. I. Sadik and T. Myrtveit, "The performance of PVD coated grade in milling of ADI 800," *World Academy of Science, Engineering and Technology*, vol. 53, pp. 527–530, 2009.

[69] F. Klocke and C. Klopper, *Machinability characteristics of Austempered Ductile Iron (ADI).* World Conference on ADI, Louisville, Kentucky, USA, 2002.

[70] M. Masuda, T. Sato, T. Kori, and Y. Chujo, "Cutting performance and wear mechanism of alumina-based tools when machining austempered ductile iron," *Wear*, vol. 174, pp. 147–153, 1994.

[71] V. A. M. Cristino, P. A. R. Rosa, and P. A. F. Martins, "Cutting under active and inert gas shields: A contribution to the mechanics of chip flow," *International Journal of Machine Tools and Manufacture*, vol. 50, no. 10, pp. 892–900, 2010.

[72] M. Goldberg, J. T. Berry, G. Littlefair, and G. Smith, "A study of the machinability of an astm grade 3 austempered ductile iron.," in *Proceedings of the 2002 World Conference on ADI for Casting Producers, Suppliers and Design Engineers, Ductile Iron Society and American Foundry Society, Galt House Hotel, Louisville, Kentucky, USA.*, 2002.

[73] K. Katuku, A. Koursaris, and I. Sigalas, "Wear mechanisms of PcBN cutting tools when dry turning ASTM Grade 2 austempered ductile iron under finishing conditions," *Wear*, vol. 268 (1), pp. 294–301, 2010.

[74] U. I. Aslantas, K and, "The performance of ceramic and cermet cutting tools for the machining of austempered ductile iron and," *International Journal of Advanced Manufacturing Technology*, vol. 41 (7-8), pp. 642–650, 2009.

[75] F. Klocke, "Dry cutting (keynote papers)," *CIRP Annals - Manufacturing Technology*, vol. 46 (2), pp. 519–526, 1997.

[76] A. Meena and M. El Mansori, "Study of dry and minimum quantity lubrication drilling of novel austempered ductile iron (ADI) for automotive applications," *Wear*, vol. 271, no. 9-10, pp. 2412–2416, 2011.

[77] H. K. Tonshoff and A. Mohlfeld, "PVD-coatings for wear protection in dry cutting operations," *Surface and Coatings Technology*, vol. 93, pp. 88–92, 1997.

[78] P. Beeley, *Foundry Technology (Second edition)*. Butterworth-Heinemann, Woburn, MA, 2001.

[79] S. O. Seidu and I. Riposan, "Thermal analysis of inoculated ductile irons," *U.P.B. Sci. Bull., Series B*, vol. 73, pp. 241–254, 2011.

[80] H. Cruz, C. Gonzalez, A. Juarez, M. Herrera, and J. Juarez, "Quantification of the microconstituents formed during solidification by the newton thermal analysis method," *Journal of Materials Processing Technology*, vol. 178 (1-3), pp. 128–134., 2006.

[81] J. Sertucha, R. Suárez, I. Asenjo, P. L. naga, J. Lacaze, I. naki Ferrer, and S. Armendariz, "Thermal analysis of the formation of chunky graphite during solidification of heavy-section spheroidal graphite iron parts," *ISIJ International*, vol. 49, no. 2, pp. 220–228, 2009.

[82] R. Zhou, Y. Jiang, D. Lu, R. Zhou, and Z. Li, "Development and characterization of a wear resistant bainite/martensite ductile iron by combination of alloying and a controlled cooling heat-treatment," *Wear*, vol. 250, no. 112, pp. 529–534, 2001.

[83] *Metallic materials-Tensile testing-Part 1: Method of test at room temperature.* ISO 6892-1, International Standards for Business, Government and Society, 2009.

[84] G. Dieter, *Mechanical Metallurgy, SI Metric Edition.* McGraw-Hill, UK, 1988.

[85] S. Zhou, K. Zhang, Y. Wang, J. Gu, and Y. Rong, "The mechanism of high strength-ductility steel produced by a novel quenching-partitioning-tempering process and the mechanical stability of retained austenite at elevated temperatures," *Metallurgical and Materials Transactions A*, vol. 43, pp. 1026–1034, 2012.

[86] Y. Waseda, E. Matsubara, and K. Shinoda, *X-Ray Diffraction Crystallography.* Springer, New York, 2011.

[87] S. K. Putatunda and P. K. Gadicherla, "Influence of austenitizing temperature on fracture toughness of a low manganese austempered ductile iron (ADI) with ferritic as cast structure," *Materials Science and Engineering: A*, vol. 268, no. 12, pp. 15–31, 1999.

[88] J. M. Allwood, M. F. Ashby, T. G. Gutowski, and E. Worrell, "Material efficiency: A white paper," *Resources, Conservation and Recycling*, vol. 55, pp. 362–381, 2011.

[89] S. Vinodh and K. Jayakrishna, "Environmental impact minimisation in an automotive component using alternative materials and manufacturing processes," *Materials & Design*, vol. 32(10), pp. 5082–5090, 2011.

[90] J. F. Janowak and R. B. Gundlach, "Approaching austempered ductile iron properties by controlled cooling in the foundry," *Journal of Heat Treating*, vol. 4 (1), pp. 25–31, 1985.

[91] A. Meena and M. El Mansori, "Drilling performance of green austempered ductile iron (ADI) grade produced by novel manufacturing technology," *International Journal of Advanced Manufacturing Technology*, vol. 59, no. 1-4, pp. 9–19, 2012.

[92] E. Haruman, Y. Sun, A. Triwiyanto, Y. H. P. Manurung, and E. Y. Adesta, "An investigation on low-temperature thermochemical treatments of austenitic stainless steel in fluidized bed furnace.," *Journal of Materials Engineering and Performance*, vol. 21 (3), pp. 388–394, 2012.

[93] F. Salazar, M. Herrera-Trejo, M. Castro, N. J. Mendez, T. J. Torres, and N. M. Mendez, "Effect of nodule count and cooling rate on as-cast matrix of a Cu-Mo spheroidal graphite," *Journal of Materials Engineering and Performance*, vol. 8 (3), pp. 325–329, 1999.

[94] U. Seker and H. Hasirci, "Evaluation of machinability of austempered ductile irons in terms of cutting forces and surface quality," *Journal of Materials Processing Technology*, vol. 173 (3), pp. 260–268, 2006.

[95] P. R. Rao and S. K. Putatunda, "Investigations on the fracture toughness of austempered ductile irons austenitized at different temperatures," *Materials Science and Engineering: A*, vol. 349, no. 12, pp. 136–149, 2003.

[96] P. Jacques, F. Delannay, X. Cornet, P. Harlet, and J. Ladriere, "Enhancement of the mechanical properties of a low-carbon, low-silicon steel by formation of a multiphased microstructure containing retained austenite," *Metallurgical and Materials Transactions A*, vol. 29, pp. 2383–2393, 1998.

[97] D. Drobnjak and J. Parr, "Deformation substructure and strain-hardening characteristics of metastable fe-mn austenites," *Metallurgical and Materials Transactions B*, vol. 1, pp. 759–765, 1970.

[98] M. R. Barkhudarov and C. W. Hirt, "Casting simulation: mold filling and solidification-benchmark calculations using FLOW-3D," tech. rep., Flow Science, Inc., 1993.

[99] S. V. Shepel and S. Paolucci, "Numerical simulation of filling and solidification of permanent mold castings," *Applied Thermal Engineering*, vol. 22 (2), pp. 229–248, 2002.

[100] F. Lau, W. B. Lee, S. M. Xiong, and B. C. Liu, "A study of the interfacial heat transfer between an iron casting and a metallic mould," *Journal of Materials Processing Technology*, vol. 79 (1-3), pp. 25–29, 1998.

[101] C. A. Santos, J. M. V. Quaresma, and A. Garcia, "Determination of transient interfacial heat transfer coefficients in chill mold castings," *Journal of Alloys and Compounds*, vol. 319 (1-2), pp. 174–186, 2001.

[102] N. Pathak, A. Kumar, A. Yadav, and P. Dutta, "Effects of mould filling on evolution of the solid-liquid interface during solidification," *Applied Thermal Engineering*, vol. 29 (17-18), pp. 3669–3678, 2009.

[103] M. M. Pariona and A. C. Mossi, "Numerical simulation of heat transfer during the solidification of pure iron in sand and mullite molds," *Journal of the Brazilian Society of Mechanical Sciences and Engineering*, vol. 27 (4), pp. 399–406, 2005.

[104] Q. Han and H. Xu, "Fluidity of alloys under high pressure die casting conditions," *Scripta Materialia*, vol. 53 (1), pp. 7–10, 2005.

[105] K. R. Ravi, R. M. Pillai, K. R. Amaranathan, B. C. Pai, and M. Chakraborty, "Fluidity of aluminum alloys and composites: A review," *Journal of Alloys and Compounds*, vol. 456 (1-2), pp. 201–210, 2008.

[106] M. A. Gafur, M. N. Haque, and K. N. Prabhu, "Effect of chill thickness and superheat on casting/chill interfacial heat transfer during solidification of commercially pure aluminium," *Journal of Materials Processing Technology*, vol. 133 (3), pp. 257–265, 2003.

[107] J. Sengupta, B. Thomas, and M. Wells, "The use of water cooling during the continuous casting of steel and aluminum alloys," *Metallurgical and Materials Transactions A: Physical Metallurgy and Materials Science*, vol. 36 A, no. 1, pp. 187–204, 2005.

[108] T. R. Vijayaram, S. Sulaiman, A. M. S. Hamouda, and M. H. M. Ahmad, "Numerical simulation of casting solidification in permanent metallic molds," *Journal of Materials Processing Technology*, vol. 178 (1-3), pp. 29–33, 2006.

[109] D. Emadi, L. V. Whiting, S. Nafisi, and R. Ghomashchi, "Applications of thermal analysis in quality control of solidification processes," *Journal of Thermal Analysis and Calorimetry*, vol. 81 (1), pp. 235–242, 2005.

[110] A. Kermanpur, S. Mahmoudi, and A. Hajipour, "Numerical simulation of metal flow and solidification in the multi-cavity casting moulds of automotive components," *Journal of Materials Processing Technology*, vol. 206 (1-3), pp. 62–68, 2008.

[111] G. Miller, "Control volume meshes using sphere packing," *In: Solving Irregularly Structured Problems in Parallel*, vol. 1457, pp. 128–131, 1998.

[112] D. V. Alexandrov, "Theory of solidification with a quasi-equilibrium two-phase zone," *Doklady Physics*, vol. 45 (11), pp. 569–573, 2000.

[113] D. V. Alexandrov, "On the theory of the formation of the two-phase concentration-supercooling region," *Doklady Physics*, vol. 48 (9), pp. 481–486, 2003.

[114] D. V. Alexandrov, "Solidification with a quasiequilibrium two-phase zone," *Acta Materialia*, vol. 49 (5), pp. 759–764, 2001.

[115] W. D. Griffiths, "A model of the interfacial heat-transfer coefficient during unidirectional solidification of an aluminum alloy," *Metallurgical and Materials Transactions B*, vol. 31 (2), pp. 285–295, 2000.

[116] M. D. Chaudhari, R. W. Heine, and C. R. Loper Jr., "Principles involved in the use of cooling curves in ductile iron process control," *Trans Am Foundrymen's Soc*, vol. 82, pp. 431–440, 1974.

[117] J. Campbell, *Castings practice*. Butterworth-Heinemann, UK, 2004.

[118] J. Campbell, *Castings, Second edition*. Butterworth-Heinemann, UK, 2003.

[119] A. K. Jha, R. Asthana, T. K. Dan, and P. K. Rohatgi, "Effect of dispersed graphite on the freezing rate of gravity die-cast lm 13 alloy-3 wt particle composite," *Journal of Materials Science Letters*, vol. 6, pp. 225–228, 1987.

[120] W. Jiang, J. Dong, L. Wang, and L. Lou, "Effect of casting modulus on microstructure and segregation in k441 superalloy casting," *Journal of Materials Science & Technology*, vol. 27, no. 9, pp. 831–840, 2011.

[121] K. Ho and R. Pehlke, "Metal-mold interfacial heat transfer," *Metallurgical and Materials Transactions B*, vol. 16, pp. 585–594, 1985.

[122] K. D. Carlson and C. Beckermann, "Prediction of shrinkage pore volume fraction using a dimensionless niyama criterion," *Metallurgical and Materials Transactions A*, vol. 40 (1), pp. 163–175, 2009.

[123] K. D. Carlson, S. Ou, R. A. Hardin, and C. Beckermann, "Development of new feeding-distance rules using casting simulation: Part i. methodology," *Metallurgical and Materials Transactions B*, vol. 33 (5), pp. 731–740, 2002.

[124] K. Kubo and R. D. Pehlke, "Mathematical modeling of porosity formation in solidification," *Metallurgical Transactions B*, vol. 16 (2), pp. 359–366, 1985.

[125] J. P. Davim, P. S. Sreejith, R. Gomes, and C. Peixoto, "Experimental studies on drilling of aluminium (AA1050) under dry, minimum quantity of lubricant, and flood-lubricated conditions," *Proceedings of the Institution of Mechanical Engineers, Part B: Journal of Engineering Manufacture*, vol. 220, no. 10, pp. 1605–1611, 2006.

[126] J. P. Davim, P. Reis, and C. C. Antonio, "Experimental study of drilling glass fiber reinforced plastics (GFRP) manufactured by hand lay-up," *Composites Science and Technology*, vol. 64, no. 2, pp. 289–297, 2004.

[127] P. S. Sreejith, R. Krishnamurthy, and S. K. Malhotra, "Effect of specific cutting pressure and temperature during machining of carbon/phenolic ablative composite using pcbn tools," *Journal of Materials Processing Technology*, vol. 183, pp. 88–95, 2007.

[128] A. Bayoumi, G. Yucesan, and D. Hutton, "On the closed form mechanistic modeling of milling: Specific cutting energy, torque, and power," *Journal of Materials Engineering and Performance*, vol. 3, pp. 151–158, 1994.

[129] K. Liu and S. N. Melkote, "Material strengthening mechanisms and their contribution to size effect in micro-cutting," *J. Manuf. Sci. Eng.*, vol. 128(3), pp. 730–738, 2006.

[130] A. Molinari and A. Moufki, "The merchant's model of orthogonal cutting revisited: A new insight into the modeling of chip formation," *International Journal of Mechanical Sciences*, vol. 50(2), pp. 124–131, 2008.

[131] W. W. Olson, S. A. Batzer, and J. W. Sutherland, "Modeling of chip dynamics in drilling," *CIRP International Workshop on Modeling of Machining Operations*, vol. 2 C7, pp. 1–15, 1998.

[132] S. A. Batzer, P. D. Rao, D. M. Haan, W. W. Olson, and J. W. Sutherland, "An experimental investigation of chip morphology in drilling," *S. M. Wu Symposium*, vol. 2, pp. 102–107, 1996.

[133] S. A. Batzer, D. M. Haan, P. D. Rao, W. W. Olson, and J. W. Sutherland, "Chip morphology and hole surface texture in the drilling of cast aluminum alloys," *Journal of Materials Processing Technology*, vol. 79, no. 1-3, pp. 72–78, 1998.

[134] T. Hoshi and H. Zhao, "Study of a high performance drill geometry," *CIRP Annals - Manufacturing Technology*, vol. 38, no. 1, pp. 87–90, 1989.

[135] J. A. Degenhardt, R. E. DeVor, and S. G. Kapoor, "Generalized groove-type chip breaker effects on drilling for different drill diameters and flute shapes," *International Journal of Machine Tools and Manufacture*, vol. 45, no. 14, pp. 1588–1597, 2005.

[136] A. Akhavan Farid, S. Sharif, and M. H. Idris, "Chip morphology study in high speed drilling of al-si alloy," *International Journal of Advanced Manufacturing Technology*, vol. 57, pp. 555–564, 2011.

[137] S. Dolinsek, S. Ekinovic, and J. Kopac, "A contribution to the understanding of chip formation mechanism in high-speed cutting of hardened steel," *Journal of Materials Processing Technology*, vol. 157-158, no. SPEC. ISS., pp. 485–490, 2004.

[138] I. S. Jawahir and C. A. Van Luttervelt, "Recent developments in chip control research and applications.," *CIRP Annals-Manufacturing Technology*, vol. 42(2), pp. 659–693, 1993.

[139] V. P. Astakhov, *Metal Cutting Mechanics.* CRC Press, Boca Raton, USA., 1998.

[140] S. Zhang and Y. B. Guo, "An experimental and analytical analysis on chip morphology, phase transformation, oxidation, and their relationships in finish hard milling," *International Journal of Machine Tools and Manufacture*, vol. 49(11), pp. 805–813, 2009.

[141] J. Barry and G. Byrne, "The mechanisms of chip formation in machining hardened steels," *Journal of Manufacturing Science and Engineering*, vol. 124, pp. 528–535, 2002.

[142] S. V. Subramanian, H. O. Gekonde, G. Zhu, X. Zhang, U. Urlau, and H. Roelofs, "Inclusion engineering of steel to prevent chemical tool wear," *Iron and Steelmaking*, vol. 31(3), pp. 249–257, 2004.

[143] J. Barry and G. Byrne, "Chip formation, acoustic emission and surface white layers in hard machining," *CIRP Annals - Manufacturing Technology*, vol. 51(1), pp. 65–70, 2002.

[144] E. M. Trent and P. K. Wright, *Metal Cutting*. Butterworth-Heinemann, Boston, 2000.

[145] V. P. Astakhov, *Geometry of single-point turning tools and drills*. Springer, London, 2010.

[146] K. Holmberg and A. Matthews, *Coatings tribology, Second edition*. Elsevier Ltd, Kidlington, Oxford, UK, 2009.

[147] A. R. Rodrigues and R. T. Coelho, "Influence of the tool edge geometry on specific cutting energy at high-speed cutting," *J. of the Braz. Soc. of Mech. Sci. & Eng*, vol. 29(3), pp. 279–283, 2007.

[148] R. S. Pawade, S. S. Joshi, and P. K. Brahmankar, "Effect of machining parameters and cutting edge geometry on surface integrity of high-speed turned inconel 718," *International Journal of Machine Tools and Manufacture*, vol. 48, pp. 15–28, 2008.

[149] A. I. Fernandez-Abia, J. Barreiro, L. N. Lopez de Lacalle, and S. Martinez, "Effect of very high cutting speeds on shearing, cutting forces and roughness in dry turning of austenitic stainless steels," *International Journal of Advanced Manufacturing Technology*, vol. 57, pp. 61–71, 2011.

APPROCHE CORRELATIVE VERS UNE PRODUCTION DURABLE DE FONTE ADI D'UN TRAITEMENT THERMIQUE INTEGRE INNOVANT ET DE SON USINABILITE

RESUME : Les impacts environnementaux dans la production des matériaux métalliques et leurs procédés de transformation sont en augmentation rapide et critique. Ils peuvent être réduits, dans une certaine mesure, par le développement soit d'un matériau de fonction ou par la mise en œuvre d'un nouveau processus de fabrication éco-durable. Dans cette optique, l'émergence récente de fonte « bainitique » (ADI –Austempered Ductile Iron-) peut être considéré comme un saut technologique important répondant à la demande croissante pour les matériaux à hautes caractéristiques mécaniques avec un coût de fabrication maîtrisé. La présente étude traite le développement d'une approche de couplage procédé par l'intégration du processus de coulée, de traitements thermiques et d'usinage de la fonte ductile ADI dans une optique de développement durable. Ce procédé innovant de fabrication de pièces en fonte ADI dit « dans la chaude de coulée » consiste à réaliser les traitements thermiques directement à la suite de la coulée en moule métallique en relation avec l'usinabilité induite. L'analyse des influences des paramètres de ce procédé intégré sur la microstructure et les propriétés mécaniques de l'ADI a été étudiée expérimentalement. Une approche méthodologique sur la coulabilité de la fonte a été développée, puis validée par simulation. Elle utilise les caractéristiques thermiques du métal en fusion pour corréler l'effet combiné du transfert de chaleur à l'état fondu, à l'interface moule/métal, et pendant l'écoulement au travers des sections critiques du moule afin de prédire les défauts de coulée. Enfin, l'usinage de la fonte ADI est étudié expérimentalement dans le cas du perçage à sec et en micro-lubrification (MQL), en lien avec les caractéristiques microstructurales, les mécanismes d'usure d'outil, de formation des copeaux et de la qualité de surface usinée. L'approche corrélative du couplage procédé visent essentiellement à (i) comprendre l'influence des caractéristiques microstructurales de cette nouvelle fonte ADI sur ses propriétés mécaniques, (ii) démontrer l'influence des caractéristiques thermophysiques sur la coulabilité de la fonte ductile dans un moule permanent, et (iii) mettre en corrélation les paramètres de perçage de cette nouvelle fonte ADI avec sa microstructure et ses paramètres de fabrication.

Mots clés : Fonte bainitique ADI, traitement thermique intégré, corrélation thermique, perçage à sec, perçage avec micro-lubrification, outils revêtus PVD.

CORRELATIVE APPROACH TOWARDS INTEGRATED CASTING-HEAT TREATMENT ROUTE AND MACHINING FOR SUSTAINABLE ADI MANUFACTURING

ABSTRACT : The environmental impacts of material production and processing are rapidly increasing and critical. These impacts can be reduced, to some extent, by development of either a suitable material or by implementing a novel process route to improve the material efficiency. In such circumstances, the recent emergence of near-net shape austempered ductile iron (ADI) can be considered as a significant economic advantage to the increasing industrial demand of cost and weight efficient materials. The present study is thus dedicated to the development of an innovative methodology for austempered ductile iron (ADI) manufacturing considering all production aspects such as melt treatment, casting, heat treatment and machining. The innovative process design advances the integrated approach towards casting and heat treatment practices for ADI production in a permanent mould. It is based on the fundamental correlation between the production conditions and its combined influences on the microstructure and mechanical properties of ADI. Moreover, the present study introduces a correlative thermal methodology approach to understand the castability of ductile iron in a permanent mould for ADI production. The simulation tool correlates the combined influences of thermal characteristics, heat transfer at melt/mould interface, and melt's castability on the final casting quality. Finally, the ecological machining of ADI is introduced by implementing the dry and MQL machining process. The key aspect of the novel ADI machinability was investigated with respect to its microstructural characteristics, tool wear mechanisms, chip formation characteristics and the machined surface's quality. The combined correlative approaches provide the key findings aim to (i) understand the influence of microstructural characteristics of novel ADI on its mechanical properties, (ii) demonstrate the influence of thermal characteristics of melt on the castability of ductile iron in a permanent mould, and (iii) correlating the machining characteristics of ADI with its microstructure and production conditions.

Keywords : Austempered ductile iron (ADI), Novel process route, Correlative thermal methodology, Dry drilling, MQL drilling, PVD-coated tools.